

**Benthic foraminiferal oxygen isotopes during
the Last Glacial Maximum and last
deglaciation: Paleoceanographic inferences
from an isotope-enabled global ocean model**

DISSERTATION

submitted in fulfillment of the requirements for the Doctoral degree in Natural Sciences
(Dr. rer. nat.) at the Department of Geosciences at the University of Bremen

presented by

Rike Völpel

Bremen, July 2018

Reviewers

Prof. Dr. Michael Schulz
MARUM and Faculty of Geosciences,
University of Bremen

Prof. Dr. Heiko Pälike
MARUM and Faculty of Geosciences,
University of Bremen

Date of colloquium: September 21, 2018

Affirmation

Name: Rike Völpel

Address: Department of Geosciences, Klagenfurter Straße 4, 28359 Bremen

Herewith, I affirm that

1. I wrote the present thesis independently and without illicit assistance from third parties,
2. I used no sources other than those indicated nor aids other than those permissible and
3. I appropriately referenced any text or content from other sources.

Place, Date

Signature

Own contribution

The first study has been autonomously prepared and conducted by the candidate with contribution from all co-authors. The technical development of the wiso and balance packages, including the development of the model code and the incorporation into the source code of a global climate model, was autonomously conducted by the candidate. The model simulation was set up by the candidate including the preparation of the forcing data sets. The candidate carried out the analysis of the model output, created all figures and wrote the manuscript, with co-authors giving scientific input. For the second study, the candidate autonomously set up the model experiment, including the preparation of the forcing data sets, and carried out the analysis of the results, while Stefan Mulitza and Jean Lynch-Stieglitz prepared the age model and analysis of the sediment cores. The DIVA script used for interpolation of the model output was provided by André Paul and revised by the candidate for the respective needs. All figures were prepared (except for Figure 4.2 and Figure 4.3 of Chapter 4) and the manuscript was authored by the candidate (except for section 4.2.4) with valuable contributions to the interpretation of the results and the discussion from all co-authors. The third study has been autonomously prepared and conducted by the candidate. Forcing data sets were prepared by the candidate. The model simulation and the analysis of the results were autonomously carried out by the candidate. The manuscript was written by the candidate with contributions from all co-authors.

Contents

List of Figures.....	i
List of Tables.....	iii
List of Abbreviations.....	v
Abstract.....	vii
Zusammenfassung.....	ix
Chapter 1 Introduction.....	1
1.1 Stable water isotopes.....	4
1.1.1 Background.....	4
1.1.2 Stable water isotopes in the hydrological cycle.....	5
1.1.3 Stable water isotopes in climate archives - $\delta^{18}\text{O}$ in foraminiferal calcite ..	8
1.1.4 Modeling stable water isotopes in the ocean.....	10
1.2 Thesis Objectives and Outline.....	11
Chapter 2 Technical Model Description.....	17
2.1 Overview of the MITgcm.....	17
2.2 Newly developed packages.....	20
Chapter 3 Stable water isotopes in the MITgcm.....	21
Abstract.....	21
3.1 Introduction.....	21
3.2 Methods.....	23
3.2.1 Ocean Model.....	23
3.2.2 Implementation of water isotopes.....	24
3.2.3 Observational data.....	27
3.2.3.1 $\delta^{18}\text{O}_w$ data.....	27
3.2.3.2 $\delta^{18}\text{O}_c$ data.....	27
3.3 Results.....	28
3.3.1 General model performance - temperature and salinity distribution.....	28
3.3.2 Stable water isotope distribution in ocean water.....	32
3.3.3 Relationship between stable water isotopes and salinity.....	35
3.3.4 $\delta^{18}\text{O}_c$ distribution.....	36
3.4 Discussion.....	38
3.4.1 Model performance.....	38
3.4.2 Sources of error for $\delta^{18}\text{O}_w$	41
3.4.3 Water mass structure.....	46
3.4.4 Planktonic foraminiferal $\delta^{18}\text{O}_c$	47

3.5	Conclusions.....	51
	Appendix A	52
Chapter 4	Water mass vs. sea-level effects on benthic foraminiferal oxygen isotope ratios in the Atlantic during the LGM	55
	Abstract.	55
4.1	Introduction	55
4.2	Materials and Methods	57
4.2.1	The ocean model - MITgcm.....	57
4.2.2	Experimental setup	58
4.2.3	Analyses	60
4.2.3.1	LGM data	60
4.2.3.2	Interpolation to higher resolution	60
4.2.4	Sediment cores off NW Africa	61
4.3	Results	66
4.3.1	SST anomalies.....	66
4.3.2	Planktonic foraminiferal $\delta^{18}\text{O}_c$ anomalies.....	66
4.3.3	Benthic foraminiferal $\delta^{18}\text{O}_c$	68
4.3.4	Modeled depth transect in the East Atlantic Ocean: sea-level change effect	71
4.4	Discussion.....	72
4.4.1	Simulated LGM state.....	72
4.4.2	Effect of the sea-level lowering on glacial-interglacial $\delta^{18}\text{O}_c$ anomalies .	79
4.4.3	Larger glacial-interglacial change in $\delta^{18}\text{O}_c$ below 2000 m water depth...	80
4.5	Conclusions.....	85
Chapter 5	Why do deep-sea $\delta^{18}\text{O}$ records resemble Antarctic temperature during Heinrich Events?	87
	Abstract.	87
5.1	Introduction	87
5.2	Material and Methods.....	89
5.2.1	The global ocean model	89
5.2.2	Experimental setup	90
5.3	Results	92
5.4	Discussion.....	94
5.4.1	What causes the benthic $\delta^{18}\text{O}_c$ pattern in marine deep-sea records?	94
5.4.2	Common origin for the resemblance between deep-sea and ice-core records?.....	98
5.5	Conclusions.....	99

Chapter 6 Conclusions and Outlook.....	101
References.....	105
Supplement S1 Technical Model Description.....	123
S1.1 MITgcm structure and compilation	123
S1.2 Packages overview	126
S1.3 Implementation of the wiso and balance packages into the source code ..	128
S1.4 Running the MITgcm with the wiso and balance packages	130
S1.5 Electronic Appendix	134
Supplement S2 Why do deep-sea $\delta^{18}\text{O}$ records resemble Antarctic temperature during Heinrich Events?	135
Acknowledgments	137

List of Figures

Figure 1.1: The benthic $\delta^{18}\text{O}$ stack.	1
Figure 1.2: Sketch of the effects of the hydrological cycle on $\delta^{18}\text{O}_w$	6
Figure 1.3: Fossil specimens of foraminifera.	10
Figure 1.4: Glacial-interglacial $\delta^{18}\text{O}_c$ values from the Brazil Margin.	13
Figure 1.5: Benthic and ice core $\delta^{18}\text{O}$ evolution.....	13
Figure 2.1: Possible processes in the MITgcm.	19
Figure 2.2: Representation of the topography in the MITgcm.	19
Figure 2.3: Common height coordinates vs. z^* coordinates.	19
Figure 2.4: Cubed sphere and regular latitude longitude grid system.	19
Figure 3.1: Annual mean SST anomaly (MITgcm - WOA13)	29
Figure 3.2: Annual mean SSS anomaly (MITgcm - WOA13).	30
Figure 3.3: Temperature and salinity zonally averaged ocean basin cross sections. ...	31
Figure 3.4: Annual mean surface $\delta^{18}\text{O}_w$ distribution.....	33
Figure 3.5: $\delta^{18}\text{O}_w$ zonally averaged ocean basin cross sections.	34
Figure 3.6: Relationship of simulated and observed $\delta^{18}\text{O}_w$ values.	35
Figure 3.7: Relationship of salinity and $\delta^{18}\text{O}_w$ in surface waters.	36
Figure 3.8: Annual mean surface $\delta^{18}\text{O}_c$ distribution.	37
Figure 3.9: Seasonal amplitude for $\delta^{18}\text{O}_c$	37
Figure 3.10: Relationship of simulated and measured $\delta^{18}\text{O}_c$ values.....	39
Figure 3.11: Annual mean precipitation and evaporation anomaly.....	40
Figure 3.12: Annual mean isotopic precipitation.	42
Figure 3.13: Annual mean $\delta^{18}\text{O}$ of river runoff.	44
Figure 3.14: Simulated and measured T-S- $\delta^{18}\text{O}_w$ diagrams.....	48
Figure 3.15: Species-specific relationship of simulated and measured $\delta^{18}\text{O}_c$ values. ...	50
Figure A.1: Time series of the correction factor.	53
Figure 4.1: Depth transects and core locations in the Atlantic Ocean.	62
Figure 4.2: Temporal variability of Fe/Ca.....	64
Figure 4.3: Benthic $\delta^{18}\text{O}_c$ records of sediment cores off NW Africa.....	65
Figure 4.4: Glacial-interglacial annual mean SST anomaly.....	67
Figure 4.5: Glacial-interglacial annual mean $\delta^{18}\text{O}_c$ anomaly.	69
Figure 4.6: Depth profiles of benthic $\delta^{18}\text{O}_c$	70
Figure 4.7: $\Delta\delta^{18}\text{O}_c$ change with depth off NW Africa.....	72
Figure 4.8: ΔT , $\Delta\delta^{18}\text{O}_c$ and $\Delta\delta^{18}\text{O}_c$ along depth transects without consideration of a sea-level change	73

Figure 4.9: ΔT , $\Delta\delta^{18}O_c$ and $\Delta\delta^{18}O_c$ along depth transects with consideration of a sea-level change. 74

Figure 4.10: Glacial-interglacial annual mean $\delta^{18}O_w$ anomaly..... 77

Figure 4.11: Stream function and dye tracer concentration in the Atlantic Ocean. 79

Figure 4.12: Sea-level effect along depth transects. 81

Figure 4.13: T-S diagrams in the Atlantic Ocean. 83

Figure 4.14: Vertical gradient along depth transects..... 85

Figure 5.1: Oxygen-isotope records from M35003-4 and BYRD..... 90

Figure 5.2: Evolution of T, $\delta^{18}O_w$ and $\delta^{18}O_c$ during the LGM and H1..... 93

Figure 5.3: Vector plots of the horizontal transport velocities..... 93

Figure 5.4: Temperature tendency analysis..... 96

Figure S1.1: Structure of the code layer in the MITgcm..... 124

Figure S2.1: Atlantic zonally averaged ΔT , $\Delta\delta^{18}O_w$ and $\Delta\delta^{18}O_c$ 135

Figure S2.2: Stream function of the AMOC for the LGM and H1..... 136

List of Tables

Table 1.1: Relative natural abundances of hydrogen and oxygen isotopes	4
Table 3.1: Main packages linked to the wiso package	27
Table 3.2: Arctic annual mean $\delta^{18}\text{O}$ of river runoff and discharge.	44
Table 3.3: $\delta^{18}\text{O}_w$ characteristics of the main water masses.....	48
Table 3.4: Data-model comparison of planktonic $\delta^{18}\text{O}_c$	50
Table 4.1: Locations and information on sediment cores	62
Table 4.2: Radiocarbon dates and age model of sediment cores	63
Table 4.3: Regional annual mean SST anomalies (LGM-PI).	66
Table 4.4: Regional annual mean $\delta^{18}\text{O}_c$ anomalies (LGM-PI).	68
Table S1.1: Model directories of the MITgcm	125
Table S1.2: Atmospheric boundary condition files.	127
Table S1.3: Subroutines of the wiso package and their purposes.....	128
Table S1.4: Subroutines of the balance package and their purposes.	129

List of Abbreviations

AABW	Antarctic Bottom Water
AAIW	Antarctic Intermediate Water
AGCM	Atmospheric General Circulation Model
AMOC	Atlantic Meridional Overturning Circulation
BP	Before present
CaCO ₃	Calcium carbonate
CCSM	Community Climate System Model
CO ₂	Carbon dioxide
CO ₃ ²⁻	Carbonate ion concentration
CORE	Coordinated Ocean-ice Reference Experiment
E	Evaporation
EMIC	Earth system Model of Intermediate Complexity
<i>G. bulloides</i>	<i>Globigerina bulloides</i>
<i>G. ruber</i> (w)	<i>Globigerinoides ruber</i> (white)
<i>G. sacculifer</i>	<i>Globigerinoides sacculifer</i>
GCM	General Circulation Model
GISS	Goddard Institute for Space Studies
GNIP	Global Network of Isotopes in Precipitation
GPCP	Global Precipitation Climatology Project
H1	Heinrich Event 1
LGM	Last Glacial Maximum
MARGO	Multiproxy Approach for the Reconstruction of the Glacial Ocean Surface
MITgcm	Massachusetts Institute of Technology general circulation model
<i>N. pachyderma</i> (s)	<i>Neogloboquadrina pachyderma</i> (sinistral)
NADW	North Atlantic Deep Water
NCAR IsoCam	National Center for Atmospheric Research Community Atmosphere Model including a water isotope scheme
NOC	National Oceanography Center
OGCM	Ocean General Circulation Model
P	Precipitation
PARTNERS	Pan-Arctic River Transport of Nutrients, Organic Matter and Suspended Sediments
PI	Pre-industrial

R	River runoff
RMSE	Root Mean Square Error
SSS	Sea Surface Salinity
SST	Sea Surface Temperature
UVic ESCM	University of Victoria Earth System Climate Model
VPDB	Vienna PeeDee Belemnite
VSMOW	Vienna Standard Mean Ocean Water
WOA09	World Ocean Atlas 2009
WOA13	World Ocean Atlas 2013
$\delta^{18}\text{O}_c$	Isotopic composition of foraminiferal calcite
$\delta^{18}\text{O}_w$	Isotopic composition of seawater

Abstract

Earth's climate system has been characterized by glacial-interglacial cycles over the last million years. Within the climate system, oceans play an important role, due to their large heat storage capacities and transport effects as well as being Earth's largest carbon dioxide sink. The understanding and prediction of the past, present, and future climate change relies on reconstructions from climate proxies. A widely used paleoclimate proxy is the oxygen isotopic composition of foraminiferal calcite shells. It reflects both the temperature and the isotopic composition of seawater, due to the thermodynamic isotope fractionation that occurs during calcite precipitation. Besides being used to, e.g., illustrate changes in temperature and global ice volume as well as to identify past meltwater events or to reconstruct past seawater densities, it has been commonly used as a tracer to infer changes in Atlantic water masses associated with shifts in the ocean circulation. However, some uncertainties remain with this proxy, since its separation into its individual components regarding the temperature and isotopic composition of seawater is challenging. In this regard, an isotope-enabled ocean modeling approach can help to gain a better understanding of the oxygen isotopic signal recorded in foraminiferal shells and the causes of the observed variations under climate change.

In this study, the three stable water isotopes H_2^{16}O , H_2^{18}O , and HDO were implemented into the Massachusetts Institute of Technology general circulation model, providing a tool, to directly compare to the wealth of the foraminiferal oxygen-isotope records and, thus, helping to infer water mass alterations due to changes in the thermohaline circulation under climate change scenarios. The stable water isotope scheme has extensively been evaluated against the modern isotopic composition of seawater on a global scale as well as against the oxygen isotope signal in foraminiferal calcite shells of plankton-tow data. The good agreement between the model and the observations implies that the here presented modeling approach can confidently be used for paleoceanographic and paleoclimatological related questions. Therefore, the ocean state during the Last Glacial Maximum was simulated to investigate the increase of the glacial-interglacial benthic oxygen isotope differences with water depth in the Atlantic Ocean. The smaller glacial-interglacial anomalies within the permanent thermocline are related to the glacial sea-level lowering of approximately 120 m, which brings the core locations closer to the surface. However, the enhanced glacial-interglacial anomalies in the deeper parts of the water column (> 2000 m) result from the expansion of the cold southern source water masses, implying that they are mainly temperature driven. Furthermore, this indicates that the enhanced vertical gradient at approximately 2000 m

water depth corresponds to the glacial water-mass boundary in the Atlantic Ocean, coinciding with estimates as seen in benthic foraminiferal stable carbon isotope values. Under the influence of an additional freshwater flux into the North Atlantic Ocean an idealized Heinrich Event 1 model experiment was performed to investigate the causes for the decrease of the oxygen isotopic composition in benthic foraminifera in response to abrupt climate change and their resemblance with Antarctic ice-core records. Due to the freshwater perturbation the Atlantic Meridional Overturning circulation weakens, whereby a substantial warming within the intermediate water depths occurs. Thus, the oxygen isotopic composition corresponds almost entirely to an enhanced temperature signal, which is driven by an initial increase in horizontal heat transport followed by downward heat transport via vertical advection. Hence, the resemblance between the oxygen-isotope records in benthic foraminifera and Antarctic ice-core records is attributable to the modulation of Antarctic atmospheric temperatures and deep water temperatures by the strength of the Atlantic Meridional Overturning circulation.

Quantifying the contribution of temperature and isotopic composition of seawater to the oxygen isotopic composition of foraminiferal calcite by using an isotope-enabled ocean model gives valuable findings and, thus, helps to advance the understanding and interpretation of this widely used proxy.

Zusammenfassung

Das Klimasystem der Erde wurde im Verlauf der vergangenen Millionen Jahren von glazialen-interglazialen Zyklen geprägt. In diesem Klimasystem spielen die Ozeane eine wichtige Rolle, da sie sowohl über eine hohe Wärmekapazität verfügen sowie den Wärmehaushalt regulieren, als auch die größte CO₂ Senke der Erde darstellen. Das Verständnis und die Prognosen für vergangene, gegenwärtige und zukünftige Klimaänderungen stützen sich auf Rekonstruktionen basierend auf Klimaproxies. Die Sauerstoffisotopenzusammensetzung der Kalzitschalen von Foraminiferen ist ein verwendeter Proxy in der Paläoklimatologie. Dieser spiegelt sowohl die Temperaturen als auch die Isotopenzusammensetzung des Meerwassers wider, da es während der Kalzitausfällung zu einer thermodynamischen Isotopenfraktionierung kommt. Verwendung findet er unter anderem für die Veranschaulichung der Änderungen der Temperaturen und des globalen Eisvolumens, wie auch das Ermitteln von vergangenen Schmelzwasserereignissen oder der Rekonstruktion vergangener Meerwasserdichten. Vor allem wurde der Proxy jedoch als Tracer für potentielle Änderungen der atlantischen Wassermassen in Verbindung mit Veränderungen in der Ozeanzirkulation verwendet. Es bleiben nichtdestotrotz Unsicherheiten in Bezug auf diesen Proxy bestehen, da die Aufteilung in die einzelnen Komponenten, Temperatur und Isotopenzusammensetzung des Meerwassers, schwierig ist. In diesem Zusammenhang kann ein Ozeanmodell kombiniert mit einem Isotopen-Modul hilfreich sein, um ein besseres Verständnis über das Sauerstoffisotopensignal in den Kalzitschalen von Foraminiferen und die Gründe ihrer durch Klimaänderungen ausgelösten Schwankungen zu erlangen.

In der vorliegenden Arbeit, wurden die drei stabilen Wasserisotope H₂¹⁶O, H₂¹⁸O und HDO in das Klimamodell des Massachusetts Instituts für Technologie eingebaut, sodass ein direkter Vergleich mit vorhandenen Sauerstoffisotopendaten gemessen an Foraminiferen möglich ist. Somit können sich Erkenntnisse über Wassermassenänderungen, aufgrund von Änderungen in der thermohalinen Zirkulation durch einen Klimawandel, ergeben. Das Wasserisotopenpaket wurde ausgiebig mit heutigen Daten der Isotopenzusammensetzung des Meerwassers sowie mit Sauerstoffisotopensignalen im Kalzit von Foraminiferen aus Planktonnetzen verglichen. Die gute Übereinstimmung zwischen dem Modell und den Beobachtungen lässt auch eine zuversichtliche Anwendung des hier vorgestellten Modellansatzes für paläoozeanographische und paläoklimatologische Fragestellungen zu. So wurde der Ozeanzustand während des letzten glazialen Maximums simuliert, um die mit der Wassertiefe größer werdenden glazialen-interglazialen Anomalien in benthischen

Sauerstoffisotopenprofilen im Atlantischen Ozean zu untersuchen. Die kleineren glazialen-interglazialen Anomalien in der permanenten Thermokline sind auf den glazialen Meeresspiegelabfall von etwa 120 m zurückzuführen, wodurch die Kernlokalisationen näher an die Oberfläche gebracht worden sind. Dahingegen sind die größeren glazialen-interglazialen Anomalien in der tiefen Wassersäule (> 2000 m) durch die Ausbreitung von kaltem Wasser südlichen Ursprungs zu erklären, was darauf schließen lässt, dass sie hauptsächlich temperaturgetrieben sind. Zudem kann der vergrößerte vertikale Gradient bei etwa 2000 m Wassertiefe mit der glazialen Wassergrenze gleichgesetzt werden, was bereits in stabilen Kohlenstoffisotopendaten benthischer Foraminiferen gesehen wurde. Ein idealisiertes Heinrich Ereignis 1 Modellexperiment wurde unter Berücksichtigung eines zusätzlichen Frischwassereintrages im Nordatlantik durchgeführt, um die Gründe für die Abnahme der Sauerstoffisotopenzusammensetzung in benthischen Foraminiferen aufgrund des abrupten Klimawandels und ihrer Ähnlichkeit zu antarktischen Eiskernen zu untersuchen. Durch die Frischwasserstörung wird die atlantische meridionale Umwälzbewegung geschwächt, wodurch es zu einer erheblichen Erwärmung in den Tiefen der Zwischenwassermassen kommt. Somit kann die Sauerstoffisotopenzusammensetzung fast ausschließlich durch ein erhöhtes Temperatursignal erklärt werden. Dieses wird verursacht durch eine anfängliche Erhöhung des horizontalen Wärmetransports gefolgt von einem nach unten gerichteten Wärmetransport überwiegend durch vertikale Advektion. Demnach ist die Ähnlichkeit zwischen den Sauerstoffisotopendaten von benthischen Foraminiferen und antarktischen Eiskernen auf die Anpassung von antarktischen Lufttemperaturen und Tiefenwassertemperaturen durch die Stärke der atlantischen meridionalen Umwälzbewegung zurückzuführen.

Die Quantifizierung der Beiträge von Temperatur und Isotopenzusammensetzung des Meerwassers zu der Sauerstoffisotopenzusammensetzung in den Kalzitschalen von Foraminiferen in einem Ozeanmodell, das mit einem Isotopen-Modul kombiniert wurde, führt zu wertvollen Ergebnissen und verbessert somit das Verständnis und die Interpretation dieses meist verwendeten Proxys.

Chapter 1 Introduction

Earth's climate has undergone major changes throughout history, that are attributable to climate forcings such as variations in the Earth's orbital parameters. For instance, over the last 500,000 years there have been five interglacial-glacial cycles, (Figure 1.1) which can be linked to the advance and retreat of the continental ice sheets leading to sea-level changes. However, since the mid-20th century, these natural variations are measurably overprinted by anthropogenic increase in greenhouse gas concentrations in the atmosphere at a rate unprecedented for the geological past [Karl and Trenberth, 2003]. For a better understanding and prediction of the past, present and future climate change, scientists rely on past climate reconstructions, which provide knowledge about the climate's response to changing climate conditions, using proxy recorders such as sediments, ice cores or corals.

Within the climate system, oceans have an important position, not only because they are Earth's largest carbon dioxide (CO₂) sink, but also because of the effect on the global temperature distribution due to their heat transport. The large-scale ocean circulation is characterized by a combination of wind-driven surface currents and currents driven by density differences dominating the deep sea. The so-called thermohaline circulation determines the general pattern of water masses, which today are formed in a few key locations of the North Atlantic and along Antarctica. Here, surface water is cooled by releasing its heat to the atmosphere or its salinity is increased by brine rejection during sea-ice formation, whereby it becomes dense enough to sink to significant depths. These

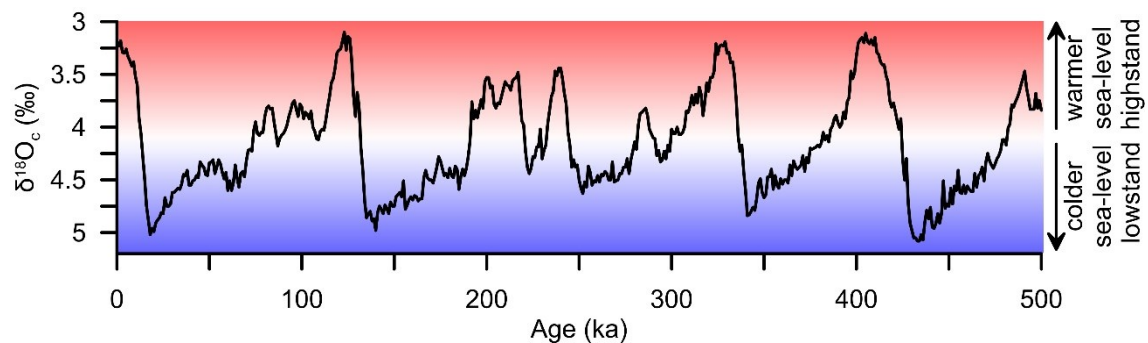


Figure 1.1: Stack of 57 globally distributed benthic foraminiferal oxygen-isotope ($\delta^{18}\text{O}_c$) records [Lisiecki and Raymo, 2005], showing the shift between glacial and interglacial cycles for the past 500,000 years. Downward trends in the benthic $\delta^{18}\text{O}_c$ curve reflect colder temperatures and increasing ice volumes on land (glacial; shaded in blue), while upward trends reflect warmer temperatures and reduced continental ice sheets (interglacial; shaded in red).

deep convection sites give rise to the presence of three distinguishable water masses in the Atlantic Ocean. The North Atlantic Deep Water (NADW) flows between 1000 m and 4000 m from the subpolar North Atlantic to the Southern Ocean, right above the northward flowing Antarctic Bottom Water (AABW), which occupies the bottom of the ocean and below the northward flowing Antarctic Intermediate Water (AAIW) [Tomczak and Godfrey, 2003]. Changes in surface heat and freshwater fluxes may have considerable effects on this circulation pattern leading to its reorganization and thus regional and global climate change. Based on the analysis of sediments in the form of microfossil assemblages, organic matter, and the elemental and isotopic composition of surface and bottom dwelling organisms (e.g., foraminifera) it was shown that the ocean has indeed experienced changes during the past [e.g., Boyle and Keigwin, 1987; Duplessy et al., 1988; Sarnthein et al., 1994; Yu et al., 1996; Rosenthal et al., 1997; Adkins et al., 2002; Curry and Oppo, 2005; Lynch-Stieglitz et al., 2006; Lippold et al., 2012; Howe et al., 2016].

Time periods, during which the climate differed significantly from today, represent excellent case studies for paleoclimate reconstructions. During the Last Glacial Maximum (LGM; 19,000 - 23,000 years before present [Mix et al., 2001]), the atmospheric CO₂ concentration was reduced by ~ 90 ppm compared to the pre-industrial [Monnin et al., 2001] and large continental ice sheets covered the Northern Hemisphere. The build-up of the continental ice sheets did not only lead to a sea-level lowering by approximately 120 m - 130 m [Fairbanks, 1989; Clark et al., 2009] and a global mean sea surface temperature (SST) cooling by about 1.9 °C compared to today [MARGO Project Members et al., 2009], but also to changes in the wind regimes, rearranging the ocean circulation pattern and thus causing a decrease in northward oceanic heat transport [Löfverström and Lora, 2017]. The subsequent deglaciation (19,000 - 11,000 years before present) is associated with the retreat of the northern hemisphere continental ice sheets due to changes in insolation [Clark et al., 2009], which led to a global mean sea-level rise of approximately 80 m [Clark et al., 2012]. However, this transition into the Holocene was interrupted by a few abrupt cooling events, such as Heinrich Event 1 (H1; [Heinrich, 1988; Hemming, 2004; Marcott et al., 2011]). H1 was characterized by massive episodic iceberg discharges from the Laurentide ice sheet, resulting in the release of large amounts of freshwater into the North Atlantic [Bond et al., 1992; Broecker, 1994; Andrews, 1998; Bard et al., 2000] and in a bipolar seesaw pattern in the SST, leading to a surface cooling in the Northern Hemisphere and a surface warming in the Southern Hemisphere [Clark et al., 2002]. Due to the addition of freshwater to the deep convection sites in the North Atlantic, the surface water density was reduced and deep-water formation weakened [Boyle and Keigwin, 1987; Clark et

al., 2002; *McManus et al.*, 2004].

Thus, both the LGM and H1 are associated with major reorganizations of the Atlantic Meridional Overturning Circulation (AMOC) [e.g. *Boyle and Keigwin*, 1987; *Sarnthein et al.*, 1994; *Curry and Oppo*, 2005; *Lynch-Stieglitz et al.*, 1999, 2006; *Keigwin and Boyle*, 2008; *Burke et al.*, 2011], which further emphasizes the importance of the ocean in regard to global climate change. Although a large number of proxy records exists, they are sometimes contradictory and suggest slightly different structures of the ocean circulation and different water mass distribution patterns for the LGM and H1 [e.g. *Sarnthein et al.*, 1994; *Lynch-Stieglitz et al.*, 2007; *Keigwin and Boyle*, 2008; *Burke et al.*, 2011; *Lippold et al.*, 2012].

The most commonly measured proxy is the oxygen isotopic composition of foraminiferal calcite ($\delta^{18}\text{O}_c$), which was first investigated by *Emiliani* [1955] and has ever since been the backbone of paleoceanographic studies. Due to the thermodynamic isotope fractionation that occurs during calcite precipitation [*Urey*, 1947; *Emiliani*, 1955; *Shackleton*, 1974], $\delta^{18}\text{O}_c$ reflects both the temperature and isotopic composition of seawater ($\delta^{18}\text{O}_w$). Over recent years it has been commonly used as a tracer to infer changes in the Atlantic water masses associated with shifts in the ocean circulation [*Lund et al.*, 2011, 2015; *Waelbroeck et al.*, 2011; *Oppo et al.*, 2015; *Voigt et al.*, 2017]. For instance, based on benthic $\delta^{18}\text{O}_c$ values, *Lund et al.* [2011] suggested that the water-mass boundary between the NADW and AABW occurred in a water depth of 2 km during the LGM, which is shallower than today. Nevertheless, to precisely interpret $\delta^{18}\text{O}_c$ records, and thus infer the ocean circulation and water mass distribution patterns, a separation of the two independent components (i.e., temperature and $\delta^{18}\text{O}_w$) is required.

This can be achieved by using an ocean modeling approach with embedded water isotopes. The understanding of climate processes in the past, present and future significantly increased since the development of numerical models. But, the model evaluation for past climate simulations is particularly difficult, because proxies do not directly record climate variables such as temperature or $\delta^{18}\text{O}_w$. However, isotope-enabled models can be directly compared to the wealth of foraminiferal $\delta^{18}\text{O}_c$ records, without an additional reconstruction of climate variables, since the isotopic fractionation processes during phase changes are explicitly simulated. This way, the causes for the $\delta^{18}\text{O}_c$ variations during the LGM and H1 can be investigated, and the current picture of water mass distribution and circulation during the respective climate period might be potentially be improved. In the long run, such a modeling approach might help to advance the understanding and interpretation of foraminiferal $\delta^{18}\text{O}_c$ data and, thus, aid to better understand climate change.

1.1 Stable water isotopes

1.1.1 Background

Isotopes physically refer to elements that occupy the same position in the periodic table, but differ in their atomic masses due to a different number of neutrons in their nucleus. Water molecules consist of two hydrogen (H) atoms bonded to a single oxygen (O) atom. Both, H and O exist in nature in the form of three isotopes. However, all three isotopes of O (^{16}O , ^{17}O and ^{18}O) are stable, while H has two stable isotopes (^1H and ^2H , also known as deuterium (D)) and one radioactive isotope (^3H). The relative natural abundances of H and O differ significantly (Table 1.1), which gives rise to the most relevant water molecules (listed with decreasing abundances): $^1\text{H}_2^{16}\text{O}$ (H_2^{16}O), $^1\text{H}_2^{18}\text{O}$ (H_2^{18}O) and $^1\text{H}^1\text{D}^{16}\text{O}$ (HDO). Since an accurate determination of the absolute abundance of the minor isotopes is challenging and cannot be carried out with sufficient precision, scientists rely on the isotopic ratio R , which is the ratio of the abundance of the heavier stable water isotope (H_2^{18}O or HDO) to the lighter stable water isotope (H_2^{16}O). For more quantitative results, these ratios are compared to an external standard and commonly expressed as δ values in parts per thousand (‰):

$$\delta i = \left(\frac{R_{sam}}{R_{std}} - 1 \right) \cdot 1000 \text{ (‰)}. \quad (1.1)$$

Here, i refers to either ^{18}O or D, while sam and std are the ratios of the sample and standard respectively. For the analysis of water samples, the Vienna Standard Mean Ocean Water (VSMOW) standard is used, which amounts to $2005.2 \cdot 10^{-6}$ for $\delta^{18}\text{O}$ [Baertschi, 1976] and $155.95 \cdot 10^{-6}$ for δD [de Wit et al., 1980]. A negative δ value indicates a depletion of the heavy isotopes, relative to the standard, while an enrichment is shown by a positive δ value. Mass differences of these stable water isotopes lead to effects in their physical and chemical properties. The consequences of these mass

Table 1.1: Relative natural abundances of hydrogen and oxygen isotopes [Mook, 2000].

Isotopes	Abundances (%)
^1H	99.985
^2H	0.015
^3H	$< 10^{-15}$
^{16}O	99.76
^{17}O	0.038
^{18}O	0.205

differences for molecules comprised of the heavy isotopes (e.g. H_2^{18}O and HDO) are (i) stronger covalent bonds and (ii) slower diffusion velocities, which conversely means that the light stable water isotopes react more easily than the heavier ones [Mook, 2000; Rohling, 2013]. This way, substances with different isotopic compositions are formed. The so called isotope fractionation between two substances A and B is quantified by the fractionation factor α , defined as

$$\alpha = \frac{R_A}{R_B}. \quad (1.2)$$

One can distinguish between equilibrium and kinetic fractionation. While equilibrium fractionation processes are mainly temperature dependent and fully reversible, kinetic effects are irreversible and cause deviations from equilibrium conditions. These fractionation processes are clearly recognizable during phase changes of stable water isotopes (e.g., evaporation and condensation), leading to an enrichment of one phase and a depletion of the other [Craig and Gordon, 1965; Gat and Gonfiantini, 1981].

1.1.2 Stable water isotopes in the hydrological cycle

The hydrological cycle, consisting of evaporation, atmospheric vapor transport and the return of freshwater to the ocean via precipitation, river runoff or iceberg melting, affects the $\delta^{18}\text{O}_w$ at the ocean surface (Figure 1.2). Seasonal sea-ice formation and melting lead to local variability of $\delta^{18}\text{O}_w$ in polar regions. In the ocean interior, $\delta^{18}\text{O}_w$ acts as a passive tracer because it does not dynamically alter the flow of the fluid [Craig and Gordon, 1965] and, thus, advection and mixing of water masses from different source regions determine its distribution. While seafloor water-rock isotope exchange processes at low (high) temperatures lead to depleted (enriched) $\delta^{18}\text{O}_w$ values [Muehlenbachs and Clayton, 1976; Walker and Lohmann, 1989], these processes are in isotopic balance on multi-millennial time scales (i.e. $< 10^5$ years) and not of concern for this study. However, the storage of freshwater in aquifers and ice sheets further affects the global $\delta^{18}\text{O}_w$ budget.

Due to evaporation an isotopic exchange occurs at the air-sea interface. Lighter water molecules evaporate more readily. Thus, they are preferentially enriched in the water vapor phase, because of the higher vapor pressure, causing a shift towards heavier $\delta^{18}\text{O}_w$ values in the remaining surface water. The relationship between the fractionation factor for equilibrium exchange, α_{l-v} , and SST (in K), is given by Majoube [1971]:

$$\alpha_{l-v} = e^{\frac{1.137}{SST^2} \cdot 10^3 - \frac{0.4156}{SST} - 2.0667 \cdot 10^{-3}}, \quad (1.3)$$

illustrating that at higher temperatures the fractionation decreases. Additionally, within the boundary layer between the air-sea interface and fully turbulent region, kinetic

fractionation during molecular diffusion occurs [Craig and Gordon, 1965; Merlivat and Jouzel, 1979; Gonfiantini, 1986]. It is controlled by the relative air humidity in the turbulent region and by the roughness of the air-sea interface with a near-surface mean wind speed of 7 m s^{-1} as a threshold. Once the water molecules are evaporated from the ocean surface, they move as water vapor poleward with progressively more rain out. Droplet formation usually experiences the same fractionation processes which occur during evaporation, but works in the opposite direction. Kinetic effects are negligible since droplets are in near equilibrium with atmospheric vapor [Ehhalt and Knott, 1965; Stewart, 1975]. The isotopic composition of the original vapor, precipitation and remaining atmospheric vapor is represented by a basic Rayleigh distillation process [Dansgaard, 1964]. Hence, the $\delta^{18}\text{O}$ of the first precipitation is similar to the original seawater composition, but with greater distance from the source region, both atmospheric vapor and associated new precipitation become more depleted. Thus, heavier water isotopes condense more readily. While atmospheric vapor is transported towards colder regions and successive condensation occurs, a quasilinear relationship

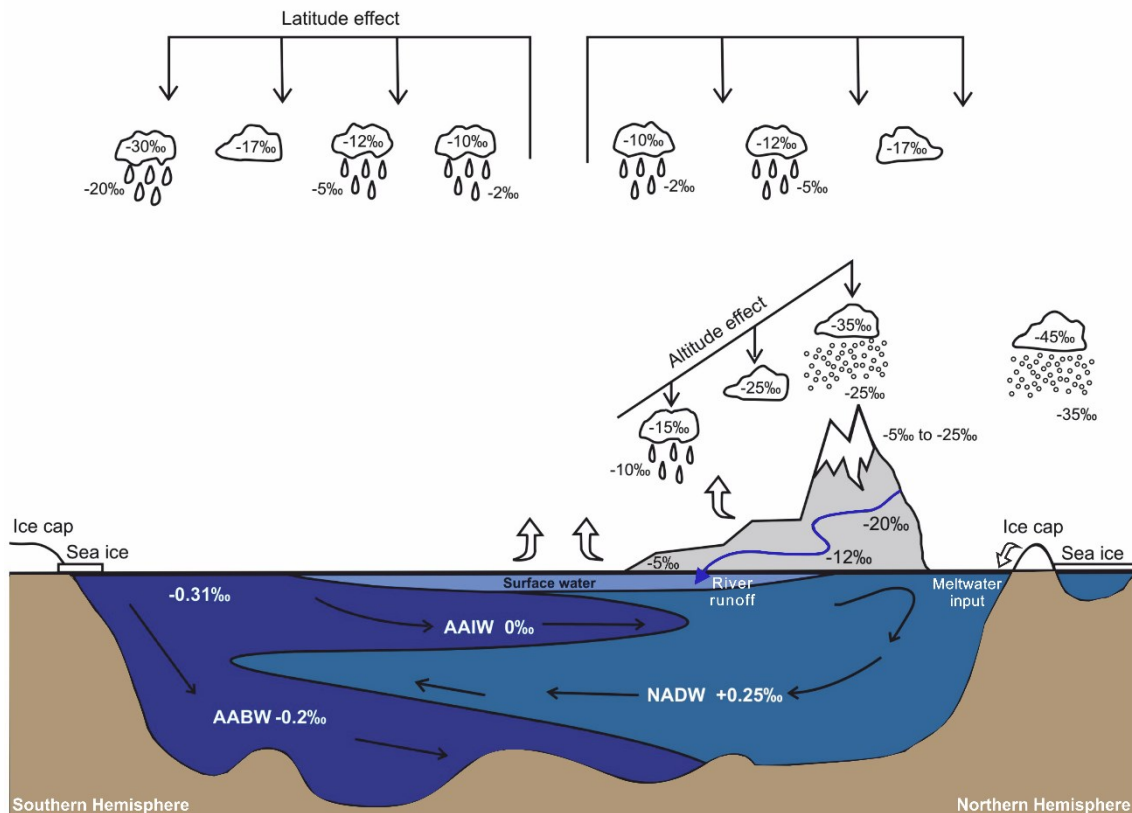


Figure 1.2: Schematic presentation of the effects of the hydrological cycle on $\delta^{18}\text{O}$ and its idealized values throughout the Atlantic Ocean. The main water masses, Antarctic Intermediate Water (AAIW), North Atlantic Deep Water (NADW) and Antarctic Bottom Water (AABW) within the Atlantic Ocean are also shown. Adapted from Paul et al. [1999].

of $0.69 \text{ ‰ } ^\circ\text{C}^{-1}$ between $\delta^{18}\text{O}$ of precipitation and temperature can be observed [Dansgaard, 1964]. This relationship applies to temperature values between $-40 \text{ }^\circ\text{C}$ and $15 \text{ }^\circ\text{C}$. Above $15 \text{ }^\circ\text{C}$, the so-called “amount effect” dominates, where for every 100 mm increase in rainfall a 1.5 ‰ depletion in $\delta^{18}\text{O}$ of precipitation is caused [Dansgaard, 1964]. Overall, these processes result in a more depleted precipitation in the high latitudes than in the tropics (latitude effect, Figure 1.2), which also applies to increasing altitudes, e.g., along high mountain ranges (altitude effect, Figure 1.2).

Consequently, effects of both evaporation and precipitation influence the $\delta^{18}\text{O}_w$ distribution at the ocean surface. Regions of net evaporation (e.g., the mid-latitudes) rather show a surface water enrichment in ^{18}O , while regions of net precipitation (e.g., the high latitudes) are dominated by depleted surface water. This gives also rise to the regional linear relationship between $\delta^{18}\text{O}_w$ and salinity, since similar physical processes determine their distribution [Craig and Gordon, 1965]. The addition of freshwater to the ocean surface may also occur via river runoff, which alters $\delta^{18}\text{O}_w$ in the proximity of river mouths. The isotopic value of the river discharge depends on the volumetrically weighted average $\delta^{18}\text{O}$ of precipitation over the catchment area, whereby river runoff in high latitudes is significantly depleted in ^{18}O compared to the low latitude river discharge (e.g., Mackenzie River: $\delta^{18}\text{O} < -18 \text{ ‰}$ and Parana River: $\delta^{18}\text{O} > -4.5 \text{ ‰}$, respectively; [Mook, 1982]). On multi-millennial time scales, the storage of precipitation in continental ice sheets, and to a lesser extent in aquifers, further affects the global $\delta^{18}\text{O}_w$ budget. Surface and deep waters are equally affected, because storage time-scales (on the order of 10^4 - 10^5 years) exceed those of the ocean ventilation (on the order of 10^3 years). Since ice sheets are formed through highly depleted precipitation (Figure 1.2), corresponding to the end of the Rayleigh distillation, the ocean is left relatively enriched in ^{18}O . Thus, the global mean $\delta^{18}\text{O}_w$ value has changed through time due to changes in continental ice volume, which are accompanied by sea-level variations. Therefore, a relationship between sea-level lowering and mean $\delta^{18}\text{O}_w$ enrichment has been estimated, which amounts to $0.012 \pm 0.001 \text{ ‰ } \text{m}^{-1}$ [Aharon, 1983; Shackleton, 1987; Fairbanks, 1989].

Furthermore, the formation and melting of sea ice may introduce some local seasonal variability in $\delta^{18}\text{O}_w$, because newly formed sea ice is enriched in ^{18}O relative to the seawater [O’Neil, 1968]. Even though the enrichment is rather small (fractionation factor for liquid-ice, $\alpha_{l-i} = 1.003$ [O’Neil, 1968]), long term seasonal changes do not have to cancel out, because brine rejection during sea-ice formation may lead to convection and transport of surface waters into the ocean interior. When sea ice melts, the renewed surface water would not have been affected by the freezing process and thus the isotopic effect would not cancel out.

Through the different processes of the hydrological cycle, the surface water is imprinted with a specific $\delta^{18}\text{O}_w$ composition, while advection and diffusion determine its distribution in the ocean interior, where no additional fractionation occurs. Consequently, the $\delta^{18}\text{O}_w$ can be considered as a conservative, passive tracer for newly formed water masses from different source regions, as long as the water mass does not get into contact with other sources or sinks. For instance, the NADW is distinguishable from the AABW (Figure 1.2), because the respective surface water isotopic composition in their formation region is determined by different processes of the hydrological cycle.

1.1.3 Stable water isotopes in climate archives - $\delta^{18}\text{O}$ in foraminiferal calcite

Since stable water isotopes are present in the hydrological cycle, they can be found in a wide variety of climate archives (e.g., ice cores, speleothems, tree-rings, peat-bog cellulose, lake and marine sediments), either as a direct or indirect record, making them one of the most useful tool in climate research.

Measurements of $\delta^{18}\text{O}$ variations in calcium carbonate (CaCO_3) of foraminiferal shells have been used in paleoceanographic studies for decades [e.g. *Urey, 1947; Emiliani, 1955, 1966; Shackleton, 1967*]. Foraminifera are single-celled eukaryotic organisms that either live in the upper water column among the ocean plankton or are benthic, living on the sea bed or just beneath the sediment surface [*Pearson, 2012*]. The shell, composed of CaCO_3 , is built from successive chambers added throughout their life cycle (ontogeny; Figure 1.3), and is deposited in sediments after death. Foraminifera can be found everywhere in the open ocean, are highly abundant and diverse, which makes them the most widely used paleoclimate proxy.

The oxygen in the foraminiferal calcite is derived from the ambient seawater, which reflects both local changes through freshwater fluxes and the global ice volume effect. However, its incorporation is further driven by temperature, because of the thermodynamic isotope fractionation that occurs during calcite precipitation [*Urey, 1947; Emiliani, 1955; Shackleton, 1974*]. Scientists have published a number of paleotemperature equations that represent the aforementioned relationship [*Epstein et al., 1953; Craig, 1965; O'Neil et al., 1969; Shackleton, 1974; Erez and Luz, 1983; Kim and O'Neil, 1997*], which reveal a $\delta^{18}\text{O}_c$ decrease of 0.21 ‰ - 0.27 ‰ for a 1° C increase in temperature. Thus, $\delta^{18}\text{O}_c$ provides information on the $\delta^{18}\text{O}$ and temperature of ambient seawater. As long as one of the two parameters is known, a detailed hydrographic description of the ancient ocean can be obtained. Nevertheless, vital effects such as the ontogenic effect, the symbiont photosynthesis effect, the respiration effect, the

gametogenic effect as well as the effect of changes in carbonate ion concentrations [CO_3^{2-}] may introduce some deviations from equilibrium fractionation [Lane and Doyle, 1956; Bé, 1980; Duplessy *et al.*, 1981; Spero and Lea, 1993, 1996; Spero *et al.*, 1997; Bemis *et al.*, 1998]. Deep-sea benthic foraminifera are less prone to these disequilibrium effects than planktonic foraminifera (at least for the glacial-interglacial cycle), since they live in an environment with very stable low temperatures and a complete absence of photosynthetic activity. The disequilibrium effects may operate in opposite directions, masking one another. For instance, while some species add an additional thick calcite layer, which is enriched in ^{18}O , at the end of their life cycle (gametogenic effect) [e.g. Bé, 1980], increased [CO_3^{2-}] lead to more depleted $\delta^{18}\text{O}_c$ values (carbonate ion effect) [e.g. Spero *et al.*, 1997]. These factors have to be kept in mind when investigating the isotopic composition in foraminiferal calcite.

Overall, the isotopic record derived from measurements of fossil foraminiferal shells is not only used to investigate past hydrographic changes of the ocean and climate. Likewise, it is an indispensable tool for stratigraphic correlation and timescale refinement, which is attributable to the early works of *Emiliani* [1955], who divided the marine foraminiferal isotope record into individual cycles (Marine Isotope Stages), which were later demonstrated to be driven by orbital cyclicity [Hays *et al.*, 1969; Broecker and van Donk, 1970; Hays *et al.*, 1976].

Furthermore, stable water isotopes can also be found in climate archives such as ice cores from Antarctica [e.g., Jouzel *et al.*, 1987a; EPICA Community Members *et al.*, 2004] as well as from Greenland [e.g., Johnsen *et al.*, 1995], which record $\delta^{18}\text{O}$ variations over several interglacial-glacial cycles. Based on the linear relationship between the $\delta^{18}\text{O}$ of precipitation forming the ice sheets, and the local surface air temperature at mid- to high latitudes [Dansgaard, 1964], scientists are able to use the isotopic signal as a paleothermometer and can thus, reconstruct past temperatures. This is a very straightforward approach, because the $\delta^{18}\text{O}$ signal is recorded with only little post-depositional alteration, albeit the source regions may change through time. In non-polar environments, $\delta^{18}\text{O}$ variations in ice cores from the tropical high altitudes (e.g. the Tibetan Himalayas) rather record the intensity of precipitation and thus give insights into the magnitude and frequency of large-scale phenomena such as the El Niño Southern Oscillation [Thompson, 2000]. Isotopic variations in peat-bog cellulose, however, depend on the plants' source water due to the biochemical fractionation between the two components and, can thus, be used as a proxy to infer environmental changes, such as temperature, humidity and/or precipitation shifts [Ménot-Combes *et al.*, 2002; Daley *et al.*, 2009; Moschen *et al.*, 2009]. Variations of $\delta^{18}\text{O}$ can further be measured in CaCO_3

of speleothems. Speleothems are composed of calcite formed from groundwater dripping in caves and thus, provide insights into climate changes via variations in their chemistry. This way, changes in the intensity and variations in the amount of monsoonal rainfall have been investigated [e.g. *Wang et al.*, 2001; *Fleitmann et al.*, 2003].

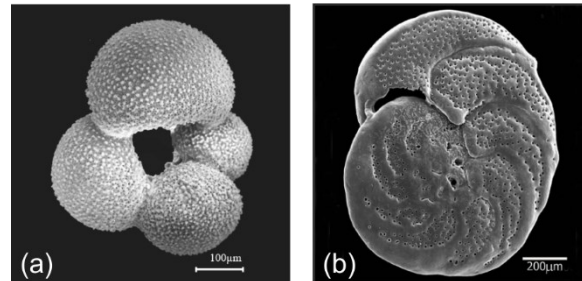


Figure 1.3: Fossil specimens of (a) *Globigerina bulloides* (planktonic foraminifera) and (b) *Cibicides wuellerstorfi* (benthic foraminifera). Photo courtesy of <http://www.foraminifera.eu> and citations therein.

1.1.4 Modeling stable water isotopes in the ocean

Modeling stable water isotopes in a numerical ocean model offers a direct comparison with the measured isotopic data in the foraminiferal calcite without any prior reconstruction of climate variables, because both temperature and $\delta^{18}\text{O}_w$ are simultaneously simulated. Thus, it can help to improve our understanding of the $\delta^{18}\text{O}_c$ signal and the causes of the observed variations through time, since the isotope-enabled models can be forced with different climatic boundary conditions.

The implementation of stable water isotopes in an ocean model always follows the same approach. By default, any ocean model code contains the “normal” water H_2^{16}O , which has to be tripled for isotope modeling to additionally simulate H_2^{18}O and HDO. As long as there is no phase change in the model’s hydrological cycle, all water tracers behave exactly the same. However, in case of a phase transition additional fractionation processes have to be considered. For the ocean component in the climate system, fractionation during evaporation is the key process. In general, it is treated as equilibrium fractionation, with a correction for wind-dependent kinetic effects [*Merlivat and Jouzel*, 1979; cf. section 1.1.2]. The required temperature-dependent fractionation coefficient is obtained from lab experiments [*Majoube*, 1971]. Further fractionation processes occur in polar regions during the formation of sea ice, but are often neglected, because they only lead to minor effects on the isotopic composition in the ocean [*Craig and Gordon*, 1965]. To simulate the isotopic variations in the ocean, the isotopic composition of the freshwater fluxes entering the ocean (precipitation and river runoff) are needed. These

can either be taken from observational data or are obtained from suitable atmospheric model output.

The implementation of stable water isotopes in atmospheric model components already started with *Dansgaard* [1964], who developed a simple Rayleigh-type model approach, and continued with *Joussaume et al.* [1984] and *Jouzel et al.* [1987b], who initiated the implementation in atmospheric general circulation models (AGCM). Only more than a decade later, *Schmidt* [1998] was the first who implemented stable water isotopes in an ocean model. Since then, stable water isotopes have been implemented in a number of different ocean models, such as Earth system Models of Intermediate Complexity (EMIC; [e.g., *Roche et al.*, 2004b; *Brennen et al.*, 2012; *Roche*, 2013]), Ocean general circulation models (OGCM; [e.g., *Schmidt*, 1998; *Paul et al.*, 1999; *Delaygue et al.*, 2000; *Wadley et al.*, 2002; *Xu et al.*, 2012]) as well as coupled GCMs [e.g., *Tindall et al.*, 2010; *Werner et al.*, 2016]. The advantage of EMICs is the reduction of the computational costs, since the complexity of model physics, typically found in GCMs, is reduced, whereby model runs for a much longer simulation period can be carried out. All GCMs (and some EMICs) however, represent a most complete three-dimensional state of the ocean. A closed model system simulates all relevant parameters determining the distribution and evolution of the isotopic composition by the model itself. This way, the dependence of the isotopic composition on climate-related variables like surface temperatures or meltwater fluxes can be analyzed in-depth. No matter which model is used, it has to be evaluated against present-day observational data. A typical target for ocean isotope-enabled models is the reasonable capturing of the regional linear relationship between $\delta^{18}\text{O}_w$ and salinity, which is, according to ocean model results, temporally variant [*Schmidt*, 1998].

Overall, implementing stable water isotopes into different ocean models enables the evaluation and comparison among one another, which will further broaden and deepen our insights in the processes affecting $\delta^{18}\text{O}_c$.

1.2 Thesis Objectives and Outline

The $\delta^{18}\text{O}_c$ of both planktonic and benthic foraminifera has been widely used as a key proxy for paleoceanographic and paleoclimatological interpretations, such as the identification of past meltwater events [*Bond et al.*, 1992; *Knies and Vogt*, 2003; *Thornalley et al.*, 2010b], reconstruction of past sea surface salinities [*Rostek et al.*, 1993; *Rohling*, 2007] and $\delta^{18}\text{O}_w$ [*Waelbroeck et al.*, 2014] as well as inferences on past sea-level changes [*Labeyrie et al.*, 1987; *Siddal et al.*, 2003; *Waelbroeck et al.*, 2002] and approximation of past seawater densities [*Lynch-Stieglitz et al.*, 1999; *Billups and*

Schrag, 2000]. However, it is probably best known for revealing the long history of global climate change based on the benthic $\delta^{18}\text{O}_c$ stack [*Lisiecki and Raymo, 2005*], which illustrates the change in temperature and global ice volume. So even though the benthic $\delta^{18}\text{O}_c$ values were mostly associated with fluctuations in continental ice volume, recent studies have demonstrated that they are also influenced by deep water hydrographic changes [*Shackleton, 2000; Elderfield et al., 2012; Rohling et al., 2014*].

Hence, although this particular proxy is extensively used some uncertainties remain, especially regarding the causes for the specific $\delta^{18}\text{O}_c$ evolution, since the separation of $\delta^{18}\text{O}_c$ into its individual temperature and $\delta^{18}\text{O}_w$ components is challenging.

A well-known feature of the LGM Atlantic Ocean is the strong vertical gradient in benthic foraminiferal stable carbon isotopes ($\delta^{13}\text{C}$), which is interpreted as the glacial water-mass boundary between the NADW and AABW at 2000 m water depth [*Curry and Oppo, 2005; Duplessy et al., 1988; Sarnthein et al., 1994*]. However, less well recognized is that a similar pattern occurs within the benthic $\delta^{18}\text{O}_c$ records. For instance, profiles at the Brazil Margin show a larger increase in glacial $\delta^{18}\text{O}_c$ below 2000 m water depth (Figure 1.4). The enhanced $\delta^{18}\text{O}_c$ values are most easily observed in the anomaly between the LGM and Holocene profiles (Figure 1.4, right panel), clearly separating the shallow (< 2000 m) and deep (> 2000 m) $\delta^{18}\text{O}_c$ anomalies from each other. The change in $\delta^{18}\text{O}_c$ between 1 and 3 km amounts to 0.3 ‰, and thus points also to a boundary at approximately 2000 m water depth as is seen in $\delta^{13}\text{C}$. This pattern has also been observed in $\delta^{18}\text{O}_c$ data from the Blake Ridge [*Keigwin, 2004; Lund et al., 2011*]. Consequently, it seems to be a rather robust pattern, at least for the western Atlantic Ocean. Nevertheless, the questions remain, what are the actual drivers behind this pattern, except for the rearrangement of the water masses associated with the LGM and whether it is also recognizable in the eastern Atlantic Ocean?

Abrupt changes in climate over the last glacial cycle are pronouncedly visible in temperature swings in Greenland ice cores inferred from the $\delta^{18}\text{O}$ record [*Dansgaard et al., 1993; Grootes et al., 1993*]. While they are characterized by fast warmings and slow coolings, a rather gradual warming and cooling is recognizable in the Antarctic temperature variations [*Johnsen et al., 1972; Jouzel et al., 1987a*]. This points out to the thermal bipolar seesaw theory [*Mix et al., 1986; Crowley, 1992; Stocker and Johnsen, 2003*], which is associated with a weaker AMOC due to freshwater perturbations and thus a reduction in northward heat transport [*Ruddiman and McIntyre, 1981; Broecker et al., 1985; Broecker and Denton, 1990; Crowley, 1992; Rühlemann et al., 2004; Came et al., 2007; Schmidt et al., 2012; Pedro et al., 2018*]. In particular, this becomes apparent

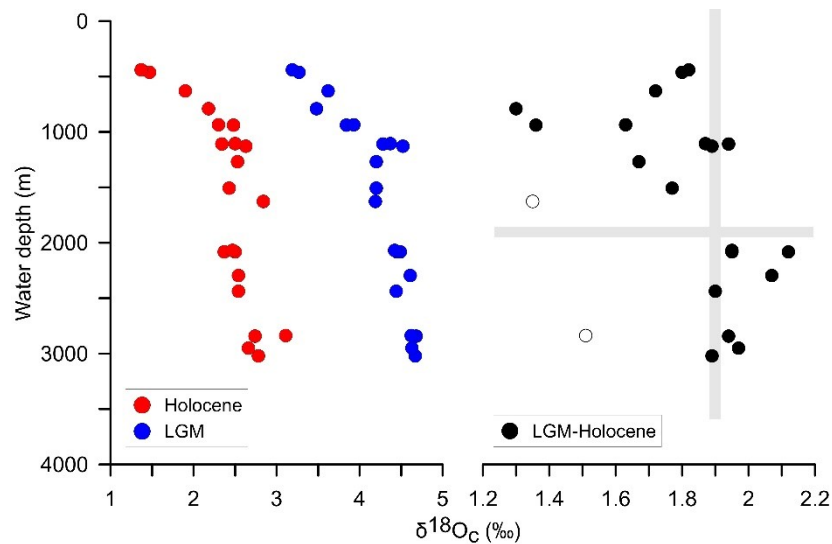


Figure 1.4: The $\delta^{18}O_c$ values with water depths for the Holocene and LGM (left panel) of the benthic foraminiferal species *Cibicidoides* spp. from the Brazil Margin [Curry and Oppo, 2005]. The $\delta^{18}O_c$ anomalies (LGM - Holocene) reveal a clear increase with water depths resulting in a boundary at approximately 2000 m water depth (right panel). The two open circles correspond to outliers defined by Lund et al. [2011]. Figure adapted from Lund et al. [2011].

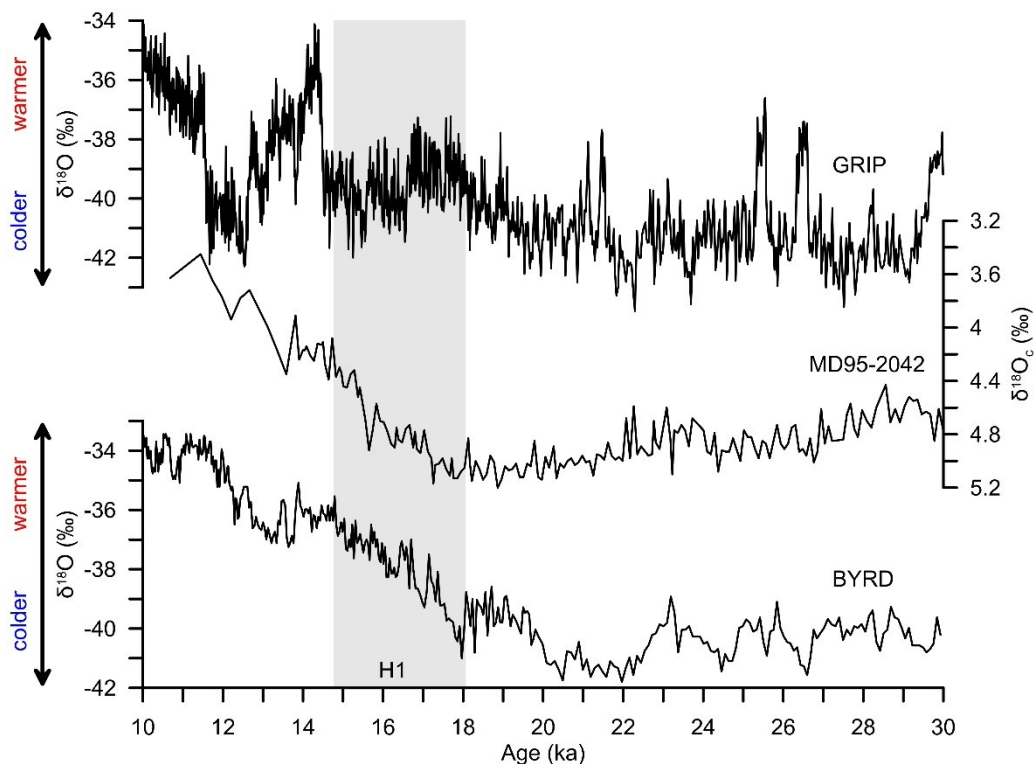


Figure 1.5: The $\delta^{18}O$ evolution of the past 10-30 ka from a Greenland ice core (GRIP [Dansgaard et al., 1993]), Antarctic ice core (BYRD [Blunier et al., 1998]) and benthic $\delta^{18}O_c$ record from a sediment core recovered on the Iberian margin (MD95-2042 [Shackleton et al., 2000]). The grey shading highlights the Heinrich Event 1 (H1), in which the warming phase in Antarctica coincides with a Greenland cooling.

during the H1 (Figure 1.5). Comparison with planktonic $\delta^{18}\text{O}_c$ records from deep-sea cores show synchronous changes of the North Atlantic with the Greenland ice-core record (e.g. GeoB 1023-5 [Schneider *et al.*, 1992]; MD95-2042 [Shackleton *et al.*, 2000]), while benthic $\delta^{18}\text{O}_c$ values seem to record a signal that appears to be linked to the Antarctic ice-core record (Figure 1.5). Based on both sediment records and model simulations a subsurface and intermediate depths warming during H1 was recognized [Skinner *et al.*, 2003; Rühlemann *et al.*, 2004; Marcott *et al.*, 2011; Ezat *et al.*, 2014; Weldeab *et al.*, 2016]. However, if this is indeed the explanation for the decreasing benthic $\delta^{18}\text{O}_c$ values during H1 is still a matter of investigation, because some authors also suggest that isotopically depleted surface water was transported into the deep ocean by brine formation [e.g. Waelbroeck *et al.*, 2006].

Thus, modeling temperature and $\delta^{18}\text{O}_w$ simultaneously in an ocean model is a straightforward approach to disentangle these unresolved causes for the $\delta^{18}\text{O}_c$ evolution. By implementing the stable water isotopes in the Massachusetts Institute of Technology general circulation model (MITgcm), a tool is provided that not only investigates their distribution in the ocean during present and past climate conditions, and, thus, infer water mass alterations due to AMOC changes, but also enables the direct comparison with the wealth of the foraminiferal $\delta^{18}\text{O}_c$ from sediment records. Consequently, the contribution of temperature and $\delta^{18}\text{O}_w$ to $\delta^{18}\text{O}_c$ can be quantified with regard to different climate conditions.

Hence, the following scientific questions will be addressed and the ensuing hypotheses will be tested:

1. How good does the newly developed water isotope package within the MITgcm simulate the $\delta^{18}\text{O}_w$ structure of the pre-industrial ocean and does the modeled $\delta^{18}\text{O}_c$ coincide with measurements from foraminifera?
2. What causes the larger difference with water depth in the benthic $\delta^{18}\text{O}_c$ anomalies between the LGM and Holocene in the Atlantic Ocean?
 - The benthic $\delta^{18}\text{O}_c$ signal from sediment records within the permanent thermocline are strongly overprinted by sea level related changes.
 - The benthic $\delta^{18}\text{O}_c$ signal in the deep Atlantic Ocean during the LGM changes due to the admixture of cold AABW.
 - Vertical gradients of the glacial-interglacial benthic $\delta^{18}\text{O}_c$ anomalies can also be interpreted as the water-mass boundary in the Atlantic Ocean as seen in $\delta^{13}\text{C}$.
3. What leads to the resemblance between deep-sea benthic $\delta^{18}\text{O}_c$ and Antarctic ice-core records during H1?

- Due to the freshwater perturbation in the North Atlantic Ocean the AMOC weakens, effectively warming the intermediate depth waters, whereby the benthic $\delta^{18}\text{O}_c$ decrease almost entirely corresponds to a deep-water temperature signal.
- Both proxies are sensitive to and driven by the strength of the AMOC.

In Chapter 2 a short overview of the MITgcm and its novel aspects is given. Furthermore, the newly stable water isotope package (wiso) and the additional balance package are introduced.

In Chapter 3 the implementation of stable water isotopes in the MITgcm is presented, including a detailed overview of the underlying equations. The results of a pre-industrial model simulation are given, which have been evaluated against modern $\delta^{18}\text{O}_w$ values of the global ocean as well as $\delta^{18}\text{O}_c$ values of plankton-tow data.

In Chapter 4 a LGM simulation with embedded stable water isotopes is set up and compared with SST reconstructions from different proxy records as well as with $\delta^{18}\text{O}_c$ values of planktonic foraminifera. It is used to investigate the increase of the glacial-interglacial $\delta^{18}\text{O}_c$ differences with water depth in the Atlantic Ocean.

In Chapter 5 a freshwater hosing experiment corresponding to H1 conditions is performed. This way, the causes and mechanism for the benthic $\delta^{18}\text{O}_c$ evolution under a nearly AMOC collapse are investigated, giving insights into the resemblance between the benthic $\delta^{18}\text{O}_c$ and Antarctic ice-core records.

Chapter 3 through Chapter 5 of this thesis are made-up of three individual manuscripts, which are either peer-reviewed and published (Chapter 3 in *Geoscientific Model Development*), in review (Chapter 4 to *Paleoceanography and Paleoclimatology*) or are in the early stages of preparation for publication (Chapter 5 to *Geophysical Research Letter*). This might lead to a few repetitions, especially in the method sections, where the model configuration is described. This thesis ends with a conclusion and outlook (Chapter 6) as well as a Supplement, which provides detailed information about the implementation of the wiso and balance packages into the source code of the MITgcm.

Chapter 2 Technical Model Description

2.1 Overview of the MITgcm

The Massachusetts Institute of Technology general circulation model (MITgcm) has been used to realize the implementation of stable water isotopes (H_2^{16}O , H_2^{18}O , and HDO) and for the investigation of their distribution in the ocean under different climate conditions.

The MITgcm is a numerical model designed to study the dynamics of both the atmosphere and the ocean, separately or even in a coupled mode using one hydrodynamical kernel [Adcroft *et al.*, 1997]. The ocean component of the MITgcm is rooted in the Navier Stokes equations for an incompressible Boussinesq fluid. The flow is assumed to be incompressible because the acoustic modes are filtered due to the large separation between those and the dynamical modes of interest (speed of sound \gg e.g., baroclinic wave speed). The Boussinesq approximation is used, since in the ocean, the resting or reference densities are typically much larger than the density variations that arise due to dynamics. This way, the momentum equations are more linear [Marshall *et al.*, 1997a, b]. A detailed description of the model equations is given in Marshall *et al.* [1997a, b].

The MITgcm further offers a non-hydrostatic capability, which allows the model to simulate both small-scale and large-scale processes (Figure 2.1). For large-scale processes, such as a gyre system or the global circulation, the hydrostatic approximation is valid. However, the non-hydrostatic approximation is gaining importance when the horizontal scale becomes comparable to its vertical scale, which presumably arises between 10 km and 1 km [Marshall *et al.*, 1997b].

Another important aspect of the MITgcm is the employment of the finite volume technique. Unlike the conventional models, which use a “full step” approach to represent topography (Figure 2.2a), the representation error of topography is reduced when the model is discretized using the finite volume methodology [Adcroft *et al.*, 1997]. Since this approach allows “partially filled” or even “piecewise” cells, the thickness of the volumes abutting the boundary can be adjusted to better match the topography (Figure 2.2b and c, respectively). At the surface, the MITgcm provides three treatments of the upper boundary, which can either be a rigid-lid or a free-surface (linear and nonlinear) assumption [Campin *et al.*, 2004]. While the rigid-lid imposes a pressure on the fluid, the linear free-surface permits the propagation of shallow water waves using a fixed

geometry. In contrast, the geometry of the upper level in the nonlinear free-surface is time dependent and can evolve freely. Especially in conjunction with real freshwater flux boundary conditions, the nonlinear free-surface is very useful, because the salinity in the global ocean changes due to altering ocean volume resulting from fluxes through the air-sea interface. As opposed to many ocean as well as coupled atmosphere-ocean models, which use a virtual salt flux to mimic this effect, the sea surface salinity can evolve freely. Thus conservation of salt is achieved. However, the freely evolving surface becomes problematic when the variations become large with respect to the vertical resolution, whereby the upper layer can vanish (Figure 2.3a) and out-crop the layer below. To avoid the possible vanishing of the upper layer, the MITgcm offers a modified height coordinate, z^* [Adcroft and Campin, 2004]. This way, the entire vertical grid is scaled with the surface elevation and, thus, transforms the physical free-surface into a fixed domain (Figure 2.3b). A detailed description on z^* coordinates and the transformation of the Navier Stokes equations into z^* coordinates is given in Adcroft and Campin [2004].

The horizontal components of the MITgcm are described by an Arakawa C-grid [Arakawa and Lamb, 1977] with a number of coordinate systems available (cartesian, spherical-polar, and curvilinear). Further, it offers gridding of the sphere on the conformally expanded spherical cube (Figure 2.4a) [Adcroft et al., 2004a]. Thus, the converging meridians of conventional latitude-longitude grids (Figure 2.4b) are avoided. This not only provides a much more uniform coverage and, thus, the polar regions are more accurately represented, but it also allows for a much higher resolution before it becomes prohibitive, due to the increased computational cost in regard to the time step length.

Additionally, the MITgcm provides adjoint counterparts, enabling it to be applied to parameter and state estimation problems [Heimbach et al., 2002], which will be of interest for future paleo-applications with the implemented stable water isotopes.

A description of the MITgcm internal structure, code compilation, experimental configuration as well as an overview of the used packages for this thesis is given in the Supplement S1.

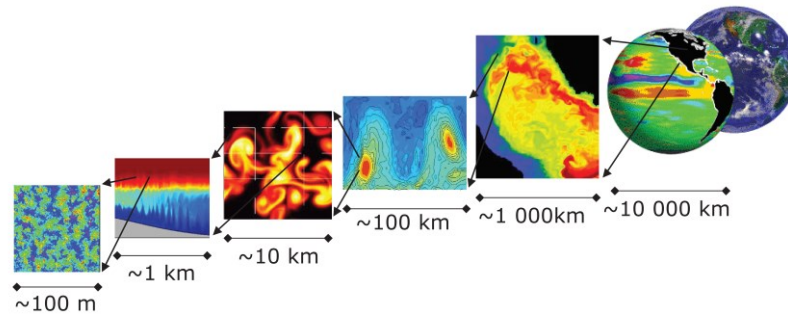


Figure 2.1: The non-hydrostatic capability of the MITgcm allows the model to address a wide range of processes on different horizontal/vertical scales - from convection (left), geostrophic eddies (middle) to global circulation patterns (right). Figure adapted from *Adcroft et al. [2004b]*.

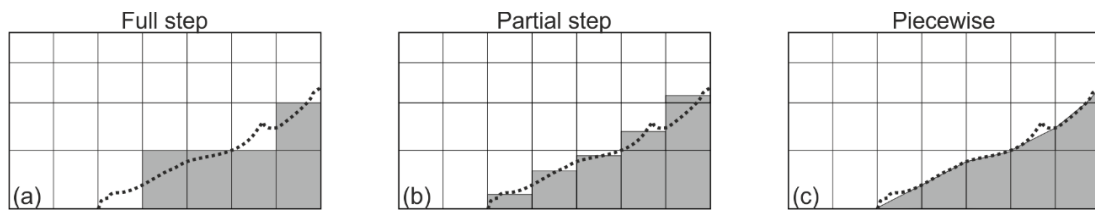


Figure 2.2: Representation of topography (dotted line) using a “full step” (a), “partial step” (b) and piecewise (c) approach in an ocean model. Figure adapted from *Adcroft et al. [1997]*.

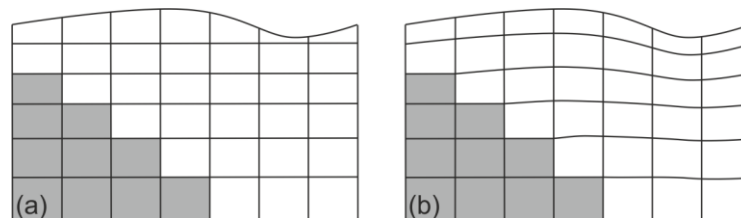


Figure 2.3: Schematic representation of a nonlinear free-surface using common height coordinates (a) and the z^* coordinates (b). Figure adapted from *Adcroft and Campin [2004]*.

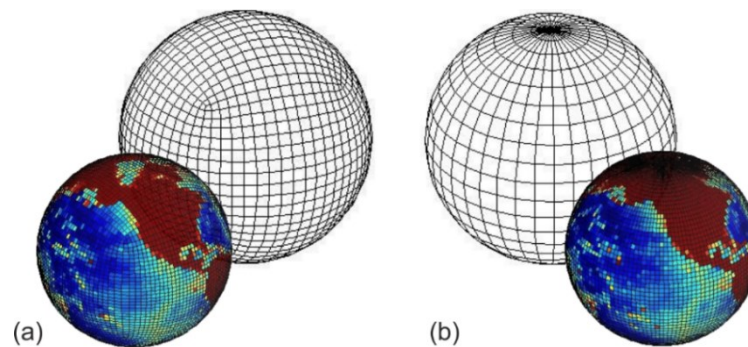


Figure 2.4: Expanded spherical cube system offered by the MITgcm (a) and a regular latitude-longitude grid (b). Picture courtesy of <http://mitgcm.org/cubedsphere/>.

2.2 Newly developed packages

The `wiso` package has been developed to simulate the stable water isotopes H_2^{16}O , H_2^{18}O , and HDO as passive tracers in the ocean component of the MITgcm. While it is forced with tracer specific humidity, precipitation, and river runoff (if available, otherwise it equals the isotopic composition of the local precipitation at the river mouth), the equilibrium and kinetic fractionation during evaporation are treated explicitly in the ocean model [Völpel *et al.*, 2017]. The isotopic forcing fields can be obtained from observational data or from suitable atmospheric model output. Fractionation during the formation of sea ice is neglected and seafloor water-rock isotope exchange processes are not considered, since they are in isotopic balance on short time scales [Muehlenbachs and Clayton, 1976; Walker and Lohmann, 1989]. Thus, only the fluxes lead to isotopic variations at the ocean surface. Each stable water isotope is treated as individual concentration (mol m^{-3}) in the ocean and is transported by the same processes (advection, diffusion and convection) as the “normal” water H_2^{16}O .

The `wiso` package is closely linked to the `gchem` package of the MITgcm, which takes care of the additional sources and sinks due to air-sea fluxes and acts as an interface between the `wiso` and `ptracers` packages, whereby the latter initializes, advects, and diffuses the tracers. A detailed description of the equations used in the `wiso` package is given in Völpel *et al.* [2017] (Chapter 3).

In conjunction with the `wiso` package and the conducted simulations the `balance` package was developed. Both, evaporation and tracer specific evaporation are calculated within the MITgcm. However, the calculated fields do not consider the amount of water entering the ocean through precipitation and/or river runoff, since there is no feedback between the ocean and atmosphere. Thus the annual freshwater flux or isotopic flux could be unbalanced, producing drifts in the resulting annual mean salinity and tracer concentrations. In order to prevent this, the `balance` package was developed. It calculates a correction factor for precipitation and tracer specific precipitation based on the changes of global salinity and tracer concentrations throughout a year. Thus, annual surface fluxes are balanced [Völpel *et al.*, 2017]. A detailed description of the equations used in the `balance` package is given in the Appendix of Völpel *et al.* [2017] (Chapter 3).

Additionally, the description of the implementation of the `wiso` and `balance` packages into the source code of the MITgcm and their internal structure including the different subroutines and their purposes are illustrated in the Supplement S1.

Chapter 3 Stable water isotopes in the MITgcm

Rike Völpe¹, André Paul¹, Annegret Krandick¹, Stefan Mulitza¹ and Michael Schulz¹

¹MARUM - Center for Marine Environmental Sciences and Faculty of Geosciences, University of Bremen, Bremen, Germany

Published in *Geoscientific Model Development*

Abstract.

We present the first results of the implementation of stable water isotopes in the ocean general circulation model MITgcm. The model is forced with the isotopic content of precipitation and water vapor from an atmospheric general circulation model (NCAR IsoCAM), while the fractionation during evaporation is treated explicitly in the MITgcm. Results of the equilibrium simulation under pre-industrial conditions are compared to observational data and measurements of plankton-tow records (the oxygen isotopic composition of planktic foraminiferal calcite). The broad patterns and magnitude of the stable water isotopes in annual mean seawater are well captured in the model, both at the sea surface as well as in the deep ocean. However, the surface water in the Arctic Ocean is not depleted enough, due to the absence of highly depleted precipitation and snow fall. A model-data mismatch is also recognizable in the isotopic composition of the seawater-salinity relationship in mid-latitudes that is mainly caused by the coarse grid resolution. Deep-ocean characteristics of the vertical water mass distribution in the Atlantic Ocean closely resemble observational data. The reconstructed $\delta^{18}\text{O}_c$ at the sea surface shows a good agreement with measurements. However, the model-data fit is weaker when individual species are considered and deviations are most likely attributable to the habitat depth of the foraminifera. Overall, the newly developed stable water isotope package opens wide prospects for long-term simulations in a paleoclimatic context.

3.1 Introduction

Stable water isotopes (H_2^{16}O , H_2^{18}O and $\text{HD}^{16}\text{O} = \text{HDO}$) are widely used tracers of the hydrological cycle [*Craig and Gordon*, 1965; *Gat and Gonfiantini*, 1981] and can be used to determine the origin and mixing pattern of different water masses [e.g. *Jacobs et al.*, 1985; *Khatwala et al.*, 1999; *Meredith et al.*, 1999]. Due to differences in their physical and chemical properties, stable water isotopes undergo fractionation processes at any

phase transition within the hydrological cycle [Craig and Gordon, 1965]. This leads to distinctive isotopic signatures for different freshwater fluxes, which are commonly expressed as δi ($i = {}^{18}\text{O}$ or D) with reference to the Vienna Standard Mean Ocean Water (VSMOW) standard and given as:

$$\delta i = \left(\frac{R}{R_{VSMOW}} - 1 \right) \cdot 1000 \text{ ‰}, \quad (3.1)$$

where R is the ratio of the abundance of the heavier water isotope $\text{H}_2{}^{18}\text{O}$ or HDO to the abundance of the lighter isotope $\text{H}_2{}^{16}\text{O}$ and $R_{VSMOW} = 2005.2 \cdot 10^{-6}$ for $\delta{}^{18}\text{O}$ [Baertschi, 1976] and $155.95 \cdot 10^{-6}$ for δD [de Wit et al., 1980].

Stable water isotopes have been used as an important proxy in a wide range of climate archives, e.g. in polar ice cores which provide past temperature records reflecting climatic changes over the past glacial-interglacial cycles [e.g. Dansgaard et al., 1969; Epstein et al., 1970; Johnsen et al., 1972; Johnsen et al., 2001] as well as speleothems which reveal intensity changes and variations in the amount of monsoonal rainfall [e.g. Wang et al., 2001; Fleitmann et al., 2003]. As an indirect record, stable water isotopes are preserved in carbonates (CaCO_3) from marine species such as planktonic and benthic foraminifers. Due to the temperature-dependent fractionation effect that occurs during the formation of CaCO_3 , the oxygen isotopic composition of foraminiferal CaCO_3 ($\delta{}^{18}\text{O}_c$) is a function of both the ambient temperature and the isotopic composition of the seawater ($\delta{}^{18}\text{O}_w$) in which the calcification takes place [Emiliani, 1955]. Hence, $\delta{}^{18}\text{O}_c$ records from sediment cores provide information on water mass changes.

During the last few decades, stable water isotopes have been incorporated more extensively in general circulation models (GCMs), first in atmospheric GCMs (AGCMs – [e.g. Joussaume et al., 1984; Jouzel et al., 1987b]) and more than a decade later in oceanic GCMs (OGCMs – [e.g. Schmidt, 1998; Paul et al., 1999; Delaygue et al., 2000; Wadley et al., 2002; Roche et al., 2004a; Xu et al., 2012]). In OGCMs the focus was mainly on the relationship between $\delta{}^{18}\text{O}_w$ and salinity, which are affected by similar physical processes. This topic is of significant interest in paleoceanography, because it is likely that changes in advection and freshwater budgets as well as the source of precipitation may have altered this relationship [Rohling and Bigg, 1998]. Using real freshwater flux boundary conditions in conjunction with the nonlinear free-surface [Huang, 1993] is essential to simulate it properly. Together, they ensure a dynamically more accurate simulation of the salinity due to the concentration and dilution effect and thus a freely evolving salinity at the sea surface. The Massachusetts Institute of Technology general circulation model (MITgcm) offers this very opportunity and further provides the adjoint method to perform data assimilation [Errico, 1997].

Here, we present first results of the implementation of stable water isotopes in the MITgcm, by performing an equilibrium pre-industrial (PI) simulation and comparing it to available observations and reconstructions.

3.2 Methods

3.2.1 Ocean Model

We used the MITgcm “checkpoint” 64w, which refers to a specific time and/or point within the development of the MITgcm code since it continuously undergoes updates. It was configured to solve the Boussinesq, hydrostatic Navier–Stokes equations with a nonlinear free-surface [Marshall *et al.*, 1997a; Adcroft *et al.*, 2004b]. A cubed-sphere grid was used which provided a nearly uniform resolution and avoided pole singularities [Adcroft *et al.*, 2004a]. It consisted of 6 faces, each of which comprised 32 x 32 grid cells, resulting in a horizontal resolution of approximately 2.8°. There were 15 vertical levels, ranging in thickness from 50 m at the surface to 690 m at the seafloor, giving a maximum model depth of 5200 m. Associated with the non-linear free-surface is the possible vanishing of the upper layer. To avoid this problem, the rescaled vertical coordinate z^* was employed [Adcroft and Campin, 2004]. This approach scales the entire vertical grid with the surface elevation and not just the surface layer [cf. Fig. 1b in Adcroft and Campin, 2004]. Furthermore, the shaved cell formulation was used, which reduced the representation error of the bathymetry [Adcroft *et al.*, 1997]. The model was coupled to a dynamic-thermodynamic sea ice model with a viscous-plastic rheology [Losch *et al.*, 2010].

Isopycnal diffusion and eddy-induced mixing was parameterized with the GM/Redi scheme [Redi, 1982; Gent and McWilliams, 1990]. Background vertical diffusivity for tracers was uniform at $3 \cdot 10^{-5} \text{ [m}^2 \text{ s}^{-1}\text{]}$, and for the equation of state the polynomial approximation of Jackett and McDougall [1995] was used. Advection of tracers was computed using third-order advection with direct space-time treatment [Hundsdorfer and Trompert, 1994].

Atmospheric forcing (air temperature, specific humidity, zonal and meridional wind velocity, wind speed, (snow-) precipitation, incoming shortwave and longwave radiation as well as river runoff – 12 climatological monthly means) was obtained from the PI ocean state estimate by Kurahashi-Nakamura *et al.*, [2017], which was based on the protocol of the Coordinated Ocean-ice Reference Experiments (COREs) project [Griffies *et al.*, 2009]. They optimized the forcing fields to reconstruct tracer distributions that were consistent with observations. Air-sea fluxes were internally computed in the model

following the bulk forcing approach by *Large and Yeager* [2004]. Furthermore, we globally balanced the freshwater flux by annually adjusting the precipitation field (Appendix A).

Our simulation was initialized with present-day salinity and temperature distributions [*Levitus et al.*, 1994 and *Levitus and Boyer* 1994, respectively] and spun up from the state of rest. We used asynchronous time stepping to accelerate computation with a time step of 1 day for the tracer equations and 20 min. for the momentum equations.

We compiled the code using the GNU Fortran compiler gfortran version 5.3.0 and performed the simulation on 6 cores of a processor of type Intel Xeon E5-2630 v3. The simulation was integrated for 3000 years (1000 model years took ~ 7.5 CPU hours) to reach a quasi-steady state (the global salinity, temperature and Atlantic Meridional Overturning Circulation were approximately steady at 34.73 psu, 2.86° C and 18.24 Sv (1 Sv = 10^6 m³ s⁻¹) respectively), continued for a further 3000 years with stable water isotopes as passive tracers. For analysis, the average of the last 100 years was used.

3.2.2 Implementation of water isotopes

We implemented the stable water isotopes H₂¹⁶O, H₂¹⁸O and HDO as conservative, passive tracers in the ocean component of the MITgcm (wiso package). Isotopic variations at the sea surface were driven by evaporation (E), precipitation (P) and river runoff (R), while advection, diffusion and convection affected the distribution in the interior of the ocean. Monthly climatological means of the isotopic content of precipitation and water vapor were available from the National Center for Atmospheric Research Community Atmosphere Model including a water isotope scheme (NCAR IsoCAM – [*Tharammal et al.*, 2013]). Note that the prescribed atmospheric forcing fields obtained from the PI ocean state estimate by *Kurahashi-Nakamura et al.*, [2017] and the corresponding isotopic fluxes are not entirely consistent and might introduce an error in our model simulation. However, to minimize the uncertainty we only took the ratio of the isotopic content of precipitation and water vapor and applied it to the corresponding atmospheric forcing fields. The isotopic composition of river runoff affects the isotopic composition of ocean water ($\delta^{18}\text{O}_w$ and δD_w) particularly in coastal regions. Since there was no land model in the MITgcm to calculate the amount and isotopic composition of continental runoff, we assumed that it equals the isotopic composition of the local precipitation at the river mouth and again applied it to the runoff forcing field.

Fractionation during evaporation, taking both equilibrium effects and kinetic effects into account, was treated explicitly in the MITgcm. The formulation for the isotopic composition of evaporation E^i (mol m⁻² s⁻¹) is

$$E^i = \Gamma^i(q^i - q_s^i). \quad (3.2)$$

Here, q^i is the specific humidity (kg kg^{-1}) multiplied by the isotopic ratio derived from the NCAR IsoCAM and

$$q_s^i = q_s \frac{J^i}{\alpha_{l-v}} \quad (3.3)$$

is the tracer specific humidity (kg kg^{-1}) in thermodynamic equilibrium with the liquid at the ocean surface [Merlivat and Jouzel, 1979], while

$$q_s = \frac{0.98}{\rho_{air}} q_{sat} \quad (3.4)$$

is the local sea surface humidity (kg kg^{-1}) with q_{sat} being the saturation specific humidity (kg m^{-3}) and ρ_{air} being the atmospheric density (kg m^{-3}),

$$J^i = \frac{c(i) \cdot M(i)}{c(H_2^{16}O) \cdot M(H_2^{16}O)} \quad (3.5)$$

is the local sea surface mass ratio with c being the concentration (mol m^{-3}) and M the molar mass (g mol^{-1}) of the respective stable water isotope. The equilibrium fractionation factor α_{l-v} between liquid water and water vapor has been found empirically as a function of temperature and was given by Majoube [1971]:

$$\alpha_{l-v}^{\delta^{18}O} = e^{\frac{1.137}{SST^2} \cdot 10^3 - \frac{0.4156}{SST} - 2.0667 \cdot 10^{-3}} \quad (3.6)$$

$$\alpha_{l-v}^{\delta D} = e^{\frac{24.844}{SST^2} \cdot 10^3 - \frac{76.248}{SST} + 5.2612 \cdot 10^{-2}} \quad (3.7)$$

with SST being the sea surface temperature (K).

Due to different molecular diffusivities of the isotopes, kinetic fractionation occurs. The kinetic fractionation factor K depends on wind speed U [m s^{-1}] through the roughness of the air-sea interface [Merlivat and Jouzel 1979; Jouzel et al., 1987b]:

$$K_{H_2^{18}O} = \begin{cases} 0.006, & \text{if } U < 7 \text{ m s}^{-1} \\ 0.000285 \cdot U + 0.00082, & \text{if } U \geq 7 \text{ m s}^{-1} \end{cases} \quad (3.8)$$

$$K_{HDO} = \begin{cases} 0.00528, & \text{if } U < 7 \text{ m s}^{-1} \\ 0.0002508 \cdot U + 0.0007216, & \text{if } U \geq 7 \text{ m s}^{-1} \end{cases} \quad (3.9)$$

The kinetic fractionation factor was used to calculate the isotopic profile coefficient Γ^i following:

$$\Gamma^i = \rho C_E U (1 - K) \quad (3.10)$$

where ρ is the air density and C_E is the transfer coefficient for evaporation as described in *Large and Yeager* [2004].

Fractionation during the formation of sea ice was neglected, because it is very small compared to other fractionation processes and thus only leads to minor effects on $\delta^{18}\text{O}_w$ and δD_w [*Craig and Gordon*, 1965]. Due to the absence of isotopes in the sea ice we approximated the isotopic surface flux F^i ($\text{mol m}^{-3} \text{s}^{-1}$) by:

$$F^i = -((E^i - P^i) \cdot (1 - A_{ice}) - R^i) \quad (3.11)$$

with A_{ice} being the ice-covered area fraction. Based on this approximation, there was no isotopic surface flux in areas covered by sea ice unless they were influenced by river runoff. Within the MITgcm, processes that affected the stable water isotopes were taken care of by the “gchem” and “ptracers” packages (Table 3.1). While the “gchem” package acted as an interface between the ptracers and wiso package and added F^i to the passive tracer surface tendency $gPtr^i$ ($\text{mol m}^{-3} \text{s}^{-1}$)

$$gPtr^i = gPtr^i + F^i, \quad (3.12)$$

the “ptracers” package mainly accounted for the transport of the isotopes by advecting and diffusing them. Furthermore, due to the freshwater flux that effectively changed the water column height, an additional tracer flux F_w^i ($\text{mol m}^{-2} \text{s}^{-1}$) associated with this input/output of freshwater ($E - P - R$ ($\text{kg m}^{-2} \text{s}^{-1}$)) was calculated following

$$F_w^i = (E - P - R) \cdot c_i \cdot x \quad (3.13)$$

with x being an units conversion factor. F_w^i was then additionally added to the tracer surface tendency within the “ptracers” package

$$gPtr^i = gPtr^i + F_w^i \cdot \frac{1}{z} \quad (3.14)$$

with z (m) being the surface grid cell thickness.

In the MITgcm, the stable water isotopes were not treated as ratios, but as individual concentrations. Therefore, we initialized the ocean with homogenous concentrations of H_2^{16}O , H_2^{18}O and HDO matching present-day $\delta^{18}\text{O}_w$ and δD_w values of 0 ‰ with reference to the VSMOW. The ratios were calculated during the analysis of the results.

Furthermore, similar to the freshwater flux, a correction factor for the tracer specific precipitation was applied, whereby the respective global tracer concentration in the ocean was conserved (cf. Appendix A).

Table 3.1: Main packages involved in the simulation of stable water isotopes and their respective purposes.

Package	Purpose
Ptracers	initializes, advects and diffuses the passive tracers
Gchem	interface between the ptracers and wiso package → takes care of the additional sources and sinks for the passive tracers (e.g. surface forcing) by calling the respective wiso routines and adding the isotopic surface flux F^i to the tracer surface tendency $gPtr^i$
Wiso	calculates the isotopic evaporation E^i and surface flux F^i

3.2.3 Observational data

3.2.3.1 $\delta^{18}\text{O}_w$ data

The Goddard Institute for Space Studies (GISS) Global Seawater Oxygen-18 Database v1.21 comprises over 26,000 seawater $\delta^{18}\text{O}$ values collected since about 1950 [Schmidt *et al.*, 1999] and therefore offers an opportunity to evaluate the modeled oceanic $\delta^{18}\text{O}$ values.

For comparison, we interpolated the GISS samples to the nearest tracer grid point of our model grid using inverse distance weighting. We excluded any data point with applied correction, from enclosed lagoons, representing estuarine or river data from near the coast or heavily influenced by meltwater, which means that we rejected all data points flagged as G, H, I, J, L and X in the GISS database [see Schmidt *et al.*, 1999 for details – 23,232 data points remained]. We could not expect our model to reproduce such conditions, based on our relatively coarse grid resolution.

Since the GISS data usually represent samples taken at a certain time during the year, we did not compare them to simulated annual mean isotope values. Instead, we used a long-term monthly mean value of the specific month, when the GISS sample was measured.

3.2.3.2 $\delta^{18}\text{O}_c$ data

Mulitza *et al.* [2003] compiled a number of $\delta^{18}\text{O}_c$ values measured on planktonic foraminifera from plankton tows [including data from Duplessy *et al.*, 1981, Kahn and Williams 1981, Ganssen, 1983, Bauch *et al.*, 1997 and Peeters and Brummer, 2002]. They limited their compilation on the four species *Globigerinoides ruber* white (*G. ruber* (w)), *Globigerina bulloides* (*G. bulloides*), *Neogloboquadrina pachyderma* sinistral (*N. pachyderma* (s)) and *Globigerinoides sacculifer* (*G. sacculifer*), since these species are very abundant, cover a broad geographical and temporal range and belong to the

shallowest-dwelling planktonic foraminifera. We extended this data set with available *in situ* $\delta^{18}\text{O}_c$ data from *Kohfeld and Fairbanks* [1996], *Moos* [2000], *Stangeew* [2001], *Volkman and Mensch* [2001], *Mortyn and Charles* [2003], *Keigwin et al.* [2005], *Wilke et al.* [2009] and *Rippert et al.* [2016]. By using inverse distance weighting, we interpolated the $\delta^{18}\text{O}_c$ data to the nearest tracer grid point of the MITgcm grid (analogous to the GISS data) and compared them to the simulated long-term monthly mean $\delta^{18}\text{O}_c$ values of the respective month of sampling. We used the paleotemperature equation from *Mulitza et al.* [2004]

$$T [^\circ\text{C}] = 14.32 - 4.28 \cdot (\delta^{18}\text{O}_c - \delta^{18}\text{O}_w) + 0.07 \cdot (\delta^{18}\text{O}_c - \delta^{18}\text{O}_w)^2 \quad (3.15)$$

to determine the dependency between the $\delta^{18}\text{O}_c$, the temperature T during calcification and the $\delta^{18}\text{O}_w$. Since water samples are reported relative to the VSMOW standard and carbonate samples relative to the Vienna PeeDee Belemnite (VPDB) standard, the $\delta^{18}\text{O}_w$ values need to be converted by subtracting -0.27 ‰ [*Hut*, 1987].

3.3 Results

3.3.1 General model performance - temperature and salinity distribution

We compare the simulated annual mean SST and sea surface salinity (SSS, upper 50 m) to the annual mean (averaged over the upper 50 m and interpolated to the cubed sphere grid) temperature (Figure 3.1a, b) and salinity (Figure 3.2a, b) of the World Ocean Atlas 2013 (WOA13, [*Locarnini et al.*, 2013, *Zweng et al.*, 2013, respectively]). In most regions of the World Ocean, SST differences are around $1 \text{ }^\circ\text{C}$ or even less (root mean square error (RMSE) = $1.18 \text{ }^\circ\text{C}$) and therefore in good agreement with the data. Larger differences are mainly located in regions of coastal and equatorial upwelling, in the Gulf Stream and around Indonesia.

A different picture emerges for the SSS anomaly. While most parts of the surface ocean are slightly too fresh, especially the Mediterranean Sea, Bay of Bengal, Hudson Bay and north of Iceland, both the Arctic Ocean and the east coast of North America are too salty. Nevertheless, we obtain a RMSE of 0.45 psu without using any salinity restoring.

This good agreement also continues in the deeper parts of the Atlantic Ocean. Calculated weighted zonal means of the simulated annual mean temperature and salinity in the Atlantic Ocean correspond well with the observations (Figure 3.3a and b respectively; temperature and salinity provided by the GISS data, [*Schmidt et al.*, 1999]). The simulated annual mean temperature gradually decreases with depth, as do the

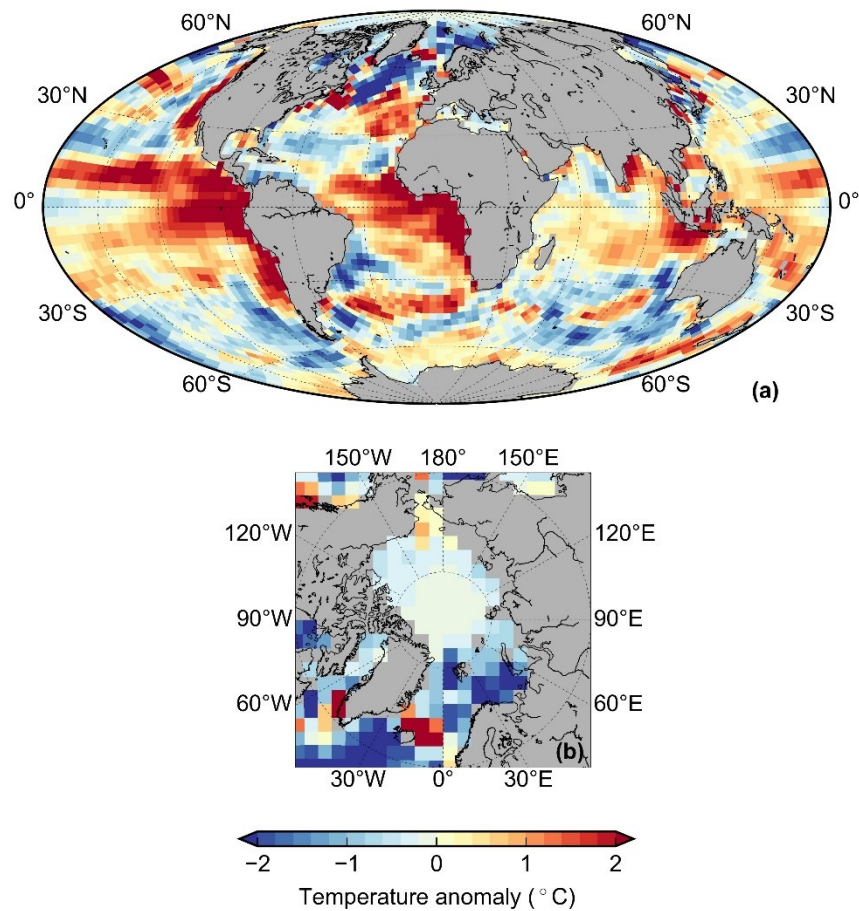


Figure 3.1: Annual mean sea surface temperature anomaly (MITgcm – WOA13, upper 50 m) for (a) the global ocean and (b) the Arctic Ocean. For the calculation of the anomaly the SST of the WOA13 was averaged over the upper 50 m and interpolated to the cubed sphere grid of the MITgcm.

observational data. It is also recognizable that the boundary towards water masses colder than 4 °C appears slightly shallower in the southern than in the northern part of the Atlantic Ocean. Coldest temperatures occur in the deep southern Atlantic Ocean, both in the simulated as well as observational data. Interpolating the observational data to the nearest tracer grid point and comparing it to the simulated long-term monthly mean values of the respective month of sampling (as described in section 3.2.3.1 for the GISS data), further underlines the agreement between simulated and observed values (Figure 3.3c - $r^2 = 0.93$; RMSE = 2.1 °C; $n = 660$). The zonally averaged cross section of the simulated annual mean salinity clearly reveals the occurrence of different water masses. While most parts of the Atlantic Ocean are filled by the North Atlantic Deep Water (NADW) coming from the north with a salinity value of around 34.9 psu (reaching a water depth of ~ 3500 m), the deepest parts of the Atlantic Ocean basin are occupied by less

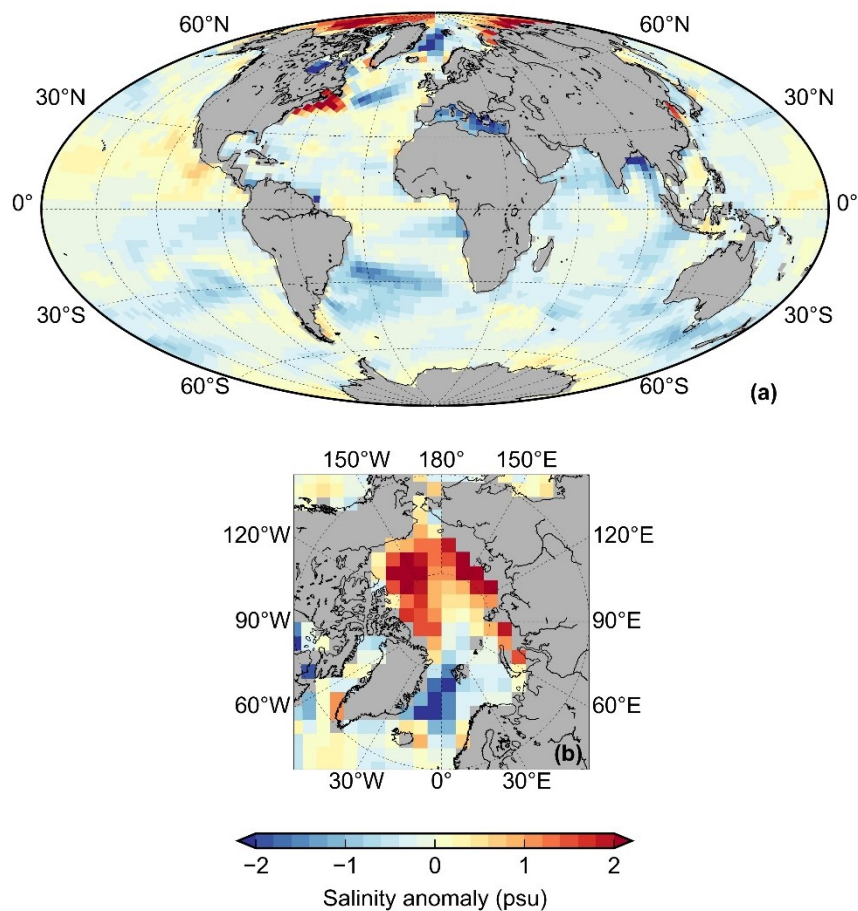


Figure 3.2: Annual mean sea surface salinity anomaly (MITgcm – WOA13, upper 50 m) for (a) the global ocean and (b) the Arctic Ocean. For the calculation of the anomaly the SSS of the WOA13 was averaged over the upper 50 m and interpolated to the cubed sphere grid of the MITgcm.

saline water (~ 34.7 psu) of the Antarctic Bottom Water (AABW) flowing from the south. The Antarctic Intermediate Water (AAIW) is the freshest water mass (~ 34.6 psu) and can be traced as a tongue, spreading from the south towards the north at a water depth of 1000 m. The most saline water appears in the upper water column of the northern tropics ($\sim 30^\circ$ N). This structure is also reflected in the observational data, however both NADW and AAIW seem to be slightly fresher. Performing a model-data comparison for salinity, as outlined above for temperature, shows a good fit (Figure 3.3d - $r^2 = 0.61$; RMSE = 0.6 psu; n 691) in general, but a few points are clearly located above the 1:1 line. These data points correspond to simulated annual mean salinity values in the upper water column near the North American coast, one of the regions with the highest positive SSS anomalies (Figure 3.2 a) and will be discussed shortly in section 3.4.1.

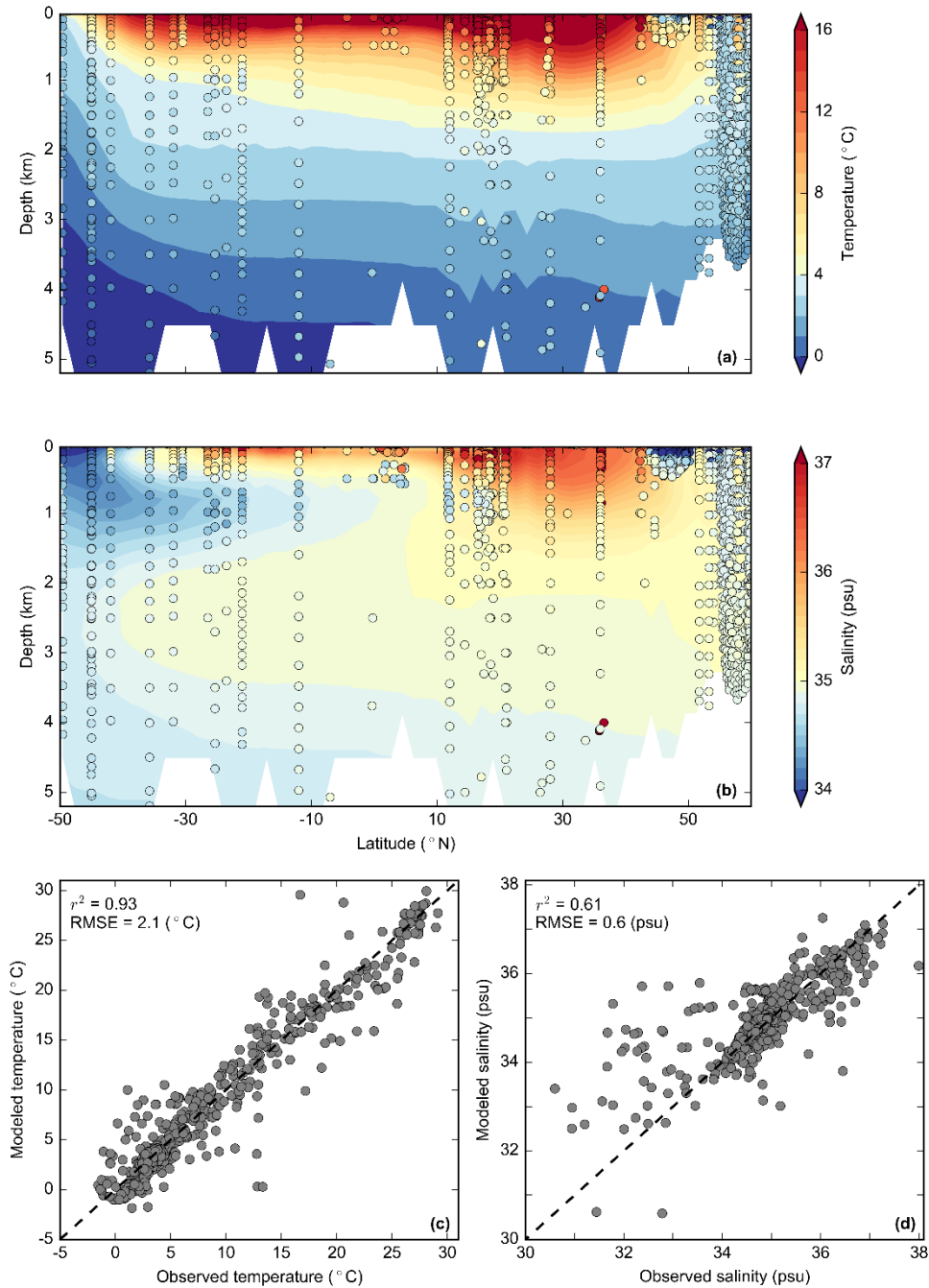


Figure 3.3: Zonally averaged cross sections through the Atlantic Ocean for (a) the simulated annual mean temperature distribution and (b) the simulated annual mean salinity distribution in comparison to the observational GISS data (colored symbols – *Schmidt et al.* [1999]; (a): $n = 2234$, (b): $n = 2666$). The zonal-averaged cross sections have been determined using the Atlantic basin mask provided by the WOA09 [*Locarnini et al.*, 2010] and dividing it into equally spaced latitudinal bands along which a weighted zonal mean was calculated. Note that the GISS data does not represent a zonal mean, but rather values from specific locations taken at a certain time during the year. The relationship between the observed data and simulated long-term monthly mean temperature and salinity in the Atlantic Ocean is presented in (c) and (d) respectively. For the comparison, the specific month of GISS sampling has been considered. Dashed lines represent the 1:1 line.

3.3.2 Stable water isotope distribution in ocean water

Even though measurements of δD exist, they are not as widespread as $\delta^{18}O$. Furthermore, the stable water isotope package will be used mainly for paleoclimatic reconstructions in conjunction with $\delta^{18}O_c$ data from benthic foraminiferal shells. Hence, we chose to focus on the comparison for $\delta^{18}O$ to validate our simulation.

The surface (upper 50 m) distribution of annual $\delta^{18}O_w$ simulated by the MITgcm gradually decreases from the mid-latitudes to high latitudes (Figure 3.4a, b). Highest values of about 1 ‰ occur in the subtropical gyre of the Atlantic Ocean, which are slightly higher than in the Pacific Ocean, reflecting the net freshwater transport by the trade winds. The Mediterranean Sea and Red Sea are regions of net evaporation and therefore contain $\delta^{18}O_w$ values of similar magnitude. The most depleted surface water is simulated in the high latitudes, showing values of -0.5 ‰ in the Southern Ocean and -1 ‰ in the Arctic Ocean. These depleted values result from negative $\delta^{18}O_w$ values in precipitation in combination with river/glacial runoff. Similarly, depleted values occur in surface waters around Indonesia.

The large-scale patterns and latitudinal gradients of simulated annual mean $\delta^{18}O_w$ values match fairly well the observations. For example, the model captures the contrast between high and low latitudes and the Atlantic and Pacific Ocean. However, some notable discrepancies are recognizable when comparing the absolute range of $\delta^{18}O_w$ at the surface. In the MITgcm, the subtropical gyres are less enriched than in the observations (annual mean value of 0.6 ‰ as compared to 1.0 ‰, respectively). The same holds true for the Mediterranean Sea. For the Arctic Ocean simulated $\delta^{18}O_w$ values are not as depleted as in the observational data (annual mean value -0.6 ‰ as compared to -1.5 ‰, respectively). Especially near large river estuaries, the model-data mismatch is large. A clear distinction between different water masses based on the annual mean isotopic composition of sea water is recognizable in our simulation, both for the Atlantic Ocean and the Pacific Ocean (Figure 3.5a and b respectively). In our model, the NADW in the Atlantic Ocean reaches down to approximately 3500 m depth and is rather enriched in $H_2^{18}O$, resulting in an annual mean $\delta^{18}O_w$ content of around 0.11 ‰ (cf. Table 3). Most enriched $\delta^{18}O_w$ values (~ 0.6 ‰) occur in the upper water column of the tropics (20° - 30° S and N). The NADW encounters the AAIW coming from the south at a water depth of approximately 1000 m. The latter is more depleted with an annual mean $\delta^{18}O_w$ value of around 0 ‰. The deepest parts of the Atlantic Ocean are characterized by negative annual mean $\delta^{18}O_w$ values of approximately -0.11 ‰ derived from AABW mixed with NADW. This water mass structure is in good agreement with the observational data. However, the NADW is not enriched enough compared to the observational data (0.21

‰), whereby the deepest parts of the Atlantic Ocean reveal too depleted $\delta^{18}\text{O}_w$ values. For the Pacific Ocean (Figure 3.5b) the vertical structure is even more homogenous. Enriched waters (~ 0.1 ‰) occur in the upper water column down to approximately 1000 m. Deeper parts of the Pacific are filled with depleted water of around -0.1 ‰. Compared to the observational data, the vertical and latitudinal gradients are in agreement. The large number of negative $\delta^{18}\text{O}_w$ measurements at 50° N is obtained from the Okhotsk Sea and thus is not representative for a zonally averaged cross section of the North Pacific. To take a closer look at the model-data fit, we interpolated the GISS data to the nearest tracer grid point and compared it to the simulated long-term monthly mean value of the respective month of sampling (see section 3.2.3.1). The separation of the model-data comparison into different ocean basins (Atlantic Ocean - Figure 3.6a, Pacific Ocean

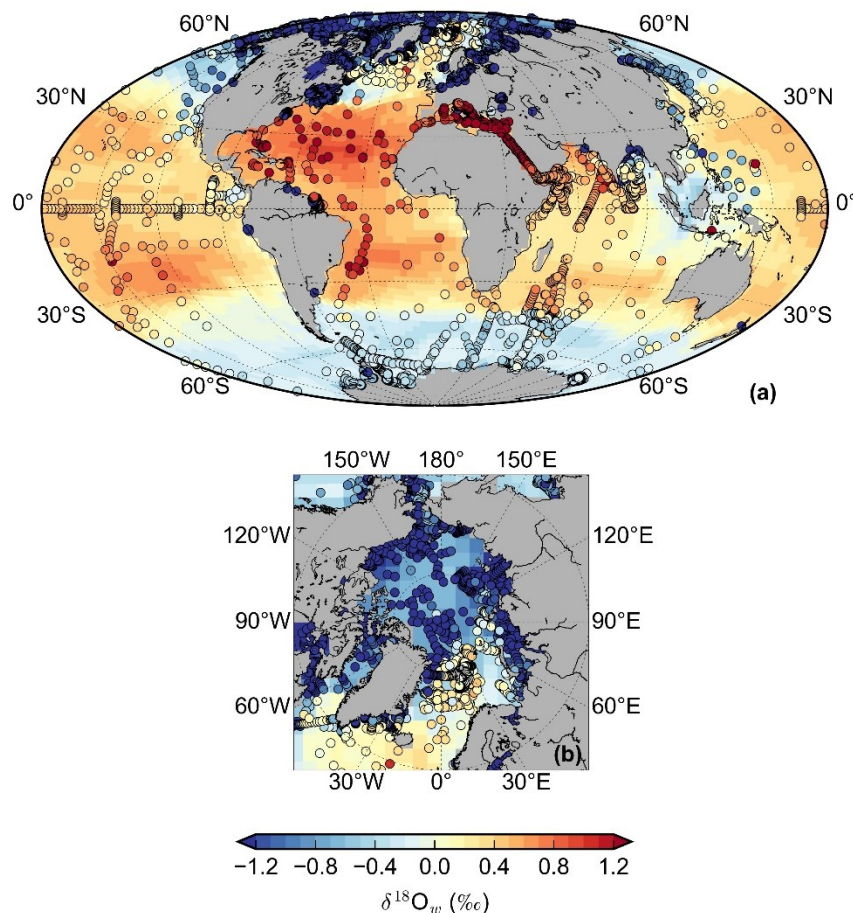


Figure 3.4: Global annual mean surface (upper 50 m) $\delta^{18}\text{O}_w$ distribution simulated by the MITgcm in comparison to the observational GISS data (colored symbols - Schmidt *et al.* [1999]) for (a) the global ocean and (b) the Arctic Ocean. The GISS data are averaged over the upper 50 m and do not represent an annual mean, but a certain time during the year.

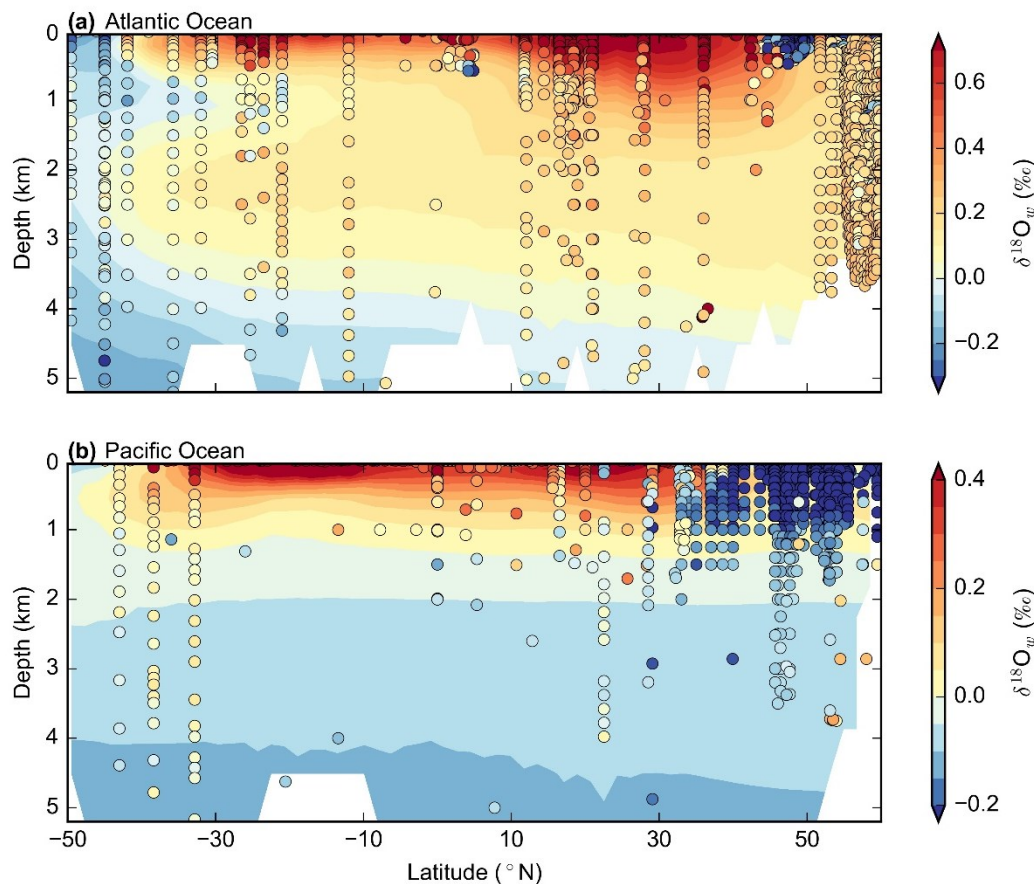


Figure 3.5: Zonally averaged cross section for the simulated annual mean $\delta^{18}\text{O}_w$ distribution in (a) the Atlantic and (b) the Pacific Ocean in comparison to the observational GISS data (colored symbols – *Schmidt et al.* [1999]; Atlantic Ocean: $n = 2713$, Pacific Ocean: $n = 2929$). The zonally averaged cross sections have been determined using the respective basin masks provided by the WOA09 [*Locarnini et al.*, 2010] and dividing it into equally spaced latitudinal bands along which a weighted zonal mean was calculated. Note that the GISS data does not represent a zonal mean, but rather values from specific locations taken at a certain time during the year.

Figure 3.6b, Arctic Ocean - Figure 3.6c and Indian Ocean - Figure 3.6d) points to deviations that mainly occur in higher latitudes. The correlation and RMSE is quite diverse, showing strong correlation for the Indian ($r^2 = 0.77$, $\text{RMSE} = 0.19 \text{ ‰}$, $n = 593$) and Pacific Ocean ($r^2 = 0.74$, $\text{RMSE} = 0.32 \text{ ‰}$, $n = 743$), medium correlation for the Atlantic Ocean ($r^2 = 0.37$, $\text{RMSE} = 0.79 \text{ ‰}$, $n = 756$) and no correlation for the Arctic Ocean ($r^2 = 0.05$, $\text{RMSE} = 1.18 \text{ ‰}$, $n = 1048$). Overall, depleted $\delta^{18}\text{O}_w$ values are not very well simulated in the MITgcm, which is particularly recognizable in the Arctic, a region highly influenced by negative $\delta^{18}\text{O}_w$ values from precipitation, snow fall and river runoff [*Yi et al.*, 2012].

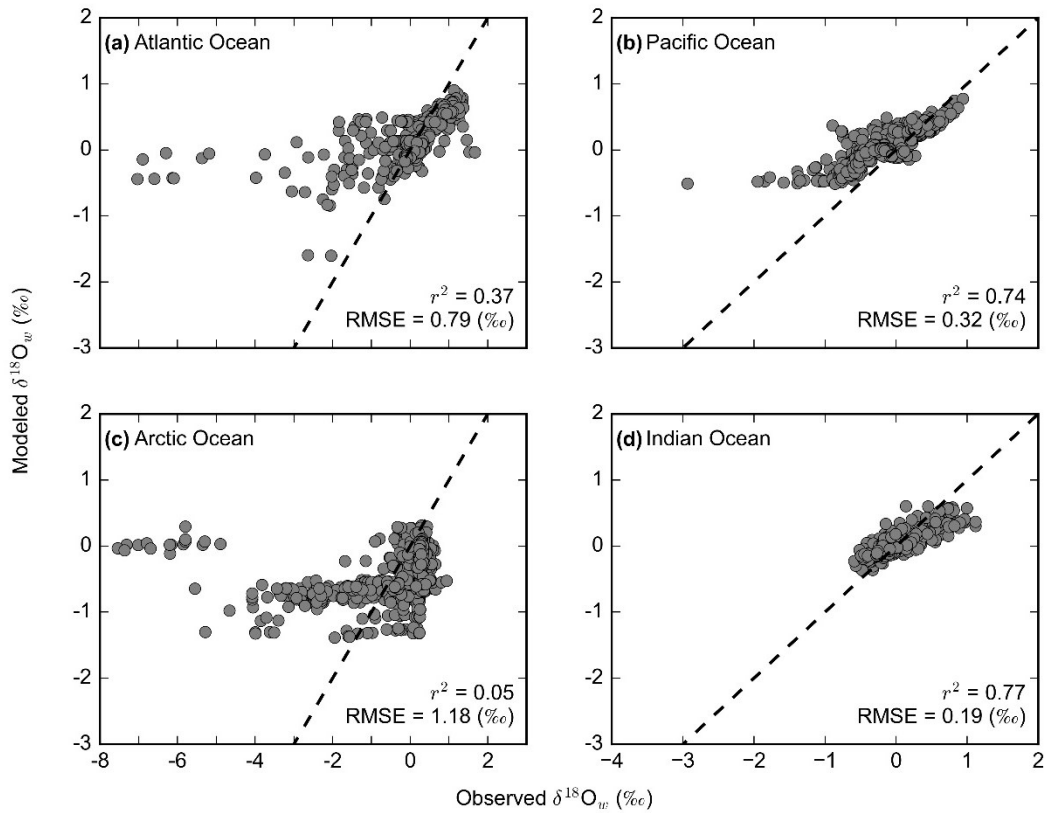


Figure 3.6: Relationship between observed $\delta^{18}\text{O}_w$ from the GISS database [Schmidt *et al.*, 1999] and simulated long-term monthly mean $\delta^{18}\text{O}_w$ from the MITgcm for the different ocean basins: (a) Atlantic Ocean, (b) Pacific Ocean, (c) Arctic Ocean and (d) Indian Ocean. For the comparison, the specific month of GISS sampling has been considered. Dashed lines represent the 1:1 line.

3.3.3 Relationship between stable water isotopes and salinity

Similar physical processes determine the salinity and $\delta^{18}\text{O}_w$ distribution at the ocean surface. Thus, locally a linear relationship between those two quantities can be expected. Therefore, we compared the modeled $\delta^{18}\text{O}_w$ -salinity relationship with the observed one by taking the closest long-term monthly mean tracer grid value of salinity and $\delta^{18}\text{O}_w$ to the GISS data points of the respective month of sampling. Restricting the comparison to the upper 50 m and the salinity range to 28 – 38 psu in order to reflect open ocean conditions, the general features of the latter relationship are well captured in our model (Figure 3.7).

The modeled $\delta^{18}\text{O}_w$ -salinity relationship in the tropics (25° S – 25° N) agrees quite well with the observed one (Figure 3.7a). Here, we find a simulated slope of 0.15 ‰ psu⁻¹, while the observed one is 0.22 ‰ psu⁻¹. A steeper slope is visible in the mid-latitudes (25° S/N – 60° S/N) for both the simulated and observed relationship (Figure 3.7b).

However, the agreement between those two slopes is smaller than in the tropics, with a simulated slope of 0.28 ‰ psu^{-1} and an observed slope of 0.49 ‰ psu^{-1} . Further, it underlines that we do not simulate salinity and $\delta^{18}\text{O}_w$ values as low as represented in the GISS data.

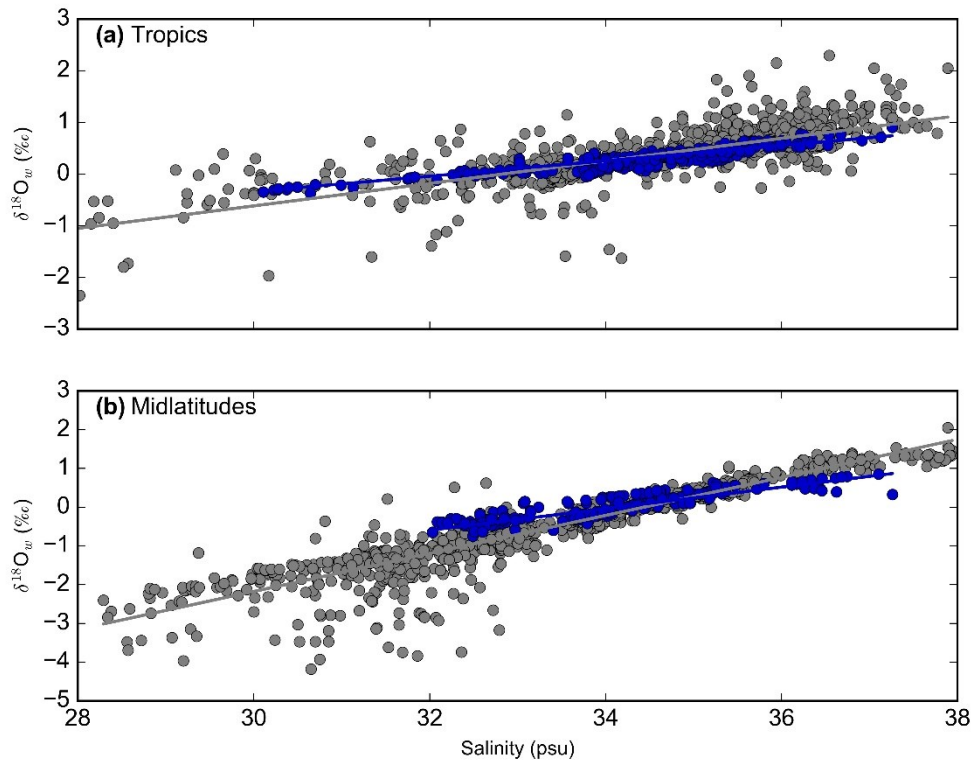


Figure 3.7: Salinity and $\delta^{18}\text{O}_w$ relation in surface waters (upper 50 m) for observational data (grey symbols – *Schmidt et al.* [1999]) and simulated values (blue symbols) in (a) the tropics ($25^\circ\text{S} - 25^\circ\text{N}$) and (b) the mid-latitudes ($25^\circ\text{S/N} - 60^\circ\text{S/N}$). All GISS data in a depth range of 0-50 m with both salinity and $\delta^{18}\text{O}_w$ values available are presented (tropics: $n = 1191$, mid-latitudes: $n = 1282$), while the closest long-term monthly mean tracer grid value of salinity and $\delta^{18}\text{O}_w$ to the GISS datapoints of the respective month of sampling were chosen (tropics: $n = 292$, mid-latitudes: $n = 245$). The $\delta^{18}\text{O}_w$ /salinity slopes are given in the text.

3.3.4 $\delta^{18}\text{O}_c$ distribution

The annual mean simulated $\delta^{18}\text{O}_c$ distribution at the surface (upper 50 m) increases from the tropical regions ($\sim 3\text{‰}$) to high latitudes ($\sim 3.5\text{‰}$), reflecting the dependency on both $\delta^{18}\text{O}_w$ and temperature (Figure 3.8). Most depleted $\delta^{18}\text{O}_c$ values develop in the Bay of Bengal and around Indonesia ($< 3.5\text{‰}$), while the transition towards positive $\delta^{18}\text{O}_c$ values occur from 40° S/N upwards. Even though the plankton-tow data are rather sparsely distributed in the global ocean, a latitudinal increase in $\delta^{18}\text{O}_c$ is also

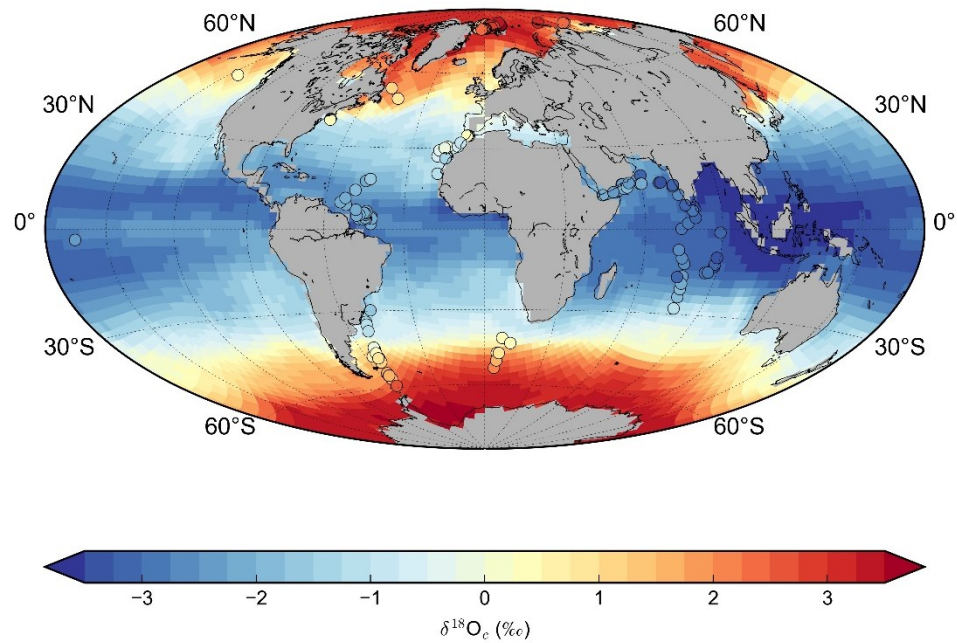


Figure 3.8: Modeled annual mean sea surface $\delta^{18}\text{O}_e$ distribution (upper 50 m) compared to $\delta^{18}\text{O}_e$ values measured on planktonic foraminifera from plankton tows (colored symbols – for references see text). The plankton-tow data are averaged over the upper 50 m and do not represent an annual mean, but a certain time during the year.

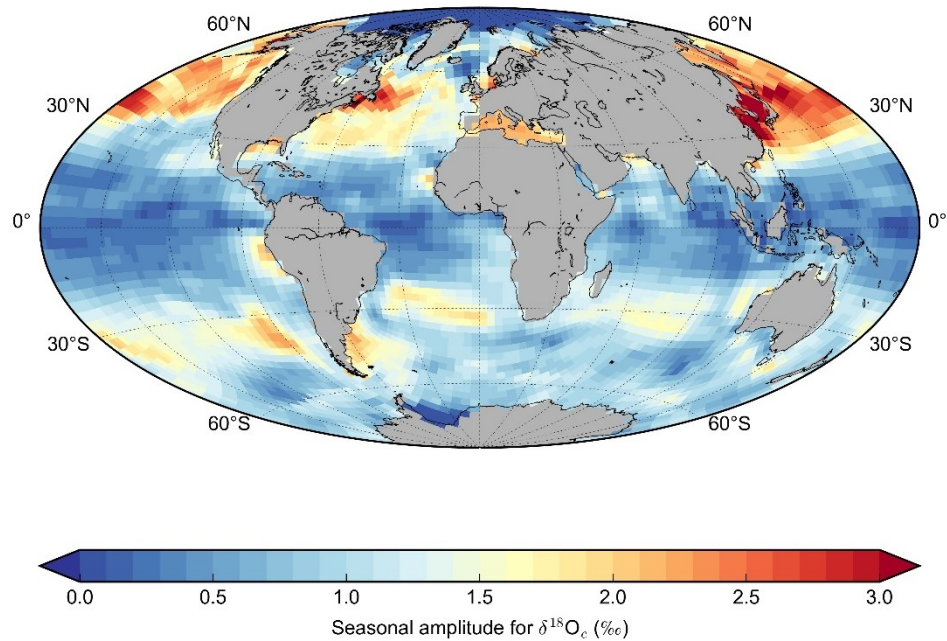


Figure 3.9: Simulated seasonal amplitude for $\delta^{18}\text{O}_e$ at the surface (upper 50 m). The seasonal amplitude is determined by calculating the absolute value between the two extreme months.

recognizable. Thus, the simulated large-scale pattern and latitudinal gradient match fairly well the measurements. Nevertheless, some model-data mismatch occurs. Simulated annual mean calcite values in the tropics seem to be slightly too low (e.g. northeast of the Amazon delta), while regions in the North Atlantic and Arctic Ocean are slightly enriched compared to the observations. The influence of the seasonal cycle on the $\delta^{18}\text{O}_c$ distribution depends on latitude (Figure 3.9). The largest seasonal effects occur in the northern mid-latitudes ($30^\circ - 60^\circ \text{ N}$) with values of up to 3 ‰, whereas a weak or almost no seasonal effect appears in low and high latitudes. Thus, when performing a model-data comparison, the respective month of plankton tow sampling must be considered. Figure 3.10a and b include not just the surface data but plankton tows taken in deeper parts of the ocean. The comparison reveals a good match ($r^2 = 0.88$, $\text{RMSE} = 0.83 \text{ ‰}$, $n = 183$). Data points that are not located along the 1:1 line but rather above, belong either to the deeper water columns of the model (Figure 3.10b) within the tropics (Figure 3.10a) or, as mentioned above, to the upper water column (Figure 3.10b) in high latitudes (Figure 3.10a).

3.4 Discussion

3.4.1 Model performance

Before we discuss the $\delta^{18}\text{O}_w$ distribution in the MITgcm, the general model performance will be shortly assessed, because an accurate presentation of the ocean circulation is essential for a reasonable simulation of stable water isotopes. Therefore, we investigate the temperature and salinity distribution, because these two quantities determine the density and thus one of the main factors influencing the vertical movement of ocean waters. The results for the simulated annual mean temperature and salinity are quite promising. Large biases at the sea surface occur in the North Atlantic, both for the SST and SSS. These biases are quite common in ocean models, especially with a low resolution, since the proper simulation of the structure, pathways and extensions of western boundary currents are difficult to achieve [cf. *Griffies et al.*, 2009]. Here, the Gulf Stream remains attached to the coast far to north and due to the coarse grid resolution subpolar surface water displaces the North Atlantic Current resulting in SST and SSS biases. Regarding the SST, warm biases also occur in the upwelling regions along the west coasts of Africa and America (intruding far into the open ocean basin), which are mainly driven by the poorly resolved coastal upwelling process. In terms of SSS biases, surface boundary conditions like P and E should be considered. In general, the large-scale patterns for P and E are accurately presented (not shown here). The prescribed

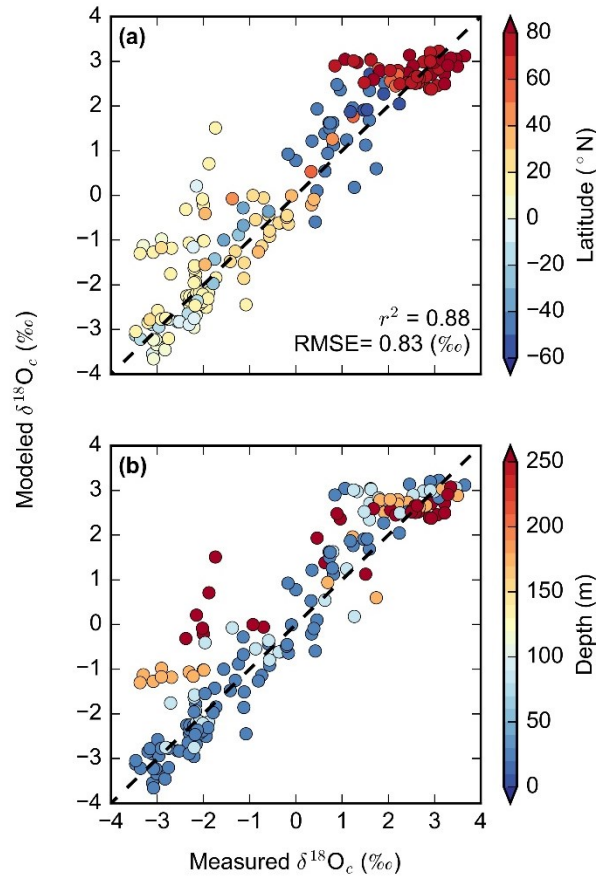


Figure 3.10: Relationship between measured $\delta^{18}\text{O}_c$ from various planktonic foraminiferas from plankton tows (for references see text) and simulated long-term monthly mean $\delta^{18}\text{O}_c$ from the MITgcm either depending on latitude (a) or depth (b). For the comparison, the specific month and depth of plankton tow sampling has been considered and plankton-tow data was interpolated to the closest tracer grid cell of the model, using inverse distance weighting. Dashed lines represent the 1:1 line.

precipitation field P clearly depicts the intertropical convergence zones (ITCZ) in the Atlantic and Pacific Oceans. Further, extremely dry ocean regions in the subtropics that are associated with high pressure zones are visible. The simulated evaporation field E is mainly zonally oriented, with increased values occurring in subtropical areas and decreased values along the equator and high latitudes. This zonal pattern is interrupted in regions of western boundary currents, where E is enhanced along the pathways. For a more precise estimate, we calculated annual anomalies for P and E (Figure 3.11a and b, respectively) using data from rain gauge stations from the Global Precipitation Climatology Project (GPCP [Huffman *et al.*, 1997]) and the latent heat flux (converted to E by dividing it with the constant latent heat of evaporation ($2.5 \cdot 10^6$ (in J kg^{-1}) [Hartmann, 1994]) from the National Oceanography Centre (NOC) Version 2.0 Surface Flux and Meteorological Dataset [Berry and Kent, 2009]. Unfortunately, no data exists for E in high

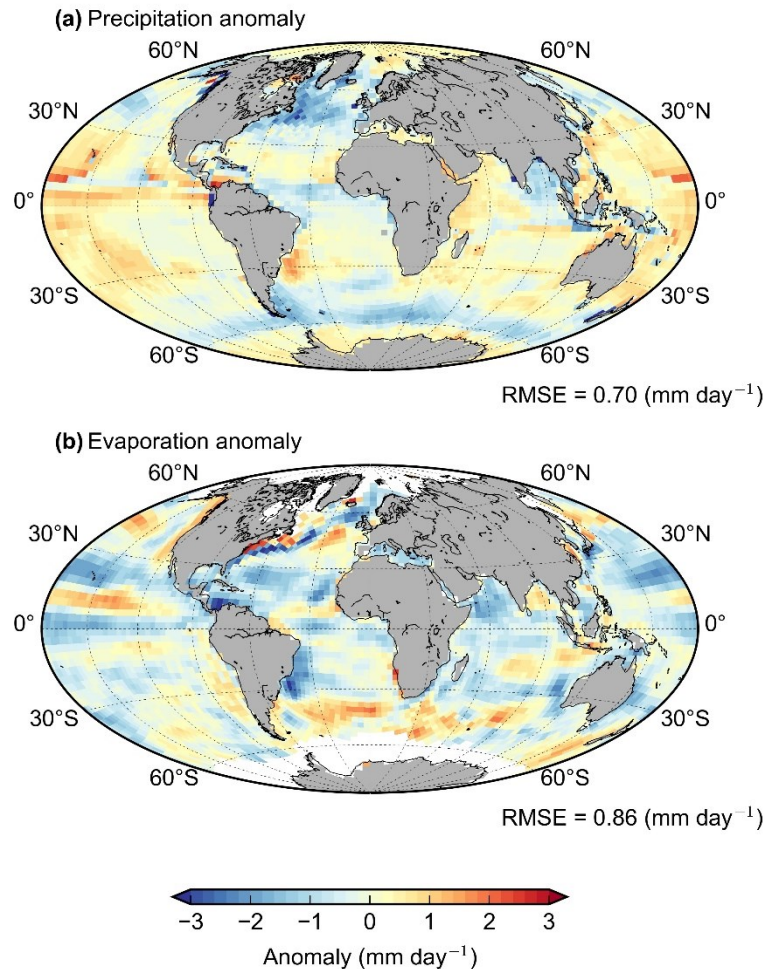


Figure 3.11: Annual mean precipitation (a) and evaporation (b) anomaly (MITgcm – observational data). The observed precipitation field is provided by GPCP [Huffmann *et al.*, 1997], while the latent heat flux from the NOC Version 2.0 Surface Flux and Meteorological Dataset [Berry *et al.*, 2009] is converted to evaporation and used for comparison.

latitudes, whereby no model-data comparison can be carried out in these regions. Since E , among others, depends on the SST, a similar picture for the anomaly should emerge. Indeed, regions with warmer (colder) SST simulated by the MITgcm also experience elevated (reduced) E values. The precipitation however, is too small in the North Atlantic, the Bay of Bengal, the equatorial Atlantic and along 60° S, while too large mainly in the tropics (especially in the Pacific) and high latitudes. Regarding the SSS, the bias in the North Atlantic appears to be caused by an interaction between the coarse grid resolution and a bias in the evaporation. Besides the Mediterranean Sea, where enhanced P and reduced E lead to a fresh bias, there is no other apparent correlation between P , E and SSS anomalies. With a RMSE of 1.18 °C and 0.45 psu, respectively, our SST and SSS results are comparable to Danabasoglu *et al.* [2012], who reported a RMSE of 0.58 °C and 0.41 psu for the POP2 ocean component of the Community Climate System Model 4 (CCSM4) using a weak salinity restoring, and Griffies *et al.* [2011], who got a RMSE of

1.3 °C and 0.77 psu with the Geophysical Fluid Dynamics Laboratory Climate Model version 3.

Likewise, the comparison with observed data for the deep Atlantic Ocean basin is good. The main water masses AAIW, NADW and AABW can be detected. Core properties of the water masses (AAIW: salinity = ~ 34.6 psu, temperature = ~ 5 °C; NADW: salinity = ~ 34.9 psu, temperature = ~ 3 °C; AABW: salinity = ~ 34.7 psu, temperature = ~ 0 °C; visual estimation based on Figure 3.3) fit reasonably well the temperature and salinity ranges reported by *Emery and Meincke* [1986] (Figure 3.14, rectangles). But both, NADW and AABW might be slightly too salty, while the AABW seems to be too cold. To maintain a realistic ocean climate, not just the water mass structure is of importance but also the circulation strength. The maximum meridional transport at 48° N simulated in the MITgcm is 17.8 Sv, consistent with 16 ± 2 Sv reported by *Ganachaud* [2003] and *Lumpkin et al.* [2008].

Thus, we find that the general model performance is reasonable and comparable to both observations and other climate simulations.

3.4.2 Sources of error for $\delta^{18}\text{O}_w$

Results of the $\delta^{18}\text{O}_w$ distribution at the sea surface showed relatively large mismatches between modeled and observed data in the Arctic Ocean. As indicated by Eq. 3.11, there is no isotopic surface flux in areas that are covered by sea ice unless they are influenced by river runoff. Since parts of the Arctic Ocean are covered by sea ice all year round and others are seasonally influenced (not shown here), these areas do not experience any isotopic surface flux during most of the year. In this way, the impact of precipitation and snow fall that is highly depleted is neglected, which could explain too high $\delta^{18}\text{O}_w$ values in the Arctic Ocean.

The spatial distribution of $\delta^{18}\text{O}_w$ in P is also a matter of debate. The Global Network of Isotopes in Precipitation (GNIP [IAEA/WMO, 2010]) provides a database with $\delta^{18}\text{O}_w$ in P at more than 950 stations all around the globe. For the comparison with modeled annual $\delta^{18}\text{O}_w$ in P only data with continuous sampling for a minimum of 5 years has been considered, resulting in 127 data points. Unfortunately, most of the data is continental, whereby a significant conclusion for the $\delta^{18}\text{O}_w$ in P over the ocean is difficult. Nevertheless, all the main characteristics in $\delta^{18}\text{O}_w$ in P can be identified (Figure 3.12a). Due to the temperature effect on the fractionation during condensation [Dansgaard, 1964], $\delta^{18}\text{O}_w$ in P decreases from mid- to high latitudes. While most enriched values occur in the regions of trade winds with slightly more depleted values along the ITCZ,

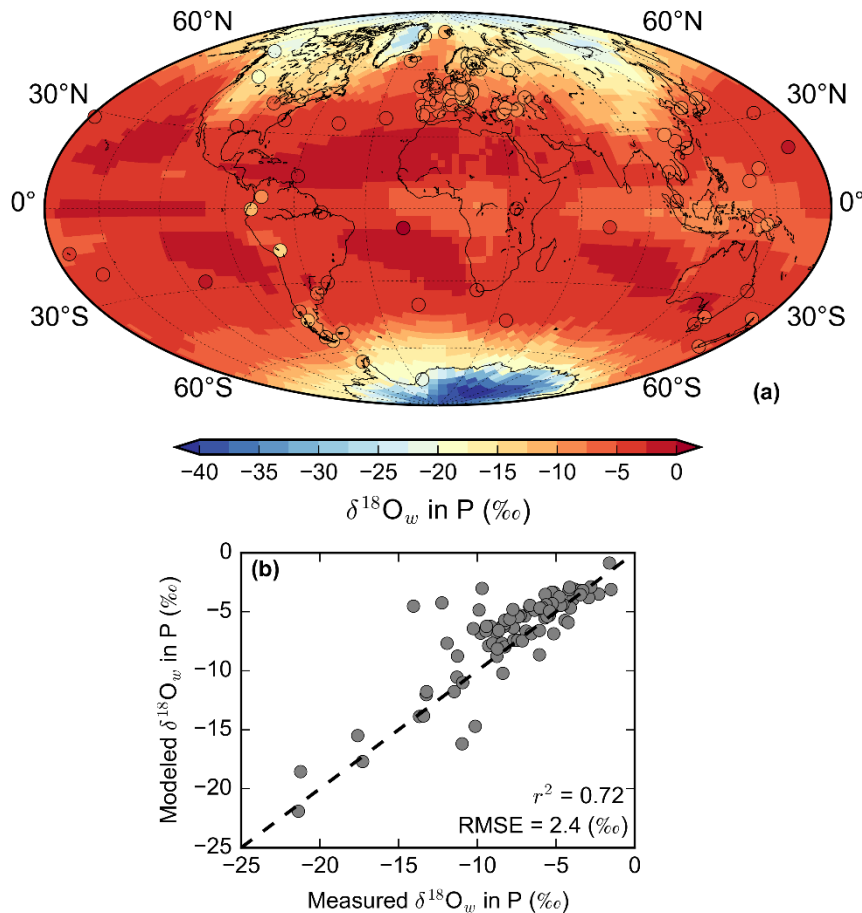


Figure 3.12: (a) Prescribed annual mean isotopic composition in precipitation compared to GNIP data (colored symbols [IAEA/WMO, 2010]). (b) Model-data comparison of the annual mean values. GNIP data was interpolated to the closest tracer grid cell of the MITgcm, using inverse distance weighting. Dashed lines represent the 1:1 line.

the strongest depletion can be found over the polar ice sheets. For a more straightforward statement, we performed a model-data comparison (Figure 3.12b) by interpolating the GNIP data to the closest tracer grid point of the MITgcm, revealing a good agreement between modeled and measured data ($r^2 = 0.72$, $RMSE = 2.4 \text{ ‰}$, $n = 91$). Linking these results to the large $\delta^{18}\text{O}_w$ mismatches that emerged in the Arctic Ocean, subtropical gyres and the Mediterranean Sea let us conclude that the decreased $\delta^{18}\text{O}_w$ values at the ocean surface in the latter two regions are caused by an interaction of P , E and $\delta^{18}\text{O}_w$ in E . Enhanced P in the MITgcm has a dilutional effect on the water, while due to reduced E not enough ^{16}O is removed from the ocean surface. $\delta^{18}\text{O}_w$ in P seems to be reasonably well simulated. Unfortunately, we cannot compare our simulated $\delta^{18}\text{O}_w$ in E to any observational data, but it could be that it is also slightly too enriched. Regarding the Arctic Ocean, except for the isotopic surface flux calculation as outlined above, insufficient river discharge and neglecting the fractionation during sea-ice

formation could be further sources for the model-data deviations. As part of the Pan-Arctic River Transport of Nutrients, Organic Matter and Suspended Sediments (PARTNERS) project, *Cooper et al.* [2008] published flow-weighted annual mean discharge and $\delta^{18}\text{O}_w$ data (collected between 2003 and 2006) from the six largest Arctic rivers (Table 3.2). According to their estimates, $\delta^{18}\text{O}_w$ values of Eurasian rivers decrease from west-to-east, thus the Ob' river discharges the most enriched freshwater (-14.9 ‰) while the water of the Kolyma river is most depleted in heavy isotopes (-22.2 ‰). This west-to-east trend is also recognizable in our model (Figure 3.13b), where the Ob' river contributes freshwater with a $\delta^{18}\text{O}_w$ value of around -15.6 ‰ and the Kolyma river of around -20.5 ‰. Even though it seems that the isotopic composition of the Ob' river is too depleted, all the other three Russian rivers are not as depleted as seen in the PARTNERS data.

Measurements of the Yukon and Mackenzie rivers reveal intermediate isotopic signals (-20.2 ‰ and -19.1 ‰ respectively). In the MITgcm these signals are slightly more enriched with $\delta^{18}\text{O}_w$ values of around -17.1 ‰ and -18.9 ‰ for the Yukon and Mackenzie rivers respectively. A consideration of the overall river discharge to the Arctic Ocean reveals a slight underestimation as the flow-weighted average for all six rivers is -18.8 ‰, while in the model it is only -18.0 ‰. Not only does the isotopic signal of the river discharge matter, but also the discharge amount. Estimating the annual discharge amount in the MITgcm is difficult, because determining the grid cells that belong to the respective river is based on visually assigning them according to the location of the river mouth. This may lead to deviations compared to observational data. While simulated annual discharge for the Yenisey, Lena, Yukon and Mackenzie rivers is in good agreement with reported values by *Cooper et al.* [2008] (Table 3.2), the amounts discharged by the Ob' and Kolyma rivers differ substantially. However, deviations of the annual discharge for all six rivers are tolerable ($\sim 400 \text{ km}^3 \text{ a}^{-1}$). *Cooper et al.* [2008] further reported that the Arctic Ocean basin receives 10 % of the global river runoff (1.3 Sv [Trenberth et al., 2007]). The MITgcm fits right into this magnitude with 9.3 % of the simulated global river runoff (1.17 Sv) received by the Arctic Ocean ($> 60^\circ \text{ N}$). Thus, the deviations that appeared for the Ob' and Kolyma rivers are most likely attributable to the grid cell assignment described above and should not matter significantly. Therefore, both the isotopic signal of river runoff and the discharge amount are rather insignificant for the model-data mismatch in the Arctic Ocean. The general pattern of the simulated isotopic river discharge shows that river runoff is more enriched in low and mid-latitudes (Figure 3.13a), which is in accordance with observations [IAEA, 2012]. Thus, simulating the isotopic composition of river runoff by taking the isotopic composition of the local

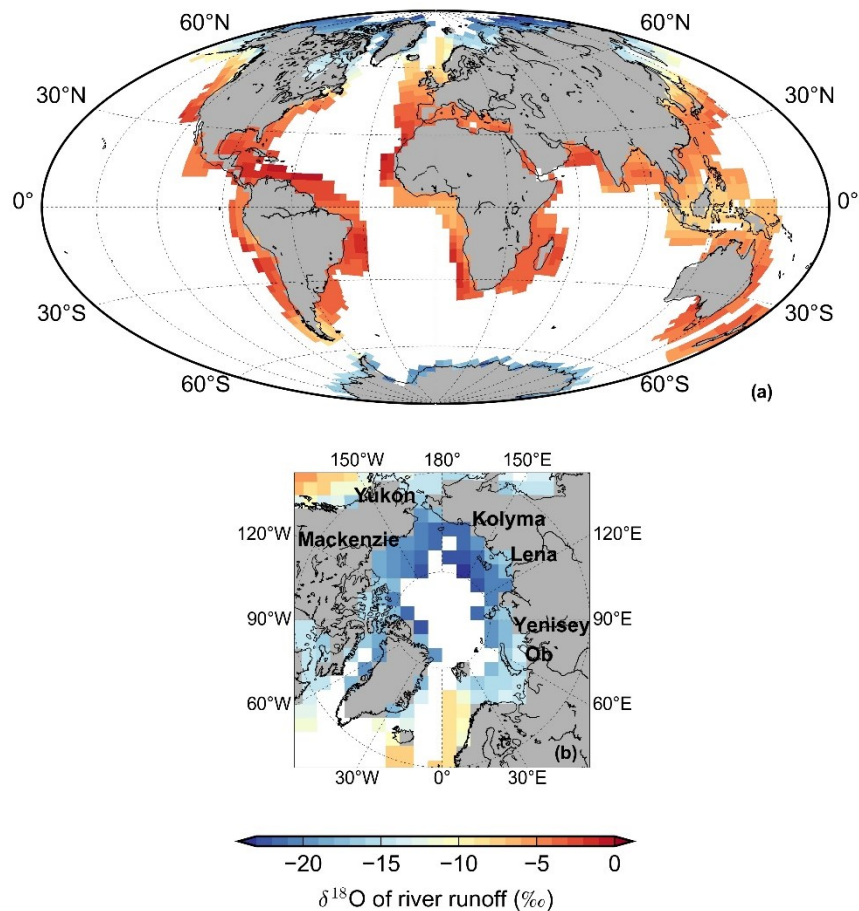


Figure 3.13: Simulated annual mean $\delta^{18}\text{O}$ of river runoff in the upper 50 m for (a) the global ocean and (b) the Arctic Ocean with the approximate location of discharge of the six largest rivers.

Table 3.2: Annual mean $\delta^{18}\text{O}$ of river runoff and discharge for each of the six largest Arctic rivers presented by *Cooper et al.* [2008] and simulated by the MITgcm. Note that the river runoff in the MITgcm is distributed along the coasts (Figure 3.13a and b) and thus the distinction which grid cell belongs to which river is just a rough approximation and can cause discrepancies.

River	$\delta^{18}\text{O}$ (‰) simulated by the MITgcm	$\delta^{18}\text{O}$ (‰) by <i>Cooper et al.</i> [2008]	Annual Discharge ($\text{km}^3 \text{ a}^{-1}$) simulated by the MITgcm	Annual Discharge ($\text{km}^3 \text{ a}^{-1}$) by <i>Cooper et al.</i> [2008]
Ob'	-15.6	-14.9	779	373
Yenisey	-17.7	-18.4	475	656
Lena	-19.8	-20.5	508	566
Kolyma	-20.5	-22.2	457	114
Yukon	-17.1	-20.2	172	214
Mackenzie	-18.9	-19.2	276	322
All Six Rivers	-18.0	-18.8	2667	2245

precipitation is a reasonable first approximation, but should be overcome by implementing a bucket model in the MITgcm, which calculates the river discharge and its isotopic content for individual catchment areas over land.

Further discrepancies between model and observations might be due to the formation and transport of sea ice. During the formation of sea ice, the heavier isotopes are entrapped in the solid ice structure, while depleted sea ice brine is expelled [O'Neil, 1968]. However, this fractionation process is relatively small. *Lehmann and Siegenthaler* [1991] reported an equilibrium fractionation constant of $2.91 \cdot 10^{-3}$ between pure water and ice under equilibrium laboratory conditions, while *Melling and Moore* [1995] estimated a fractionation constant of $2.09 \cdot 10^{-3}$ for ~1 m thick ice in the Canadian Beaufort Sea. So even though sea ice is highly dynamic, excluding not only the fractionation during the formation of sea ice but also the transportation of isotopes within the sea ice might lead to minor local changes but should not be one of the main sources of error. Indeed, *Brennan et al.* [2013] investigated the impact of a fractionation factor for sea ice on $\delta^{18}\text{O}_w$ in the University of Victoria Earth System Climate Model (UVic ESCM). They conclude that local changes in $\delta^{18}\text{O}_w$ due to the contribution of sea ice are smaller than 0.14 ‰ and therefore rather negligible.

Furthermore, the coarse resolution of our model may cause some of the model-data discrepancies, since it is not able to resolve all of the physical processes. For instance, water that is transported towards the Nordic Seas as parts of the Gulf Stream System is displaced by water from the Labrador Sea due to the coarse horizontal grid system. Also, vertically the thermocline might not be as pronounced and located as in the real ocean, since e.g. the upper 500 m in the MITgcm are only represented by four layers. Observational data corresponding to depths within that transition layer might reflect a different signal than resolved by the ocean model.

Since $\delta^{18}\text{O}_w$ is a passive tracer, shifts at the ocean surface might propagate in the ocean interior. Errors in the general model performance might further add to the deviations in the deeper ocean. However, the water masses in the MITgcm in terms of structure, extent and magnitude are faithfully simulated (cf. 3.4.1) and thus can be ruled out as a significant error source.

Additionally, our isotopic forcing was not obtained from the same source as the atmospheric forcing for the freshwater, heat and momentum flux, whereby a maximum consistency cannot be ensured and an additional uncertainty to our sources of error is added.

Despite these sources of error, the simulated pattern of $\delta^{18}\text{O}_w$ both at the sea surface as well as in the deep ocean agrees fairly well with other recent studies such as the study by *Xu et al.* [2012] with an OGCM as well as the studies by *Roche and Caley* [2013] and *Werner et al.* [2016] with fully coupled models.

3.4.3 Water mass structure

The seawater oxygen isotope ratio and salinity are controlled by the same processes such as evaporation, precipitation, river runoff and sea-ice formation. In this way, they are locally linearly related, resulting in a slope that varies between 0.1 ‰ psu^{-1} in low latitudes and up to 1 ‰ psu^{-1} in high latitudes. However, water that is evaporated from the ocean surface does not carry any salt, but stable water isotopes. The agreement between the simulated slope and observational slope in the tropical regions is good, but significantly weaker in the mid-latitudes. This mismatch is mainly caused by the stable water isotopes since the overall comparison to observed SSS is quite good and comparable with other ocean models (cf. section 3.4.1).

Subtropical gyres are characterized by high salinity and $\delta^{18}\text{O}_w$ values. While the model shows reasonable salinities in these regions (Figure 3.2a), its surface water is too depleted (Figure 3.4a). As discussed in section 3.4.2 these discrepancies rather stem from an interaction of reduced E whereby not enough ^{16}O is removed from the ocean surface, $\delta^{18}\text{O}_w$ in E that is probably slightly too enriched and the dilutional effect of enhanced P . As opposed to this are the values of low salinity and $\delta^{18}\text{O}_w$ at the other end of the slope. They are mainly located around the upper boundary of the mid-latitudes ($\sim 60^\circ \text{ N/S}$) near the coast (e.g. the Okhotsk Sea and Bering Sea) and within the western boundary currents (e.g. Gulf Stream). While the modeled salinity is slightly too salty, the $\delta^{18}\text{O}_w$ values are not as depleted as seen in observations, causing the deviations in the slope of the $\delta^{18}\text{O}_w$ -salinity relationship. We infer, that the coarse grid resolution is the main driver for this mismatch.

Despite these discrepancies at the sea surface, the investigation of the water mass structure of the deeper parts of the ocean reveals that the model is suitable to determine the large-scale distribution of water masses in terms of the $\delta^{18}\text{O}_w$ signature. Water mass formation regions are mainly located in the high-latitude Atlantic Ocean and produce large parts of the deep and bottom waters of the World Ocean. Hence, our investigation focuses on the main water masses (AAIW, AABW and NADW) within that basin. *Emery and Meincke* [1986] used published temperature and salinity data to determine the core properties of the main water masses of the World Ocean. Applying these characteristics of the Atlantic Ocean to both the GISS data and modeled values (Figure 3.14; Table 3.3),

clearly shows the resemblance. All three water masses are found in the ocean model, but their temperature-salinity ranges differ slightly from those given by *Emery and Meincke* [1986] as discussed in section 3.4.1. Nevertheless, even though the absolute range of $\delta^{18}\text{O}_w$ values is narrower in the model than in the observations, the modeled mean values are remarkably close to the observations (cf. Table 3.3). Our results are quite encouraging, suggesting that the nonlinear free surface and real freshwater flux boundary conditions of the MITgcm indeed leads to an improvement compared to other ocean models using salinity restoring [e.g. *Paul et al.*, 1999; *Xu et al.*, 2012].

Overall, even though some regions at the surface reveal localized biases regarding the $\delta^{18}\text{O}_w$ distribution, the water mass structure of the deeper parts of the ocean and their characteristic $\delta^{18}\text{O}_w$ values are successfully simulated. Hence, the ocean model is well suited to perform long-term simulations in a paleoclimatic context and investigating the respective $\delta^{18}\text{O}_w$ changes.

3.4.4 Planktonic foraminiferal $\delta^{18}\text{O}_c$

To address questions regarding the evolution and history of the ocean and climate, oxygen-isotopic records derived from measurements of foraminiferal shells have been used extensively. Particularly, the last glacial maximum (LGM) and last deglaciation are time periods, for which the evidence comes from proxy data recorded as oxygen isotopes in CaCO_3 . Hence, before using the model for paleostudies, an evaluation of modeled and measured $\delta^{18}\text{O}_c$ for the PI climate is necessary.

The $\delta^{18}\text{O}_c$ of planktonic foraminifera is not only determined by $\delta^{18}\text{O}_w$ and temperature of the ambient water in which the calcification takes place, but also altered by vital effects and modifications after death. Vital effects involve, for example, the photosynthetic activity of algal symbionts. Species like *G. ruber* (w) and *G. sacculifer* harbor symbionts [*Kucera*, 2007] that change the microenvironment around the shell by increasing the calcification rates through CO_2 uptake and thus shifting the pH towards more alkaline conditions corresponding to elevated carbonate ion concentrations ($[\text{CO}_3^{2-}]$). This mechanism will induce a kinetic fractionation that leads to relatively ^{18}O -depleted shells [*Ravelo and Hillaire-Marcel*, 2007]. Furthermore, in the course of ontogenesis successive shell chambers reveal more enriched $\delta^{18}\text{O}_c$ values [*Bemis et al.*, 1998], while significant changes also occur during reproduction. *Bé* [1980], *Duplessy et al.* [1981] and *Mulitza et al.* [2004] as well as others argue that some planktonic foraminifera add an additional layer of calcite during reproduction (gametogenic calcification). This additional calcite layer is secreted in deeper and cooler water masses, introducing an

Table 3.3: $\delta^{18}\text{O}_w$ characteristics of the main water masses (Antarctic Intermediate Water – AAIW, North Atlantic Deep Water – NADW and Antarctic Bottom Water – AABW) in the Atlantic Ocean for the observational (GISS) and simulated data (MIT). The $\delta^{18}\text{O}_w$ characteristics are determined by applying the temperature and salinity ranges of the respective water masses, reported by *Emery and Meincke* [1986], to the data within in the Atlantic Ocean (basin mask is based on the WOA09).

	AAIW	NADW	AABW
$\delta^{18}\text{O}_w^{\text{GISS}}$ range [‰]	-2.50 – 1.41	-0.49 – 0.88	-0.31 – 0.00
$\delta^{18}\text{O}_w^{\text{GISS}}$ mean value [‰]	-0.09	0.21	-0.14
$\delta^{18}\text{O}_w^{\text{GISS}}$ standard deviation [‰]	0.42	0.09	0.08
$\delta^{18}\text{O}_w^{\text{MIT}}$ range [‰]	-0.25 – 0.10	0.02 – 0.14	-0.16 – -0.03
$\delta^{18}\text{O}_w^{\text{MIT}}$ mean value [‰]	0.00	0.11	-0.11
$\delta^{18}\text{O}_w^{\text{MIT}}$ standard deviation [‰]	0.07	0.03	0.06

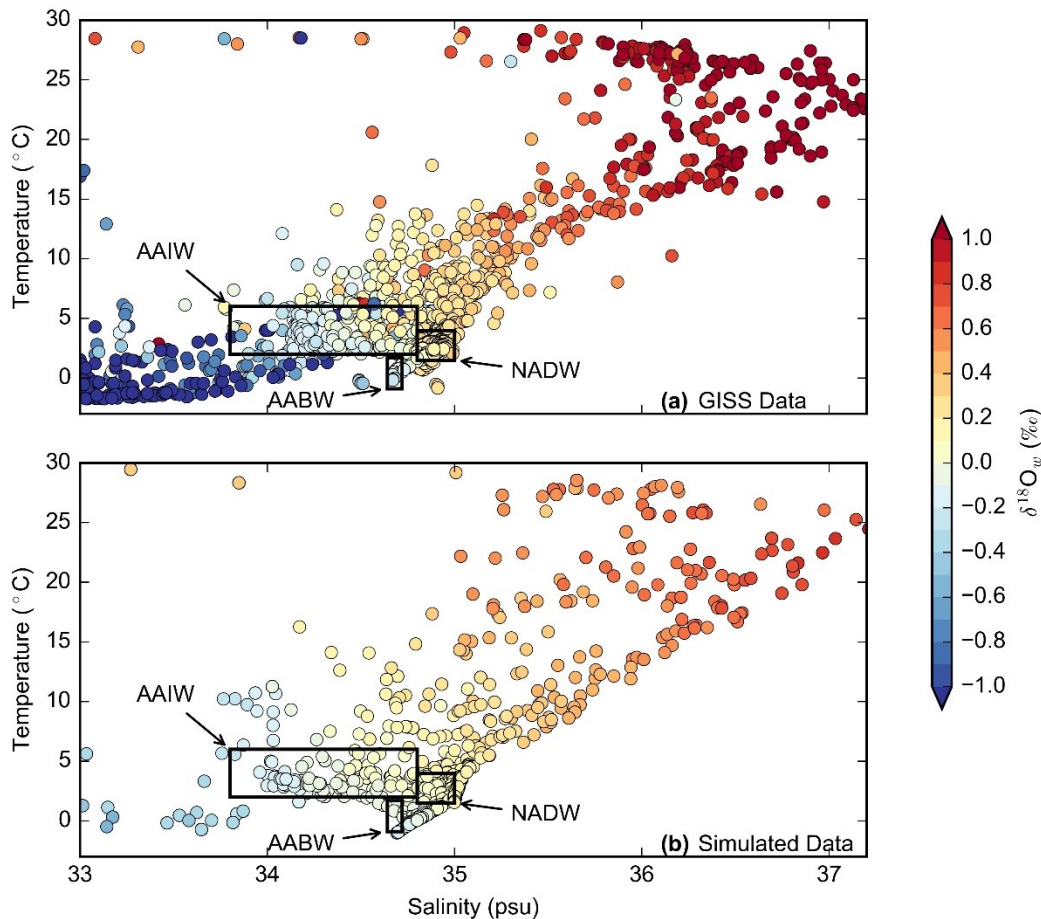


Figure 3.14: Combined T-S- $\delta^{18}\text{O}_w$ diagrams for the (a) GISS data and (b) simulated data (annual mean) in the Atlantic Ocean. The temperature and salinity ranges for the different water masses in the Atlantic Ocean are defined according to *Emery and Meincke* [1986].

^{18}O enrichment in the shell. Duplessy *et al.* [1981] ascertained a $\delta^{18}\text{O}$ mean enrichment of 0.78 ‰ and 0.92 ‰ in the shells of *G. ruber* and *G. sacculifer* from core-top sediments, respectively. Mulitza *et al.* [2004] also showed that foraminiferal shells from the sediment are increased in $\delta^{18}\text{O}$ by approximately 0.5-1 ‰. The average $\delta^{18}\text{O}$ composition recorded by a foraminiferal species at the sea floor is further influenced not only by the vertical migration within the water column, whereby signals from different depths are incorporated into the foraminiferal shell, but also by seasonal variations in shell production. Species that prefer polar waters (e.g. *N. pachyderma* (s)) rather peak during summer, whereas species that are distributed in warm provinces (e.g. *G. bulloides*) reflect a spring signal followed by a smaller autumn peak [Kucera, 2007]. Additionally, the isotopic composition of foraminiferal shells can also be altered after deposition due to dissolution. This is especially the case, if the initial shell is dissolved rather than the crust formed during gametogenesis (gametogenic calcite is often more resistant to dissolution [Bé *et al.*, 1975]), further shifting the $\delta^{18}\text{O}$ towards higher values.

All these mechanisms described above cannot be captured in our model, because it does not have an ecosystem module included, which could represent the life cycle of foraminifera and factors that determine the incorporation of oxygen isotopes in foraminiferal shells. Neglecting these processes might lead to additional model-data discrepancies. To avoid them, a comparison with plankton-tow data is more reliable for testing the general capability of the model to simulate $\delta^{18}\text{O}_c$, since the depth and month of sampling is known (thus excluding any deviations due to seasonality or depth habitat) and the foraminifera are sampled alive (thus excluding any deviations due to gametogenic calcification or modifications after death).

For the surface distribution of $\delta^{18}\text{O}_c$, the largest discrepancies between model and data occurred in the Arctic Ocean. While the SST is too low, the $\delta^{18}\text{O}_w$ is not depleted enough in this region. These two effects could compensate each other, but the $\delta^{18}\text{O}_c$ reveals a slight overestimate, which results from the underestimated SST. To disentangle the background of any model-data mismatch it is best to investigate the model-data fit considering individual species (Figure 3.15). Therefore, we use species-specific paleotemperature equations published by Mulitza *et al.* [2003] (Table 3.4). First, we notice that the correlation is weaker when individual species are considered compared to investigating them grouped together. The best model-data fit is captured for *G. bulloides* ($r^2 = 0.72$, RMSE = 0.65 ‰, $n = 35$), while it is significantly weaker for *N. pachyderma* ((s); $r^2 = 0.41$, RMSE = 0.71 ‰, $n = 61$). While the largest deviations for *N. pachyderma* (s) occur in the upper surface column, data points that deviate from the 1:1

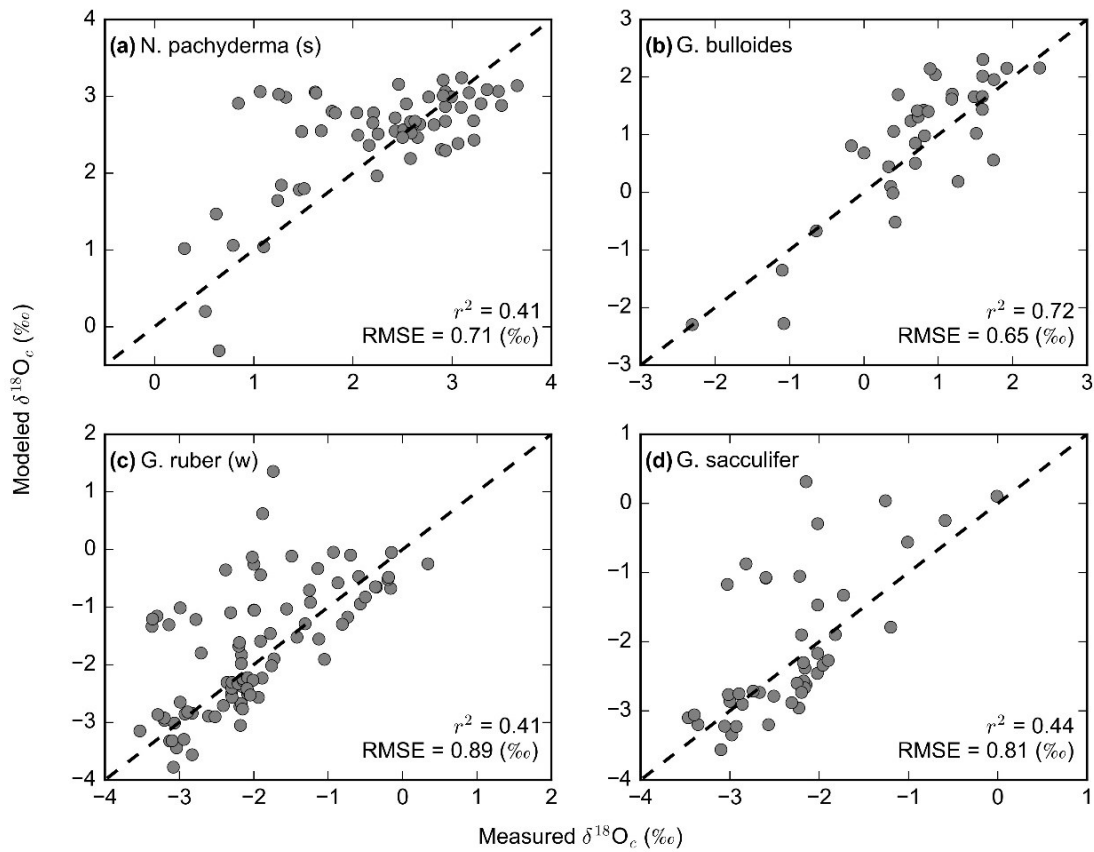


Figure 3.15: Relationship between measured $\delta^{18}O_c$ from plankton-tow data (for references see text) and simulated long-term monthly mean $\delta^{18}O_c$ from the MITgcm for the individual species: (a) *N. pachyderma* (s), (b) *G. bulloides*, (c) *G. ruber* (w) and (d) *G. sacculifer*. For the comparison the specific month and depth of plankton tow sampling has been considered. Dashed lines represent the 1:1 line.

Table 3.4: Data-model comparison of $\delta^{18}O_c$ of planktonic foraminifera data using species specific palaeotemperature equations [Mulitza *et al.* 2003].

Foraminiferal species	Palaeotemperature equation	RMSE [‰]	r^2	slope [‰ ‰ ⁻¹]
<i>G. ruber</i> (w)	$T = -4.44 \cdot (\delta^{18}O_c - \delta^{18}O_w) + 14.20$	0.89	0.41	0.77
<i>G. sacculifer</i>	$T = -4.35 \cdot (\delta^{18}O_c - \delta^{18}O_w) + 14.91$	0.81	0.44	0.97
<i>G. bulloides</i>	$T = -4.70 \cdot (\delta^{18}O_c - \delta^{18}O_w) + 14.62$	0.65	0.71	1.05
<i>G. pachyderma</i> (s)	$T = -3.55 \cdot (\delta^{18}O_c - \delta^{18}O_w) + 12.69$	0.71	0.41	0.53

line for the other three species mainly correspond to depths larger than 100 m (not shown here). This becomes clearer, when the model-data comparison is carried out for data that only falls in the upper level (< 50 m) of the ocean model, resulting in a significant improvement of the RMSE and r^2 for *G. ruber* ((w); $r^2 = 0.86$, RMSE = 0.41 ‰), *G. sacculifer* ($r^2 = 0.80$, RMSE = 0.37 ‰) and *G. bulloides* ($r^2 = 0.83$, RMSE = 0.56 ‰), while the RMSE worsens for *N. pachyderma* ((s); $r^2 = 0.46$, RMSE = 0.89 ‰). Even though the sampling depth of the plankton-tow data is known and was used for interpolation to the respective grid cell, we suppose that the $\delta^{18}\text{O}_c$ signal recorded by the living foraminifera rather corresponds to a shallower water depth (at least for the first three species mentioned before). *Schiebel and Hemleben* [2005] illustrated the average depth inhabited by planktonic foraminifera (cf. Figure 2 therein). While *G. ruber* (w), *G. sacculifer* and *G. bulloides* inhabit the upper surface column (~ 25 m, ~ 40 m and ~ 50 m, respectively), *N. pachyderma* (s) lives on average in deeper parts (~ 90 m) and thus might confirm the assumption above. Another source of error may be the coarse vertical resolution of the model.

Overall, modeled $\delta^{18}\text{O}_c$ values can be compared to data successfully with a better result when all species are grouped together compared to individual species. Taking into account the processes that potentially affect the $\delta^{18}\text{O}_c$ of foraminifera and considering the species-specific influence by habitat depth and seasonality, a comparison with $\delta^{18}\text{O}_c$ collected from sediment cores appears to be feasible in a future study.

3.5 Conclusions

Stable water isotopes have been successfully implemented in the MITgcm, using real freshwater and isotopic flux boundary conditions in conjunction with the non-linear free surface. The model captures well the broad pattern and magnitude of $\delta^{18}\text{O}$ in annual mean seawater, reflecting accurately regions of net evaporation. The most enriched surface water occurs in the subtropical gyre of the Atlantic Ocean, while the surface water in the Arctic Ocean is isotopically most depleted. However, the latter ocean basin is the one with largest model-data discrepancies. They mostly result from the absence of highly depleted precipitation and snow fall in areas covered by sea ice. The simulated $\delta^{18}\text{O}_w$ -salinity relationship is in good agreement with observations in tropical regions but less so in mid-latitudes, due to the misrepresentation of $\delta^{18}\text{O}_w$ caused by the coarse grid resolution of the model as well as an interaction of P , E and $\delta^{18}\text{O}_w$ in E . But even though the $\delta^{18}\text{O}_w$ distribution at the sea surface reveals some deviations, the water mass structure of the deeper parts of the ocean and their characteristic $\delta^{18}\text{O}_w$ values are well captured in our model and show that $\delta^{18}\text{O}_w$ indeed can be used to characterize different

water masses. Further, we tested simulated $\delta^{18}\text{O}_c$ against measurements of planktonic foraminiferal shells from plankton-tow data. Again, the latitudinal gradients and large-scale patterns are faithfully reproduced. The model-data fit is better when all species are grouped together, compared to individual species and the largest discrepancies are most likely attributable to different depth habitats. A better understanding of the factors that determine the recording of oxygen isotopes in foraminiferal shells might be provided by ecosystem models including foraminifera [Fraile *et al.*, 2008; Lombard *et al.*, 2009; Kretschmer *et al.*, 2016].

The MITgcm and its newly developed stable water isotope package offer a great opportunity to perform long-term simulations in a paleoclimatic context and assimilating water isotopes with the adjoint method. Thus, investigations of not only the respective changes in $\delta^{18}\text{O}_w$ but also in foraminiferal $\delta^{18}\text{O}_c$ during the LGM or last deglaciation can be performed.

Code availability

The water isotope package incorporated in the MITgcm can be obtained by contacting the first author: R. Völpel (rvoelpel@marum.de). Additionally, a release of the package through the MITgcm repository will be prepared.

Appendix A

The MITgcm provides a scheme that balances the freshwater flux (net fluxes are set to zero) at each time step, preventing uncontrolled drifts in salinity and sea surface height caused by an imbalance in precipitation, evaporation and runoff. However, this scheme adversely affects the seasonality of the net surface freshwater flux.

Following Large *et al.* [1997], a precipitation correction factor $f_P(y)$ (a tracer specific precipitation correction factor $f_P^i(y)$) is implemented in the MITgcm and computed each year y , whereby the global freshwater flux (the global isotopic flux) is annually balanced.

The correction factor is applied to the precipitation field (tracer specific precipitation field), such that the precipitation throughout a model year y is given by:

$$P = f_P(y) \cdot P(y) \quad \text{A(3.1)}$$

$$P^i = f_P^i(y) \cdot P^i(y) \quad \text{A(3.2)}$$

The size of f_P ($f_P^i(y)$) depends on the change in volume of global ocean freshwater throughout a year (ΔV_y^F) (change in the amount of the global isotopic tracer in the ocean throughout a year - Δn_y^i) and the volume of precipitation falling on the ice-free ocean

(amount of tracer specific precipitation) and river runoff (amount of tracer specific river runoff) as an annual integral ($V^P (n^{P^i})$ and $V^R (n^{R^i})$, respectively). These values are used to compute the correction factor for the following year:

$$f_P(y+1) = f_P(y) \left(1 - \frac{\Delta V_y^F}{(V^P + V^R)} \right) \quad \text{A(3.3)}$$

$$f_P^i(y+1) = f_P^i(y) \left(1 - \frac{\Delta n_y^i}{(n^{P^i} + n^{R^i})} \right) \quad \text{A(3.4)}$$

If the change in volume of global ocean freshwater is positive (negative), the global salinity will decrease (increase) and the correction factor is decreased (increased) for the next year ($y+1$). For the tracer specific correction factor, it applies that a positive (negative) change in the amount of the global isotopic tracer leads to an increase (decrease) in global tracer concentration and thus a decreased (increased) tracer specific correction factor for the next year ($y+1$). Throughout the model integration changes are getting smaller resulting in a precipitation correction factor (tracer specific precipitation correction factor) that remains approximately constant at $f_P(y) = 1.0014$ after ~ 1500 model years ($f_P^{H_2^{16}O}(y) = 1.0241$ after ~ 600 model years and $f_P^{H_2^{18}O}(y) = 1.0253$ after ~ 1200 model years - Figure A.1).

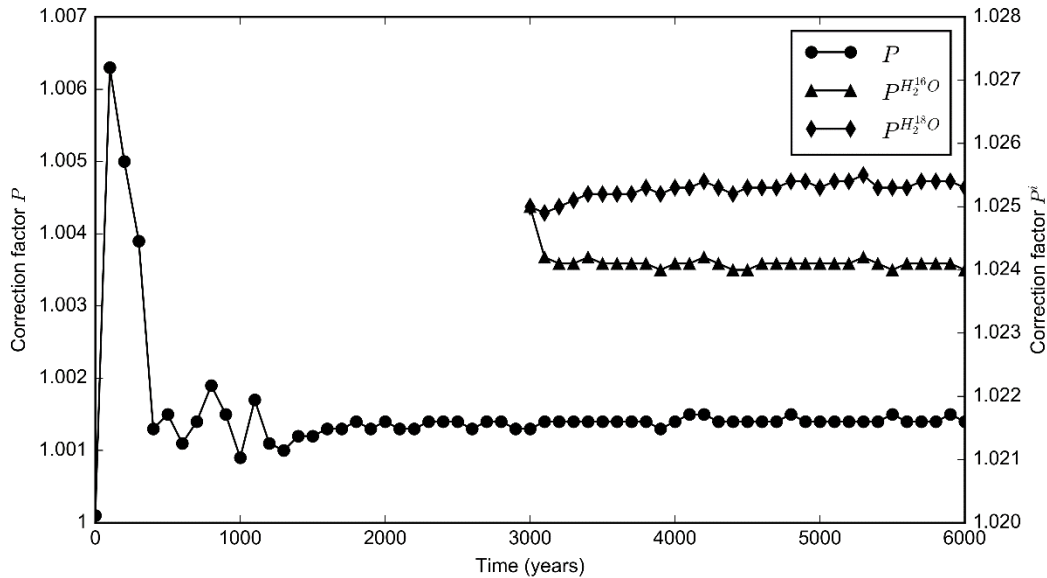


Figure A.1: Time series of the correction factor for both, the precipitation and tracer specific precipitation throughout the model integration.

Acknowledgments

We would like to thank T. Tharammal for providing the isotopic data of NCAR IsoCAM and T. Kurahashi-Nakamura for providing the atmospheric forcing fields obtained with the adjoint model. Further, we would like to thank Martin Losch for his advice throughout the model development. Comments and suggestions by the three anonymous reviewers and the Editor highly improved the quality and clarity of the manuscript. This project was funded through the DFG Research Center/Center of Excellence MARUM – “The Ocean in the Earth System”.

Chapter 4 Water-mass vs. sea-level effects on benthic foraminiferal oxygen isotope ratios in the Atlantic during the LGM

R. Völpel¹, S. Mulitza¹, A. Paul¹, J. Lynch-Stieglitz² and M. Schulz¹

¹MARUM - Center for Marine Environmental Sciences and Faculty of Geosciences, University of Bremen, Bremen, Germany

²School of Earth and Atmospheric Sciences, Georgia Institute of Technology, Atlanta, GA, USA

In review in *Paleoceanography and Paleoclimatology*

Abstract.

Depth transects of benthic foraminiferal oxygen isotopes from the Atlantic Ocean show that glacial-interglacial changes are higher at deep (> ~2000 m) than at intermediate water levels. Our model results suggest that the smaller changes in the upper 1000 m of the water column are a result of the glacial sea-level lowering of about 120 m, leading to warmer temperatures of around 1 °C and hence a smaller glacial-interglacial stable oxygen isotope difference. In contrast, a shoaling of the water-mass boundary to ~ 2000 m water depth between the northern source and southern source water is accompanied by the expansion of a cold (close to the freezing point) southern source water in the abyssal ocean, increasing the oxygen isotope values of benthic foraminifera from the LGM in the deep Atlantic. These two effects explain the different amplitudes of glacial-interglacial stable oxygen isotope differences in the upper and deeper water column of the Atlantic Ocean.

4.1 Introduction

The climate of the Last Glacial Maximum (LGM, 19,000 - 23,000 years before present (BP) [e.g. *Mix et al.*, 2001]) was characterized by a reduction in sea-surface temperatures of ~2 °C [*MARGO Project Members et al.*, 2009], tightly linked to low atmospheric CO₂ concentrations of ~190 ppm [*Monnin et al.*, 2001] and associated with large northern hemisphere continental ice sheets leading to a sea-level lowering of ~120 m [*Clark et al.*, 2009; *Fairbanks*, 1989]. Thus, the LGM constitutes a climate that differed significantly from today. Changes in climate are closely related to changes in ocean circulation, in particular the Atlantic Meridional Overturning Circulation (AMOC), which plays a key role in regulating heat transport especially in the Atlantic realm and in altering glacial-

interglacial global atmospheric CO₂ concentrations [Brovkin *et al.*, 2007, Ganopolski and Brovkin, 2017] by storing carbon in the deep ocean for long time scales.

So far, model studies and proxy reconstructions have produced conflicting results regarding the strength of the glacial AMOC: some estimate a weaker and shallower, others a stronger and deeper AMOC [Lippold *et al.*, 2012; Lynch Stieglitz *et al.*, 1999, 2006; McManus *et al.*, 2004; Otto-Bliesner *et al.*, 2007; Yu *et al.*, 1996]. A recurring hypothesis emerging from paleoceanographic reconstructions is the shoaling of the glacial water-mass boundary between the North Atlantic Deep Water (NADW) and Antarctic Bottom Water (AABW) to approximately 2000 m water depth, based on the distribution of the ratio of stable carbon isotopes ($\delta^{13}\text{C}$) in benthic foraminiferal carbonate [Curry and Oppo, 2005; Duplessy *et al.*, 1988; Sarnthein *et al.*, 1994]. This shoaling is suggested to be accompanied by the expansion of a cold (close to the freezing point) southern source water in the deep abyssal ocean [Duplessy *et al.*, 2002; Labeyrie *et al.*, 1992]. The processes behind the rearrangement of the water mass distribution during the LGM are controversial, but may be linked to the expansion of summer sea ice around Antarctica [e.g. Ferrari *et al.*, 2014; Mackensen *et al.*, 1996; Paul and Schäfer-Neth, 2003]. This would also explain the salt stratification as well as the reversed meridional gradient of salt in the glacial ocean as reported in pore fluid measurements [Adkins *et al.*, 2002], because the southern deep water upwelled to the surface under sea ice, which imprinted it with high salinities due to strong brine rejection. Moving the water-mass boundary away from the zone of intense mixing near the seafloor might have led to a reduced vertical mixing of the southern source water with the overlying northern source water, which may have enhanced the ocean's ability to store carbon [Adkins, 2013; Ferrari *et al.*, 2014; Lund *et al.*, 2011].

However, the interpretation of the water mass distribution based on $\delta^{13}\text{C}$ can be complicated, due to the non-conservative nature of the tracer. While it is affected by ocean circulation, biological remineralization of organic matter further alters its signal. The individual concentrations of H₂¹⁶O and H₂¹⁸O as well as temperature are conservative in the interior of the ocean away from the sources and sinks at the sea surface. Using these to calculate the ratio of stable oxygen isotopes in benthic foraminiferal carbonate ($\delta^{18}\text{O}_c$) may be a more accurate attempt to reconstruct ocean circulation.

For the glacial western Atlantic Ocean, Lund *et al.* [2011] and Keigwin [2004] showed that below 2000 m water depth the $\delta^{18}\text{O}_c$ differences between the LGM and Holocene are driven by a large increase (~ 0.3 ‰) in glacial $\delta^{18}\text{O}_c$, which may be linked to a rearrangement of the water masses. This seems to be a rather robust pattern, because

similar observations have been reported before from the Indian [*Kallel et al.*, 1988] and Pacific Oceans [*Herguera et al.*, 1992].

Here we investigate, whether the increased glacial-interglacial $\delta^{18}\text{O}_c$ anomalies below 2000 m water depth are also recognizable in the eastern Atlantic Ocean and may as well correspond to the glacial water-mass boundary consistent with other proxy reconstructions. Therefore, we analyzed benthic $\delta^{18}\text{O}_c$ values of five sediment cores off North West Africa (NW Africa) and compared their depth profile to ocean model results obtained from the Massachusetts Institute of Technology general circulation model (MITgcm) including stable water isotopes as passive tracers [*Völpe et al.*, 2017]. In this way, we evaluated the effect of water-mass and sea-level changes on the glacial-interglacial $\delta^{18}\text{O}_c$ profile. By means of the model simulation, we further analyzed the LGM ocean state and assessed the strength of the glacial AMOC.

4.2 Materials and Methods

4.2.1 The ocean model - MITgcm

For the reconstruction of the LGM ocean, the Massachusetts Institute of Technology general circulation model (MITgcm) was employed. It solved the Boussinesq form of the hydrostatic Navier-Stokes equations in conjunction with a nonlinear free-surface [*Adcroft et al.*, 2004b; *Marshall et al.*, 1997a]. Using a cubed-sphere grid that consisted of 6 faces with 32x32 horizontal grid cells, a nearly uniform resolution of $\sim 2.8^\circ$ was provided and pole singularities were avoided [*Adcroft et al.*, 2004a]. The ocean was divided into 15 vertical levels of increasing thickness, ranging from 50 m at the surface to 690 m at the seafloor. This relatively coarse resolution provides an efficient tool to study the large-scale circulation pattern of the global circulation. We used the vertical coordinate z^* to avoid the possible vanishing of the upper layer associated with the nonlinear free-surface [*Adcroft and Campin*, 2004] and the partial cell formulation of *Adcroft et al.* [1997] to represent the bathymetry.

A dynamic-thermodynamic sea ice model with viscous-plastic rheology [*Losch et al.*, 2010] was coupled to the ocean model. By using the GM/Redi scheme [*Gent and McWilliams*, 1990; *Redi*, 1982], isopycnal diffusion and eddy-induced mixing was parametrized. We set the background vertical diffusivity for tracers uniformly to $3 \cdot 10^{-5}$ (in $\text{m}^2 \text{s}^{-1}$) and used the polynomial approximation of *Jackett and McDougall* [1995] for the equation of state. The advection of tracers was computed using third-order advection with direct space-time treatment [*Hundsdorfer and Trompert*, 1994].

Within this model-setup, the stable water isotopes H_2^{16}O , H_2^{18}O and HDO were simultaneously simulated as passive tracers. To account for the isotopic fluxes at the sea surface, the model was forced with the isotopic content of precipitation and water vapor while the fractionation during evaporation was treated explicitly in the MITgcm. A detailed description of the implementation of the stable water isotopes and the evaluation of the model results under PI conditions is given in *Völpel et al.* [2017]. This PI simulation will also be used as a reference for the new LGM simulation when analyzing the anomalies between those two time periods. Even though the fractionation during the formation of sea ice was neglected and the isotopic content of river runoff was only estimated based on the isotopic composition of the local precipitation at the river mouth, a good agreement between the modeled $\delta^{18}\text{O}_w$ values and observational data (the NASA GISS Global Seawater Oxygen-18 Database [*Schmidt et al.*, 1999]), both at the sea surface and in the deep ocean, was obtained. Further, the comparison with plankton-tow data [e.g. *Mulitza et al.*, 2003] agreed quantitatively well with the model results. This gives us confidence in the investigation of changes in the distribution of foraminiferal $\delta^{18}\text{O}_c$ during the LGM with respect to PI conditions using the same numerical model.

4.2.2 Experimental setup

Because of the build-up of large continental ice sheets and its associated sea-level lowering of approximately 120 m during the LGM, the model bathymetry was adjusted by remapping the ICE-5G topography [*Peltier*, 2004] onto our model grid. Thus, both the PI and LGM simulations used the same vertical grid (15 levels with the same resolution), but the land-sea mask and bottom topography differed, resulting in a smaller volume of the glacial ocean.

The model was forced with climatological monthly mean atmospheric fields (air temperature, specific humidity, zonal and meridional wind velocity, wind speed, (snow-) precipitation, incoming shortwave radiation as well as river runoff) derived from an LGM simulation with the fully coupled Community Climate System Model Version 3 (CCSM3) [*Merkel et al.*, 2010] following the Paleoclimate Modeling Intercomparison Project 2 [*Braconnot et al.*, 2007a, 2007b], but modified by *Kurahashi-Nakamura et al.* [2017] to be consistent with proxy reconstructions of annual mean SST [*MARGO Project Members et al.*, 2009], benthic $\delta^{18}\text{O}_c$ [*Marchal and Curry*, 2008] and benthic $\delta^{13}\text{C}_c$ [*Hesse et al.*, 2011] using a data assimilation technique [*Errico*, 1997; *Giering and Kaminski*, 1998; *Heimbach et al.*, 2005]. These optimized atmospheric fields were based on a model simulation without the Mediterranean Sea. To avoid any artificial signals, we also

excluded the Mediterranean Sea, even though this may have influenced the subtropical North Atlantic Ocean.

Climatological monthly means of the isotopic content of precipitation and water vapor were available from the National Center for Atmospheric Research Community Atmosphere Model including a water isotope scheme (NCAR IsoCAM) [Tharammal *et al.*, 2013]. Since Tharammal *et al.* [2013] used the SST from Merkel *et al.* [2010] as a boundary condition, a consistency of our forcing fields from two different sources was obtained. Besides the above-mentioned atmospheric fields, the MITgcm also needed incoming longwave radiation $Q_{L\downarrow}$ (in $W\ m^{-2}$) as an external forcing field for calculating the net surface heat flux. Only the net longwave flux Q_{L^*} (in $W\ m^{-2}$) was available from the CCSM3. Thus we estimated $Q_{L\downarrow}$ following

$$Q_{L\downarrow} = (1 - A_{ice}) \cdot \varepsilon_0 \cdot \sigma \cdot SST^4 + A_{ice} \cdot \varepsilon_I \cdot \sigma \cdot IST^4 - Q_{L^*} \quad (4.1)$$

where A_{ice} was the ice-covered area fraction, $\varepsilon_0 = 1$ and $\varepsilon_I = 0.95$ were the emissivity for ocean and ice, respectively, $\sigma = 5.56 \cdot 10^{-8}$ (in $W\ m^{-2}\ K^{-4}$) was the Stefan-Boltzmann constant and SST (in K) and IST (in K) were the surface temperatures of the ocean and ice, respectively. All variables were taken from the CCSM3 to reproduce $Q_{L\downarrow}$ as accurately as possible.

Both, the freshwater and isotopic air-sea fluxes were internally computed in the model following the bulk formulae by Large and Yeager [2004]. Furthermore, to prevent uncontrolled drifts in salinity and tracer concentration, a correction factor for the precipitation field / tracer specific precipitation field has been implemented, whereby the global freshwater flux / isotopic flux was annually balanced [cf. Völpel *et al.*, 2017].

The ocean was initialized with the salinity, temperature and tracer distributions from the PI simulation [Völpel *et al.*, 2017]. To account for the lower sea level due to the continental ice sheets during the LGM [Adkins and Schrag, 2001], the global mean salinity of the initial state was increased by 1.1. Starting the model from a state of rest, we integrated it for 3000 years to reach a quasi-steady state and continued it for a further 3000 years with the individual stable water isotopes added. For analysis, we used the average of the last 100 years. The $\delta^{18}O_w$ values were calculated from the modeled $H_2^{16}O$ and $H_2^{18}O$ concentrations of the simulation according to the definition

$$\delta^{18}O = \left(\frac{R}{R_{STD}} - 1 \right) \cdot 1000\ ‰, \quad (4.2)$$

where R is the ratio of the abundance of the heavier water isotope $H_2^{18}O$ to the abundance of the lighter isotope $H_2^{16}O$ and R_{STD} is the Vienna Standard Mean Ocean Water (VSMOW) standard [Baertschi, 1976]. The continental ice volume effect of 1.1 ‰

[Adkins *et al.*, 2002; Duplessy *et al.*, 2002; Schrag *et al.*, 2002] was added to the computed $\delta^{18}\text{O}_w$ values.

4.2.3 Analyses

4.2.3.1 LGM data

The LGM state of the model is assessed by comparing simulated SSTs and computed $\delta^{18}\text{O}_c$ values with reconstructions. The latest global reconstruction of SST during the LGM is provided by the Multiproxy Approach for the Reconstruction of the Glacial Ocean Surface (MARGO) project [MARGO Project Members *et al.*, 2009] and includes an assessment of its uncertainty, thus permitting the evaluation of the simulated LGM climate. Here, we compare to the annual mean MARGO SST anomalies based on foraminiferal assemblages, dinoflagellate cysts, alkenones and Mg/Ca measurements [MARGO Project Members *et al.*, 2009].

To further test the models' suitability to simulate conditions that correspond to the LGM period, we computed $\delta^{18}\text{O}_c$ for both the PI and LGM simulation using the paleotemperature equation from Marchitto *et al.* [2014]:

$$T = \frac{0.245 - \sqrt{0.045461 + 0.0044 \cdot (\delta^{18}\text{O}_c - \delta^{18}\text{O}_w)}}{0.0022} \quad (4.3)$$

with T being the temperature. Due to the different standards of water and carbonate samples (VSMOW and Vienna Peedee belemnite standard (VPDB)), the $\delta^{18}\text{O}_w$ values needed to be converted by subtracting 0.27 ‰ [Hut, 1987].

The $\delta^{18}\text{O}_c$ anomalies were then compared against a planktonic $\delta^{18}\text{O}_c$ dataset compiled by Waelbroeck *et al.* [2014]. They used the same LGM chronozone quality levels as defined for the MARGO SST reconstruction by Kucera *et al.* [2005]. Anomalies were calculated for the most abundant species: *Globigerinoides ruber* white (*G. ruber* (w)), *Globigerina bulloides* (*G. bulloides*), *Neogloboquadrina pachyderma sinistral* (*N. pachyderma* (s)) and *Globigerinoides sacculifer* (*G. sacculifer*). However, data coverage is relatively sparse, especially in the Southern and Pacific Oceans and most of the data is located along continental margins.

4.2.3.2 Interpolation to higher resolution

Investigating anomalies between the LGM and PI requires the consideration of the sea-level change, which especially becomes apparent when benthic foraminiferal $\delta^{18}\text{O}_c$ anomalies are considered. Since benthic foraminifera live on the sea bed or just beneath the sediment surface, properties of the water at the sea floor might have changed during

the LGM due to the reduction of the overlying water column. To take into account this reduced height of the glacial water column, a LGM depth level shallower by 120 m (e.g. 1880 m) had to be compared to the PI depth level (e.g. 2000 m). So far this is the first model study where the sea-level effect on $\delta^{18}\text{O}_c$ anomalies was considered, whereas other studies compare the same water depth levels.

To do so, we interpolated the ocean levels to a higher vertical resolution, because with only 15 levels of unequal level spacing the comparison could not be realized. We used the Data-Interpolating Variational Analysis (DIVA) software [Troupin *et al.*, 2012], which is an open-source software that employs a variational inverse method [Brasseur *et al.*, 1996]. This method consists of a minimization of a cost function solved by a finite-element approach, finding a smooth analyzed field close to the data set and taking bathymetric constraints into account. Thus, our vertical distribution along the transects shown in Figure 4.1 was divided in 86 equally spaced levels, each of which was 60 m thick (commensurate with the thickness of the first model level of 50 m and a sea-level change of 120 m) starting from a depth of 30 m at the surface and spanning the water column down to a depth of 5190 m. Simultaneously, we increased the horizontal resolution of each transect by a factor of 10.

4.2.4 Sediment cores off NW Africa

We compare our model results to five high-resolution sediment cores retrieved from the continental slope off NW-Africa (Figure 4.1) on Meteor-Expedition M65/1 [Mulitza *et al.*, 2006]. The isotope records of core GeoB9508-5 and GeoB9526-5 have been previously published [Mulitza *et al.* 2008, Zariess and Mackensen, 2011]. Oxygen-isotope analyses have been performed on *Cibicidoides wuellerstorfi* and *Cibicidoides pachyderma* in different isotope laboratories (see Table 4.1). Downcore calendar age distributions were modeled with the R-script BACON [Blaauw and Christen, 2011] using the IntCal13 calibration curve and a local reservoir age of 540 years (± 200 years, 2σ) [Mulitza *et al.*, 2010]. BACON was employed with a memory (mem.mean) set to 0.4 and a flat prior distribution of the accumulation rate (acc.shape) of 0.5. A shape parameter of 9 and a scale parameter of 10 was used to model the age distributions (see Table 4.2). For GeoB9512-5 and GeoB9510-1 the age models are based on a mix of radiocarbon ages (two for each core) and a graphic correlation of uncalibrated XRF Fe/Ca ratios to those of GeoB9508-5 (Figure 4.2). Fe/Ca elemental ratios were measured on the three cores every 2 cm downcore using the AVAATECH XRF Core Scanner I at MARUM, University of Bremen. Variations in sedimentary Fe/Ca are mainly driven by changes in dust deposition related to continental aridity and are therefore likely synchronous in

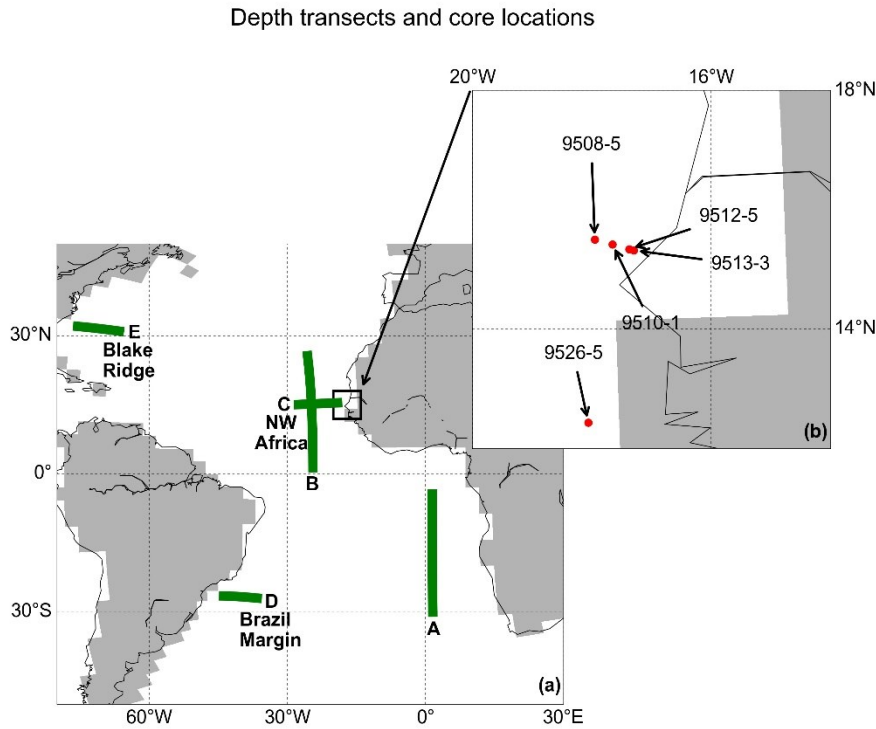


Figure 4.1: Locations of depth transects A, B, C (NW Africa), D (Brazil Margin) and E (Blake Ridge) (green lines) in the Atlantic Ocean used to investigate $\delta^{18}\text{O}_c$ anomalies in the model (a) and sediment cores GeoB9513-3, GeoB9512-5, GeoB9510-1, GeoB9508-5 and GeoB9526-5 (red dots) off NW Africa (b). The land-sea mask used in the LGM model simulation is shaded in grey and the black lines mark the recent coastline.

Table 4.1: Locations and information on sediment cores

Core	Location (° N/° E)	Water depth (m)	Species	Isotope Laboratory	Reference
GeoB9513-3	15.32/- 17.29	-494	<i>Cibicoides pachyderma</i> <i>Cibicoides</i>	MARUM	this study
GeoB9512-5	15.34/- 17.37	-793	<i>pachyderma</i> , <i>Cibicoides</i> <i>wuellerstorfi</i> <i>Cibicoides</i>	GeorgiaTech	this study
GeoB9510-1	15.42/- 17.65	-1566	<i>pachyderma</i> , <i>Cibicoides</i> <i>wuellerstorfi</i>	GeorgiaTech	this study
GeoB9508-5	15.50/- 17.95	-2384	<i>Cibicoides</i> <i>wuellerstorfi</i>	MARUM	<i>Mulitza et al.</i> [2008]
GeoB9526-5	12.44/- 18.06	-3223	<i>Cibicoides</i> <i>wuellerstorfi</i>	AWI	<i>Zarries and</i> <i>Mackensen</i> [2011]

Table 4.2: Radiocarbon dates and age model of sediment cores

Core	Label/Event	Depth (cm)	Radiocarbon Age \pm 1 σ (years BP)	Correlation Age \pm 1 σ (years BP)
GeoB9513-3	KIA31287	3	2860 \pm 35	-
GeoB9513-3	KIA31286	148	15640 \pm 80	-
GeoB9513-3	KIA31284	198	19820 \pm 120	-
GeoB9513-3	KIA35177	268	32130 \pm 1100	-
GeoB9510-1	-	2	-	4593 \pm 229
GeoB9510-1	Holocene Minimum	18	-	7097 \pm 139
GeoB9510-1	EndHS1	88	-	14245 \pm 188
GeoB9510-1	OS-53319	133	14350 \pm 100	-
GeoB9510-1	OnsetHS1	179	-	19241 \pm 218
GeoB9510-1	EndHS2	243	-	23240 \pm 174
GeoB9510-1	OS-53219	268	20600 \pm 110	-
GeoB9510-1	OnsetHS2	287	-	25554 \pm 164
GeoB9512-5	-	18	-	1307 \pm 163
GeoB9512-5	Holocene Minimum	54	-	7097 \pm 139
GeoB9512-5	EndHS1	232	-	14245 \pm 188
GeoB9512-5	OS-53564	303	15000 \pm 210	-
GeoB9512-5	OnsetHS1	412	-	19241 \pm 218
GeoB9512-5	OS-53220	513	20600 \pm 100	-
GeoB9512-5	OnsetHS2	528	-	25554 \pm 164

geographically restricted areas. We identified Fe/Ca maxima related to Heinrich-Stadials (HS) 1 and 2 and the Fe/Ca minimum during the mid-Holocene in gravity core GeoB9508-5. The mean age and the 1 σ age uncertainty of the Fe/Ca events was subsequently assigned to the corresponding events in the gravity cores GeoB9512-5 and GeoB9510-1 and used for age modeling with BACON together with the radiocarbon ages in each the two cores. For each core, 10,000 oxygen isotope time series were generated by combining age-depth models generated with BACON with 10,000 noisy downcore $\delta^{18}\text{O}$ realizations, obtained through Monte Carlo resampling within an analytical uncertainty of 0.1 ‰ (1 σ) (Figure 4.3). The respective $\Delta\delta^{18}\text{O}_c$ values were calculated taking the mean of the LGM (19,000-23,000 years BP) minus the Holocene (< 7000 years BP).

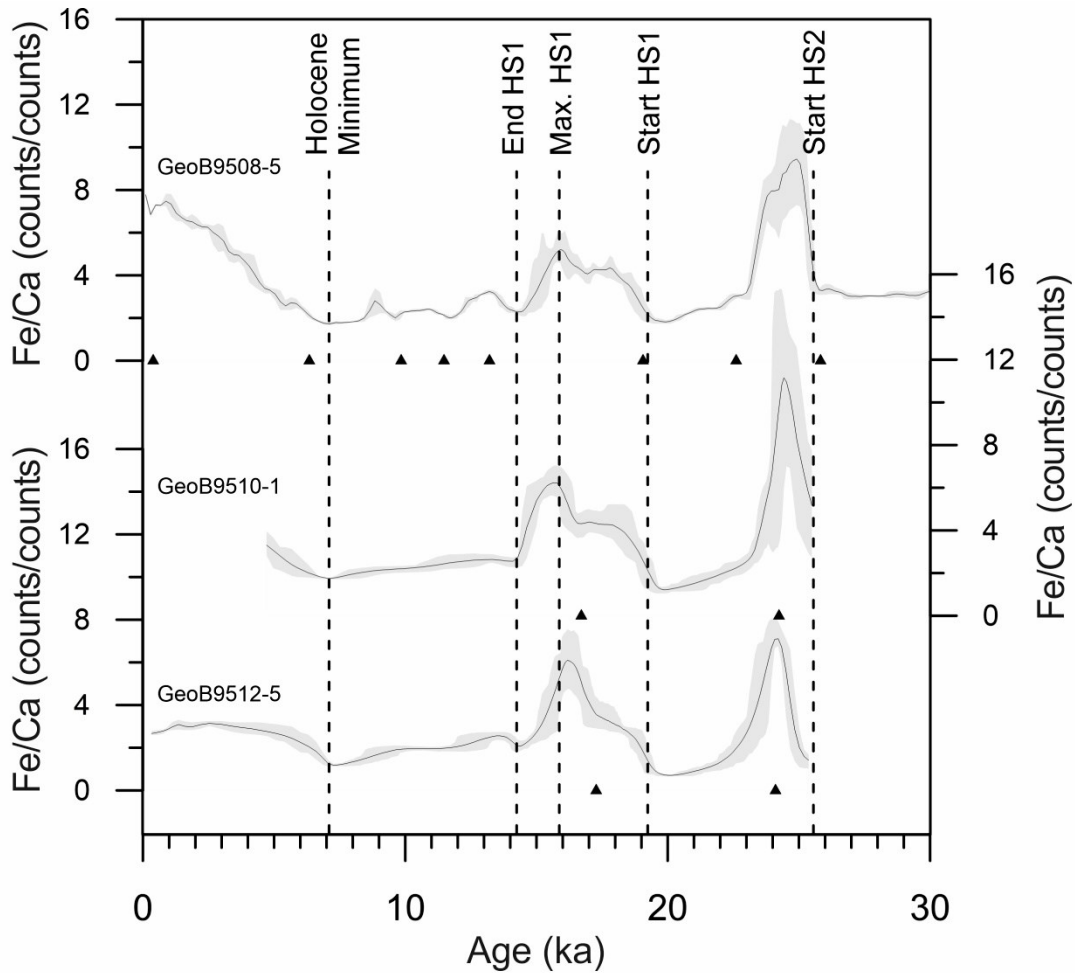


Figure 4.2: Uncalibrated Fe/Ca ratios of cores GeoB9508-5, GeoB9510-1 and GeoB1912-5 versus age. The age model of GeoB9508-5 is entirely based on radiocarbon datings. The age models of GeoB9510-1 and GeoB9512-5 have been derived by aligning (vertical dashed lines) the Fe/Ca records to the Fe/Ca record of GeoB9508-5. Grey shading shows the 95 % confidence interval. Triangles indicate the used radiocarbon datings plotted at the mean calendar age of the sample depth.

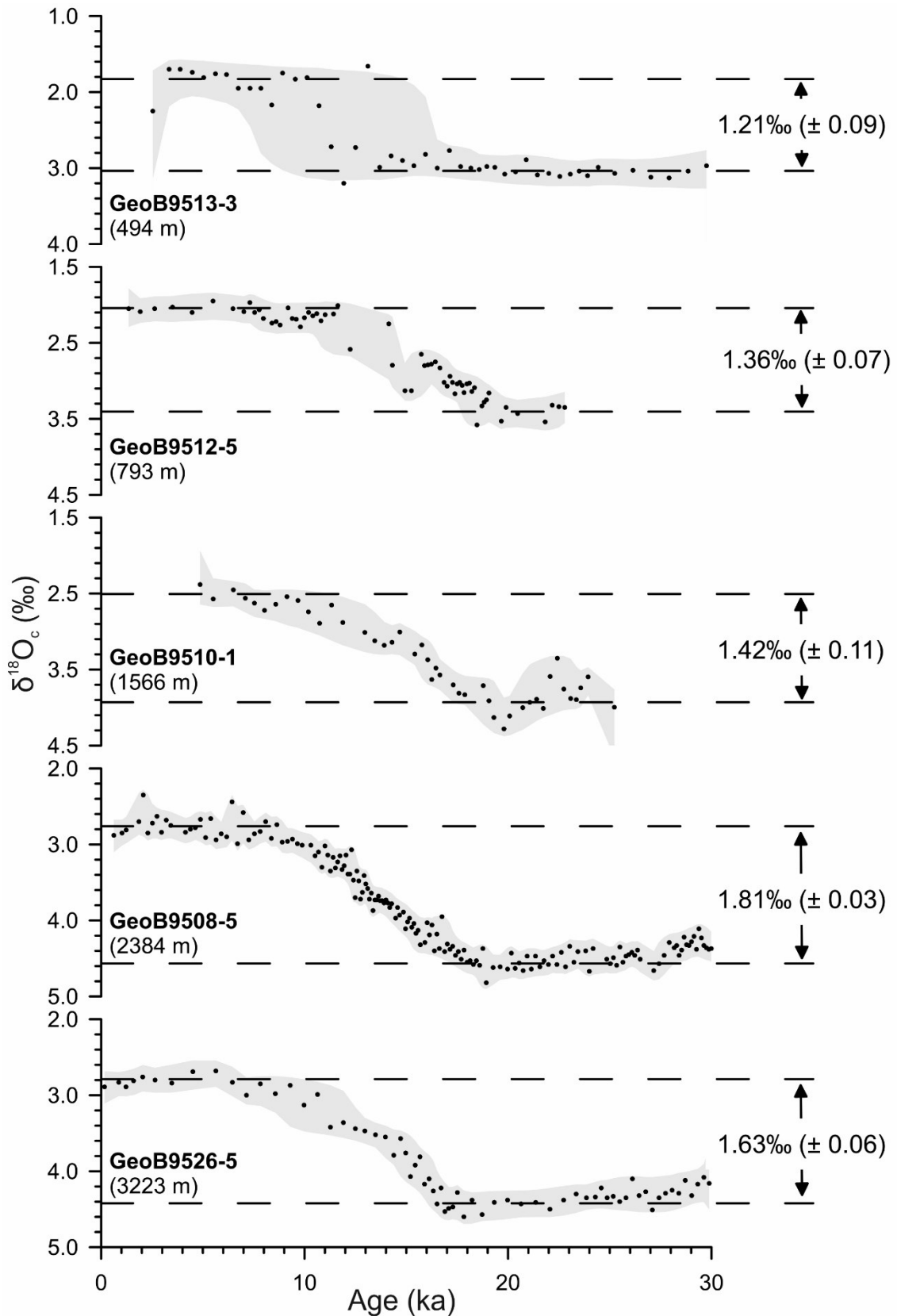


Figure 4.3: Benthic $\delta^{18}O_c$ records of cores GeoB9513-3, GeoB9512-5, GeoB9510-1 (this study respectively), GeoB9508-5 [Mulitza *et al.*, 2008] and GeoB9526-5 [Zarries and Mackensen, 2011]. Dashed horizontal lines indicate $\delta^{18}O_c$ difference between the LGM (23-19 ka) and the Holocene (< 7 ka). Grey shading shows the 95 % confidence interval.

4.3 Results

4.3.1 SST anomalies

Simulated SST anomalies are generally in good agreement with the MARGO data (Figure 4.4 and Table 4.3). On an ocean basin perspective, the Atlantic Ocean underwent stronger cooling than the Pacific and Indian Ocean. Strongest annual mean cooling in the modeled surface ocean (upper 50 m) occurred in the mid-latitude North Atlantic (Figure 4.4 and Table 4.3) and is consistent with proxy reconstructions. However, the cooling is locally more pronounced in the model (up to $-15\text{ }^{\circ}\text{C}$) than observed in the MARGO data (Figure 4.4b). Overall, most of the global surface ocean reveals negative temperature anomalies resulting in a globally area averaged difference of $-1.9\text{ }^{\circ}\text{C}$. However, regions with positive temperature anomalies are traceable along the latitude of 30° S or are located within the upwelling regions along the west coasts of the South American and African continent.

Table 4.3: Regional annual mean SST anomalies (LGM-PI) based on the MITgcm and foraminifera assemblages, dinoflagellate cysts, alkenones and Mg/Ca measurements of the MARGO Project [MARGO Project Members *et al.*, 2009].

Latitude zone	Reference	Regional annual mean ($^{\circ}\text{C}$) $\pm 1\sigma$			Number n of data points		
		Atlantic Ocean	Pacific Ocean	Indian Ocean			
15° S –	Model	-1.86 ± 1.18	-1.59 ± 1.00	-1.22 ± 0.84	204	570	215
15° N	MARGO	-3.01 ± 2.16	-1.53 ± 1.86	-1.31 ± 0.90	56	66	53
15° S/N –	Model	-1.42 ± 1.63	-1.04 ± 1.13	-0.80 ± 1.52	278	577	186
30° S/N	MARGO	-2.02 ± 2.52	-1.29 ± 1.76	-1.10 ± 1.43	62	37	57
30° S/N –	Model	-4.29 ± 3.35	-2.57 ± 2.16	-2.11 ± 1.91	506	777	427
60° S/N	MARGO	-3.02 ± 3.91	-3.58 ± 2.65	-2.66 ± 1.70	104	75	44
60° S/N –	Model	-1.67 ± 2.16	-0.73 ± 0.66	-1.25 ± 0.45	114	135	55
90° S/N	MARGO	-1.23 ± 3.79	-	-	58	-	-

4.3.2 Planktonic foraminiferal $\delta^{18}\text{O}_c$ anomalies

The simulated annual mean $\Delta\delta^{18}\text{O}_c$ at the ocean surface (upper 50 m) are lowest in the tropics and subtropics (Figure 4.5, Table 4.4). They increase towards the mid-latitudes, especially in the North Atlantic, where the highest $\delta^{18}\text{O}_c$ anomalies occur (up to $4\text{ }_{\text{‰}}$). Along 30° S a band of lower values can be identified, which also emerge within the upwelling regions along the west coasts of the South American and African continent as

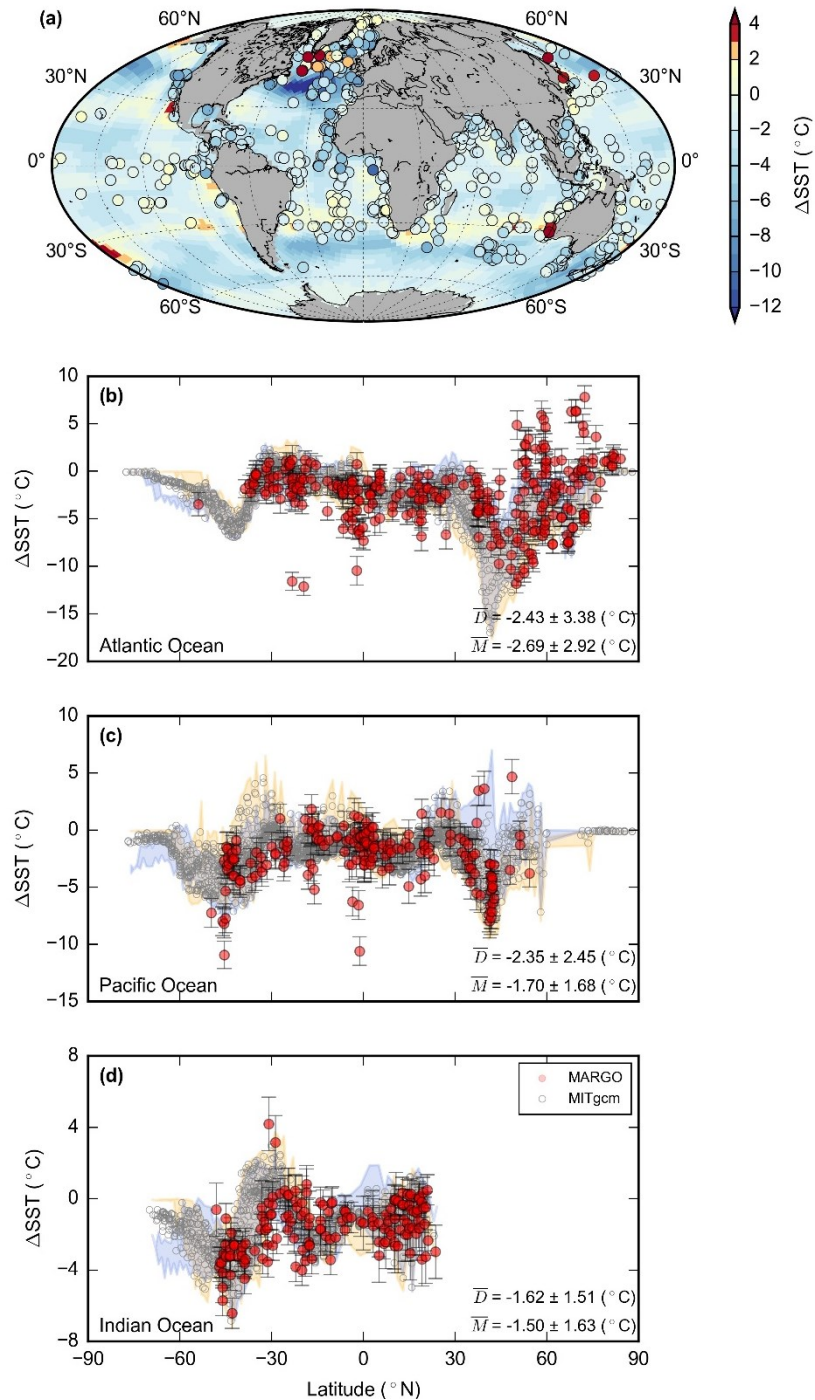


Figure 4.4: (a) Annual mean SST anomalies (ΔSST) at the surface simulated in the MITgcm (upper 50 m; LGM - PI) compared to proxy reconstructions (colored dots) derived from foraminiferal assemblages, dinoflagellate cysts, alkenones and Mg/Ca measurements of the MARGO project [MARGO Project Members *et al.*, 2009]. Model-data comparison as a function of latitude for (b) the Atlantic Ocean, (c) the Pacific Ocean and (d) the Indian Ocean. Simulated annual mean values (grey dots) were taken from every grid cell within the respective ocean basin. Seasonal amplitude for Northern-hemisphere summer (July, August and September) and Northern-hemisphere winter (January, February and March) simulated in the MITgcm are shaded in yellow and blue respectively, while annual mean proxy reconstructions correspond to the red dots. Furthermore, the annual mean anomalies are given for both the proxy reconstructions (\bar{D}) and model (\bar{M}) at the bottom right corner.

well as the modern Pacific warm pool and thus partially mimic the pattern of the SST anomaly. Compared to proxy reconstructions from *Waelbroeck et al.* [2014], the general pattern in terms of latitude agrees well (Figure 4.5 b, c, d, Table 4.4). However, apart from the North Atlantic, the model underestimates the actual change in all three ocean basins.

Table 4.4: Regional annual mean $\delta^{18}\text{O}_c$ anomalies (LGM-PI) based on the MITgcm and planktonic foraminifera reconstructions [*Waelbroeck et al.*, 2014].

Latitude zone	Reference	Regional annual mean (‰) $\pm 1\sigma$			Number <i>n</i> of data points		
		Atlantic Ocean	Pacific Ocean	Indian Ocean			
15° S – 15° N	Model <i>Waelbroeck et al.</i> [2014]	0.96 \pm 0.29	0.81 \pm 0.36	0.83 \pm 0.22	204	570	215
15° S/N – 30° S/N	Model <i>Waelbroeck et al.</i> [2014]	1.23 \pm 0.36	0.87 \pm 0.24	0.85 \pm 0.28	278	577	186
30° S/N – 60° S/N	Model <i>Waelbroeck et al.</i> [2014]	2.11 \pm 1.03	1.22 \pm 0.19	1.41 \pm 0.24	2	9	3
60° S/N – 90° S/N	Model <i>Waelbroeck et al.</i> [2014]	1.82 \pm 0.66	1.15 \pm 0.53	1.34 \pm 0.46	506	777	427
		2.15 \pm 0.44	1.51 \pm 1.04	1.48 \pm 0.51	21	19	5
		1.51 \pm 0.52	1.09 \pm 0.30	1.48 \pm 0.12	114	135	55
		1.48 \pm 0.69	-	-	11	-	-

4.3.3 Benthic foraminiferal $\delta^{18}\text{O}_c$

Interglacial and glacial $\delta^{18}\text{O}_c$ values in the sediment cores off NW Africa gradually increase with water depth (Figure 4.6a). However, their glacial $\delta^{18}\text{O}_c$ values show a larger increase with water depth below ~ 2000 m than their corresponding interglacial values (Figure 4.6a). This is most easily observed in the $\delta^{18}\text{O}_c$ anomaly profiles. While the $\Delta\delta^{18}\text{O}_c$ of the three upper sediment cores (GeoB9513-3, GeoB9512-5 and GeoB9510-1) is 1.21 \pm 0.09 ‰, 1.36 \pm 0.07 ‰ and 1.42 \pm 0.11 ‰ respectively, it increases to 1.81 \pm 0.03 ‰ and 1.63 \pm 0.06 ‰ for the deeper cores (GeoB9508-5 and GeoB9526-5, respectively), resulting in a total shift of approximately 0.40 ‰ between the upper and deeper water column. This is a common pattern, which has also been observed in the West Atlantic in data from the Blake Ridge [*Keigwin*, 2004] and Brazil Margin [*Curry and Oppo*, 2005] (Figure 4.6 b, c). In both regions larger glacial $\delta^{18}\text{O}_c$ values of approximately 0.3 ‰ exist, but the shift occurs at a shallower depth at the Brazil Margin (~1800 m) and

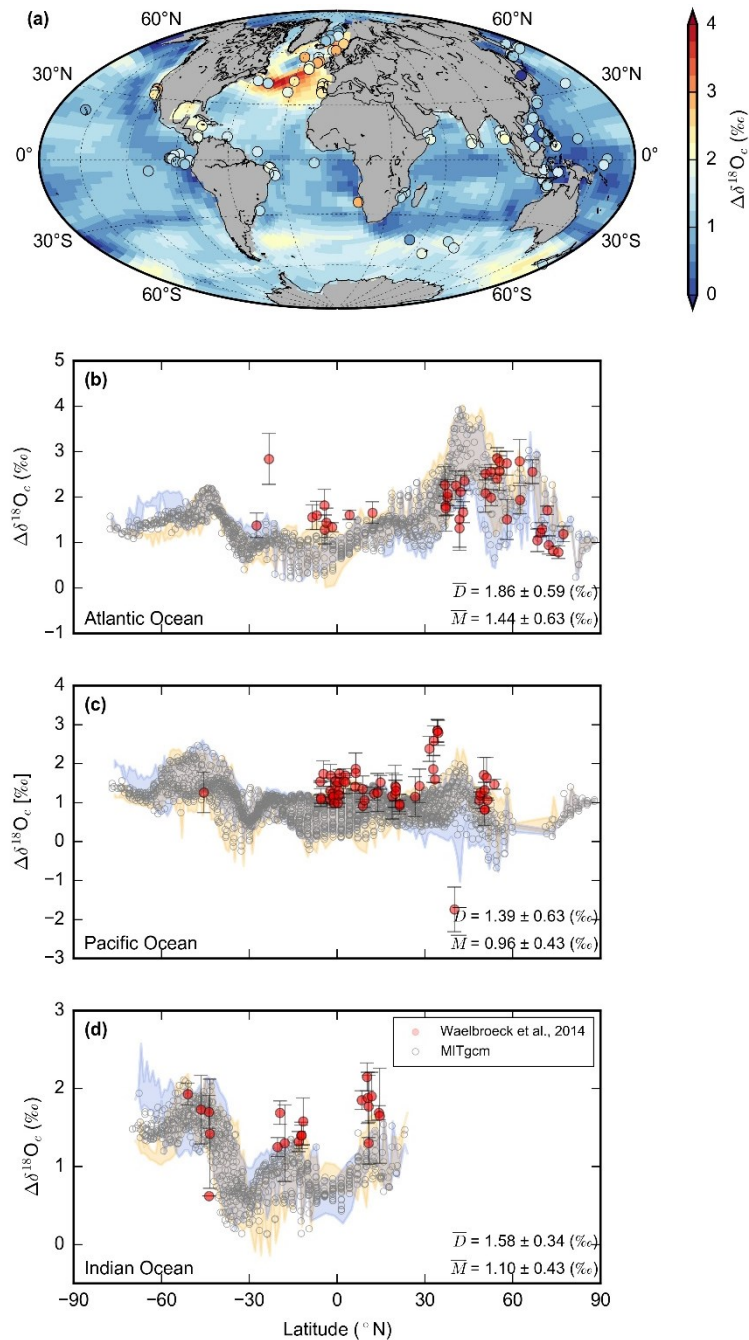


Figure 4.5: (a) Annual mean $\delta^{18}\text{O}_c$ anomalies ($\Delta\delta^{18}\text{O}_c$) at the surface simulated in the MITgcm (upper 50 m; LGM - PI) compared to proxy reconstructions (colored dots) derived from planktonic foraminifera [Waelbroeck et al., 2014] such as *G. ruber* (w), *G. bulloides*, *N. pachyderma* (s) and *G. sacculifer*. A 1.1 ‰ ice volume effect has been added to the simulated glacial $\delta^{18}\text{O}_w$ values prior to the computation of $\delta^{18}\text{O}_c$. Model-data comparison as a function of latitude for (b) the Atlantic Ocean, (c) the Pacific Ocean and (d) the Indian Ocean. Simulated annual mean values (grey dots) were taken from every grid cell within the respective ocean basin. Seasonal amplitude for Northern-hemisphere summer (July, August and September) and Northern-hemisphere winter (January, February and March) simulated in the MITgcm are shaded in yellow and blue respectively, while annual mean proxy reconstructions correspond to the red dots. Furthermore, the annual mean anomalies are given for both the proxy reconstructions (\bar{D}) and model (\bar{M}) at the bottom right corner.

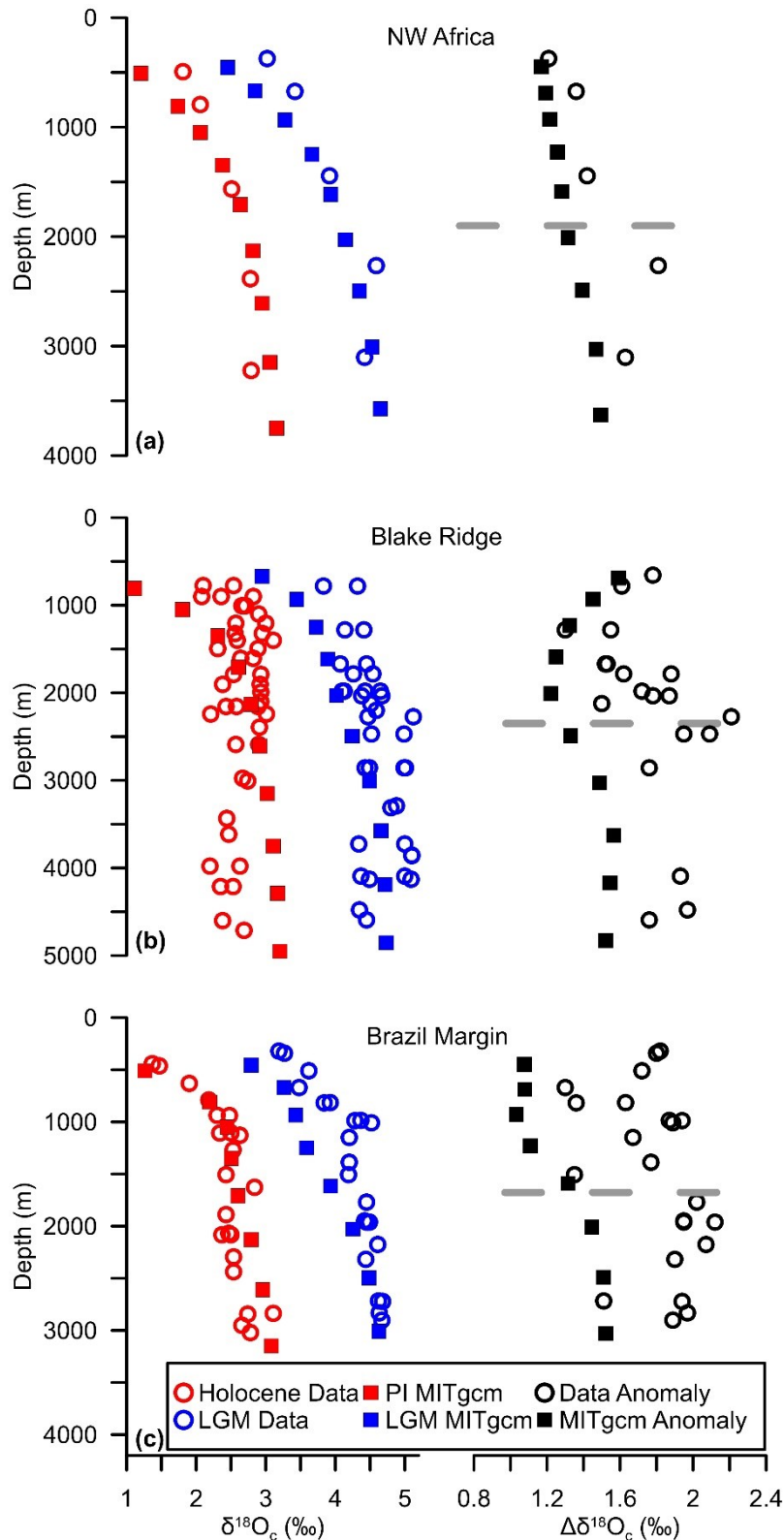


Figure 4.6: Depth profiles of benthic $\delta^{18}O_c$ from (a) NW Africa, (b) Blake Ridge [Keigwin, 2004] and (c) Brazil Margin [Curry and Oppo, 2005] for the reconstructed data (open circles) and model results (rectangles; area weighted mean of transect C (Figure 4.1)). Markers in red, blue and black correspond to the $\delta^{18}O_c$ values of the Holocene/PI, LGM and anomaly, respectively. The grey dashed line roughly marks the depth at which the larger gradient in $\delta^{18}O_c$ occurs.

at a greater depth at the Blake Ridge (~2500 m) (Figure 4.6 b, c). Nevertheless, in all three profiles $\delta^{18}\text{O}_c$ anomalies are highest close to the glacial chemocline (between 2000 m and 2500 m).

A similar pattern can be observed in the depth profiles of our model simulation. The $\delta^{18}\text{O}_c$ values from the PI and LGM simulation also gradually increase with water depth (Figure 4.6). But compared to the proxy data, they tend to underestimate the actual $\delta^{18}\text{O}_c$ values especially above ~1500 m. The larger glacial $\delta^{18}\text{O}_c$ gradient with water depth is also recognizable in the $\delta^{18}\text{O}_c$ anomaly profiles, considering a 120 m sea-level change. For the modeled $\delta^{18}\text{O}_c$ anomalies off NW Africa, the shift between the upper and deeper water column amounts to 0.3 ‰ (Figure 4.6a, Figure 4.7). In the West Atlantic the larger glacial gradient is more pronounced, resulting in a $\delta^{18}\text{O}_c$ shift of ~0.3 ‰ at the Blake Ridge and ~0.4 ‰ at the Brazil Margin. The model does not reproduce the high $\delta^{18}\text{O}_c$ anomalies close to the glacial chemocline and underestimates the absolute $\delta^{18}\text{O}_c$ anomalies. But its shift between the upper and deeper water column is comparable to the shift seen in the reconstructed data as well as its overall distribution.

4.3.4 Modeled depth transect in the East Atlantic Ocean: sea-level change effect

Model results of the $\delta^{18}\text{O}_c$ anomalies off NW Africa (Figure 4.1, transect C) that do not take into account a 120 m sea-level change, do not show a gradual increase with water depth. Instead they show $\Delta\delta^{18}\text{O}_c$ values of 1.5 ‰ at a water depth of ~500 m, which decrease to 1.4 ‰ at a water depth of ~2000 m and subsequently increase to 1.5 ‰ again at depth (Figure 4.7). Thus, the change in $\Delta\delta^{18}\text{O}_c$ between the upper and lower water column is in the order of only 0.1 ‰ and therefore inconsistent with the proxy data. However, if a 120 m sea-level change is considered, the simulated $\Delta\delta^{18}\text{O}_c$ distribution along the depth transects in the East Atlantic Ocean (Figure 4.1, transect A, B and C) resembles the sediment core reconstructions (Figure 4.7 and Figure 4.9 g, h, i). Since the $\delta^{18}\text{O}_c$ of foraminiferal shells is mainly controlled by ambient temperature and $\delta^{18}\text{O}_w$ during calcification [Emiliani, 1955; Shackleton, 1974; Urey, 1947], simulated ΔT and $\Delta\delta^{18}\text{O}_w$ are also shown in Figure 4.8 and Figure 4.9 (here the 1.1 ‰ $\delta^{18}\text{O}_w$ contribution from the LGM ice sheet build-up has not been applied to the simulated glacial $\delta^{18}\text{O}_w$ values). The consideration of the sea-level change only has a minor effect on the glacial-interglacial difference in $\delta^{18}\text{O}_w$. The $\delta^{18}\text{O}_w$ anomalies of the upper ~800 m are negative (Figure 4.8 and Figure 4.9 d, e, f) except for the most northern part of Transect B, where a bulge of positive anomalies at 1000 m water depth reaches the surface. Highest $\delta^{18}\text{O}_w$ anomalies (~0.15 ‰) occur in waters between 1000 m and 2000 m water depth, while

below they tend to be close to 0 ‰. Overall, changes in $\Delta\delta^{18}\text{O}_w$ are rather small. The effect of the sea-level change on glacial-interglacial temperatures is comparatively larger. When the sea-level change is not considered, almost the whole water column shows negative temperature anomalies, with smallest changes ($> -0.5\text{ }^\circ\text{C}$) between 1000 m and 2000 m water depth (Figure 4.8 a, b, c). Taking into account the 120 m sea-level drop results in positive temperature anomalies of up to $1\text{ }^\circ\text{C}$ around 1000 m and above 200 m water depth (Figure 4.9 a, b, c). In between a shallow tongue of negative temperature anomalies ($\sim -0.5\text{ }^\circ\text{C}$) can be observed. Beneath 1000 m to 1500 m water depth, temperatures anomalies are negative, reaching up to $-1.5\text{ }^\circ\text{C}$ below 3000 m water depth (Figure 4.9 a, b, c).

$\Delta\delta^{18}\text{O}_c$ of sediment cores and vertical model transect C

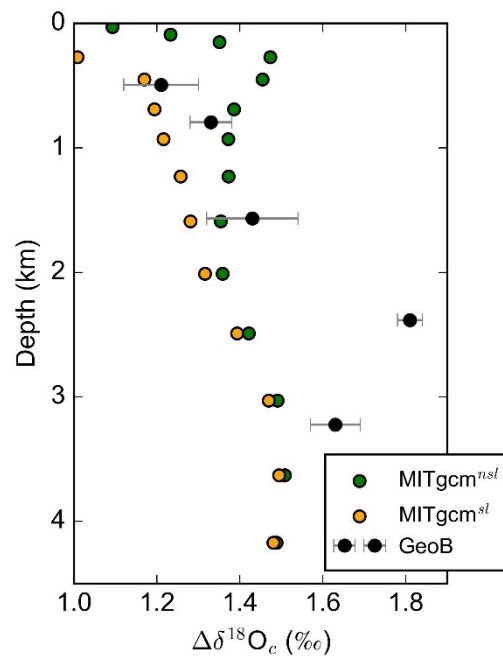


Figure 4.7: $\Delta\delta^{18}\text{O}_c$ change with depth in sediment cores GeoB9513-3, GeoB9512-5, GeoB9510-1, GeoB9508-5 and GeoB9526-5 (black dots, top down), model simulation with consideration of a 120 m sea-level change (orange dots) and model simulation without consideration of a 120 m sea-level change (green dots) off NW Africa (transect C, area weighted mean).

4.4 Discussion

4.4.1 Simulated LGM state

The comparison of the simulated and reconstructed SST anomalies between the LGM and PI revealed a good agreement. The strongest annual mean cooling in the North Atlantic is consistent with the MARGO reconstruction and the latitudinal gradients are

reasonably reproduced. Small deviations in regions of upwelling along the west coasts of the South American and African continent as well as the equator (Figure 4.4) are likely attributable to the coarse grid resolution ($\sim 3^\circ$) of the model, which cannot realistically represent the upwelling process

During the LGM, the sea-level lowering may have caused narrow (~ 100 km) upwelling cells to migrate seawards over the core locations, resulting in large SST anomalies, that would be recorded by the microfossil-based and geochemical paleothermometers [cf. *Giraud and Paul, 2010*]. In addition, it is claimed that enhanced upwelling of subpolar waters off the coast of southwest Africa occurred, due to increased winds and sea-ice extent around Antarctica that are associated with a northward shift in westerlies and

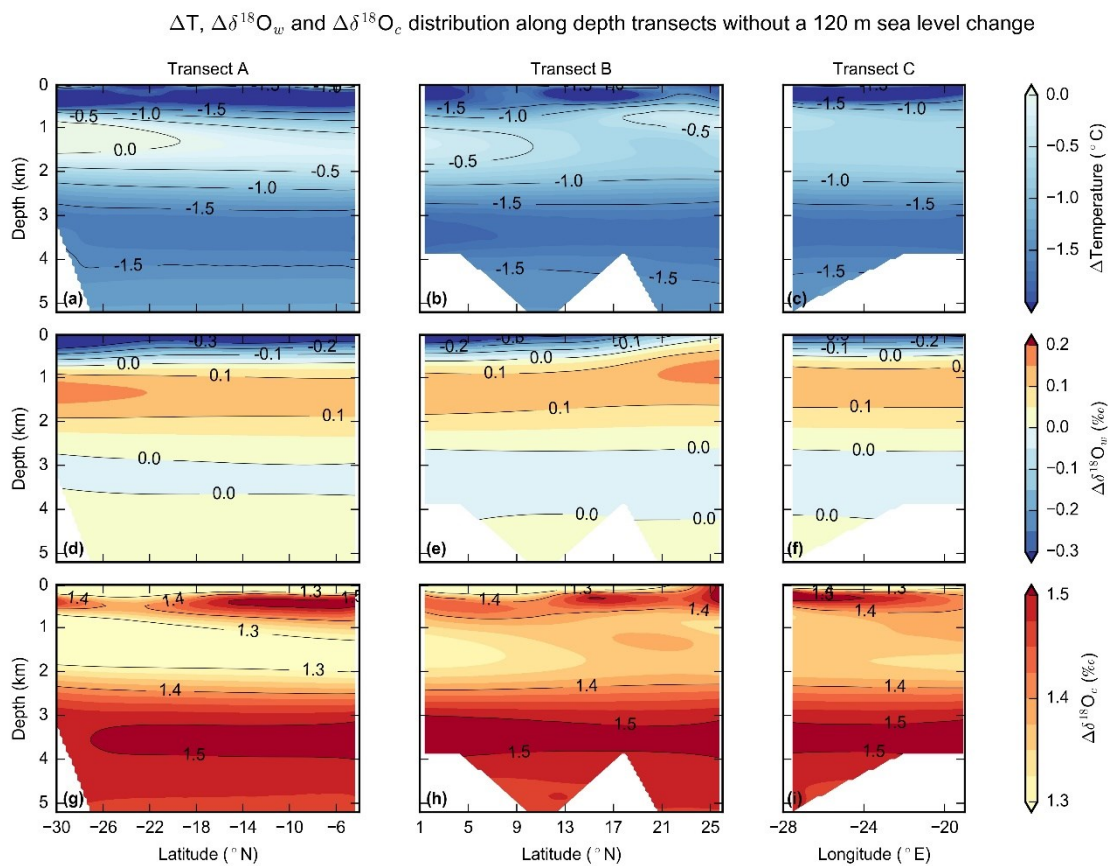


Figure 4.8: Simulated ΔT (a, b, c), $\Delta\delta^{18}O_w$ (d, e, f) and $\Delta\delta^{18}O_c$ (g, h, i; LGM - PI) without consideration of a 120 m sea-level change along the depth transects (A, B and C Figure 4.1) in the East Atlantic basin. A 1.1 ‰ ice volume effect has been added to the simulated glacial $\delta^{18}O_w$ values prior to the computation of $\delta^{18}O_c$, but is not considered within the $\Delta\delta^{18}O_w$ plots, to emphasize the actual water mass changes.

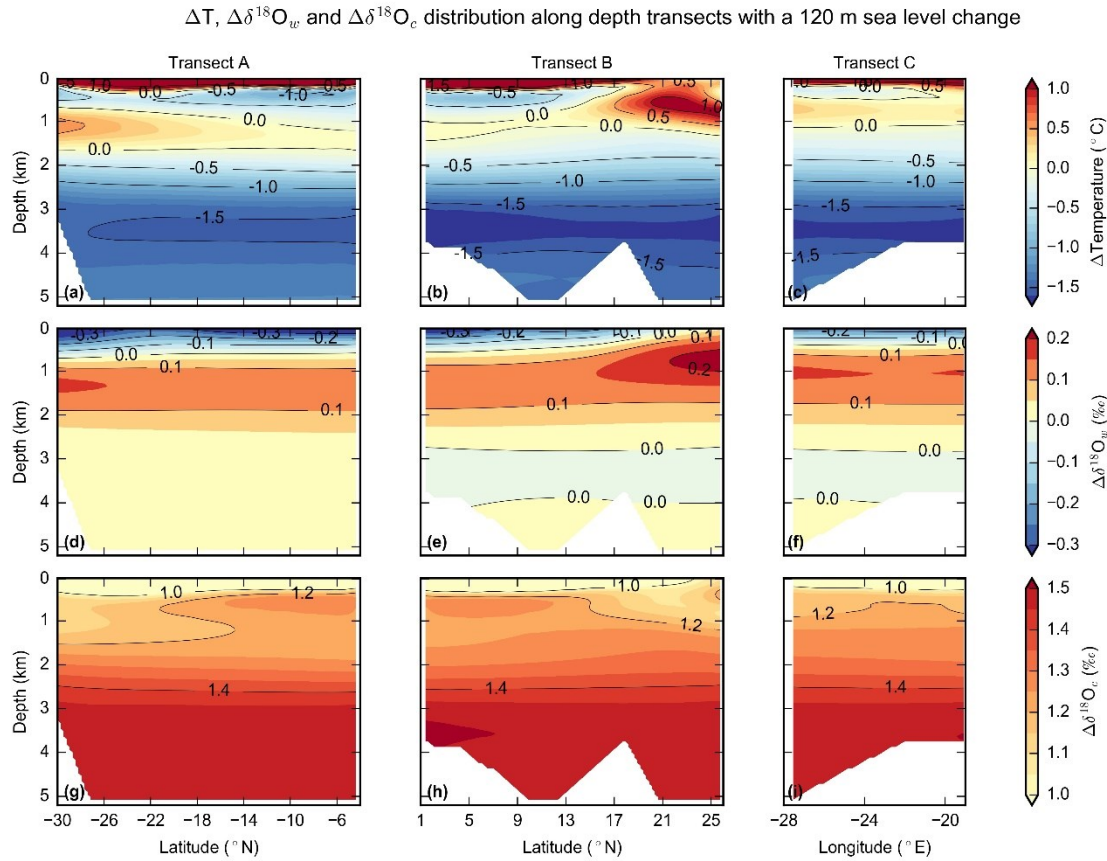


Figure 4.9: Simulated ΔT (a, b, c), $\Delta\delta^{18}\text{O}_w$ (d, e, f) and $\Delta\delta^{18}\text{O}_c$ (g, h, i; LGM - PI) with consideration of a 120 m sea-level change along the depth transects (A, B, and C in Figure 4.1) in the East Atlantic basin. A 1.1 ‰ ice volume effect has been added to the simulated glacial $\delta^{18}\text{O}_w$ values prior to the computation of $\delta^{18}\text{O}_c$, but is not considered within the $\Delta\delta^{18}\text{O}_w$ plots, to emphasize the actual water mass changes.

Southern Ocean frontal system [Kucera *et al.*, 2005; MARGO Project Members *et al.*, 2009]. Further, locally a tongue of very cold temperatures due to divergence along the equator might have been responsible for the low SST anomalies seen in proxy reconstructions especially in the East Atlantic Ocean. Neither the coastal nor the equatorial upwelling process can be adequately resolved within our global model, leading to discrepancies in the regional means (Table 4.3).

The positive temperature anomalies along the latitude of 30° S within the model are likely attributable to the state estimate by Kurahashi-Nakamura *et al.* [2017], which this study depends on. It seems to already have a warm bias along 30° S, although some of it could be related to the warm anomalies in the original MARGO data [MARGO Project Members *et al.*, 2009] themselves. Furthermore, the PI simulation, which is used as a reference state, is too cold along 30° S [Völpel *et al.*, 2017] and thus might lead to the positive temperature anomalies as well.

However, these deviations only correspond to specific regions, and thus are not of global concern. The root mean square error of model-data discrepancy for the glacial-interglacial global SST anomaly was 2.54 °C. Furthermore, the globally averaged difference in SST was -1.9 °C based on our model simulation, which agrees with the MARGO estimate of -1.9 °C ± 1.8 °C for the glacial-interglacial globally averaged SST anomaly, even though some of the regional anomalies differ from the MARGO data (Table 4.3). Deviations in the North Atlantic and North Pacific Oceans as well as along 30° S in the Indian Ocean may rather stem from the proxy reconstructions. These SST anomalies are based on alkenones and dinoflagellate cysts. In the case of the dinoflagellate cyst abundances, these particular anomalies may correspond to “no-analog” situations [de Vernal *et al.*, 2006]. Dinoflagellate cysts are also substantially smaller and lighter than planktonic foraminifera shells and thus more prone to reworking and lateral transport in the water column, which may alter the actual signal. SST anomalies based on alkenones on the other hand might be biased at very low temperatures [Conte *et al.*, 2006] and affected by laterally advected allochthonous input [Mollenhauer *et al.*, 2006; Rühlemann and Butzin, 2006]. Alkenones as well as most of the dinoflagellate cysts are related to autotrophic production and thus likely record signals of a warm season which could introduce an error when comparing annual mean values. Not only does the disagreement occur with our model results but also with the other proxy reconstructions, which rather indicate negative anomalies within the aforementioned regions. Thus, the reconstructed SST anomalies based on alkenones and dinoflagellate cysts should be considered carefully. Furthermore, one of the very cold Δ SST proxy record in the equatorial Pacific Ocean is based on the Mg/Ca ratios of planktonic foraminifera shells and exemplary for their susceptibility to dissolution under the influence of undersaturated bottom-waters or pore-water, whereby values are biased towards colder temperatures [Brown and Elderfield, 1996; Rosenthal *et al.*, 2000]. Thus, SST reconstructions based on foraminiferal assemblages seem to be more reliable and compare well with our model simulation.

Regarding the surface $\delta^{18}\text{O}_c$ anomalies of the model simulation, we can conclude that they are mainly controlled by the SST changes. The latitudinal pattern of $\delta^{18}\text{O}_c$ anomalies (Figure 4.5) reflects the latitudinal pattern of SST anomalies (Figure 4.4), whereby deviations in the $\delta^{18}\text{O}_c$ anomalies may occur. For instance, discrepancies between the simulated and reconstructed $\delta^{18}\text{O}_c$ anomalies in the North Atlantic region correspond to the strong annual mean cooling, which is, compared to proxy records, too low. However, further to the north the agreement between simulated and reconstructed $\delta^{18}\text{O}_c$ is good, which supports the assumption that the warm SST anomalies based on alkenones and dinoflagellate cysts are biased and the simulated temperature is reasonable. As

discussed before, coastal upwelling cannot be properly simulated by the model and thus might account for larger discrepancies between the model and the proxy reconstruction, as seen at 30° S in the Atlantic Ocean. Here, one proxy $\Delta\delta^{18}\text{O}_c$ value is anomalously high, which reveals a rather local change in coastal upwelling that corresponds to a large SST anomaly, recorded within the foraminiferal shell. Nevertheless, the general latitudinal pattern and gradient seen in the model match the proxy reconstructions.

Since the $\delta^{18}\text{O}_c$ is mainly controlled by temperature and $\delta^{18}\text{O}_w$, the simulated $\delta^{18}\text{O}_w$ pattern is also of interest when investigating simulated $\Delta\delta^{18}\text{O}_c$. The latitudinal $\Delta\delta^{18}\text{O}_w$ pattern at the surface in the different ocean basins is shown in Figure 4.10. Except for some local regions in the Pacific Ocean all annual mean $\Delta\delta^{18}\text{O}_w$ values are positive with latitudinal variations. While for example the high latitudes of the ocean basins are rather close to or exceed the mean ocean $\delta^{18}\text{O}$ signal of 1.1 ‰ resulting from changes in global ice volume [Adkins *et al.*, 2002; Duplessy *et al.*, 2002; Schrag *et al.*, 2002], regions around the equator are less enriched in ^{18}O . Thus, the simulated $\Delta\delta^{18}\text{O}_c$ values around the equator are likely a mixture of slightly too warm ΔSST and too low $\Delta\delta^{18}\text{O}_w$ values. Overall, the comparison of simulated $\Delta\delta^{18}\text{O}_c$ with proxy reconstructions is good, even though the proxy data is sparse and mainly located along the coasts presenting very local patterns of glacial-interglacial changes at the sea surface.

Regarding the comparison of simulated $\delta^{18}\text{O}_c$ with the sediment cores off NW Africa, the exclusion of the Mediterranean Sea in the LGM simulation might introduce a small error at least in the upper water column. To test, whether this is indeed the case, we performed an additional simulation, in which the Mediterranean Sea was included. According to this simulation the Mediterranean outflow led to warmer waters, that were also enriched in H_2^{18}O at a water depth of around 1000 m. These two parameters (warmer temperatures and more enriched $\delta^{18}\text{O}_w$) have compensating effects on the $\delta^{18}\text{O}_c$. Thus, an additional decrease of only ~ 0.1 ‰ was observed for the $\delta^{18}\text{O}_c$ values off NW Africa including the Mediterranean Sea, while the rest of the water column experienced even smaller changes (< 0.03 ‰). Hence, the influence on the $\delta^{18}\text{O}_c$ values of the subtropical North Atlantic Ocean was rather insignificant.

Despite the reasonably good match of temperature and $\delta^{18}\text{O}_c$ anomalies at the surface between the simulated data and proxy records, additional properties of the LGM climate should be taken into account. The AMOC and the water mass structure of the Atlantic Ocean are extensively discussed from the viewpoint of both paleoceanographic proxy records [e.g. Adkins *et al.*, 2002; Curry and Oppo, 2005; Howe *et al.*, 2016; Lynch-Stieglitz *et al.*, 2007] and numerical modeling [e.g. Paul and Schäfer-Neth, 2003; Otto-

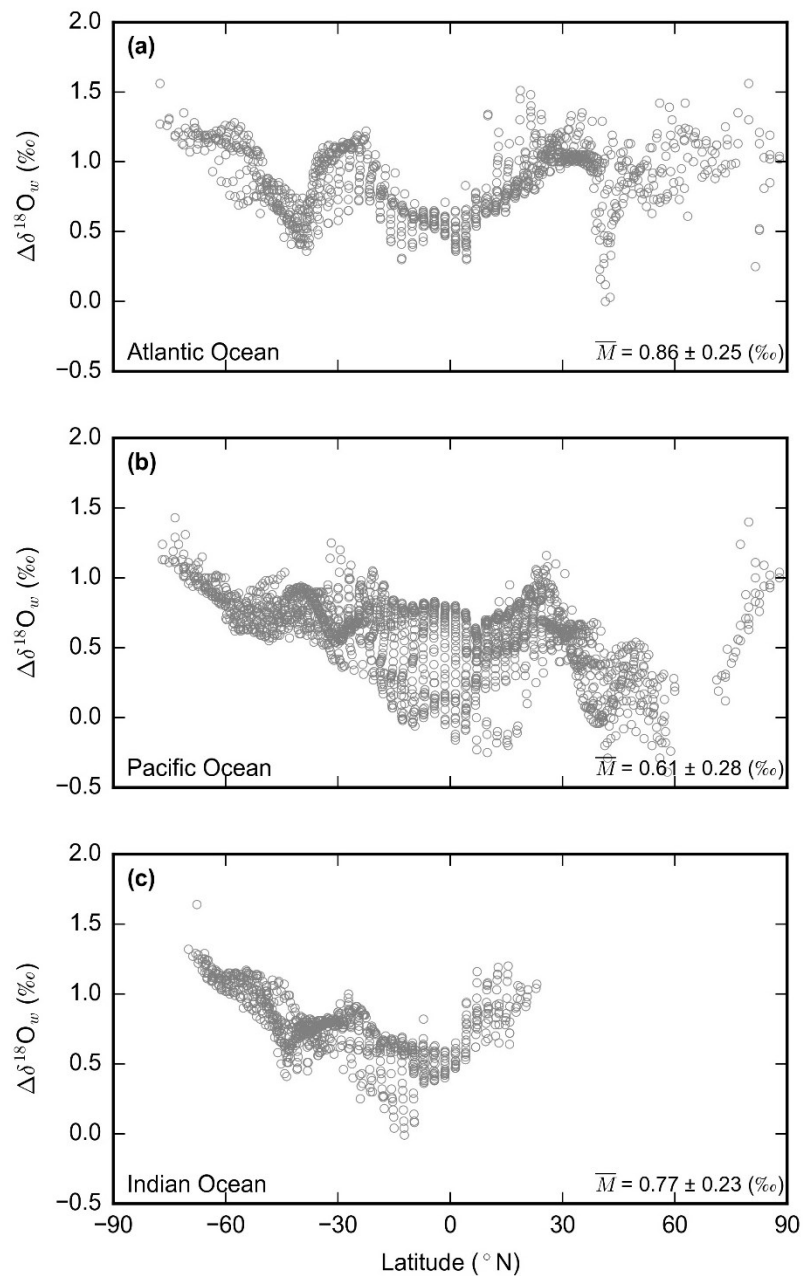


Figure 4.10: Simulated annual mean $\Delta\delta^{18}\text{O}_w$ distribution at the surface (upper 50 m; LGM- PI) as a function of latitude for (a) the Atlantic Ocean, (b) the Pacific Ocean and (c) the Indian Ocean. Simulated annual mean values (grey dots) were taken from every grid cell within the respective ocean basin. A 1.1 ‰ ice volume effect has been added to the simulated glacial $\delta^{18}\text{O}_w$ values. Furthermore, the annual mean anomalies are given for the model (\bar{M}) at the bottom right corner.

Bliesner et al., 2007] and thus enable further assessment of the model. For a clear visualization of the distribution of water masses, passive dye tracers were additionally implemented in the MITgcm [cf. *Gebbie*, 2014; *Kurahashi-Nakamura et al.*, 2017], representing the northern source water and southern source water (Figure 4.11b, c, e,

f). The dye tracers for the northern source water were released at the sea surface of the Atlantic Ocean between 50° N and 80° N and the southern source water tracers were released below 2000 m water depth between 50° S and 60° S. Their concentrations were fixed at 1 for every grid cell within the initial field. The NADW cell in the PI simulation (Figure 4.11b) is slightly too shallow as compared to modern observations. A similar systematic error may also affect the LGM simulation. Keeping these caveats in mind, our model results show only a slight reduction in the AMOC during the LGM (the maximum of the overturning streamfunction amounts to 15.5 Sv as compared to 18.2 Sv for the PI, where 1 Sv = $10^6 \text{ m}^3 \text{ s}^{-1}$), but a northern source water cell that occupies shallower depths, and the presence of the associated water mass in the deeper parts of the Atlantic Ocean is reduced (Figure 4.11). The influence of southern source water in the deep Atlantic seems to be increased especially north of the equator. However, the deep Atlantic is not solely occupied by southern source water during the LGM, since some remnants of northern source water are still visible. These observations are in accord with proxy reconstructions from e.g. *Curry and Oppo* [2005]. Based on stable carbon isotopes ($\delta^{13}\text{C}$) and benthic $\delta^{18}\text{O}_c$, they suggest that a water mass originating in the North Atlantic occupied the Atlantic Ocean at a shallower depth than today (centered around 1500 m) and penetrated as far south as 30° S. Below 2000 m, *Curry and Oppo* [2005] identify a sharp property gradient, which marks the presence of southern source water reaching as far as 60° N. Measurements of Zn/Ca as well as Cd/Ca ratios in benthic foraminifera support the assumption that the deepest parts of the North Atlantic were filled to a greater extent with southern source water [*Marchitto et al.*, 2002]. A clear decrease of Cd concentration in the upper 2200 m at the LGM suggests that the intermediate ocean was dominated by low-nutrient northern source waters while high-nutrient waters expanded at depth [*Marchitto and Broecker*, 2006]. Together with combined radiocarbon and stable isotope data, *Freeman et al.* [2016] interpret these changes as an expansion of southern source water in the deep Atlantic. Based on neodymium isotopes measured on foraminiferal shells (ϵ_{Nd}), *Howe et al.* [2016] also conclude that even though the deep Atlantic Ocean during the LGM must have been filled with a greater proportion of southern source water, it was not the only water mass occurring but rather a mixture of northern and southern source waters. All these findings are in line with our model results (Figure 4.11) and confirm that the simulated LGM climate state is consistent not only with the surface proxy data, but also with the proxy data from the deep ocean. In comparison to *Kurahashi-Nakamura et al.* [2017] it further implies that the shallower overturning cell is a robust result for the LGM ocean, while the strength of the AMOC remains uncertain. Both proxy-based reconstructions as well as modeling studies show controversial AMOC strength estimates. Our results of an (albeit slightly) weakened AMOC, however,

corroborates the estimates of water column density gradients from $\delta^{18}\text{O}_c$ of benthic foraminifera across the Florida Straits or the upper South Atlantic [Lynch-Stieglitz *et al.*, 1999, 2006] and $^{231}\text{Pa}/^{230}\text{Th}$ ratios suggesting a reduction by up to 30-40 % [McManus *et al.*, 2004]. This would rule out some of the more extreme AMOC scenarios seen in e.g. Otto-Bliesner *et al.* [2007] implying that it was neither extremely sluggish nor enhanced compared to the PI.

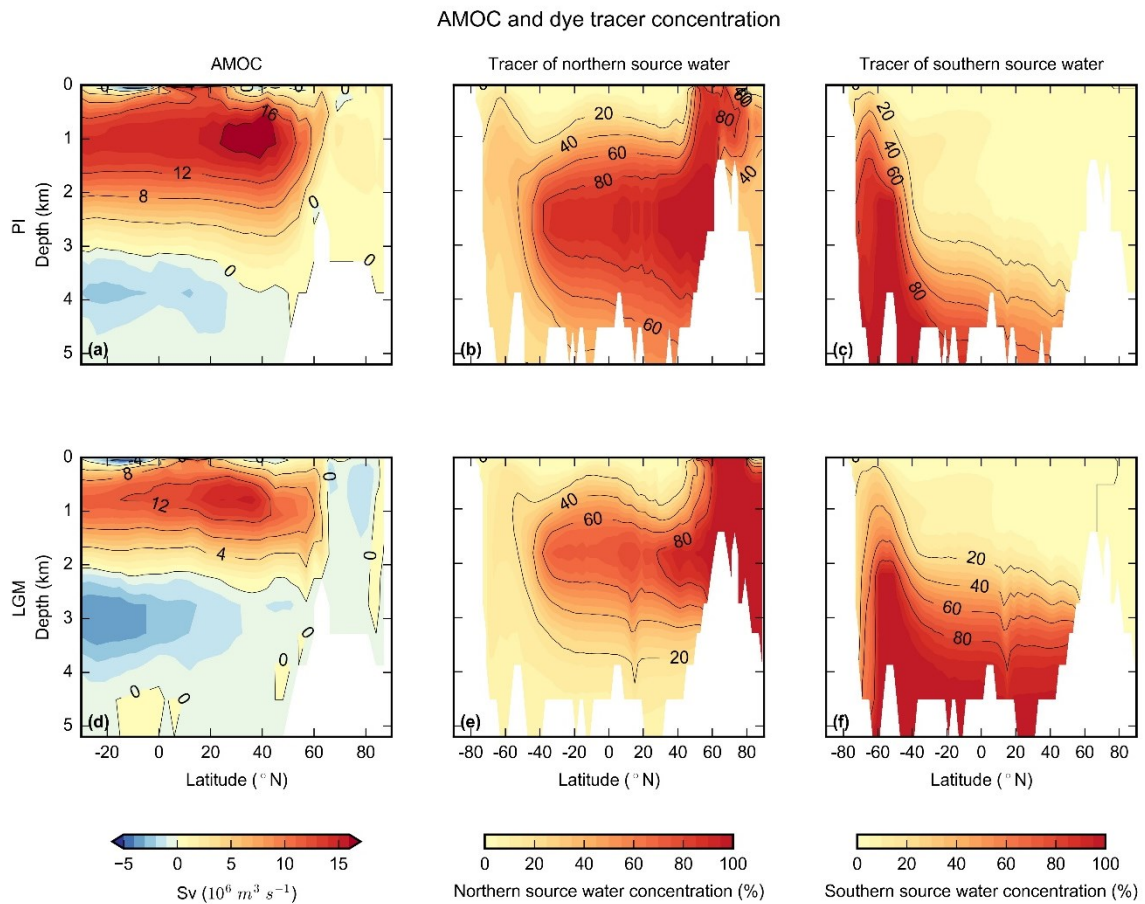


Figure 4.11: Stream function of the AMOC calculated for (a) the PI and (d) the LGM. Concentration of the dye tracer representing northern source water for (b) the PI and (e) the LGM as well as southern source water for (c) the PI and (f) the LGM. The northern source water tracer was initialized at the surface in the North Atlantic while the tracer for the southern source water was initialized within the water column of the South Atlantic. Hence, the two water masses may exceed 100 % especially close to the initial field of southern source water.

4.4.2 Effect of the sea-level lowering on glacial-interglacial $\delta^{18}\text{O}_c$ anomalies

During the LGM the sea level was approximately 120 m lower [Clark *et al.*, 2009; Fairbanks, 1989] than during modern times. Whether this is an explanation for the smaller glacial-interglacial $\delta^{18}\text{O}_c$ difference in the sediment cores GeoB9513-3,

GeoB9512-5 and GeoB9510-1 from the upper water column (Figure 4.7), is tested with the ocean model.

Results of the model simulation show a similar picture, smaller glacial-interglacial changes in $\delta^{18}\text{O}_c$ above 2000 m water depth (Figure 4.7 and Figure 4.9 g, h, j), as seen in the sediment cores off NW Africa. The effect of the sea-level change on temperature, $\delta^{18}\text{O}_w$ and $\delta^{18}\text{O}_c$ becomes most apparent when the two glacial-interglacial anomalies with and without a 120 m sea-level change ($\Delta\Delta$) are compared (Figure 4.12). Due to the sea-level lowering, core locations were exposed to warmer temperatures since they experienced relatively shallower water depths (Figure 4.12 a, b, c). The temperatures of the water column above 1000 m was warmer by $\sim 1^\circ\text{C}$ and more. The relative warming decreased towards 2000 m depth and became negligible below. Since the differences in modeled $\delta^{18}\text{O}_w$ are very small ($\Delta\Delta\delta^{18}\text{O}_w \leq 0.06\text{‰}$; Figure 4.12 d, e, f), the temperature change of 1°C can entirely explain the observed change in $\delta^{18}\text{O}_c$, consistent with a slope of $0.21\text{‰} - 0.27\text{‰}$ for a 1°C increase in temperature [Craig, 1965; Erez and Luz, 1983; McCrea, 1950; O'Neil et al., 1969]. This effect is most pronounced in the permanent thermocline where the vertical temperature gradient is largest, while in the deep ocean, the influence of the water column shift is no longer apparent. Hence, a glacial sea-level lowering of 120 m brings the core locations closer to the surface, which results in warmer temperatures and smaller glacial-interglacial $\delta^{18}\text{O}_c$ differences ($< -0.2\text{‰}$) especially in the upper 1000 m (Figure 4.12). Since this sea-level effect is recognizable in all three transects (A, B and C in Figure 4.1) of the model simulation (Figure 4.12), we propose that this is not only a local pattern off NW Africa but also representative for at least the open tropical eastern Atlantic Ocean.

4.4.3 Larger glacial-interglacial change in $\delta^{18}\text{O}_c$ below 2000 m water depth

The two deepest sediment cores (GeoB9508-5 and GeoB9526-5) off NW Africa reveal $\delta^{18}\text{O}_c$ anomalies that exceed the glacial-interglacial ice sheet change. This picture is confirmed by our model results. Although the absolute $\delta^{18}\text{O}_c$ anomalies are not completely consistent, the total shift between the upper and deeper water column in the Atlantic Ocean is of similar magnitude (0.3‰ in the model vs. 0.4‰ in the sediment cores). This is a common pattern for the Atlantic Ocean (Figure 4.6) and by means of the model simulation, we can suggest possible causes for the increase of the glacial-interglacial $\delta^{18}\text{O}_c$ difference with depth.

To determine the temperature (T) and salinity (S) properties of the different water masses within the Atlantic Ocean, T-S diagrams were produced (Figure 4.13). GEOSECS data were taken from ten stations in the East Atlantic and eight stations in the West Atlantic

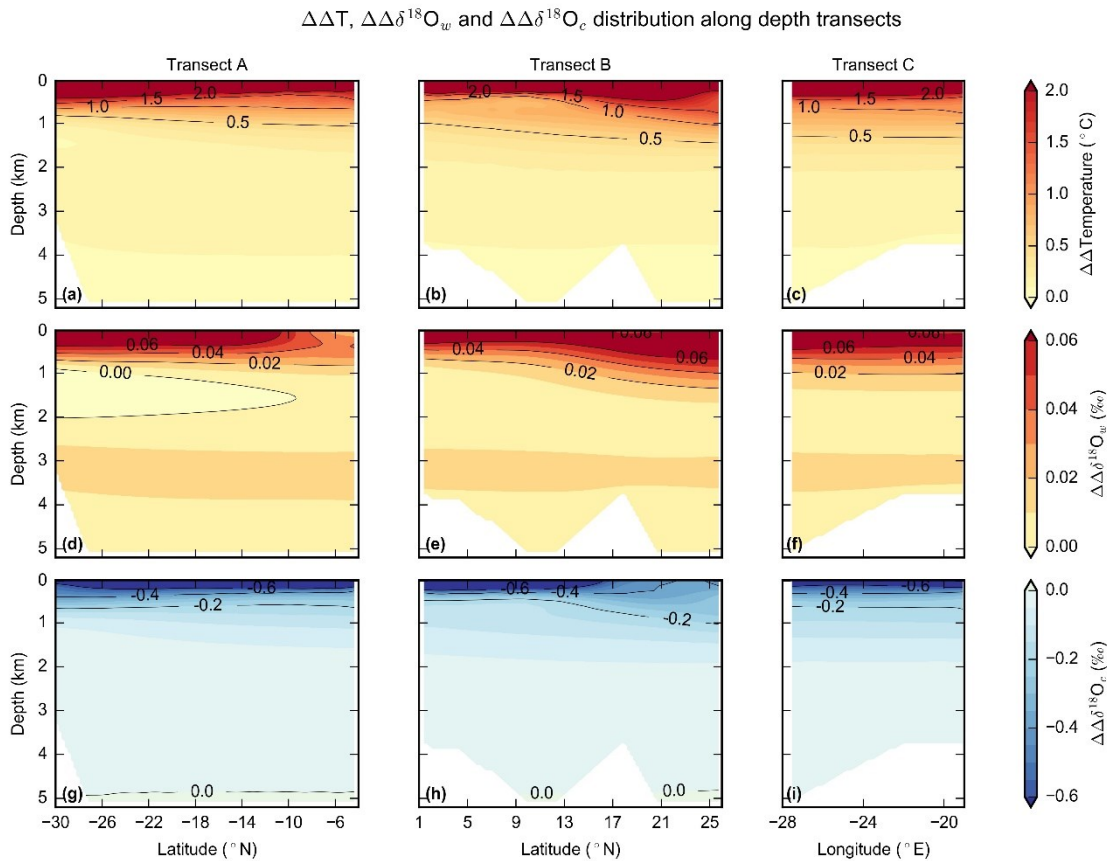


Figure 4.12: Simulated $\Delta\Delta T$ (a, b, c), $\Delta\Delta\delta^{18}O_w$ (d, e, f) and $\Delta\Delta\delta^{18}O_c$ (g, h, i) along the depth transects shown in Figure 4.1 in the East Atlantic basin. The $\Delta\Delta$ values were calculated by considering the anomaly (LGM-PI) including a 120 m sea-level change minus the anomaly without it. This way the effect of the sea-level change is recognizable. A 1.1 ‰ ice volume effect has been added to the simulated glacial $\delta^{18}O_w$ values prior to the computation of $\delta^{18}O_c$, but is not considered within the $\Delta\delta^{18}O_w$ plots, to emphasize the actual water mass changes.

(Figure 4.13c), while the ocean model output of the PI and LGM (Figure 4.13b) simulations was sampled at the closest grid cells. The GEOSECS data fall right into the respective T-S ranges for Antarctic Intermediate Water (AAIW), NADW and AABW defined by *Emery and Meincke* [1986]. In contrast, the NADW and AABW of the PI run seem to be slightly too salty, while the AAIW is less pronounced than in the observations in the East Atlantic compared to the West Atlantic (GEOSECS station 105-114 and 44-56, respectively). During the LGM the density of both the AABW and NADW (or the southern and northern source water, respectively) increased. Regarding the northern source water, it is most likely attributable to an increase in salinity, since the temperature remained nearly unchanged. At the same time, the southern source water density

increase results from a combination of more saline and colder waters, with temperatures approaching the freezing point. *Duplessy et al.* [2002] investigated the benthic $\delta^{18}\text{O}$ change between the LGM and the Holocene together with the $\delta^{18}\text{O}$ and $\delta^{13}\text{C}$ of the benthic foraminifera species *Cibicides* and came to the same conclusion that glacial Southern Ocean deep waters were close to the freezing point. A direct comparison with pore fluid measurements of $\delta^{18}\text{O}_w$ (interpreted as temperature; [*Adkins et al.*, 2002; *Adkins and Schrag*, 2003; *Schrag et al.*, 1996; 2002]) however, reveals that the simulated temperature anomalies are not cold enough in the North Atlantic ($< -2\text{ }^\circ\text{C}$ in the model vs. $\sim -4\text{ }^\circ\text{C}$ reconstructed by pore fluid measurements). It is likely that the southern source water influence in these regions is too low (e.g. pore fluid measurements on OPD site 981; Feni Drift; 55° N and 14° W ; 2184 m water depth), since the overturning during the LGM might be slightly too strong and/or the region of northern source water formation is still too far north in the model simulation whereby it occupies with great extent water depths of 2000 m (Figure 4.11).

Nevertheless, the northern source water is still the saltiest water mass within the model, while the southern source water is by far the coldest. Water masses corresponding to the modern AAIW are more diffuse during the LGM and thus hardly distinguishable. Pore fluid measurements of [Cl] (interpreted as salinity) suggest that the glacial deep ocean was filled with cold-salty water formed around Antarctica and that the modern salt gradient was reversed [*Adkins et al.*, 2002; *Adkins and Schrag*, 2003; *Schrag et al.*, 1996; 2002]. In particular, the salinity estimates based on pore fluid measurements of ODP site 1063 (Bermuda Rise; 33° N and 57° W) and 981 (Feni Drift; 55° N and 14° W) are faithfully simulated in the model, but the Southern Ocean ODP site 1093 (Shona Rise; 49° S and 5° E) indicates that the modeled southern source water might not be salty enough. On the one hand it is likely attributable to the non-realistic simulation of brine rejection in the model itself. During sea-ice formation, salt accumulates into brines and over time drains out, sinks as dense plumes with high salinities and mixes with the surrounding water. This process is not simulated in the MITgcm and might lead to biased salinities that characterize the respective water masses formed in regions of sea-ice formation. On the other hand, this may indicate issues in the model derived pore fluid reconstructions, attributable to both temperature and salinity estimates [*Miller et al.*, 2015; *Wunsch*, 2016]. Both, *Miller et al.* [2015] and *Wunsch* [2016] concluded that the pore water data may be inconclusive, because the given error may underestimate the true uncertainty. Furthermore, similar T-S profile results were obtained by *Gebbie and Huybers* [2006], which also point out to a more saline glacial NADW [cf. Figure 8 in *Gebbie and Huybers*, 2006].

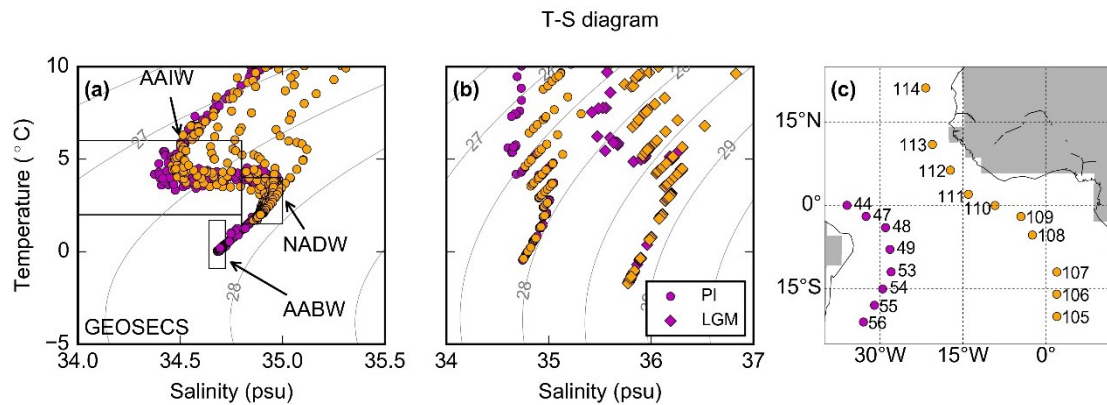


Figure 4.13: Temperature-salinity diagrams for (a) the GEOSECS data taken from ten stations in the East Atlantic (orange colored) and eight stations in the West Atlantic (purple colored). The model output for (b) the PI (circles) and the LGM (diamonds) was sampled at the closest geographic grid cell to the GEOSECS stations. The number of the respective GEOSECS stations are given in (c). The potential density of sea water at atmospheric pressure is shown in grey and replicates the sigma-theta (density -1000 (kg m⁻³)) value. Rectangles correspond to the temperature and salinity ranges for the different water masses in the Atlantic Ocean defined by *Emery and Meincke [1986]*.

Apart from this, based on the changes of the water mass properties in combination with the increased influence of southern source water in the deep Atlantic Ocean (Figure 4.11), we claim that the continuously decreasing temperatures with depth, especially below 2000 m (Figure 4.9), are driven by the glacial AABW. Conversely, this means that the larger differences in $\Delta\delta^{18}\text{O}_c$ below 2000 m are mainly related to a temperature effect, because the changes in $\Delta\delta^{18}\text{O}_w$ in these depths are negligible. This implies that the larger gradient with water depth in the glacial-interglacial $\delta^{18}\text{O}_c$ anomalies also corresponds to the glacial water-mass boundary as indicated by previous studies [*Curry and Oppo, 2005; Duplessy et al., 1988; Sarnthein et al., 1994*]. Therefore, we calculated the vertical gradient for the PI, LGM and glacial-interglacial anomaly for the depth profiles off NW Africa, at the Blake Ridge and Brazil Margin (Figure 4.14). During the PI, locations off NW Africa and at the Blake Ridge are mainly bathed in NADW, whereby no clear maximum vertical gradient occurs (Figure 4.14 a, b). The more southerly location at the Brazil Margin however, experiences relatively more influence by AABW, which leads to a maximum vertical gradient at ~2000 m water depth (Figure 4.14 c). During the LGM, the influence of the southern source water increases in the deep Atlantic Ocean even north of the equator (Figure 4.11). This can be seen in both transects at the Blake Ridge and Brazil Margin. While a distinct vertical gradient in $\delta^{18}\text{O}_c$ occurs at a water depth of ~2500 m at the Blake Ridge it is shallower (~1800 m) at the Brazil Margin (Figure 4.14

e, f), due to the more southerly position. However, in our model the glacial profile off NW Africa seems to lack such a distinct vertical gradient (Figure 4.14 d), which is most likely attributable to the fact that water mass changes in our model are less pronounced in the eastern Atlantic Ocean far away from the deep western boundary current. Furthermore, differences between the eastern and western Atlantic Ocean are expected, because the thermocline is shallower at the eastern side and deeper at the western side of the Atlantic Ocean, whereby lighter $\delta^{18}\text{O}_c$ values reach further down on the western side and thus increase the shift between the upper and lower water column. By investigating the glacial-interglacial $\delta^{18}\text{O}_c$ anomalies, a clear vertical gradient appears in all three profiles, even though it is strongly weakened off NW Africa (Figure 4.14 e, f, g). These, maximum vertical gradients likely correspond to the glacial water-mass boundary in the model, which occurs approximately at 2500 m in the northern subtropical Atlantic and at 1800 m in the southern subtropical Atlantic.

The model does not simulate the high $\delta^{18}\text{O}_c$ anomaly as seen in the sediment core GeoB9508-5. It could be argued that this high value is in error, but a similar pattern is observed in the vertical profiles at the Brazil Margin and Blake Ridge from the western Atlantic (Figure 4.6). Therefore, the reconstructed higher $\delta^{18}\text{O}_c$ anomalies close to the glacial chemocline are probably a real signal. We surmise that these core locations received more glacial NADW than the deeper cores, which was possibly more enriched in $\delta^{18}\text{O}_w$ in the real glacial ocean than in our model. Hence, cores close to the main glacial water-mass boundary seem to be more sensitive to water mass alterations.

Overall, the $\Delta\delta^{18}\text{O}_c$ values of the sediment cores as well as simulated by the MITgcm support previous conclusions based on other proxy records [e.g. *Curry and Oppo*, 2005; *Marchitto et al.*, 2002]. The maximum vertical gradient in $\Delta\delta^{18}\text{O}_c$ at approximately 2000 m to 2500 m likely corresponds to the water-mass boundary of southern and northern source water. The shoaling of the glacial NADW fits well the estimates based on ϵ_{Nd} [*Howe et al.*, 2016], whereby southern source water with a colder signature expanded further into the Atlantic Ocean. Even though sea ice around Antarctica increased in our model simulation, we do not see the modern Atlantic meridional gradient of salt reversed during the LGM. Thus we cannot confirm the hypothesis by *Ferrari et al.* [2014] that the southern deep water came only to the surface under sea ice, imprinting it with high salinities due to strong brine rejection and leading to the reversed salinity pattern. However, since we simulate a shallower water-mass boundary the assumption made by *Lund et al.* [2011] might still hold: The shifting of the water-mass boundary to shallower water depths and thus away from the zone of intense mixing near the sea floor might have reduced the mixing between southern and northern source water. This together

with the increased volume of southern component water might have led to a more stratified deep ocean with a higher ability to trap carbon [Adkins, 2013; Lund et al., 2011].

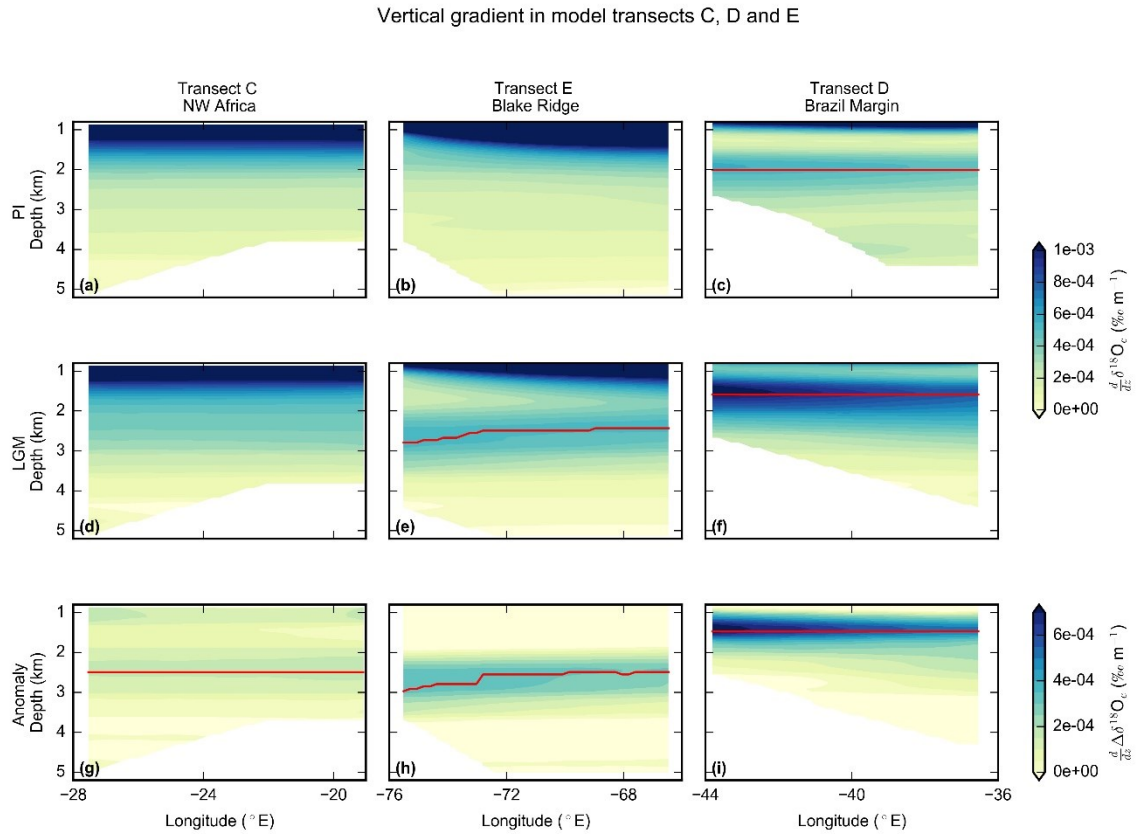


Figure 4.14: Calculated vertical $\delta^{18}O_c$ gradient for the PI (a, b and c), LGM (d, e and f) and glacial-interglacial anomaly (e, f and g) off NW Africa (transect C in Figure 4.1), at the Blake Ridge (transect E in Figure 4.1) and Brazil Margin (transect D in Figure 4.1), respectively. The red line marks the water depth at which the maximum vertical $\delta^{18}O_c$ gradient occurs.

4.5 Conclusions

A common pattern in profiles of benthic LGM-Holocene $\delta^{18}O_c$ differences from the western Atlantic Ocean is that they increase with depth [Keigwin, 2004; Lund et al., 2011]. This pattern is also recognizable in a new transect of sediment cores off NW Africa. While the $\delta^{18}O_c$ anomalies above 2000 m water depth show a signal of around 1.3 ‰, they increase to approximately 1.7 ‰ below. To determine the causes of the shift of 0.4 ‰ between the upper and deeper water column, an equilibrium simulation of the LGM ocean with the MITgcm, including a water isotope scheme, was performed.

The modeled LGM ocean state is consistent with both the surface proxy data and the proxy data from the deep ocean, simulating a shoaling of the water-mass boundary accompanied by greater expansion of southern source water and a slight reduction in the AMOC. The occurrence of the glacial water-mass boundary can also be observed in the vertical gradients of the modeled glacial-interglacial $\delta^{18}\text{O}_c$ anomalies at a water depth of approximately 2000 m. However, it is slightly more pronounced in the western Atlantic Ocean than in the eastern Atlantic Ocean. Based on this glacial ocean state a similar shift in $\Delta\delta^{18}\text{O}_c$ (0.3 ‰) between the upper and lower water column off NW Africa is simulated. Our model results suggest that the glacial-interglacial $\delta^{18}\text{O}_c$ anomalies in the upper 1000 m are strongly affected by the sea-level lowering of 120 m during the LGM. Thereby, deeper waters are shifted closer to the surface, resulting in temperatures relatively warmer by around 1 °C and smaller glacial-interglacial $\delta^{18}\text{O}_c$ differences. This sea-level effect does not affect the deep ocean (> 2000 m), since it is mainly recognizable in the permanent thermocline, where the vertical temperature gradient is largest. However, the ocean model shows that the sea-level change needs to be considered, when investigating glacial $\delta^{18}\text{O}_c$ values. Thus, while the glacial-interglacial $\delta^{18}\text{O}_c$ anomalies in the upper water column are reduced due to the sea-level lowering, increased glacial-interglacial $\delta^{18}\text{O}_c$ differences in the deep ocean are related to a greater influence of cold, close to the freezing point, southern source water. Hence, we claim that the shift in glacial-interglacial $\delta^{18}\text{O}_c$ anomalies between the upper and lower water column is a combined result of the sea-level lowering and cooling of the southern source water. Since we get similar results for the western Atlantic Ocean, it is not only a local signal off North West Africa but representative for at least both the tropical eastern and western Atlantic Ocean.

Acknowledgments

We are thankful to Thejna Tharammal for providing the isotopic data of NCAR IsoCAM and to Takasumi Kurahashi-Nakamura for providing the optimized atmospheric forcing fields obtained with the adjoint method. This research used data acquired at the XRF Core Scanner Lab at the MARUM—Center for Marine Environmental Sciences, University of Bremen, Germany. Thanks to Ursula Röhl, Vera Lukies, and Jan-Berend Stuuat for support during XRF scanning. Comments and suggestions by the two anonymous reviewers highly improved the quality and clarity of the manuscript. This project was supported by the DFG Research Center/Center of Excellence MARUM - “The Ocean in the Earth System”. The stable isotope can be obtained from the PANGAEA database.

Chapter 5 Why do deep-sea $\delta^{18}\text{O}$ records resemble Antarctic temperature during Heinrich Events?

R. Völpel¹, A. Paul¹, S. Mulitza¹ and M. Schulz¹

¹MARUM - Center for Marine Environmental Sciences and Faculty of Geosciences, University of Bremen, Bremen, Germany

In preparation for *Geophysical Research Letter*

Abstract.

The amplitude, phase and general character of isotopic records derived from calcite shells of fossil benthic foraminifera are remarkably similar to the temperature records obtained from Antarctic ice cores. This resemblance is especially striking during time periods of rapid changes in Greenland and the entire North Atlantic. Using the Massachusetts Institute of Technology general circulation model with water isotopes, we investigated the mechanism responsible for the benthic oxygen isotopic decrease of 0.8 ‰ during Heinrich Event 1 in a sediment core from the western tropical Atlantic. Due to the addition of freshwater to the North Atlantic, the Atlantic Meridional Overturning Circulation substantially weakened, inducing a thermal bipolar seesaw associated with the build-up of heat in the South Atlantic and a warming of intermediate-depth waters. The simulated oxygen isotopic decrease was not influenced by the depleted meltwater but corresponded almost entirely to a deep-water temperature signal, which emerged from an initial increase in horizontal heat transport followed by downward heat transport mainly via vertical advection. The resemblance between the oxygen-isotope records of Antarctic ice cores and benthic foraminifera is thus a consequence of the modulation of Antarctic atmospheric temperature and bottom-water temperature by the strength of the AMOC.

5.1 Introduction

Antarctic and Greenland ice cores record oxygen isotopic ($\delta^{18}\text{O}$) variations over the last glacial cycle [Johnsen *et al.*, 1972; Jouzel *et al.*, 1987a; Dansgaard *et al.*, 1993; Grootes *et al.*, 1993], whereby past air temperatures can be reconstructed [Dansgaard, 1964]. Accordingly, temperatures in Greenland experienced rapid changes during the last ice age, which were associated with equally rapid temperature changes over the entire North Atlantic region [Johnsen *et al.*, 1992; Bond *et al.*, 1993]. However, these fluctuations did

not occur in the same way in ice cores from Antarctica. Instead an anti-phasing of temperatures in Greenland and Antarctica is found, which demonstrates the asynchronous variation in the two hemispheres [Blunier and Brook, 2001; EPICA Community Members et al., 2006] that may be related to changes in the thermohaline circulation [Blunier et al., 1998; Lynch-Stieglitz, 2017]. By linking the $\delta^{18}\text{O}$ ice-core records to the oxygen-isotope signal in planktonic and benthic foraminifera ($\delta^{18}\text{O}_c$) of a deep-sea core recovered from the Iberian margin off southern Portugal, Shackleton et al. [2000, 2004] showed that the benthic $\delta^{18}\text{O}_c$ record closely resembles Antarctic temperature, while the planktonic $\delta^{18}\text{O}_c$ record matches the Greenland temperature. Thus, both the benthic $\delta^{18}\text{O}_c$ record and the Antarctic $\delta^{18}\text{O}$ ice-core record differ significantly in amplitude, phase and general form (i.e. triangular vs. square-wave) from the planktonic and Greenland records. The resemblance with Antarctic temperature is a striking feature of the majority of benthic deep-sea cores.

One of the most recent abrupt climate events, in which an anti-phasing of the two hemispheres is apparent, is the Heinrich Event 1 (H1). It occurred during the last deglaciation (14,670 - 18,100 years before present (BP) [Bond et al., 1992, 1997, 1999; Bard et al., 2000; Sarnthein et al., 2001; Rohling et al., 2003; Hemming, 2004]) and is thought to be associated with a weakening of the Atlantic Meridional Overturning Circulation (AMOC) [e.g. Boyle and Keigwin, 1987; Sarnthein et al., 1994; Clark et al., 2002; McManus et al., 2004; Keigwin and Boyle, 2008; Gherardi et al., 2009; Burke et al., 2011] due to the injection of meltwater from iceberg surges into the North Atlantic [Heinrich, 1988; Duplessey et al., 1992], either triggered by subsurface ocean warming [Bassis et al. 2017] or ice sheet instabilities [MacAyeal, 1993; Calov et al., 2002; Hulbe et al., 2004]. In this way, the Northern Hemisphere experienced a return to near-glacial climate conditions, while a pronounced warming (AIM 1) of the same duration occurred over Antarctica indicating a thermal bipolar seesaw [Clark et al., 2002; EPICA Community Members et al., 2006]. During this time period benthic foraminiferal $\delta^{18}\text{O}_c$ records from the Atlantic Ocean reveal decreasing signals (e.g. JM11-F1-19PC [Ezat et al., 2014]; MD99-2334K [Skinner et al., 2003]; M35003-4 [Rühlemann et al., 2004]). The causes for the depleted $\delta^{18}\text{O}_c$ values are controversial. Some authors suggest that isotopically depleted surface water was transported into the deep water of the Nordic Sea and northern North Atlantic by brine formation [e.g. Dokken and Jansen, 1999; Meland et al., 2008; Thornalley et al., 2010a]. Waelbroeck et al. [2006] even go as far as proposing that these waters extended far enough in the South Atlantic to be deflected by the circumpolar currents. However, Rühlemann et al. [2004] investigated benthic $\delta^{18}\text{O}_c$ values from a sediment core in the western tropical Atlantic (M35003-4) recovered from 1299 m water depth and suggest a warming of the intermediate water as the main cause

of the depleted $\delta^{18}\text{O}_c$ signal. This mechanism is also favored by e.g. *Rasmussen and Thomsen* [2004] and *Ezat et al.* [2014].

The deep-sea core M35003-4 is a typical example for the decreasing $\delta^{18}\text{O}_c$ values corresponding to the seesaw-related warming seen in Antarctic ice cores (Figure 5.1), particularly during Heinrich events. Thus, it serves as a reference and target region to investigate the evolution of $\delta^{18}\text{O}_c$ [*Emiliani*, 1955; *Shackleton*, 1974; *Urey*, 1947] during H1. Using the Massachusetts Institute of Technology general circulation model (MITgcm) including a stable water isotope scheme [*Völpel et al.*, 2017], which quantifies the contribution of local $\delta^{18}\text{O}_w$ and temperature changes to $\delta^{18}\text{O}_c$ changes, we show the results of an idealized H1 ocean simulation. In this way, we will test whether the decreasing $\delta^{18}\text{O}_c$ signal during H1 is indeed related to intermediate depth warming or a result of the depleted freshwater introduced by the iceberg discharges and give insights into the causes for the resemblance between benthic $\delta^{18}\text{O}_c$ records and Antarctic $\delta^{18}\text{O}$ ice-core records.

5.2 Material and Methods

5.2.1 The global ocean model

The ocean state during the H1 was simulated using the MITgcm. It solved the Boussinesq form of the hydrostatic Navier-Stokes equations in conjunction with a nonlinear free-surface [*Marshall et al.*, 1997a; *Adcroft et al.*, 2004b]. A cubed-sphere grid with six faces was employed, whereby a nearly uniform horizontal resolution of $\sim 2.8^\circ$ was achieved and pole singularities were avoided [*Adcroft et al.*, 2004a]. The vertical was divided into 15 levels of varying thickness increasing from 50 m at the surface to 690 m at depth. To avoid the possible vanishing of the upper layer associated with the variable free-surface height, the so-called z^* coordinate was used [*Adcroft and Campin*, 2004]. The bathymetry was represented by the partial cell formulation of *Adcroft et al.* [1997]. The ocean model was coupled to a viscous-plastic dynamic-thermodynamic sea ice model [*Losch et al.*, 2010]. Due to the coarse resolution, processes associated with the advection and mixing by eddies were parametrized [*Redi*, 1982; *Gent and McWilliams*, 1990]. The background vertical diffusivity for tracers was uniformly set to $3 \cdot 10^{-5} \text{ m}^2 \text{ s}^{-1}$, and the fully nonlinear equation of state of *Jackett and McDougall* [1995] was used. Tracers were advected using a third-order advection scheme with direct space-time treatment [*Hundsdorfer and Trompert*, 1994].

Three stable water isotopes (H_2^{16}O , H_2^{18}O and HDO) were simultaneously simulated as passive tracers. Their implementation and evaluation is described in detail in *Völpel et*

al. [2017]. A simulation of the Last Glacial Maximum (LGM) [Völpel *et al.*, in review] was used as an initial state for the H1 simulation and served as a reference when investigating the anomalies between those two time periods.

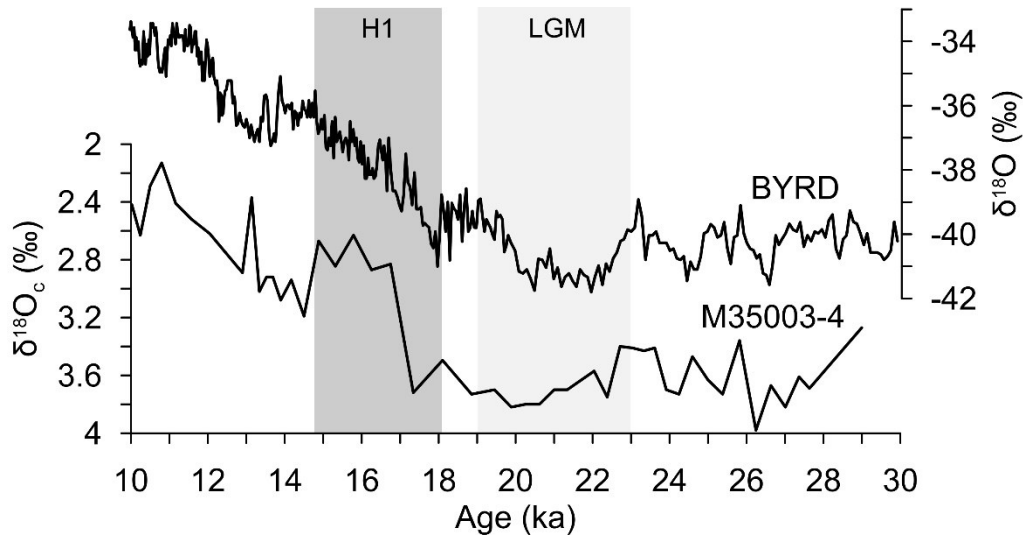


Figure 5.1: Oxygen-isotope records from the sediment core M35003-4 in the Caribbean measured on the benthic foraminifera *Cibicides wuellerstorfi* [Hüls, 2000] and from Antarctica (BYRD on the GRIP timescale; [Blunier *et al.*, 1998]). LGM (19,000 - 23,000 years BP [Mix *et al.*, 2001]) and H1 (14,670 - 18,100 years BP [Sarnthein *et al.*, 2001]) denote the Last Glacial Maximum and Heinrich Event 1, respectively.

5.2.2 Experimental setup

The model was driven by climatological monthly mean atmospheric fields (air temperature, specific humidity, zonal and meridional wind velocity, wind speed, (snow-) precipitation, incoming shortwave radiation as well as river runoff) corresponding to the climate state during the H1 obtained from a simulation with the fully coupled Community Climate System Model Version 3 (CCSM3) [Merkel *et al.*, 2010]. Because the incoming longwave radiation was also needed as an external forcing field, but was not readily available from the CCSM3 simulation, it was estimated following Eq. (1) in Völpel *et al.* [in review], taking all variables from the CCSM3 to reproduce it as accurately as possible.

Regarding the isotopic fields, the model was forced with climatological monthly means of the isotopic content of precipitation and water vapor provided by the National Center for Atmospheric Research Community Atmosphere Model version 3 (CAM3) including a water isotope scheme (NCAR IsoCAM) [Tharammal, 2013]. Since the SST from Merkel *et al.* [2010] was used as a boundary condition in the H1 simulation by Tharammal [2013]

and both simulations employed the same atmospheric model, we obtained a high consistency of our forcing fields. While the fractionation during evaporation was treated explicitly in the MITgcm, the fractionation during the formation of sea ice was neglected and the isotopic content of river runoff was estimated based on the isotopic composition of the local precipitation at the river mouth.

Using the bulk formulae by *Large and Yeager* [2004] both, the freshwater and isotopic air-sea fluxes were internally computed in the model. Asynchronous time stepping to accelerate computation with a time step of 1 day for the tracer equations and 20 min for the momentum equations was used. The initial hydrographic and tracer stratification as well as velocity fields were based on the LGM experiment [*Völpel et al.*, in review] and the H1 simulation was integrated for 2500 model years. The precipitation and tracer specific precipitation were corrected by a constant correction factor [cf. Appendix A in *Völpel et al.*, 2017], which was previously determined by an additional equilibrium simulation with H1 atmospheric boundary conditions without any freshwater perturbations. This way, the model simulation did not produce any uncontrolled drifts and only responded to the additional freshwater flux of 0.05 Sv ($1 \text{ Sv} = 10^6 \text{ m}^3 \text{ s}^{-1}$), representing an idealized Heinrich event. The additional freshwater flux was introduced into the ice-free area of the North Atlantic between 50°N and 70°N , and was equivalent to a sea level rise of approximately 12 m over the entire length of the simulation of 2500 years.

Paleo-proxy reconstructions rather suggest a 12 m sea level rise per 1000 years [*Lambeck et al.*, 2014], however the models' overturning circulation is quite sensitive to an additional freshwater flux and collapses above a threshold of 0.05 Sv. Since paleo-proxy reconstructions as well as other model simulations imply that a total collapse is unlikely [e.g. *Burke et al.*, 2011; *Bradtmiller et al.*, 2014; *Roche et al.*, 2014], we kept the additional freshwater flux at a rate of 0.05 Sv.

The isotopic content of the freshwater flux was prescribed to -30‰ for $\delta^{18}\text{O}$, which is a common glacial value used in many model simulations [e.g. *Ganapolski and Roche*, 2009; *Roche et al.*, 2014] and is close to the end member of -35‰ used to calculate the volume of freshwater entering the Nordic Seas during H1 [*Standford et al.*, 2011]. Since the MITgcm treats the stable water isotopes as individual concentrations, the $\delta^{18}\text{O}_w$ values were calculated from the results following

$$\delta^{18}\text{O} = \left(\frac{R}{R_{\text{STD}}} - 1 \right) \cdot 1000 \text{‰} \quad (5.1)$$

with R being the ratio of the abundance of the heavier water isotope H_2^{18}O to the abundance of the lighter isotope H_2^{16}O and R_{STD} being the Vienna Standard Mean Ocean

Water (VSMOW) standard [Baertschi, 1976]. Using the paleotemperature equation from Marchitto *et al.* [2014], $\delta^{18}\text{O}_c$ values were computed from the $\delta^{18}\text{O}_w$ ratios and temperatures (T) as follow:

$$\delta^{18}\text{O}_c = -0.245 \cdot T + 0.0011 \cdot T^2 + 3.58 + \delta^{18}\text{O}_w - 0.27. \quad (5.2)$$

The analysis was carried out using 50 year averages and mainly focuses on the area close to the core location of M35003-4 in the western Atlantic Ocean.

5.3 Results

In response to the additional freshwater flux of 0.05 Sv, the area close to the core location of the deep-sea core M35003-4 (Figure 5.3, marked by the black square) experienced substantial warming. While during the last 500 years of the LGM simulation [Völpel *et al.*, in review] the water temperature was stable at 4.3 °C, it increased by ~3 °C during the course of the 2500 year-long H1 simulation (Figure 5.2, blue line). Apart from a short initial increase after the instantaneous switch from LGM to H1 atmospheric boundary conditions, the $\delta^{18}\text{O}_w$ decreased by 0.1 ‰ (Figure 5.2, purple line). This was not just a regional occurrence, but an Atlantic wide response (see Figure S2.1 in the Supplement S2). Sub-surface water warmed by up to ~4 °C in the upper 1500 m and to a smaller degree all the way down to the seafloor. Changes in $\delta^{18}\text{O}_w$ were rather small south of 60 °N (about ± 0.3 ‰). Resulting $\delta^{18}\text{O}_c$ values for the M35003-4 area decreased by 0.8 ‰ from 3.7 ‰ to 2.9 ‰ (Figure 5.2, orange line). This is consistent with both absolute values and order of magnitude as seen in the $\delta^{18}\text{O}_c$ measurements of M35003-4 (Figure 5.1) [Hüls, 2000; Rühlemann *et al.*, 2004]. The $\delta^{18}\text{O}_c$ values mimic both the shape of the temperature increase (Figure 5.2) as well as the temperature pattern in the Atlantic wide response (see Figure S2.1 in the Supplement S2). This co-evolution of temperature, $\delta^{18}\text{O}_w$ and $\delta^{18}\text{O}_c$ simulated by the MITgcm was accompanied by a distinct reduction in the horizontal transport (the sum of meridional and zonal transports) within the water column between 1080 m and 1420 m depth (Figure 5.3). The core location is influenced by the Atlantic deep western boundary current. While it transported water from the North Atlantic to the South Atlantic with a velocity of ~ 0.03 m s⁻¹ during the LGM, this transport velocity was reduced by two-thirds during the H1 within the first 200 years of the model simulation (Figure 5.3). Due to the additional freshwater flux released in the North Atlantic Ocean, the North Atlantic Deep Water (NADW) formation substantially weakened compared to the LGM and shifted to the south of 30 °N (see Figure S2.2 in the Supplement S2), leading to decreasing horizontal velocities in the deep western current.

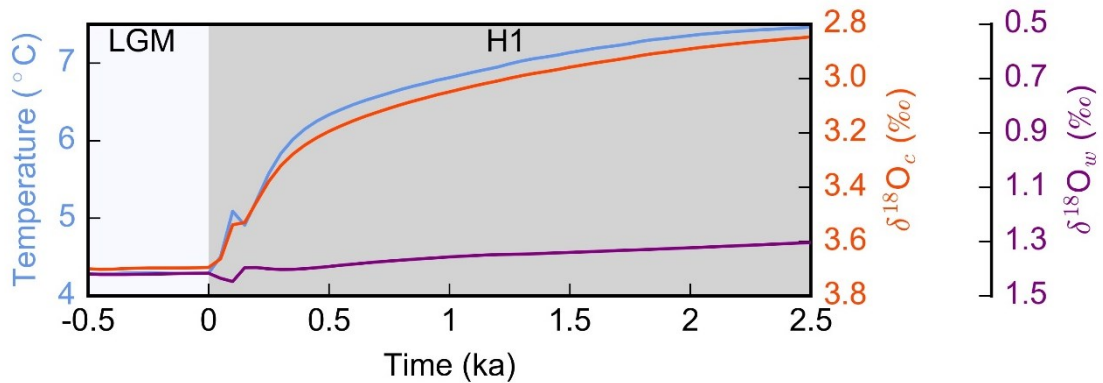


Figure 5.2: Evolution of temperature (blue line), $\delta^{18}\text{O}_w$ (purple line) and $\delta^{18}\text{O}_c$ (orange line) during the last 500 years of the LGM simulation [Vöpel *et al.*, in review] and the 2500 year-long H1 simulation plotted as 50 year mean values averaged over the area marked by the black square in Figure 5.3 in a water depth between 1080 m and 1420 m.

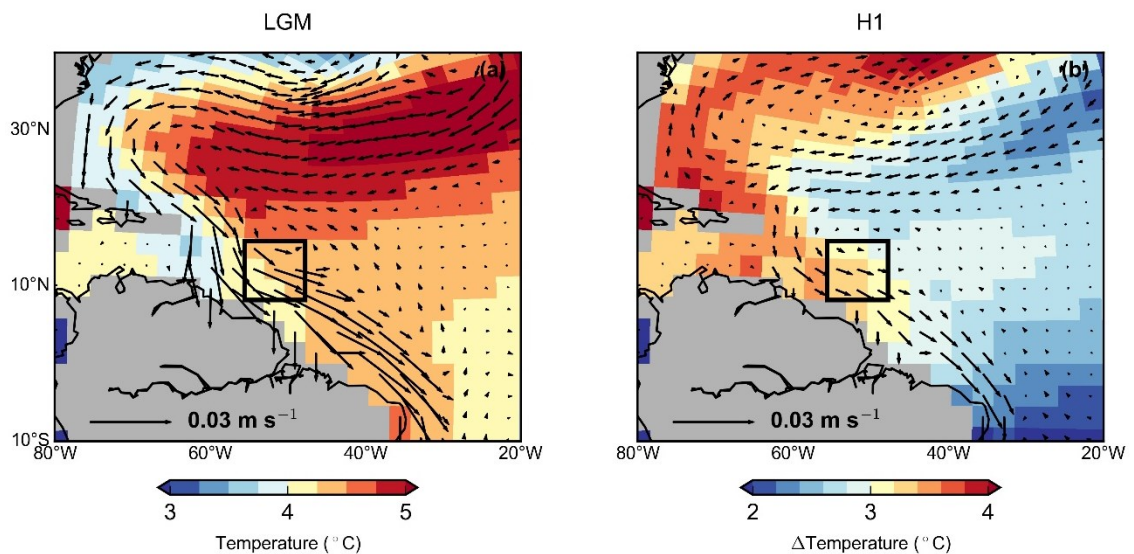


Figure 5.3: Vector plots of the horizontal transport velocities during the LGM (a) and H1 (b) simulations in a water depth between 1080 m and 1420 m. Color contours show the LGM water temperature and temperature anomaly (H1-LGM), respectively. The vector plot for the H1 simulation shows the velocities after the first 200 years, when the temperature tendency starts to decrease (Figure 5.4). The area within the black square marks the grid cells used to calculate the area weighted averages of temperature, $\delta^{18}\text{O}_w$ and $\delta^{18}\text{O}_c$ (Figure 5.2) as well as the heat fluxes (Figure 5.4).

5.4 Discussion

5.4.1 What causes the benthic $\delta^{18}\text{O}_c$ pattern in marine deep-sea records?

Based on our model results it is shown that the area of investigation was not directly influenced by isotopically light meltwater (Figure S2.1b in the Supplement S2). There was only a small decrease in $\delta^{18}\text{O}_w$ of 0.1 ‰ (Figure 5.2), which was equivalent to the amount of water added to the ocean during the H1 experiment with an isotopic value of -30 ‰. Thus, the model results confirmed earlier estimates of the $\delta^{18}\text{O}_w$ change, based on a simulated salinity decrease of 0.2 and an assumed linear relationship with $\delta^{18}\text{O}_w$ [Rühlemann *et al.*, 2004]. Hence, $\delta^{18}\text{O}_w$ as the main driver for the decreasing $\delta^{18}\text{O}_c$ signal can be ruled out. Further, modeled $\delta^{18}\text{O}_c$ values in the tropical Western Atlantic Ocean not require the suggestion by Waelbroeck *et al.* [2006] that $\delta^{18}\text{O}$ depleted waters were incorporated into the deep waters by brine formation and extended far enough in the South Atlantic to be deflected by the circumpolar currents. Consequently, the $\delta^{18}\text{O}_c$ shift of 0.8 ‰ may be attributed to increasing temperatures, as already suggested by Rühlemann *et al.* [2004]. Assessing the potential contribution of temperature to the benthic $\delta^{18}\text{O}_c$ records from paleo-proxies is difficult, because it requires to back out the $\delta^{18}\text{O}_w$ signal from the paleotemperature equation using temperature reconstructions based on e.g., Mg/Ca measurements, which entails large uncertainties [Lea, 2014]. However, the model simultaneously simulated $\delta^{18}\text{O}_w$ and temperature and suggested a substantial warming of 3 °C (Figure 5.2). This fits well the estimated change in $\delta^{18}\text{O}_c$ assuming a slope of 0.21 ‰ to 0.27 ‰ per 1 °C temperature increase in various paleotemperature equations [Craig, 1965; Erez and Luz, 1983; McCrea, 1950; O'Neil *et al.*, 1969]. Similar results were obtained by a number of ocean model simulations, which all indicate a mid-depth warming within the Atlantic Ocean during H1 [Rühlemann *et al.*, 2004; Marcott *et al.*, 2011; Schmidt *et al.*, 2012; Lynch-Stieglitz *et al.*, 2014; Zhang *et al.*, 2017; Weldeab *et al.*, 2016]. Furthermore, Weldeab *et al.* [2016] successfully reconstructed temperatures from Mg/Ca measurements from a sediment core at 1295 m water depth and conclude that temperatures were elevated by 3.9 ± 0.5 °C. This estimate from the eastern equatorial Atlantic supports our simulated basin-wide response (see Figure S2.1 in the Supplement S2).

Since both the absolute $\delta^{18}\text{O}_c$ values and the amplitude of our modeled $\delta^{18}\text{O}_c$ change compare reasonably well with the reconstructed M35003-4 calcite values, we propose that the pattern of the reconstructed $\delta^{18}\text{O}_c$ record was mainly driven by increasing temperatures. This warming would be tightly linked to the AMOC slowdown caused by the addition of freshwater, leading to a redistribution of heat in the Atlantic Ocean. While

in our model the transport of Antarctic Bottom Water (AABW) only decreased slightly, the NADW formation and transport was reduced strongly (see Figure S2.2 in the Supplement S2). This pattern is consistent with various proxies [Clark *et al.*, 2012; Buizert *et al.*, 2014] such as measurements of $^{231}\text{Pa}/^{230}\text{Th}$ revealing a nearly eliminated AMOC [McManus *et al.*, 2004] as well as benthic $\delta^{13}\text{C}$, which tend to show the accumulation of respired carbon [Schmittner and Lund, 2015; Voigt *et al.*, 2017]. The shutdown of the circulation caused a decrease of northward ocean heat export from the South Atlantic and thus a cooling of the ocean and atmosphere in the North Atlantic region, resulting in a bipolar seesaw at the surface [Crowley, 1992; Broecker, 1998; Stocker, 1998]. According to the modeled basin wide temperature response (Figure S2.1a in the Supplement S2) the warming of intermediate depth waters was not only restricted to the investigated area of M35003-4, but even recognizable in the North Atlantic below 1000 m water depth. Thus, model results suggest that the decreasing $\delta^{18}\text{O}_c$ values in the Nordic Sea and North Atlantic were related to both warmer temperatures and more depleted $\delta^{18}\text{O}_w$, which contradicts the hypothesis by e.g. Dokken and Jansen [1999] that it is solely a result of brine formed by isotopically depleted surface water.

To investigate the cause of the substantial mid-depth warming, we additionally conducted a temperature tendency analysis, that differentiates between the net horizontal and vertical heat fluxes and their components (Figure 5.4). The net vertical and horizontal heat fluxes consist of both advective and diffusive terms, while the net horizontal heat flux further comprises both zonal and meridional components. During the LGM, the temperature tendency was balanced between the vertical and horizontal fluxes (Figure 5.4c), whereby a constant temperature of 4.3 °C was achieved (Figure 5.2). The horizontal transport components across the northern, southern, western and eastern boundaries were an order of magnitude larger than the vertical transport components (Figure 5.4a, b). Only a small amount of heat was transported across the northern boundary (about $-1 \cdot 10^{13}$ W; the negative sign indicates a southward transport), while most of the heat entered the region from the western side (Figure 5.4a). The heat was then transported across the eastern and southern boundaries, resulting in a negative horizontal divergence (Figure 5.4c). Vertically, slightly more heat was transported downwards across the upper boundary than across the lower boundary (Figure 4b), resulting in a positive vertical divergence.

After the instantaneous switch from LGM to H1 atmospheric boundary conditions, heat transport across all horizontal boundaries started to decrease (Figure 5.4a). During the first 50 years of the slowdown of the AMOC, temporarily more heat entered the

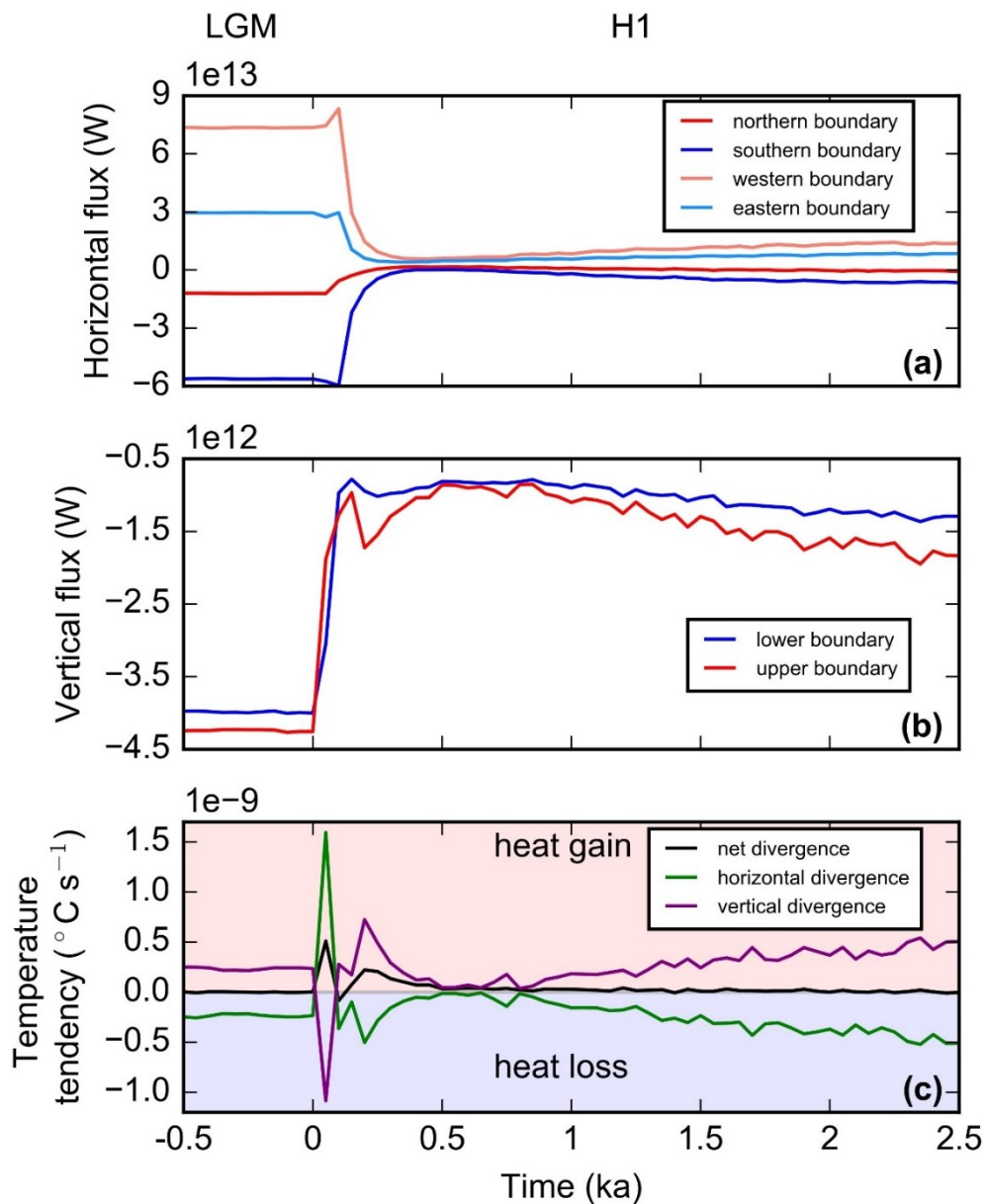


Figure 5.4: Temperature tendency analysis for the last 500 years of the LGM experiment and the 2500 year H1 experiment within the area of the black square displayed in Figure 5.3. The horizontal heat transports across the northern, southern, eastern and western boundaries are shown in (a), while the vertical heat transport across the upper and lower boundaries are shown in (b). In (c) the temperature tendency resulting from the interaction of the net horizontal and vertical heat fluxes is displayed. All curves are based on 50 year averages.

investigated area from the west than left it to the east and south, resulting in a net heat gain (Figure 5.4c). Meanwhile, the vertical transport across the upper and lower boundaries decreased as well (Figure 5.4b), but slightly more heat was transported

across the lower boundary, whereby a heat loss was obtained (Figure 5.4c). These heat transport mechanisms marked the first substantial warming (Figure 5.4c) of intermediate depth waters, since the net horizontal heat flux was no longer balanced by the vertical heat flux. While the AMOC increasingly weakened, the heat transport across the vertical boundaries became more significant. Especially around 200 years of the model simulation, when the temperature tendency indicated the second substantial heat gain (Figure 5.4c), a greater portion of heat that originated from the surface and upper layers of the water column of the South Atlantic, entered the investigated area across the upper boundary than left it across the lower one (Figure 5.4b). This continued all the way through the H1 experiment. Furthermore, while during the LGM vertical diffusion was the dominating transport mechanism, throughout the H1 experiment it was vertical advection. The mean velocity across the upper and lower boundaries decreased slightly, even though the mean velocity across the lower boundary experienced greater change. However, the vertical temperature gradient substantially increased, whereby it overwhelmed the velocity effect leading to a substantial warming through the vertical heat transport. *Zhang et al.* [2017] reported similar results from their transient simulation with the ocean general circulation model POP2, also pointing to enhanced vertical advection. In our model, the positive vertical divergence was responsible for the mid-depth warming in the Atlantic Ocean after the transition from a vigorous to a nearly collapsed AMOC, since it was not balanced by the negative horizontal divergence (Figure 5.4c; Figure 5.2). The net horizontal heat transport out of the region across the southern and eastern boundaries, was too small to compensate for the net downward heat transport mainly via vertical advection.

Thus we conclude that in our simulation the addition of freshwater to the North Atlantic during H1 resulted in a substantial weakening of the AMOC by a reduction of NADW formation and transport, which decreased the heat transport to the North Atlantic, concomitant with heat storage and warming in the South Atlantic (see Figure S2.1 in the Supplement S2). The model results reveal that during the transition from a vigorous to a nearly collapsed AMOC, heat gain was first due to horizontal advection, but then due vertical processes, mainly vertical advection. Hence, the vertical heat transport played a dominant role during the weakened AMOC although it was a magnitude smaller than the horizontal heat transport.

5.4.2 Common origin for the resemblance between deep-sea and ice-core records?

As shown by e.g. *Shackleton et al.* [2000, 2004] benthic $\delta^{18}\text{O}_c$ records are remarkably similar to the $\delta^{18}\text{O}_c$ records in Antarctic ice cores, both indicating increasing temperatures in two different climate components (ocean and atmosphere, respectively) and revealing a contrasting behavior compared to the temperature variations over Greenland and the North Atlantic. Thus it is likely that the two records are affected by processes that are related to the same cause. The thermal bipolar seesaw is a commonly accepted conceptual model, whereby the interhemispheric heat distribution changes in response to modifications in the AMOC [*Crowley*, 1992; *Broecker*, 1998; *Stocker and Johnsen*, 2003].

Pedro et al. [2018] suggest a chain of processes, leading to increased poleward heat and moisture transport, both contributing to the more enriched $\delta^{18}\text{O}$ ratios and thus warming of Antarctica. According to them, the weaker AMOC leads to a reduction in the northward advection of heat, allowing heat to accumulate in the South Atlantic interior. The warmer water is then mixed by eddies across the Antarctic Circumpolar Current, where it drives sea ice retreat. Due to the ice-albedo feedback the initial warming is further amplified and the overlying atmosphere warms, whereby heat for the atmospheric heat flux to Antarctica is provided. Thus, Antarctic temperatures would rather follow the South Atlantic heat content. *Shackleton* [2000] on the other hand proposes that the temperature of the deep ocean follows the Antarctic temperature. Based on the oxygen-isotope records from the sediment core M35003-4 and the Antarctic ice core (Figure 5.1), the suggestion by *Shackleton* [2000] seems to be reasonable, since the benthic $\delta^{18}\text{O}_c$ decrease lags the initial warming signal in the ice core by ~600 years. This equals two times the e-folding time of the modeled temperature change, which might point to the time for the deep ocean to respond. However, modeling the downcore calendar age distribution for M35003-4 with the R-script BACON [*Blaauw and Christen*, 2011] yields an age uncertainty of ± 500 years at the beginning of H1, which is in the range of the estimated lag. Furthermore, the resolution of H1 in the sediment core is poor, since the sedimentation rate is low. Hence, any lead/lag estimation is fraught with uncertainty. Even though, the response time of the deep ocean is slow, it cannot be fully determined with our model, whether the deep ocean temperature follows the Antarctic temperature [*Shackleton*, 2000] or vice versa [*Pedro et al.*, 2018]. However, we obtained decreasing $\delta^{18}\text{O}_c$ values that corresponded almost entirely to a deep-water temperature signal caused by warmer waters at intermediate depths. Thus, we suggest that these warmer waters initially resulted from an increase in horizontal heat transport across the western

boundary accompanied by less removal and followed by downward heat transport via vertical advection through the build-up of heat at the surface and upper layers of the water column in the South Atlantic, due to a reduced AMOC. Hence, the link between the benthic $\delta^{18}\text{O}_c$ and Antarctic ice-core records is the strength of the AMOC, which determines the meridional heat transport and NADW production resulting in increasing temperatures in both types of records.

5.5 Conclusions

A striking feature of the majority of benthic deep-sea cores is the decrease in $\delta^{18}\text{O}_c$ during H1, matching temperatures over Antarctica while differing from the Greenland counterpart. Based on our model results, we can conclude that the $\delta^{18}\text{O}_c$ decrease of 0.8 ‰ in the tropical western Atlantic Ocean was mainly driven by a temperature increase of 3 °C. Isotopically light meltwater did not influence the area of investigation. Thus, the suggestion by *Waelbroeck et al.* [2006] that $\delta^{18}\text{O}$ depleted surface water was incorporated into the deep waters by brine formation in the Nordic Sea and extended far enough in the South Atlantic to be deflected by the circumpolar current, can be ruled out. Instead, it was caused by the substantial intermediate depth warming resulting from the weakening AMOC, confirming earlier assumptions by e.g. *Rühlemann et al.* [2004]. In our model, this temperature increase initially resulted from the dominance of the horizontal heat transport across the western side accompanied by less removal. In the course of the cessation of the AMOC vertical heat transport mechanisms became more significant. Heat that was stored at the surface and upper layers of the water column of the South Atlantic was transported downward mainly via vertical advection, thus effectively heating the waters at intermediate depth. Hence, the resemblance of benthic $\delta^{18}\text{O}_c$ records with Antarctic ice cores can be attributed to the fact that they correspond almost entirely to a deep-water temperature signal and that both the sediment and ice proxies are sensitive to the strength of the AMOC.

Acknowledgment

We are thankful to Thejna Tharammal for providing the isotopic data of NCAR IsoCAM and to Ute Merkel for providing the atmospheric forcing fields obtained from the CCSM3. This project was supported by the DFG Research Center/Center of Excellence MARUM - "The Ocean in the Earth System".

Chapter 6 Conclusions and Outlook

The oxygen isotopic composition of benthic foraminiferal calcite is the most measured proxy in paleoceanographic studies, and is commonly used as a tracer to infer changes in the Atlantic water masses associated with shifts in ocean circulation. It reflects both the temperature and the $\delta^{18}\text{O}_w$, whereby a precise interpretation of the $\delta^{18}\text{O}_c$ records requires a separation of these two factors. In this study, an isotope-enabled ocean model approach was developed and used to solve this challenge, providing a tool, which enables the comparison to the wealth of the foraminiferal $\delta^{18}\text{O}_c$ from sediment records and, thus, infer water mass alterations due to AMOC changes under climate change.

The three stable water isotopes H_2^{16}O , H_2^{18}O and HDO were implemented into the numerical ocean model MITgcm. The model was forced with the isotopic content of precipitation and water vapor obtained from an isotope-enabled AGCM, while the isotopic composition of river runoff was estimated from the isotopic composition of the local precipitation at individual river mouths. The equilibrium and kinetic effects during evaporation were treated explicitly in the MITgcm and the fractionation during the formation of sea ice was neglected.

In line with observational data, the newly developed package *wiso* captures well the broad pattern and magnitude of annual mean $\delta^{18}\text{O}_w$, both at the sea surface as well as in the deeper parts of the ocean under pre-industrial climate conditions. The enrichment of net evaporation in low latitude regions as well as its depletion in high latitudes are accurately reproduced, whereby the $\delta^{18}\text{O}_w$ -salinity relationship is in good agreement with observations. However, the model is not able to simulate $\delta^{18}\text{O}_w$ values as depleted as seen in the observations in the northern high latitudes due to the absence of highly depleted precipitation and snow fall in areas covered by sea ice and due to the neglect of fractionation during sea-ice formation. Based on the $\delta^{18}\text{O}_w$ distribution in the oceans' interior, the different water masses are easily distinguishable. Testing the model against $\delta^{18}\text{O}_c$ measurements on planktonic foraminiferal shells from plankton-tow data shows a quantitatively consistency, which is better as long as all foraminiferal species are grouped together. Comparisons with individual planktonic foraminiferal species are more challenging, because of the species-specific depth habitats. This is, however, not of greater concern when benthic foraminiferal $\delta^{18}\text{O}_c$ is investigated. Thus, the implementation of stable water isotopes in the MITgcm provides a robust tool that simulates the key proxy $\delta^{18}\text{O}_c$, offering the investigation of the causes of the observed

$\delta^{18}\text{O}_c$ variations in regard to different climate conditions, which might help to improve the understanding and interpretation of the $\delta^{18}\text{O}_c$ data.

Following the successful implementation of the stable water isotopes, this modeling approach was applied to investigate the vertically increasing glacial-interglacial $\delta^{18}\text{O}_c$ anomalies recorded in benthic foraminifera from a transect of five depth-stratified sediment cores off North West Africa. The smaller $\delta^{18}\text{O}_c$ anomalies in the upper 1000 m of the water column are a result of the sea-level lowering of approximately 120 m during the LGM, which brings the glacial waters closer to the surface. This leads to warmer temperatures of around 1 °C and, thus, entirely explains the observed change in $\delta^{18}\text{O}_c$. These sea level related changes are mainly restricted to the permanent thermocline, where the vertical temperature gradient is largest, and do no longer affect the deep ocean (> 2000 m). Here, lower temperatures due to the greater influence of cold southern source water, which results from a slight reduction in the AMOC accompanied by a shoaling of the water-mass boundary, dominate the large increase in glacial $\delta^{18}\text{O}_c$. These results indicate that the transition from smaller to larger glacial-interglacial $\delta^{18}\text{O}_c$ differences at approximately 2000 m water depth, which is apparent in the open tropical Atlantic Ocean of the model simulation, can indeed be interpreted as the boundary between the northern source and southern source water during the LGM. Thus, it coincides with estimates from other climate proxies such as $\delta^{13}\text{C}$. Further, it reveals that ocean modeling approaches investigating $\delta^{18}\text{O}_c$ cannot neglect the effect of sea-level changes, which would otherwise result in misinterpretations of $\delta^{18}\text{O}_c$ data. Apart from the $\delta^{18}\text{O}_c$ anomalies, the LGM model simulation further supports the assumption, that the strength of the glacial AMOC was neither extremely sluggish nor enhanced compared to the pre-industrial. In combination with the shoaling of the water-mass boundary between northern and southern source water in the Atlantic Ocean and, thus, away from the zone of intense mixing near the seafloor, the glacial ocean was probably more stratified. This, in turn, could explain the lower atmospheric CO_2 concentrations during the LGM, as the ocean might have operated as a more effective carbon trap likely resulting in a glacial climate state.

Under H1 atmospheric boundary conditions, the mechanism responsible for the decreasing benthic $\delta^{18}\text{O}_c$ values has been investigated, whereby the long-standing phenomenon of the resemblance between the deep-sea isotopic records and the temperature records of Antarctic ice cores has been addressed. The strength of the AMOC significantly weakens, due to the addition of freshwater into the North Atlantic Ocean. This leads to a reduction in the northward heat transport from the South Atlantic, initiating a thermal bipolar seesaw and substantial warming within the intermediate depth

waters. A core location in the western tropical Atlantic served as representative for the aforementioned phenomenon and revealed a benthic $\delta^{18}\text{O}_c$ decrease of ~ 0.8 ‰ during the course of H1. This decrease is not influenced by depleted meltwater, but driven by a temperature increase of 3 °C that originates from the transition from a vigorous to a nearly collapsed AMOC associated with an initial increase in horizontal heat transport followed by downward heat transport mainly via vertical advection. Thus, the oxygen-isotope records of benthic foraminifera and Antarctic ice cores are sensitive to the strength of the AMOC, which modulates Antarctic atmospheric temperatures and bottom water temperatures causing the resemblance between both proxies.

Even though the implementation of the *wiso* package into the MITgcm resulted in successful simulations of both the pre-industrial and paleo oceans and, thus, gave insights into the causes of benthic $\delta^{18}\text{O}_c$ variations, further modifications to improve future simulations are recommended. Implementing stable water isotopes into the sea ice component of the MITgcm could decrease the biases in the high latitudes. Fractionation during sea-ice formation leads to a slight increase of the lighter isotopes in the surrounding surface water, while the sea-ice transport and the subsequent melting of sea ice would increase the $\delta^{18}\text{O}_w$ values at a distant location, whereby an isotopic shift in surface waters is produced. Additionally, the source of highly depleted precipitation and snow fall over areas covered by sea ice would no longer be neglected, because it would either be accumulated as a snow layer on the sea ice or be transformed into ice. Since it retains its isotopic content, transferring it to the surface ocean via melting would sooner or later result in an additional source of highly depleted $\delta^{18}\text{O}_w$.

Depending on the aim of the isotope-enabled ocean simulation it is worth considering to increase the model resolution. In particular, an increase of the vertical resolution in the upper water column could lead to a better model-data comparison for species-specific planktonic foraminifera $\delta^{18}\text{O}_c$. Currently, the upper 500 m are only divided into four vertical levels, whereas a higher resolution would make the assessment of species-specific depth habitats more reasonable.

Apart from these modifications, the *wiso* package already offers a great opportunity to investigate the ocean and its isotopic composition during different climate states and their effects imprinted in the $\delta^{18}\text{O}_c$ proxy records. Thus, it provides a robust tool to be used in the paleoclimate data assimilation framework with the adjoint method of the MITgcm, which minimizes the error between model and data. Nevertheless, for an even more detailed investigation of changes in the ocean circulation during present and past climate states, as inferred from deep-sea records, the *wiso* package should be combined with a carbon isotope module, containing at least the fractionation processes during

photosynthesis and air-sea gas exchange. This combined simulation would allow a direct comparison with both $\delta^{18}\text{O}_c$ and $\delta^{13}\text{C}_c$, whereby the interpretation of these records as well as our understanding of past ocean circulation changes might be further improved. Furthermore, combining the wiso package with an ecosystem model including the fractionation during calcium carbonate formation of individual foraminiferal species might improve the interpretation of any particular temporal or spatial pattern of foraminiferal-based proxy records. With this approach the main effects (temperature, $\delta^{18}\text{O}_w$, biological vital effects and possible ecological changes) on the $\delta^{18}\text{O}_c$ data in response to climate change, such as during the LGM and H1, could be simultaneously investigated. In the long run, it might be feasible to couple the wiso package to an atmospheric isotope-enabled model component to be more independent of forcing fields from other climate simulations.

References

- Adcroft, A. and J.-M. Campin (2004), Rescaled height coordinates for accurate representation of free-surface flows in ocean circulation models. *Ocean Modelling.*, 7, 269-284.
- Adcroft, A., C. Hill and J. Marshall (1997), Representation of Topography by Shaved Cells in a Height Coordinate Model. *Month. Weath. Rev.* 125, 2293-2315.
- Adcroft, A., J.-M. Campin, C.N. Hill and J.C. Marshall (2004a), Implementation of an atmosphere-ocean general circulation model on the expanded spherical cube, *Month. Weath. Rev.*, 132, 2845–2863, doi:10.1175/MWR2823.1.
- Adcroft, A., C. Hill, J. Campin, J. Marshall, and P. Heimbach (2004b), Overview of the formulation and numerics of the MIT GCM, in *Proceedings of the ECMWF Seminar Series on Numerical Methods: Recent Developments in Numerical Methods for Atmosphere and Ocean Modelling*, ECMWF, 139–149.
- Adcroft, A., J.-M. Campin, S. Dutkiewicz, C. Evangelinos, D. Ferreira, G. Forget, B. Fox-Kemper, P. Heimbach, C. Hill, E. Hill, H. Hill, O. Jahn, M. Losch, J. Marshall, M. Maze, D. Menemenlis, and A. Molod (2018), MITgcm user manual, MIT Department of EAPS, Cambridge.
- Adkins, J. F. (2013), The role of deep ocean circulation in setting glacial climates, *Paleoceanography*, 28, 539–561, doi:10.1002/palo.20046.
- Adkins, J. F., and D. P. Schrag (2001), Pore fluid constraints on deep ocean temperature and salinity during the Last Glacial Maximum, *Geophys. Res. Lett.*, 28, 771–774, doi:10.1029/2000GL011597.
- Adkins, J. F., and D. P. Schrag (2003), Reconstructing Last Glacial Maximum bottom water salinities from deep-sea sediment pore fluid profiles, *Earth Planet. Sc. Letts.*, 216, 109–123.
- Adkins, J. F., K. McIntyre, and D. P. Schrag (2002), The salinity, temperature, and $\delta^{18}\text{O}$ of the glacial deep ocean, *Science*, 298, 1769–1773, doi:10.1126/science.1076252.
- Aharon, P. (1983), 140,000-yr isotope climatic record from raised coral reef in New Guinea, *Nature*, 304, 720-723.
- Andrews, J. T. (1998), Abrupt changes (Heinrich events) in late Quaternary North Atlantic marine environments: a history and review of data and concepts. *J. Quaternary Sci.*, 13, 3–16, doi:10.1002/(SICI)1099-1417(199801/02)13:1<3::AID-JQS361>3.0.CO;2-0.
- Arakawa A. and V. R. Lamb (1977), *Methods of Computational Physics*, 17, Academic Press.
- Baertschi, P. (1976), Absolute ^{18}O content of standard mean ocean water, *Earth Planet. Sc. Lett.*, 31, 341–344, doi:10.1016/0012-821X(76)90115-1.
- Bard, E., F. Rostek, J.-L. Turon, and S. Gendreau (2000), Hydrological Impact of Heinrich Events in the Subtropical Northeast Atlantic, *Science*, 289, 1321–1324.
- Bassis, J. N., S. V. Petersen and L. M. Cathles (2017), Heinrich events triggered by ocean forcing and modulated by isostatic adjustment, *Nature*, 542, 332-334, doi:10.1038/nature21069.
- Bauch, D., J. Carstens, and G. Wefer (1997), Oxygen isotope composition of living *Neogloboquadrina pachyderma* (sin.) in the Arctic Ocean, *Earth Planet. Sc. Lett.*, 146, 47-58, doi:10.1016/S0012-821X(96)00211-7.
- Bé, A. W. H. (1980), Gametogenic calcification in a spinose planktonic foraminifer, *Globigerinoides sacculifer* (Brady), *Mar. Micropaleontol.*, 5, 283-310.

- Bé, A. W. H., J. W. Morse, and S. M. Harrison (1975), Progressive dissolution and ultrastructural breakdown of planktonic foraminifera, in *Dissolution of Deep Sea Carbonates*, edited by: W. V. Sliter, A. W. H. Bé, and W. H. Berger, Cushman Foundation for Foraminiferal Research, Special Publication, 13, 27-55.
- Bemis B., H. Spero, J. Bijma, and D. W. Lea (1998), Reevaluation of the oxygen isotopic composition of planktonic foraminifera: Experimental results and revised paleotemperature equations, *Paleoceanography*, 13, 150–160.
- Berry, D. I. and E. C. Kent (2009), A New Air-Sea Interaction Gridded Dataset from ICOADS with Uncertainty Estimates, *B. Am. Meteorol. Soc.*, 90, 645-656, doi:10.1175/2008BAMS2639.1.
- Billups, K., and D. P. Schrag (2000), Surface ocean density gradients during the last glacial maximum, *Paleoceanography*, 15, 110-123, doi:10.1029/1999PA000405.
- Blaauw, M., and J. A. Christen (2011), Flexible paleoclimate age-depth models using an autoregressive gamma process, *Bayesian Analysis*, 6, 457-474.
- Blunier, T., and E. J. Brook (2001), Timing of millennial-scale climate change in Antarctica and Greenland during the last glacial period, *Science*, 291, 109-112.
- Blunier, T., J. Chappellaz, J. Schwander, A. Dällenbach, B. Stauffer, T. F. Stocker, D. Raynaud, J. Jouzel, H. B. Clausen, C. U. Hammer, and S. J. Johnsen (1998), Asynchrony of Antarctic and Greenland climate change during the last glacial period, *Nature*, 394, 739-743, doi: 10.1038/29447.
- Bond, G., H. Heinrich, W. Broecker, L. Labeyrie, J. McManus, J. Andrews, S. Huon, R. Jantschik, S. Clasen, C. Simet, K. Tedesco, M. Klas, G. Bonani, and S. Ivy (1992), Evidence for massive discharges of icebergs into the North Atlantic Ocean during the last glacial period, *Nature*, 360, 245–249.
- Bond, G., W. Broecker, S. Johnsen, J. McManus, L. Labeyrie, J. Jouzel, and G. Bonani (1993), Correlations between climate records from North Atlantic sediments and Greenland ice, *Nature*, 365, 143-147, doi:10.1038/365143a0.
- Bond, G., W. Showers, M. Cheseby, R. Lotti, P. Almasi, P. deMenocal, P. Priore, H. Cullen, I. Hajdas, G. Bonani (1997), A pervasive millennial-scale cycle in North Atlantic Holocene and glacial climates, *Science*, 278, 1257-1266.
- Bond, G., W. Showers, M. Elliot, M. Evans, R. Lotti, I. Hajdas, G. Bonani, and S. Johnson (1999), The north Atlantic's 1–2 kyr climate rhythm: relation to Heinrich events, Dansgaard/Oeschger cycles and the little ice age, in *Mechanisms of Global Climate Change at Millennial Time Scales*, edited by: P. U. Clark, R.S. Webb, and L.D. Keigwin, pp. 35-38, American Geophysical Union, Washington.
- Boyle, E. A. and L. D. Keigwin (1987), North Atlantic thermohaline circulation during the past 20,000 years linked to high-latitude surface temperature, *Nature*, 330, 35-40.
- Braconnot, P., et al. (2007a), Results of PMIP2 coupled simulations of the Mid-Holocene and Last Glacial Maximum—Part 1: Experiments and large-scale features, *Clim. Past*, 3, 261–277, doi:10.5194/cp-3-261-2007.
- Braconnot, P., et al. (2007b), Results of PMIP2 coupled simulations of the Mid-Holocene and Last Glacial Maximum—Part 2: Feedbacks with emphasis on the location of the ITCZ and mid- and high latitudes heat budget, *Clim. Past*, 3, 279–296, doi:10.5194/cp-3-279-2007.
- Bradt Miller, L. I., J. F. McManus, and L. F. Robinson (2014), $^{231}\text{Pa}/^{230}\text{Th}$ evidence for a weakened but persistent Atlantic meridional overturning circulation during Heinrich Stadial 1, *Nat. Commun.*, 5, 5817, doi:10.1038/ncomms681.
- Brasseur, P., J. M. Beckers, J. M. Brankart, and R. Schoenauen (1996), Seasonal temperature and salinity fields in the Mediterranean Sea: Climatological analyses of a historical data set, *Deep-Sea Res. Pt. I*, 43, 159–192, doi:10.1016/0967-0637(96)00012-X.

- Brennan, C. E., A. J. Weaver, M. Eby, and K. J. Meissner (2012), Modelling Oxygen Isotopes in the University of Victoria Earth System Climate Model for Pre-industrial and Last Glacial Maximum Conditions, *Atmosphere-Ocean*, 50, 447-465, doi:10.1080/07055900.2012.707611.
- Brennan, C. E., K. J. Meissner, M. Eby, C. Hillaire-Marcel, and A. J. Weaver (2013), Impact of sea ice variability on the oxygen isotope content of seawater under glacial and interglacial conditions, *Paleoceanography*, 28, 388-400, doi:10.1002/palo20036.
- Broecker, W. S. (1994), Massive iceberg discharge as triggers for global climate change, *Nature*, 372, 421-424.
- Broecker, W. S. (1998), Paleocean circulation during the last deglaciation: A bipolar seesaw?, *Paleoceanography*, 13, 119-121.
- Broecker, W. S. and J. van Donk (1970), Insolation changes, ice volumes, and the O¹⁸ record in deep-sea cores, *Rev. Geophys.*, 8, 169-198.
- Broecker, W. S. and G. H. Denton (1990), The role of ocean-atmosphere reorganizations in glacial cycles, *Quaternary Sci. Rev.*, 9, 305-347.
- Broecker, W. S., D. M. Peteet, and D. Rind (1985), Does the ocean-atmosphere system have more than one stable mode of operation?, *Nature*, 315, 21-26.
- Brovkin, V., A. Ganopolski, D. Archer, and S. Rahmstorf (2007), Lowering of glacial atmospheric CO₂ in response to changes in oceanic circulation and marine biogeochemistry, *Paleoceanography*, 22, PA4202, doi:10.1029/2006PA001380.
- Brown, S. J., and H. Elderfield (1996), Variations in Mg/Ca and Sr/Ca ratios of planktonic foraminifera caused by postdepositional dissolution: evidence of shallow Mg-dependent dissolution. *Paleoceanography*, 11, 543–551, doi: 10.1029/96PA01491.
- Burke, A., O. Marchal, L. I. Bradtmiller, J. F. McManus, and R. François (2011), Application of an inverse method to interpret ²³¹Pa/²³⁰Th observations from marine sediments, *Paleoceanography*, 26.
- Buizert, C., V. Gkinis, J. P. Severinghaus, F. He, B. S. Lecavalier, P. Kindler, M. Leuenberger, A. E. Carlson, B. Vinther, V. Masson-Delmotte, J. W. C. White, Z. Liu, B. Otto-Bliesner, and E. J. Brook (2014), Greenland temperature response to climate forcing during the last deglaciation, *Science*, 345, 1177-1180.
- Calov, R., A. Ganopolski, V. Petoukhov, M. Claussen, and R. Greve (2002), Large-scale instabilities of the Laurentide ice sheet simulated in a fully coupled climate-system model, *Geophys. Res. Lett.*, 29, 2216, doi: 10.1029/2002GL016078.
- Came R. E., D. W. Oppo, W. B. Curry, A. J. Broccoli, R. J. Stouffer, and J. Lynch-Stieglitz (2007), North Atlantic intermediate depth variability during the Younger Dryas: evidence from benthic foraminiferal Mg/Ca and the GFDL R30 coupled climate model, in: *Past and Future Changes in the Ocean's Overturning Circulation: Mechanisms and Impacts on Climate and Ecosystems*, edited by: A. Schmittner, J. Chiang, and S. Hemming, pp. 247–63. Washington, DC: Am. Geophys. Union.
- Campin, J.-M., A. Adcroft, C. Hill and J. Marshall (2004), Conservation of properties in a free-surface model, *Ocean Modelling*, 6, 221-244.
- Clark, P. U., N. G. Pisias, T. F. Stocker, and A. J. Weaver (2002), The role of the thermohaline circulation in abrupt climate change, *Nature*, 415, 863–869.
- Clark, P. U., A. S. Dyke, J. D. Shakun, A. E. Carlson, J. Clark, B. Wohlfarth, S. W. Hostetler, and A. M. McCabe (2009), The Last Glacial Maximum, *Science*, 325, 710–714, doi:10.1126/science.1172873.
- Clark, P. U., J. D. Shakun, P. A. Baker, P. J. Bartlein, S. Brewer, E. Brook, A. E. Carlson, H. Cheng, D. S. Kaufman, Z. Liu, T. M. Marchitto, A. C. Mix, C. Morrill, B. L. Otto-Bliesner,

- K. Pahnke, J. M. Russell, C. Whitlock, J. F. Adkins, J. L. Blois, J. Clark, S. M. Colman, W. B. Curry, B. P. Flower, F. He, T. C. Johnson, J. Lynch-Stieglitz, V. Markgraf, J. McManus, J. X. Mitrovica, P. I. Moreno, and J. W. Williams (2012), Global climate evolution during the last deglaciation, *Proceedings of the National Academy of Sciences*, 109, E1134–E1142, 2012.
- Conte, M. H., M.-A. Sicre, C. Rühlemann, J. C. Weber, S. Schulte, D. Schulz-Bull, and T. Blanz, (2006), Global temperature calibration of the alkenone unsaturation index (UK'37) in surface waters and comparison with surface sediments, *Geochem. Geophys. Geosy.*, 7, Q02005. doi:10.1029/2005GC001054.
- Cooper, L.W., J. W. McClelland, R. M. Holmes, P. A. Raymond, J. J. Gibson, G. K. Guay, and B. J. Peterson (2008), Flow-weighted values of runoff tracers ($\delta^{18}\text{O}$, DOC, BA, alkalinity) from the six largest Arctic rivers, *Geophys. Res. Lett.*, 35, L18606, doi:10.1029/2008GL035007.
- Craig, H. (1965), Measurement of oxygen isotope paleotemperatures, in *Stable Isotopes in Oceanographic Studies and Paleotemperatures*, edited by: E. Tongiorgi, pp. 161-182, Cons. Naz. Delle Ric., Spoleto, Italy.
- Craig, H. and L. I. Gordon (1965), Deuterium and oxygen 18 variations in the ocean and the marine atmosphere, edited by E. Tongiorgi, pp. 9-130, Cons. Naz. Delle Ric., Spoleto, Italy.
- Crowley, T. (1992), North Atlantic deepwater cools the southern hemisphere, *Paleoceanography*, 7, 489-497.
- Curry, W. B., and D. W. Oppo (2005), Glacial water mass geometry and the distribution of $\delta^{13}\text{C}$ of ΣCO_2 in the western Atlantic Ocean, *Paleoceanography*, 20, PA1017, doi:10.1029/2004PA001021.
- Daley, T.J., F. A. Street-Perrott, N. J. Loader, K. E. Barber, P. D. M. Hughes, E. H. Fisher, and J. D. Marshall (2009), Terrestrial climate signal of the "8200 yr B.P. cold event" in the Labrador Sea region. *Geology*, 37, 831–834.
- Danabasoglu, G., S. C. Bates, B. P. Briegleb, S. R. Jayne, M. Jochum, W. G. Large, S. Peacock, and S. G. Yeager (2012), The CCSM4 Ocean Component, *J. Climate*, 25, 1361-1389, doi:10.1175/JCLI-D-11-00091.1.
- Dansgaard, W. (1964), Stable isotopes in precipitation, *Tellus*, 16, 436-468.
- Dansgaard, W., S. J. Johnsen, J. Møller, and C. C. J. Langway (1969), One thousand centuries of climatic record from Camp Century on the Greenland ice sheet, *Science*, 166, 377-381, doi:10.1126/science.166.3903.377.
- Dansgaard, W., S. J. Johnsen, H. B. Clausen, D. Dahl-Jensen, N. S. Gundestrup, C. U. Hammer, C. S. Hvidberg, J. P. Steffensen, A. E. Sveinbjörndóttir, J. Jouzel, and G. Bond (1993), Evidence for general instability of past climate from a 250-kyr ice-core record, *Nature*, 364, 218-220, doi:10.1038/364218a0.
- Delaygue, G., J. Jouzel, and J.-C. Dutay (2000), Oxygen 18-Salinity relationship simulated by an oceanic general circulation model, *Earth Planet. Sci. Lett.*, 178, 113–123, doi:10.1016/S0012-821X(00)00073-X.
- de Vernal, A., A. Rosell-Melé, M. Kucera, C. Hillaire-Marcel, F. Eynaud, M. Weinelt, T. Dokken, and M. Kageyama (2006), Comparing proxies for the reconstruction of LGM sea-surface conditions in the northern North Atlantic, *Quat. Sci. Rev.*, 25, 2820–2834, doi:10.1016/j.quascirev.2006.06.006.
- de Wit, J. C., C. M. van der Straaten, and W. G. Mook (1980), Determination of the absolute hydrogen isotopic ratio of V-SMOW and SLAP, *Geostandard. Newslett.*, 4, 33-36, doi:10.1111/j.1751-908X.1980.tb00270.x.

- Dokken, T. M., and E. Jansen (1999), Rapid changes in the mechanism of ocean convection during the last glacial period, *Nature*, 401, 458-461, doi: 10.1038/46753.
- Duplessy, J. C., P. Blanc, and A. W. H. Bé (1981), Oxygen-18 enrichment of planktonic foraminifera due to gametogenic calcification below the euphotic zone, *Science*, 213, 1247-1250.
- Duplessy, J.-C., N. J. Shackleton, R. G. Fairbanks, L. Labeyrie, D. Oppo, and N. Kallel (1988), Deep water source variations during the last climatic cycle and their impact on the global deep water circulation, *Paleoceanography*, 3, 343-360.
- Duplessy, J. C., L. Labeyrie, M. Arnold, M. Paterne, J. Duprat, and T. C. E. VanWeering (1992), Changes in surface salinity of the North Atlantic Ocean during the last deglaciation, *Nature*, 358, 485-488.
- Duplessy, J.-C., L. Labeyrie, and C. Waelbroeck (2002), Constraints on the ocean oxygen isotopic enrichment between the Last Glacial Maximum and the Holocene: Paleoceanographic implications, *Quat. Sci. Rev.*, 21, 315-330, doi:10.1016/S0277-3791(01)00107-X.
- Ehhalt, D. and K. Knott (1965), Kinetische Isotopentrennung bei der Verdampfung von Wasser, *Tellus*, 17, 389-397.
- Elderfield, H., P. Ferretti, M. Greaves, S. Crowhurst, I. N. McCave, D. Hodell, and A. M. Piotrowski (2012), Evolution of ocean temperature and ice volume through the mid-Pleistocene climate transition, *Science*, 337, 704-709.
- Emery, W. J. and J. Meincke (1986), Global water masses: summary and review, *Oceanol Acta*, 9, 383-391.
- Emiliani, C. (1955), Pleistocene temperatures, *J. Geol.*, 63, 538-578.
- Emiliani, C. (1966), Isotopic paleotemperatures, *Science*, 154, 851-857.
- EPICA Community Members et al., (2004), Eight glacial cycles from an Antarctic ice core, *Nature*, 429, 623-238.
- EPICA Community Members et al. (2006), One-to-one coupling of glacial climate variability in Greenland and Antarctica, *Nature*, 444, 195-198, doi:10.1038/nature05301.
- Epstein, S., R. Buchsbaum, H. A. Lowenstam, and H. C. Urey (1953), Revised carbonate-water isotopic temperature scale, *Geol. Soc. Am. Bull.*, 64, 1315-1325.
- Epstein, S., R. P. Sharp and A. J. Gow (1970), Antarctic ice sheet: stable isotope analyses of Byrd station cores and interhemispheric climatic implications, *Science*, 16, 1570-1572, doi:10.1126/science.168.3939.1570.
- Erez, J. and B. Luz (1983), Experimental paleotemperature equation for planktonic foraminifera, *Geochim. Cosmochim. Acta*, 47, 1025-1031.
- Errico, R. M. (1997), What Is an Adjoint Model?, *B. Am. Meteorol. Soc.*, 78, 2577-2591, doi:10.1175/1520-0477(1997)078<2577:WIAAM>2.0.CO;2.
- Ezat, M. M., T. L. Rasmussen, and J. Groeneveld (2014), Persistent intermediate water warming during cold stadials in the southeastern Nordic seas during the past 65 k.y., *Geology*, 42, 663-666.
- Fairbanks, R.G. (1989), A 17,000-year glacio-eustatic sea level record: influence of glacial melting rates on the Younger Dryas event and deep-ocean circulation. *Nature*, 342, 637-642, doi:10.1038/342637a0.
- Ferrari, R., M. F. Jansen, J. F. Adkins, A. Burke, A. L. Stewart, and A. F. Thompson (2014), Antarctic sea ice control on ocean circulation in present and glacial climates, *Proceedings of the National Academy of Sciences*, 111(24), 8753-8758.

- Fleitmann, D., S. J. Burns, M. Mudelsee, U. Neff, J. Kramers, A. Mangini, and A. Matter (2003), Holocene Forcing of the Indian Monsoon Recorded in a Stalagmite from Southern Oman, *Science*, 300, 1737-1739, doi:10.1126/science.1083130.
- Fraile, I., M. Schulz, S. Mulitza, and M. Kucera (2008), Predicting the global distribution of planktonic foraminifera using a dynamic ecosystem model, *Biogeosciences*, 5, 891-911, doi:10.5194/bg-5-891-2008.
- Freeman, E., L. C. Skinner, C. Waelbroeck, and D. Hodell (2016), Radiocarbon evidence for enhanced respired carbon storage in the Atlantic at the Last Glacial Maximum, *Nat. Commun.*, 7, 11998, doi: 10.1038/ncomms11998.
- Ganachaud, A. (2003), Large-scale mass transport, water mass formation, and diffusivities estimated from World Ocean Circulation Experiment (WOCE) hydrographic data, *J. Geophys. Res.*, 108, 3213, doi:10.1029/2002JC001565.
- Ganopolski, A., and D. M. Roche (2009), On the nature of lead-lag relationships during glacial-interglacial climate transitions, *Quat. Sci. Rev.*, 28, 3361-3378, doi:10.1016/j.quascirev.2009.09.019.
- Ganopolski, A., and V. Brovkin (2017), Simulation of climate, ice sheets and CO₂ evolution during the last four glacial cycles with an Earth system model of intermediate complexity, *Clim. Past*, 13, 1695-1716, doi:10.5194/cp-13-1695-2017.
- Ganssen, G. (1983), Dokumentation von küstennahem Auftrieb anhand stabiler Isotope in rezenten Foraminiferen vor Nordwest-Afrika, "Meteor"-Forschungsergebnisse 37C, 1-46.
- Gat, J. R. and R. Gonfiantini (Eds) (1981), Stable isotope hydrology: Deuterium and Oxygen-18 in the water cycle, Int. At. Energy Agency, Vienna.
- Gebbie, G. (2014), How much did glacial North Atlantic water shoal?, *Paleoceanography*, 29, 190–209, doi:10.1002/2013PA002557.
- Gebbie, G., and P. Huybers (2006), Meridional circulation during the Last Glacial Maximum explored through a combination of South Atlantic $\delta^{18}\text{O}$ observations and a geostrophic inverse model, *Geochem. Geophys. Geosyst.*, 7, Q11N07, doi:10.1029/2006GC001383.
- Gent, P. R. and J. C. McWilliams (1990), Isopycnal Mixing in Ocean Circulation Models, *J. Phys. Oceanogr.*, 20, 150–160, doi:10.1175/1520-0485(1990)020<0150:IMIOCM>2.0.CO;2.
- Gherardi, J.-M., L. Labeyrie, S. Nave, R. Francois, J. F. McManus, and E. Cortijo (2009), Glacial-interglacial circulation changes inferred from $^{231}\text{Pa}/^{230}\text{Th}$ sedimentary record in the North Atlantic region, *Paleoceanography*, 24, PA2204, doi: 10.1029/2008PA001696.
- Giering, R., and T. Kaminski (1998), Recipes for adjoint code construction, *ACM Trans. Math. Softw.*, 24(4), 437–474, doi:10.1145/293686.293695.
- Giraud X., and A. Paul (2010), Interpretation of the paleo–primary production record in the NW African coastal upwelling system as potentially biased by sea level change, *Paleoceanography*, 25:PA4224, doi:10.1029/2009PA001795.
- Gonfiantini, R. (1986), Environmental isotopes in lake studies, in *Handbook of Environmental Isotope Geochemistry*, v. 2, edited by: P. Fritz and J. C. Fontes, pp. 113-168, Elsevier, Amsterdam, Netherlands.
- Griffies, S. M., A. Biastoch, C. Böning, F. Bryan, G. Danabasoglu, E. P. Chassignet, M. H. England, R. Gerdes, H. Haak, R. W. Hallberg, W. Hazeleger, J. Jungclaus, W. G. Large, G. Madec, A. Pirani, B. L. Samuels, M. Scheinert, A. S. Gupta, C. A. Severijns, H. L. Simmons, A. M. Treguier, M. Winton, S. Yeager, and J. Yin (2009), Coordinated Ocean-ice Reference Experiments (COREs), *Ocean Model.*, 26, 1-46, doi:10.1016/j.ocemod.2008.08.007.
- Griffies, S. M., M. Winton, L. J. Donner, L. W. Horowitz, S. M. Downes, R. Farneti, A. Gnanadesikan, W. J. Hurlin, H.-C. Lee, Z. Liang, J. B. Palter, B. L. Samuels, A. T.

- Witternberg, B. L. Wyman, J. Yin, and N. Zadeh (2011), The GFDL CM3 Coupled Climate Model: Characteristics of the Ocean and Sea Ice Simulations, *J. Climate*, 24, 3520-3544, doi:10.1175/2011JCLI3964.1.
- Grootes, P. M., M. Stuiver, J. W. C. White, S. Johnsen, and J. Jouzel (1993), Comparison of oxygen isotope records from the GISP2 and GRIP Greenland ice cores, *Nature*, 366, 552-554.
- Hartmann, D. L. (1994), *Global Physical Climatology*, 1st edition, Volume 56, Academic Press, San Diego, 411 pp..
- Hays, J. D., T. Saito, N. D. Opdyke, and L. H. Burckle (1969), Pliocene-Pleistocene sediments of the equatorial Pacific: Their paleomagnetic, biostratigraphic and climate record, *Geol. Soc. Am. Bull.*, 80, 1481-1514.
- Hays, J. D., J. Imbrie, and N. J. Shackleton (1976), Variations in the Earth's orbit: Pacemakers of the ice ages, *Science*, 194, 1121-1132.
- Heimbach, P., C. Hill, and R. Giering (2002), Automatic Generation of Efficient Adjoint Code for a Parallel Navier-Stokes Solver, in: *Lecture Notes in Computer Science (LNCS)*, edited by: J.J. Dongarra, P.M.A. Sloot, and C.J.K. Tan, pp. 1019-1028, Springer-Verlag.
- Heimbach, P., C. Hill, and R. Giering (2005), An efficient exact adjoint of the parallel MIT General Circulation Model, generated via automatic differentiation, *Future Gener. Comput. Syst.*, 21(8), 1356–1371, doi:10.1016/j.future.2004.11.010.
- Heinrich, H. (1988), Origin and consequences of cyclic ice rafting in the Northeast Atlantic Ocean during the past 130,000 years, *Quaternary Res.*, 29, 142-152, doi:10.1016/0033-5894(88)90057-9.
- Hemming, S. R. (2004), Heinrich events: Massive late Pleistocene detritus layers of the North Atlantic and their global climate imprint, *Rev. Geophys.*, 42, RG1005, doi:10.1029/2003RG000128.
- Herguera, J. C., E. Jansen, and W. H. Berger (1992), Evidence for a bathyal front at 2000-M depth in the glacial Pacific based on a depth transect on Ontong Java Plateau, *Paleoceanography*, 7(3), 273–288, doi:10.1029/92PA00869.
- Hesse, T., M. Butzin, T. Bickert, and G. Lohmann (2011), A model-data comparison of $\delta^{13}\text{C}$ in the glacial Atlantic Ocean, *Paleoceanography*, 26, PA3220, doi:10.1029/2010PA002085.
- Howe, J. N. W., A. M. Piotrowski, T. L. Noble, S. Mulitza, C. M. Chiessi, and G. Bayon (2016), North Atlantic Deep Water Production during the Last Glacial Maximum, *Nat. Commun.*, 7:11765, doi:10.1038/ncomms11765.
- Huang, R. X. (1993), Real freshwater flux as a natural boundary condition for the salinity balance and thermohaline circulation forced by evaporation and precipitation, *J. Phys. Oceanogr.*, 23, 2428-2446.
- Hüls, C. M. (2000), Millennial-scale SST variability as inferred from Planktonic foraminiferal census counts in the western subtropical Atlantic, Ph.D. thesis, Christian Albrechts Univ., Kiel, Germany.
- Huffman, G. J., R. F. Adler, P. Arkin, A. Chang, R. Ferraro, A. Gruber, J. Janowiak, A. McNab, B. Rudolf, and U. Schneider (1997), The Global Precipitation Climatology Project (GPCP) Combined Precipitation Dataset, *B. Am. Meteorol. Soc.*, 78, 5-20.
- Hulbe, C. L., D. R. MacAyeal, G. H. Denton, J. Kleman, and T. V. Lowell (2004), Catastrophic ice shelf breakup as the source of Heinrich event icebergs, *Paleoceanography*, 19, PA1004, doi: 10.1029/2003PA000890.
- Hundsdoerfer, W. and R. A. Trompert (1994), Method of lines and direct discretization: a comparison for linear advection, *Appl. Numer. Math.*, 13, 469-490.

- Hut, G. (1987), Stable Isotope Reference Samples for Geochemical and Hydrological Investigations. Consultant Group Meeting IAEA, Vienna, 16-18 September 1985, Report to the Director General, International Atomic Energy Agency, Vienna, Austria.
- IAEA, (2012), Global Network of Isotopes in Rivers (GNIR), available at: http://www-naweb.iaea.org/napc/ih/IHS_resources_gnir.html (last access: 31 August 2016).
- IAEA/WMO, (2010), Global Network of Isotopes in Precipitation (GNIP), available at: http://www-naweb.iaea.org/napc/ih/IHS_resources_gnip.html (last access: 31 August 2016).
- Jackett, D. R. and T. J. McDougall (1995), Minimal adjustment of hydrographic profiles to achieve static stability, *J. Atmos. Ocean. Tech.*, 12, 381-389, doi:10.1175/1520-0426(1995)012<0381:MAOHPT>2.0.CO;2.
- Jacobs, S. S., R. G. Fairbanks, and Y. Horibe (1985), Origin and evolution of water masses near the Antarctic continental margin: Evidence from $H_2^{18}O/H_2^{16}O$ ratios in seawater, in *Oceanology of the Antarctic Continental Shelf*, edited by: S. S. Jacobs, vol. 43 of Antarctic Res. Ser., 59-85, AGU, Washington, D.C., doi:10.1029/AR043p0059.
- Johnsen, S. J., W. Dansgaard, H. B. Clausen, and C. C. Langway (1972), Oxygen isotope profiles through the Antarctic and Greenland ice sheet, *Nature*, 235, 429-434, doi:10.1038/235429a0.
- Johnsen, S. J., H. B. Clausen, W. Dansgaard, K. Fuhrer, N. Gundestrup, C. U. Hammer, P. Iversen, J. Jouzel, B. Stauffer, and J. P. Steffensen (1992), Irregular glacial interstadials recorded in a new Greenland ice core, *Nature*, 359, 311-313, doi:10.1038/359311a0.
- Johnsen, S. J., D. Dahl-Jensen, W. Dansgaard, and N. Gundestrup (1995), Greenland paleotemperatures derived from GRIP bore hole temperature and ice core isotopic profiles, *Tellus*, 47B, 624-629.
- Johnsen, S. J., D. Dahl-Jensen, N. Gundestrup, J. P. Steffensen, H. B. Clausen, H. Miller, V. Masson-Delmotte, A. E. Sveinbjornsdottir, and J. White (2001), Oxygen isotope and palaeotemperature records from six Greenland ice-core stations: Camp Century, Dye-3, GRIP, GISP2, Renland and NorthGRIP, *J. Quaternary Sci.*, 16, 299-307, doi:10.1002/jqs.622.
- Joussaume, S., R. Sadourny, and J. Jouzel (1984), A general circulation model of water isotope cycle in the atmosphere, *Nature*, 311, 24-29.
- Jouzel, J., C. Lorius, J. R. Petit, C. Genthon, N. I. Barkov, V. M. Kotlyakov, and V. M. Petrov (1987a), Vostok ice core: a continuous isotope temperature record over the last climatic cycle (160000 years), *Nature*, 329, 402-408.
- Jouzel, J., G. L. Russel, R. J. Suozzo, R. D. Koster, J. W. White, and W.S. Broecker (1987b), Simulations of the HDO and $H_2^{18}O$ atmospheric cycles using the NASA/GISS general circulation model: the seasonal cycle for present-day conditions, *J. Geophys. Res.*, 92, 14739-14760.
- Kahn, M. and D. F. Williams (1981), Oxygen and carbon isotopic composition of living planktonic foraminifera from the northeast Pacific Ocean, *Palaeogeogr. Palaeoclimatol.*, 33, 47-69, doi:10.1016/0031-0182(81)90032-8.
- Kallel, N., L. D. Labeyrie, A. Juillet-Laclerc, and J. C. Duplessy (1988), A deep hydrological front between intermediate and deep water masses in the glacial Indian Ocean, *Nature*, 333, 651-655.
- Karl, T. R. and K. E. Trenberth (2003), Modern global climate change, *Science*, 302, 1719-1723.
- Keigwin, L. D. (2004), Radiocarbon and stable isotope constraints on Last Glacial Maximum and Younger Dryas ventilation in the western North Atlantic, *Paleoceanography*, 19, PA4012, doi:10.1029/2004PA001029.

- Keigwin, L. D. and E. A. Boyle (2008), Did North Atlantic overturning halt 17,000 years ago?, *Paleoceanography*, 23.
- Keigwin, L., M. Bice, and N. Copley (2005), Seasonality and stable isotopes in planktonic foraminifera off Cape Cod, Massachusetts, *Paleoceanography*, 20, PA4011, doi:10.1029/2005PA001150.
- Khatiwala, S. P., R. G. Fairbanks, and R. W. Houghton (1999), Freshwater sources to the coastal ocean off northeastern North America: Evidence from $H_2^{18}O/H_2^{16}O$, *J. Geophys. Res.*, 104, 18,241-18,255, doi:10.1029/1999JC900155.
- Kim, S.-T. and J. R. O'Neil (1997), Equilibrium and non-equilibrium oxygen isotope effects in synthetic carbonates, *Geochim. Cosmochim. Acta*, 61, 3461-3475.
- Knies, J. and C. Vogt (2003), Freshwater pulses in the eastern Arctic Ocean during Saalian and Early Weichselian ice-sheet collapse, *Quaternary Res.*, 60, 243-251, doi:10.1016/j.yqres.2003.07.008.
- Kohfeld, K. E. and R. G. Fairbanks (1996), *Neogloboquadrina pachyderma* (sinistral coiling) as paleoceanographic tracers in polar oceans: Evidence from Northeast Water Polynya plankton tows, sediment traps, and surface sediments, *Paleoceanography*, 11, 676-699, doi:10.1029/96PA02617.
- Kretschmer, K., M. Kucera and M. Schulz (2016), Modeling the distribution and seasonality of *Neogloboquadrina pachyderma* in the North Atlantic Ocean during Heinrich Stadial 1, *Paleoceanography*, 31, 986-1010, doi:10.1002/2015PA002819.
- Kucera, M. (2007), Planktonic foraminifera as tracers of past oceanic environments, in *Developments in Marine Geology, Volume 1, Proxies in Late Cenozoic Paleoclimatology*, edited by: C. Hillaire-Marcel and A. De Vernal, Elsevier, Amsterdam, 213-262.
- Kucera, M., M. Weinelt, T. Kiefer, U. Pflaumann, A. Hayes, M. Weinelt, M.-T. Chen, A. C. Mix, T. T. Barrows, E. Cortijo, J. Duprat, S. Juggins, and C. Waelbroeck (2005), Reconstruction of sea-surface temperatures from assemblages of planktonic foraminifera: multi-technique approach based on geographically constrained calibration data sets and its application to glacial Atlantic and Pacific Oceans. *Quat. Sci. Rev.*, 24, 951-998, doi:10.1016/j.quascirev.2004.07.014.
- Kurahashi-Nakamura, T., A. Paul, and M. Losch (2017), Dynamical reconstruction of the global ocean state during the Last Glacial Maximum, *Paleoceanography*, 32, doi:10.1002/2016PA003001.
- Labeyrie, L. D., J. C. Duplessy, and P. L. Blanc (1987), Variations in mode of formation and temperature of oceanic deep waters over the past 125,000 years, *Nature*, 327, 447-483, doi:10.1038/327477a0.
- Labeyrie, L. D., J.-C. Duplessy, J. Duprat, A. Juillet-Leclerc, J. Moyes, E. Michel, N. Kallel, and N. Shackleton (1992), Changes in the vertical structure of the North Atlantic Ocean between glacial and modern times, *Quat. Sci. Rev.*, 11, 401-413, doi:10.1016/0277-3791(92)90022-Z.
- Lambeck K., H. Rouby, A. Purcell, Y. Sun, and M. Sambridge (2014), Sea level and global ice volumes from the last glacial maximum to the Holocene, *Proc. Natl. Acad. Sci. USA*, 111, 15296-15303.
- Lane, G. A. and M. Doyle (1956), Fractionation of oxygen isotopes during respiration, *Science*, 123, 574.
- Large, W. G. and S. G. Yeager (2004), Diurnal to decadal global forcing for ocean and sea-ice models: The data sets and flux climatologies, *NCAR Technical Note*, 4-15, doi:10.5065/D6KK98Q6.

- Large, W. G., G. Danabasoglu, S. C. Doney, and J. C. McWilliams (1997), Sensitivity to surface forcing and boundary layer mixing in a global ocean model: Annual-mean climatology, *J. Phys. Oceanogr.*, 27, 2418-2447, doi:10.1175/1520-0485(1997)027<2418:STSFAB>2.0.CO;2.
- Lea D.W., (2014), Elemental and Isotopic Proxies of Past Ocean Temperatures, in *Treatise on Geochemistry*, edited by: H. D. Holland, and K. K. Turekian, pp. 373-397, Oxford, Elsevier.
- Lehmann, M. and U. Siegenthaler (1991), Equilibrium oxygen- and hydrogen-isotope fractionation between ice and water, *J. Glaciol.*, 37, 23-26.
- Levitus, S. and T. Boyer (1994), *World Ocean Atlas 1994, Vol. 4: Temperature*, NOAA Atlas NESDIS 4.
- Levitus, S., R. Burgett, and T. Boyer (1994), *World Ocean Atlas 1994, Vol. 3: Salinity*, NOAA Atlas NESDIS 3.
- Lippold J., Y. Luo, R. Francois, S. E. Allen, J. Gherardi, S. Pichat, B. Hickey, and H. Schulz (2012), Strength and geometry of the glacial Atlantic Meridional Overturning Circulation. *Nat. Geosci.*, 5, 813–816.
- Lisiecki, L. E., and M. E. Raymo (2005), A Pliocene-Pleistocene stack of 57 globally distributed benthic $\delta^{18}\text{O}$ records, *Paleoceanography*, 20, PA1003, doi:10.1029/2004PA001071.
- Locarnini, R. A., A. V. Mishonov, J. I. Antonov, T. P. Boyer, H. E. Garcia, O. K. Baranova, M. M. Zweng, and D. R. Johnson (2010), *World Ocean Atlas 2009, Volume 1: Temperature*, edited by: Levitus, S., NOAA Atlas NESDIS, 68, 184 pp..
- Locarnini, R. A., A. V. Mishonov, J. I. Antonov, T. P. Boyer, H. E. Garcia, O. K. Baranova, M. M. Zweng, C. R. Paver, J. R. Reagan, D. R. Johnson, M. Hamilton, and D. Seidov (2013), *World Ocean Atlas 2013, Volume 1: Temperature*, edited by: S. Levitus, technical edited by: A. Mishonov, NOAA Atlas NESDIS, 73, 40 pp., 2013.
- Löfverström, M., and J. M. Lora (2017) Abrupt regime shifts in the North Atlantic atmospheric circulation over the last deglaciation, *Geophys. Res. Lett.*, 44, 8047–8055, doi:10.1002/2017GL074274.
- Lombard, F., L. Labeyrie, E. Michel, H. Speor, and D. W. Lea (2009), Modelling the temperature dependent growth rates of planktic foraminifera, *Mar. Micropaleontol.*, 70, 1-7.
- Losch, M., D. Menemenlis, J.-M. Campin, P. Heimbach, and C. Hill (2010), On the formulation of sea-ice models. Part 1: Effects of different solver implementations and parameterizations, *Ocean Model.*, 33, 129–144, doi:10.1016/j.ocemod.2009.12.008.
- Lumpkin, R., K. Speer, and K. Koltermann (2008), Transport across 48°N in the Atlantic Ocean, *J. Phys. Oceanogr.*, 38, 733-752, doi:10.1175/2007JPO3636.1.
- Lund, D., J. F. Adkins, and R. Ferrari (2011), Abyssal Atlantic circulation during the Last Glacial Maximum: Constraining the ratio between transport and vertical mixing, *Paleoceanography*, 26, PA1213, doi:10.1029/2010PA001938.
- Lund, D. C., A. C. Tessin, J. L. Hoffman, and A. Schmittner (2015), Southwest Atlantic water mass evolution during the last deglaciation, *Paleoceanography*, 30, doi:10.1002/2014PA002657.
- Lynch-Stieglitz, J. (2017), The Atlantic Meridional Overturning Circulation and abrupt climate change, *Annu. Rev. Mar. Sci.*, 9 83-104, doi:10.1146/annurev-marine-010816-060415.
- Lynch-Stieglitz, J., W. B. Curry, and N. Slowey (1999), A geostrophic transport estimate for the Florida Current from the oxygen isotope composition of benthic foraminifera, *Paleoceanography*, 14, 360–373, doi:10.1029/1999PA900001.

- Lynch-Stieglitz, J., W. B. Curry, D. W. Oppo, U. S. Ninneman, C. D. Charles, and J. Munson (2006), Meridional overturning circulation in the South Atlantic at the last glacial maximum, *Geochem. Geophys. Geosyst.*, 7, Q10N03, doi:10.1029/2005GC001226.
- Lynch-Stieglitz, J., J. F. Adkins, W. B. Curry, T. Dokken, I. R. Hall, J. C. Herguera, J. J.-M. Hirschi, E. V. Ivanova, C. Kissel, O. Marchal, T. M. Marchitto, I. N. McCave, J. F. McManus, S. Mulitza, U. Ninnemann, F. Peeters, E.-F. Yu, and R. Zahn (2007), Atlantic meridional overturning circulation during the Last Glacial Maximum, *Science*, 316, 66–69.
- Lynch-Stieglitz, J., M. W. Schmidt, L. G. Henry, W. B. Curry, L. C. Skinner, S. Mulitza, R. Zhang, and P. Chang (2014), Muted change in Atlantic overturning circulation over some glacial-aged Heinrich events, *Nature Geoscience*, 7, 144–150, doi: 10.1038/ngeo2045.
- MacAyeal, D. R., (1993), Binge/purge oscillations of the Laurentide ice sheet as a cause of the North Atlantic's Heinrich events. *Paleoceanography*, 8, 775–784.
- Mackensen, A., H.-W. Hubberten, N. Scheele, and R. Schlitzer (1996), Decoupling of $\delta^{13}\text{C}_{\text{SCO}_2}$ and phosphate in Recent Weddell Sea Deep and Bottom Water: Implications for glacial Southern Ocean paleoceanography, *Paleoceanography*, 11(2) 203–215.
- Majoube, M. (1971), Fractionnement en oxygène 18 et en deutérium entre l'eau et sa vapeur, *Journal de Chimie et de Physique*, 68, 1423–1436.
- Marchal, O., and W. B. Curry (2008), On the abyssal circulation in the glacial Atlantic, *J. Phys. Oceanogr.*, 38, 2014–2037, doi:10.1175/2008JPO3895.1.
- Marchitto, T. M., and W. S. Broecker (2006), Deep water mass geometry in the glacial Atlantic Ocean: A review of constraints from the paleonutrient proxy Cd/Ca, *Geochem. Geophys. Geosyst.*, 7, Q12003, doi:10.1029/2006GC001323.
- Marchitto T.M. Jr., D. W. Oppo, and W. B. Curry (2002), Paired benthic foraminiferal Cd/Ca and Zn/Ca evidence for a greatly increased presence of Southern Ocean Water in the glacial North Atlantic, *Paleoceanography*, 17, doi:10.1029/2000PA000598.
- Marchitto, T. M., W. B. Curry, J. Lynch-Stieglitz, S. P. Bryan, K. M. Cobb, and D. C. Lund (2014), Improved oxygen isotope temperature calibrations for cosmopolitan benthic foraminifera, *Geochim. Cosmochim. Ac.*, 130, 1–11, doi:10.1016/j.gca.2013.12.034.
- Marcott, S. A., P. U. Clark, L. Padman, G. P. Klinkhammer, S. R. Springer, Z. Liu, B. L. Otto-Bliesner, A. E. Carlson, A. Ungerer, J. Padman, F. He, J. Cheng, and A. Schmittner (2011), Ice-shelf collapse from subsurface warming as a trigger for Heinrich events, *Proc. Natl. Acad. Sci. U.S.A.*, 108, 13, 415–419, doi:10.1073/pnas.1104772108.
- MARGO Project Members et al. (2009), Constraints on the magnitude and patterns of ocean cooling at the Last Glacial Maximum, *Nat. Geosci.*, 2, 127–132, doi:10.1038/ngeo411.
- Marshall, J., A. Adcroft, C. Hill, L. Perelman and C. Heisey (1997a), A finite-volume, incompressible Navier Stokes model for studies of the ocean on parallel computers. *J. Geophys. Res.*, 102, 5753–5766.
- Marshall, J., C. Hill, L. Perelman, C. Heisey and A. Adcroft (1997b), Hydrostatic, quasi-hydrostatic and nonhydrostatic ocean modeling. *J. Geophys. Res.*, 102, 5733–5752.
- McCrea, J. M. (1950), On the isotopic chemistry of carbonates and a palaeotemperature scale, *J. Chem. Phys.*, 18, 849–857.
- McManus, J. F., R. Francois, J.-M. Gherardi, L. D. Keigwin, and S. Brown-Leger (2004), Collapse and rapid resumption of Atlantic meridional circulation linked to deglacial climate changes, *Nature*, 428, 834–837, doi:10.1038/nature02494.
- Meland, M. Y., T. M. Dokken, E. Jansen, and K. Hevroy (2008), Water mass properties and exchange between the Nordic seas and the northern North Atlantic during the period 23–6 ka: Benthic oxygen isotopic evidence, *P a l e o c e a n o g r a p h y*, 23, PA1210, doi:10.1029/2007PA001416.

- Melling, H. and R. M. Moore (1995), Modification of halocline source waters during freezing on the Beaufort Sea shelf: evidence from oxygen isotopes and dissolved nutrients, *Continental Shelf Res.*, 15, 89-113, doi:10.1016/0278-4343(94)P1814-R.
- Ménot-Combes, G., S. J. Burns, and M. Leuenberger (2002), Variations of $^{18}\text{O}/^{16}\text{O}$ in plants from temperate peat bogs (Switzerland): implications for paleoclimatic studies, *Earth Planet. Sc. Lett.*, 202, 419-434.
- Meredith, M. P., K. J. Heywood, R. D. Frew, and P. F. Dennis (1999), Formation and circulation of the water masses between the Southern Indian Ocean and Antarctica: Results from $\delta^{18}\text{O}$, *J. Mar. Res.*, 57, 449-470.
- Merkel, U., M. Prange, and M. Schulz (2010), ENSO variability and teleconnections during glacial climates, *Quat. Sci. Rev.*, 29, 86-100, doi:10.1016/j.quascirev.2009.11.006.
- Merlivat, L. and J. Jouzel (1979), Global climatic interpretation of the deuterium-oxygen 18 relationship for precipitation, *J. Geophys. Res.*, 84, 5029-5033, doi:10.1029/JC084iC08p05029.
- Miller, M. D., M. Simons, J. F. Adkins, and S. E. Minson (2015), The information content of pore fluid $\delta^{18}\text{O}$ and [Cl-], *J. Phys. Oc.*, 45, 2070-2094.
- Mix, A. C., W. F. Ruddiman, and A. McIntyre (1986), Late Quaternary paleoceanography of the Tropical Atlantic, 1: Spatial variability of annual mean sea-surface temperatures, 0-20,000 years B.P., *Paleoceanography*, 1, 43-66.
- Mix, A. C., E. Bard, and R. Schneider (2001), Environmental processes of the Ice Age: Land, oceans, glaciers (EPILOG), *Quat. Sci. Rev.*, 20, 627-657, doi:10.1016/S0277-3791(00)00145-1.
- Mollenhauer, G., J. F. McManus, A. Benthien, P. J. Müller, and T. I. Eglinton (2006) Rapid lateral particle transport in the Argentine Basin: molecular ^{14}C and $^{230}\text{Th}_{\text{xs}}$ evidence, *Deep Sea Res., Part I*, 53, 1224-1243, doi:10.1016/j.dsr.2006.05.005.
- Monnin, E., A. Indermühle, A. Dällenbach, J. Flückiger, B. Stauffer, T. F. Stocker, D. Raynaud, and J.-M. Barnola (2001) Atmospheric CO_2 Concentrations over the Last Glacial Termination, *Science*, 291, 112-114, doi: 10.1126/science.291.5501.112.
- Mook, W. (1982), The oxygen-18 content of rivers. *SCOPE* 52, 565-570.
- Mook, W. G. (2000), Environmental isotopes in the hydrological cycle: Principles and Applications, Vol. 1, UNESCO/IAEA, Paris/Vienna.
- Moos, C. (2000), Reconstruction of upwelling intensity and paleo-nutrient gradients in the northwest Arabian Sea derived from stable carbon and oxygen isotopes of planktic foraminifera, Ph.D. thesis, Faculty of Geosciences, University of Bremen, Bremen, Germany.
- Mortyn, P. G. and C. D. Charles (2003), Planktonic foraminiferal depth habitat and $\delta^{18}\text{O}$ calibrations: Plankton tow results from the Atlantic sector of the Southern Ocean, *Paleoceanography*, 18, 15-1-15-14, doi:10.1029/2001PA000637.
- Moschen, R., N. Kühl, I. Rehberger, and A. Lücke (2009), Stable carbon and oxygen isotopes in sub-fossil Sphagnum: assessment of their applicability for palaeoclimatology, *Chem. Geol.*, 259, 262-272.
- Muehlenbachs, K. and R. N. Clayton (1976), Oxygen Isotope Composition of the Oceanic Crust and its bearing on seawater, *J. Geophys. Res.*, 81, 4365-4369.
- Mulitza, S., D. Boltovskoy, D. Donner, H. Meggers, A. Paul, and G. Wefer (2003), Temperature: $\delta^{18}\text{O}$ relationships of planktic foraminifera collected from surface waters, *Palaeogeogr. Palaeoclimatol.*, 202, 143-152, doi:10.1016/S0031-0182(03)00633-3.
- Mulitza, S., B. Donner, G. Fischer, A. Paul, J. Pätzold, C. Rühlemann, and M. Segl (2004), The South Atlantic oxygen-isotope record of planktic foraminifera, in *The South Atlantic in the*

- Late Quaternary: Reconstruction of Mass Budget and Current Systems, edited by: G. Fischer and G. Wefer, 121-142, Springer, New York.
- Mulitza, S., I. Bouimtarhan, M. Bruening, A. Freeseemann, N. Gussone, H. Filipsson, G. Heil, S. Hessler, A. Jaeschke, H. Johnstone, M. Klann, F. Klein, K. Kuester, C. Maerz, H. McGregor, M. Minning, H. Mueller, W.-T. Ochsenhirt, A. Paul, M. Pokorna, F. Schewe, M. Schulz, J. Steinloechner, J.-B. Stuu, R. Tjallingii, T. von Dobeneck, S. Wiesmaier, M. Zabel, and C. Zonneveld (2006), Report and preliminary results of Meteor-Cruise M65/1 Dakar – Dakar, 11.06.-01.07.2005. Bremen.
- Mulitza, S., M. Prange, J.-B. Stuu, M. Zabel, T. von Dobeneck, A. C. Itambi, J. Nizou, M. Schulz, and G. Wefer (2008), Sahel megadroughts triggered by glacial slowdowns of Atlantic meridional overturning, *Paleoceanography*, 23, PA4206, doi:10.1029/2008PA001637.
- Mulitza, S., D. Heslop, D. Pittauerova, H. W. Fischer, I. Meyer, J.-B. Stuu et al. (2010), Increase in African dust flux at the onset of commercial agriculture in the Sahel region, *Nature*, 466, 226-228, doi:10.1038/nature09213.
- O'Neil, J. R. (1968), Hydrogen and oxygen isotopic fractionation between ice and water, *J. Phys. Chem.*, 72, 3683-3684, doi:10.1021/j100856a060.
- O'Neil, J. R., R. N. Clayton, and T. K. Mayeda (1969), Oxygen isotope fractionation in divalent metal carbonates, *J. Chem. Phys.*, 51, 5547-5558.
- Oppo, D. W., W. B. Curry, and J. F. McManus (2015), What do benthic $\delta^{13}\text{C}$ and $\delta^{18}\text{O}$ data tell us about Atlantic circulation during Heinrich Stadial 1?, *Paleoceanography*, 30, 353–368, doi:10.1002/2014PA002667.
- Otto-Bliesner, B. L., C. D. Hewitt, T. M. Marchitto, E. Brady, A. Abe-Ouchi, M. Crucifix, and S. Murakami (2007), Last Glacial Maximum ocean thermohaline circulation: PMIP2 model intercomparisons and data constraints, *Geophys. Res. Lett.*, 34, L12706, doi:10.1029/2007GL029475.
- Paul, A., S. Mulitza, J. Pätzold, and T. Wolff (1999), Simulation of oxygen isotopes in a global ocean model, in *Use of proxies in paleoceanography: examples from the South Atlantic*, edited by: G. Fisher and G. Wefer, pp 655-686, Springer, Berlin, Heidelberg, Germany.
- Paul, A., and C. Schäfer-Neth (2003), Modeling the water masses of the Atlantic Ocean at the Last Glacial Maximum, *Paleoceanography*, 18, 1058, doi:10.1029/2002PA000783.
- Pearson, P. N. (2012), Oxygen isotopes in foraminifera: overview and historical review, in: *Reconstructing Earth's Deep-time Climate*, edited by: L. C. Ivanov and B. T. Huber, *The Paleontological Society Papers*, 18, 1–38.
- Pedro, J. B., M. Jochum, C. Buizert, F. He, S. Barker, and S. O. Rasmussen (2018), Beyond the bipolar seesaw: Toward a process understanding of interhemispheric coupling, *Quat. Sci. Rev.*, 192, 27-46, doi:10.1016/j.quascirev.2018.05.005.
- Peeters, F. J. C. and G.-J. A. Brummer (2002), The seasonal and vertical distribution of living planktonic foraminifera in the NW Arabian Sea, in *Tectonic and Climate Evolution of the Arabian Sea Region*, Special Publication, 195, edited by: P. Clift, D. Kroon, C. Gaedicke, and J. Craig, Geological Society, London, 463-497.
- Peltier, W. R. (2004), Global glacial isostasy and the surface of the Ice-Age Earth: The ICE-5G (VM2) model and GRACE, *Annu. Rev. Earth Planet. Sci.*, 32, 111–149, doi:10.1146/annurev.earth.32.082503.144359.
- Pedro, J. B., M. Jochum, C. Buizert, F. He, S. Barker, and S. O. Rasmussen (2018), Beyond the bipolar seesaw: Toward a process understanding of interhemispheric coupling, *Quaternary Sci. Rev.*, 192, 27-46, doi:10.1016/j.quascirev.2018.05.005.
- Rasmussen, T.L., and E. Thomsen (2004), The role of the North Atlantic Drift in the millennial timescale glacial climate fluctuations, *Palaeogeogr. Palaeoecol.*, 210, 101–116, doi:10.1016/j.palaeo.2004.04.005.

- Ravelo, C. and C. Hillaire-Marcel (2007), The use of oxygen and carbon isotopes of foraminifera in Paleoceanography, in *Developments in Marine Geology, Volume 1, Proxies in Late Cenozoic Paleoceanography*, edited by: C. Hillaire-Marcel and A. de Vernal, Elsevier, Amsterdam, 735-764.
- Redi, M. H. (1982), Oceanic Isopycnal Mixing by Coordinate Rotation, *J. Phys. Oceanogr.*, 12, 1154–1158, doi:10.1175/1520-0485(1982)012<1154:OIMBCR>2.0.CO;2.
- Rippert, N., D. Nürnberg, J. Raddatz, E. Maier, E. Hathorne, J. Bijma, and R. Tiedemann (2016), Constraining foraminiferal calcification depths in the western Pacific warm pool, *Mar. Micropaleontol.*, 128, 14-27, doi:10.1016/j.marmicro.2016.08.004.
- Roche, D. M. (2013), $\delta^{18}\text{O}$ water isotope in the iLOVECLIM model (version 1.0) – Part 1: Implementation and verification, *Geosci. Model Dev.*, 6, 1481–1491, doi:10.5194/gmd-6-1481-2013.
- Roche, D. M. and T. Caley (2013), $\delta^{18}\text{O}$ water isotope in the iLOVECLIM model (version 1.0) – Part 2: Evaluation of the model results against observed $\delta^{18}\text{O}$ in water samples, *Geosci. Model Dev.*, 6, 1493-1504, doi:10.5194/gmd-6-1493-2013.
- Roche, D. M., D. Paillard, and E. Cortijo (2004a), Constraints on the duration and freshwater release of Heinrich event 4 through isotopes modelling, *Nature*, 432, 379-382.
- Roche, D. M., D. Paillard, A. Ganopolski, and G. Hoffmann (2004b), Oceanic oxygen-18 at the present day and LGM: Equilibrium simulations with a coupled climate model of intermediate complexity, *Earth Planet. Sci. Lett.*, 218, 317–330.
- Roche, D. M., D. Paillard, T. Caley, and C. Waelbroeck (2014), LGM hosing approach to Heinrich Event 1: results and perspectives from data-model integration using water isotopes, *Quat. Sci. Rev.*, 106, 247-261, doi:10.1016/j.quascirev.2014.07.020.
- Rohling, E. J. (2007), Progress in paleosalinity: Overview and presentation of a new approach, *Paleoceanography*, 22, PA3215, doi:10.1029/2007PA001437.
- Rohling, E. J. (2013), Oxygen isotope composition of seawater, in *Encyclopedia of Quaternary Science*, v.2, edited by: S. A. Elias, pp. 915-922, Amsterdam, Netherlands.
- Rohling, E. J. and G. R. Bigg (1998), Paleosalinity and $\delta^{18}\text{O}$: a critical assessment, *J. Geophys. Res.*, 103, 1307-1318, doi:10.1029/97JC01047.
- Rohling, E. J., P.A. Mayewski, and P. Challenor (2003), On the timing and mechanism of millennial-scale climate variability during the last glacial cycle, *Climate Dynamics*, 20, 257-267.
- Rohling, E. J., G. L. Foster, K. M. Grant, G. Marino, A. P. Roberts, M. E. Tamisiea, and F. Williams (2014), Sea-level and deep-sea-temperature variability over the past 5.3 million years, *Nature*, 508, 477-482.
- Rosenthal, Y., E. A. Boyle, and L. Labeyrie (1997), Last glacial maximum paleochemistry and deepwater circulation in the Southern Ocean: evidence from foraminiferal cadmium, *Paleoceanography*, 12, 787-796.
- Rosenthal, Y., G. P. Lohmann, K. C. Lohmann, and R. M. Sherrell (2000), Incorporation and preservation of Mg in Globigerinoides sacculifer: implications for reconstructing the temperature and O-18/O-16 of seawater. *Paleoceanography*, 15, 135–145, doi: 10.1029/1999PA000415.
- Rostek, F., G. Ruhland, F. Bassinot, P. Müller, L. Labeyrie, Y. Lancelot, and E. Bard (1993), Reconstructing sea surface temperature and salinity using $\delta^{18}\text{O}$ and alkenone records, *Nature*, 364, 319-321.
- Ruddiman, W. F. and A. McIntyre (1981), The mode and mechanism of the last deglaciation: oceanic evidence, *Quat. Res.*, 16, 125-134.

- Rühlemann, C. and M. Butzin (2006), Alkenone temperature anomalies in the Brazil-Malvinas Confluence area caused by lateral advection of suspended particulate material, *Geochem. Geophys. Geosyst.*, 7, Q10015, doi:10.1029/2006GC001251.
- Rühlemann C, S. Mulitza, G. Lohmann, A. Paul, M. Prange, and G. Wefer (2004), Intermediate depth warming in the tropical Atlantic related to weakened thermohaline circulation: combining paleoclimate data and modeling results for the last deglaciation, *Paleoceanography*, 19, PA1025, doi:10.1029/2003PA000948.
- Sarnthein, M., K. Winn, S. J. A. Jung, J.-C. Duplessy, L. Labeyrie, H. Erlenkeuser, and G. Ganssen (1994), Changes in East Atlantic Deepwater Circulation over the last 30,000 years: Eight time slice reconstructions, *Paleoceanography*, 9(2), 209–267, doi:10.1029/93PA03301.
- Sarnthein M. et al. (2001), Fundamental Modes and Abrupt Changes in North Atlantic Circulation and Climate over the last 60 ky — Concepts, Reconstruction and Numerical Modeling, in *The Northern North Atlantic*, edited by: P. Schäfer, W. Ritzrau, M. Schlüter, and J. Thiede, pp. 365-410, Springer, Berlin, Heidelberg.
- Schiebel, R. and C. Hemleben (2005), Modern planktic foraminifera, *Palaeont. Z.*, 79, 135-148.
- Schmidt G. A. (1998), Oxygen-18 variations in a global ocean model, *Geophys. Res. Lett.*, 25, 1201-1204.
- Schmidt, G. A., G. R. Bigg, and E. J. Rohling (1999), Global seawater oxygen-18 database, available at: <http://data.giss.nasa.gov/o18data> (last access: 08 July 2016).
- Schmidt, M. W., P. Chang, J. E. Hertzberg, T. R. II Them, L. Ji, and B. L. Otto-Bliesner (2012), Impact of abrupt deglacial climate change on tropical Atlantic subsurface temperatures, *PNAS*, 109, 14348-14352; doi:10.1073/pnas.1207806109.
- Schmittner, A., and D. C. Lund (2015), Early deglacial Atlantic overturning decline and its role in atmospheric CO₂ rise inferred from carbon isotopes ($\delta^{13}\text{C}$), *Clim. Past*, 11, 135-152, doi:10.5194/cp-11-135-2015.
- Schneider, R., A. Dahmke, A. Kölling, P. J. Müller, H. D. Schulz, and G. Wefer (1992), Strong deglacial minimum in the $\delta^{13}\text{C}$ record from planktonic foraminifera in the Benguela upwelling region: Palaeoceanographic signal or early diagenetic imprint?, in *Upwelling Systems: Evolution since the early Miocene*, edited by: C. P. Summerhayes, W. L. Prell, and K. C. Emeis, pp. 285-297, Geological Society Special Publication.
- Schrag, D. P., G. Hampt, and D. W. Murray (1996), Pore fluid constraints on the temperature and oxygen isotopic composition of the glacial ocean, *Science*, 272, 1930–1932.
- Schrag, D. P., J. F. Adkins, K. McIntyre, J. L. Alexander, D. A. Hodell, C. D. Charles, and J. F. McManus (2002), The oxygen isotopic composition of seawater during the Last Glacial Maximum, *Quat. Sci. Rev.*, 21, 331–342, doi:10.1016/S0277-3791(01)00110-X.
- Shackleton, N. J. (1967), Oxygen isotope analyses and Pleistocene temperatures reassessed, *Nature*, 215, 15–17.
- Shackleton, N. J. (1974), Attainment of isotopic equilibrium between ocean water and the benthonic foraminifera genus *Uvigerina*: Isotopic changes in the ocean during the last glacial, *Cent. Nat. Rech. Sci. Colloq. Int.*, 219, 203-209.
- Shackleton, N. J. (1987), Oxygen isotopes, ice volume and sea-level, *Quaternary Sci. Rev.*, 6, 183-190.
- Shackleton, N. J. (2000), The 100,000-year ice-age cycle identified and found to lag temperature, carbon dioxide, and orbital eccentricity, *Paleoceanography*, 25, PA1211, doi:10.1029/2009PA001833.

- Shackleton, N. J., M. A. Hall, and E. Vincent (2000), Phase relationships between millennial-scale events 64,000–24,000 years ago, *Paleoceanography*, 15, 565–569, doi:10.1029/2000PA000513.
- Shackleton, N. J., R. G. Fairbanks, T. Chiu, and F. Parrenin (2004), Absolute calibration of the Greenland time scale: implications for Antarctic time scales and for $\Delta^{14}\text{C}$, *Quat. Sci. Rev.*, 23, 1513-1522, doi:10.1016/j.quascirev.2004.03.006.
- Siddal, M., E. J. Rohling, A. Almogi-Labin, Ch. Hemleben, D. Meischner, I. Schmelzer, and D. A. Smeed (2003), Sea-level fluctuations during the last glacial cycle, *Nature*, 423, 853-858.
- Skinner, L. C., N. J. Shackleton, and H. Elderfield (2003), Millennial-scale variability of deep-water temperature and $d^{18}\text{O}_{\text{dw}}$ indicating deep-water source variations in the Northeast Atlantic, 0–34 cal. ka BP, *Geochem. Geophys. Geosyst.*, 4, 1098, doi:10.1029/2003GC000585.
- Spero, H. J. and D. W. Lea (1993), Intraspecific stable isotope variability in the planktonic foraminifer *Globigerinoides sacculifer*: results from laboratory experiments, *Mar. Micropaleontol.*, 22, 221-234.
- Spero, H. J. and D. W. Lea (1996), Experimental determination of stable isotope variability in *Globigerina bulloides*: implications for paleoceanographic reconstructions, *Mar. Micropaleontol.*, 28, 231-246.
- Spero, H. J., J. Bijma, D. W. Lea, and B. E. Bemis (1997), Effect of seawater carbonate concentration on foraminiferal carbon and oxygen isotopes, *Nature*, 390, 497-500.
- Stanford, J. D., E. J. Rohling, S. Bacon, A. P. Roberts, F. E. Grousset, and M. Bolshaw (2011), A new concept for the paleoceanographic evolution of Heinrich event 1 in the North Atlantic, *Quat. Sci. Rev.*, 30, 1047–1066.
- Stangeew, E. (2001), Distribution and isotopic composition of living planktonic foraminifera *N. pachyderma* (sinistral) and *T. quinqueloba* in the high latitude North Atlantic, Ph.D. thesis, Faculty of Mathematics and Natural Sciences, University of Kiel, Kiel, Germany.
- Stewart, M. K. (1975), Stable isotope fractionation due to evaporation and isotopic exchange of falling waterdrops: applications to atmospheric processes and evaporation of lakes, *J. Geophys. Res.*, 80, 1133-1146.
- Stocker, T. F. (1998), The seesaw effect, *Science*, 282 61-62.
- Stocker, T. F., and S. J. Johnsen (2003), A minimum thermodynamic model for the bipolar seesaw, *Paleoceanography*, 18, 1087, doi:10.1029/2003PA000920.
- Tharammal, T. (2013), Stable water isotopes in the global water cycle: Atmospheric model simulations and application to proxy data, Ph.D. thesis, University of Bremen, Bremen, Germany.
- Tharammal, T., A. Paul, U. Merkel, and D. Noone (2013), Influence of Last Glacial Maximum boundary conditions on the global water isotope distribution in an atmospheric general circulation model, *Clim. Past*, 9, 789-809, doi:10.5194/cp-9-789-2013.
- Thompson, L. G. (2000), Ice core evidence for climate change in the Tropics: implications for our future, *Quaternary Sci. Rev.*, 19, 19-35.
- Thornalley, D. J. R., H. Elderfield, and I. N. McCave (2010a), Intermediate and deep water paleoceanography of the northern North Atlantic over the past 21,000 years, *Paleoceanography*, 25, PA1211, doi:10.1029/2009PA001833.
- Thornalley, D. J. R., I. N. McCave, and H. Elderfield (2010b), Freshwater input and abrupt deglacial climate change in the North Atlantic, *Paleoceanography*, 25, PA1201, doi:10.1029/2009PA001772.
- Tindall, J., R. Flecker, P. Valdes, D. N. Schmidt, P. Markwick, and J. Harris (2010), Modelling the oxygen isotope distribution of ancient seawater using a coupled ocean-atmosphere GCM:

- Implication for reconstructing early Eocene climate, *Earth Planet. Sci. Lett.*, 292, 265–273, doi:10.1016/j.epsl.2009.12.049.
- Tomczak, M. and J. S. Godfrey (2003), *Regional Oceanography: An Introduction*, 2nd ed. New Delhi, Daya Publishing House, 390 pp.
- Trenberth, K. E., L. Smith, T. Qian, A. Dai, and J. Fasullo (2007), Estimates of the Global Water Budget and Its Annual Cycle Using Observational and Model Data, *J. Hydrometeorol.*, 8, 758-769, doi:10.1175/JHM600.1.
- Troupin, C., A. Barth, D. Sirjacobs, M. Ouberdous, J.-M. Brankart, P. Brasseur, M. Rixen, A. Alvera Azcarate, M. Belounis, A. Capet, F. Lenartz, M.-E. Toussaint, and J.-M. Beckers (2012), Generation of analysis and consistent error fields using the Data Interpolating Variational Analysis (Diva), *Ocean Model.*, 52-53, 90–101, doi:10.1016/j.ocemod.2012.05.002.
- Urey, H. C. (1947), The thermodynamic properties of isotopic substances, Liversidge lecture of 1946, *Journal of the Chemical Society*, 562–581.
- Volkman, R. and M. Mensch (2001), Stable isotope composition ($\delta^{18}\text{O}$, $\delta^{13}\text{C}$) of living planktic foraminifers in the outer Laptev Sea and Fram Strait, *Mar. Micropaleontol.*, 42, 163-188, doi:10.1016/S0377-8398(01)00018-4.
- Völpel, R., A. Paul, A. Krandick, S. Mulitza, and M. Schulz (2017), Stable water isotopes in the MITgcm, *Geosci. Model Dev.*, 10, 3125–3144, doi:10.5194/gmd-10-3125-2017.
- Völpel, R., S. Mulitza, A. Paul, J. Lynch-Stieglitz, and M. Schulz (in review), Water-mass vs. sea-level effects on benthic foraminiferal oxygen isotope ratios in the Atlantic during the LGM, *Paleoceanography and Paleoclimatology*.
- Voigt, I., A. P. S. Cruz, S. Mulitza, C. M. Chiessi, A. Mackensen, J. L. Lippold, B. Antz, M. Zabel, Y. Zhang, C. F. Barbosa, and A. A. Tisserand (2017), Variability in mid-depth ventilation of the western Atlantic Ocean during the last deglaciation, *Paleoceanography*, 32, 948–965, doi:10.1002/2017PA003095.
- Wadley, M. R., G. R. Bigg, E. J. Rohling, and A. J. Payne (2002), On modeling present-day and last glacial maximum oceanic $\delta^{18}\text{O}$ distributions, *Global Planet. Change*, 32, 89–109, doi:10.1016/S0921-8181(01)00084-4.
- Waelbroeck C., L. Labeyrie, E. Michel, J. C. Duplessy, J. F. McManus, K. Lambeck, E. Balbon, and M. Labracherie (2002), Sea-level and deep water temperature changes derived from benthic foraminifera isotopic records, *Quat. Sci. Rev.*, 21, 295-305.
- Waelbroeck, C., C. Levi, J.C. Duplessy, L. Labeyrie, E. Michel, E. Cortijo, F. Bassinot, and F. Guichard (2006), Distant origin of circulation changes in the Indian Ocean during the last deglaciation, *Earth and Planetary Science Letters*, 243, 244-251, doi:10.1016/j.epsl.2005.12.031.
- Waelbroeck, C., L. C. Skinner, L. Labeyrie, J.-C. Duplessy, E. Michel, N. Vazquez Riveiros, J.-M. Gherardi, and F. Dewilde (2011), The timing of deglacial circulation changes in the Atlantic, *Paleoceanography*, 26, PA3213, doi:10.1029/2010PA002007.
- Waelbroeck, C., T. Kiefer, T. Dokken, M.-T. Chen, H. Spero, S. Jung, M. Weinelt, M. Kucera, and A. Paul (2014), Constraints on surface seawater oxygen isotope change between the Last Glacial Maximum and the Late Holocene. *Quat. Sci. Rev.*, 105, 102–111, doi:10.1016/j.quascirev.2014.09.020.
- Walker, J. C. and K. C. Lohmann (1989), Why the oxygen isotopic composition of sea water changes with time. *Geophys. Res. Lett.*, 16, 323-326.
- Wang, Y. J., H. Cheng, R. L. Edwards, Z. S. An, J. Y. Wu, C. C. Shen, and J. A. Dorale (2001), A High-Resolution Absolute-Dated Late Pleistocene Monsoon Record from Hulu Cave, China, *Science*, 294, 2345-2348, doi:10.1126/science.1064618.

- Weldeab, S., T. Friedrich, A. Timmermann, and R. R. Schneider (2016), Strong middepth warming and weak radiocarbon imprints in the equatorial Atlantic during Heinrich 1 and Younger Dryas, *Paleoceanography*, 31, 1070-1082, doi:10.1002/2016PA002957.
- Werner, M., B. Haese, X. Xu, X. Zhang, M. Butzin, and G. Lohmann (2016), Glacial-interglacial changes in H₂¹⁸O, HDO and deuterium excess – results from the fully coupled ECHAM5/MPI-OM Earth system model, *Geosci. Model Dev.*, 9, 647-670, doi:10.5194/gmd-9-647-2016.
- Wilke, I., H. Meggers, and T. Bickert (2009), Depth habitats and seasonal distributions of recent planktic foraminifers in the Canary Islands region (29°N) based on oxygen isotopes, *Deep Sea Research Part I: Oceanographic Research Papers*, 56, 89-106, doi:10.1016/j.dsr.2008.08.001.
- Wunsch, C. (2016), Pore fluids and the LGM ocean salinity-reconsidered, *Quat. Sci. Rev.*, 135, 154–170.
- Xu, X., M. Werner, M. Butzin, and G. Lohmann (2012), Water isotope variations in the global ocean model MPI-OM, *Geosci. Model Dev.*, 5, 809-818, doi:10.5194/gmd-5-809-2012.
- Yi, Y., J. J. Gibson, L. W. Cooper, J.-F. Helle, S. J. Birks, J. W. McClelland, R. M. Holmes, and B. J. Peterson (2012), Isotopic signals (¹⁸O, ²H, ³H) of six major rivers draining the pan-Arctic watershed, *Global Biogeochem. Cy.*, 26, GB1027, doi:10.1029/2011GB004159.
- Yu, E.-F., R. Francois, and M. P. Bacon (1996), Similar rates of modern and last-glacial ocean thermohaline circulation inferred from radiochemical data, *Nature*, 379, 689-694.
- Zarriess, M., and A. Mackensen (2011), Testing the impact of seasonal phytodetritus deposition on δ¹³C of epibenthic foraminifer *Cibicides wuellerstorfi*: A 31,000 year high-resolution record from the northwest African continental slope, *Paleoceanography*, 26, PA2202, doi:10.1029/2010PA001944.
- Zhang, J., Z. Liu, E. C. Brady, D. W. Oppo, P. U. Clark, A. Jahn, S. A. Marcott, and K. Lindsay (2017), Asynchronous warming and δ¹⁸O evolution of deep Atlantic water masses during the last deglaciation, *Proc. Natl. Acad. Sci. USA*, 114, 11075-11080, doi:10.1073/pnas.1704512114.
- Zweng, M. M., J. R. Reagan, J. I. Antonov, R. A. Locarnini, A. V. Mishonov, T. P. Boyer, H. E. Garcia, O. K. Baranova, D. R. Johnson, D. Seidov, M. M. Biddle (2013), *World Ocean Atlas 2013, Volume 2: Salinity*, edited by: S. Levitus, technical edited by: A. Mishonov, NOAA Atlas NESDIS, 74, 39 pp..

Supplement S1 Technical Model Description

S1.1 MITgcm structure and compilation

The code of the MITgcm is structured in several layers. The core software is the base of any MITgcm simulation and provides a basic numerical and computational foundation (Figure S1.1, “Foundation Code”). It is the only layer that is not organized in packages, while the rest of the code within the MITgcm is given in packages, which is a useful way for the user to keep track of the code and help organizing and performing any specific experiment. Above the “Foundation Code” a number of computational packages are available (Figure S1.1, “General purpose computational packages”). These packages provide parallelism, reading and writing input and output data, and time-keeping functions implemented in non-numerical algorithms. The code for kernel numerical algorithms, which can be applied to many different simulation scenarios, are provided in the general purpose numerical packages above the latter layer (Figure S1.1, “General purpose numerical packages”). The top layer includes all packages that are specialized to specific simulation types, dealing with biogeochemical and tracer processes, coupled simulations, state estimation, ocean, atmosphere, and sea ice processes (Figure S1.1, “Specialized packages”). The two new packages, `wiso` and `balance`, developed within this project can be classified in the tracer subgroup of the “Specialized packages” and the “General purpose numerical packages”, respectively (Figure S1.1).

Below, a short overview on obtaining and building the code of the MITgcm is given.

The source code can be downloaded from:

http://mitgcm.org/public/source_code.html

in two ways, using the GitHub repository or a tar file. The advantages of using the GitHub is that it can record the history of the source files. Thus, each change of the source code is traceable, making it an efficient and elegant way to organize the code. Further, one can choose whether to obtain the latest source type or a specific release type like “`checkpoint64w`” as used in the current study. Additionally, there is always the possibility to upgrade from an earlier version to the most recent version without downloading the entire repository.

Either way, users will get a number of directories, as outlined in Table S1.1, containing the code layers outlined in Figure S1.1.

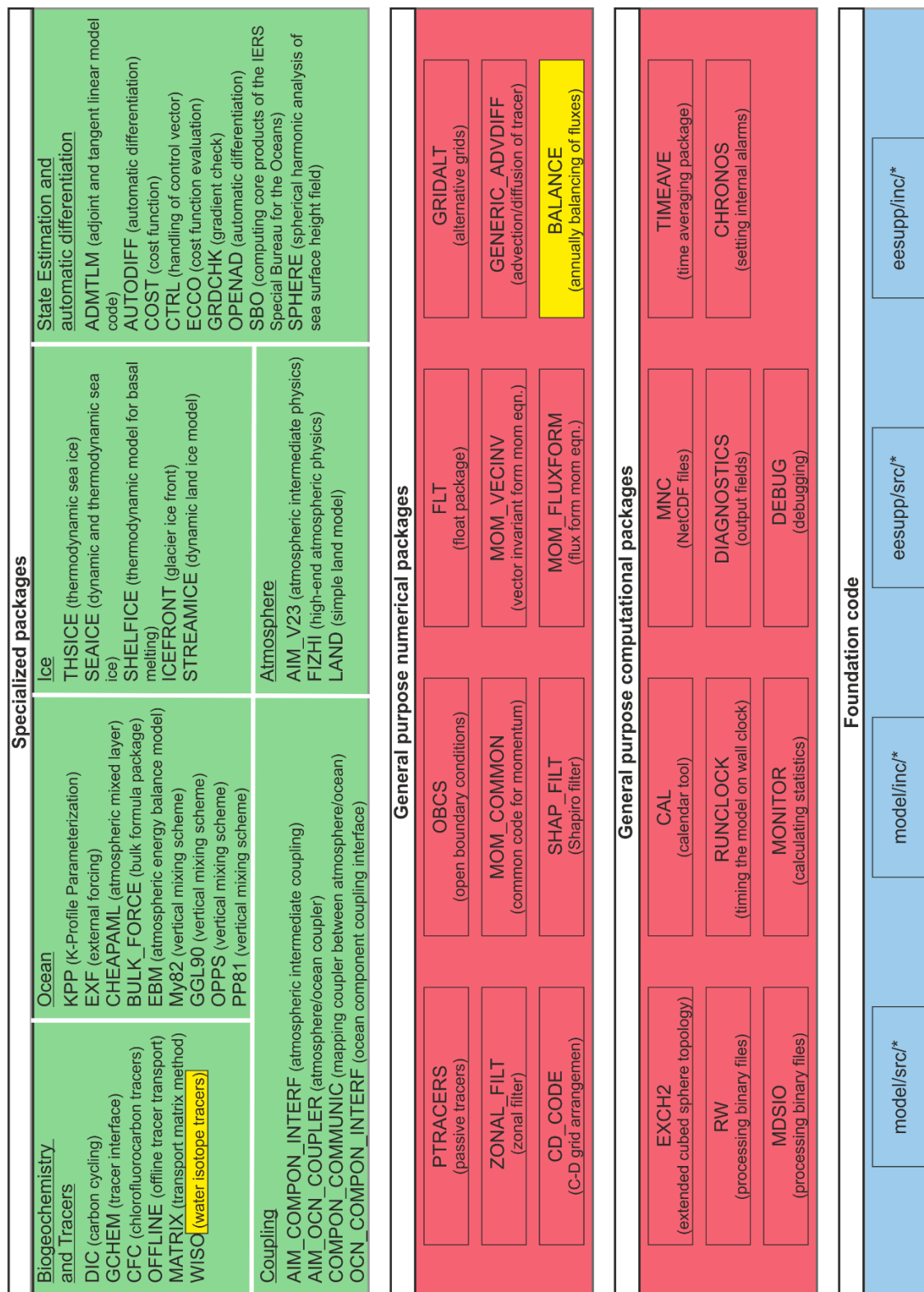


Figure S1.1: Structure of the code layers in the MITgcm. Short description or purpose of each package is given in brackets. For more details, readers are referred to the MITgcm User Manual [Adcroft et al., 2018]. Packages that have been newly developed within this study are highlighted in yellow. Figure adapted from Adcroft et al. [2018].

Table S1.1: Model directories of the MITgcm under the root tree and their purposes.

Directory	Purpose
doc	Brief documentation notes are located in here.
eesupp	The execution environment source code (wrapper) is located in here.
model	The main source code (core) is located in here.
pkg	All packages and their source code are located in here. Each package has one specific purpose. All packages can be individually turned on/off.
tools	Various useful tools such as the <code>genmake2</code> script to generate the users, makefile, and the compiler options for the different compilers and machines are located in here.
utils	This directory contains some useful utilities for pre-/post-processing, for example to read and process model output with MATLAB or Python.
verification	To get familiar with the MITgcm a few model examples are located in here that are documented and can be tested by the user.
jobs	Sample runtime shell scripts for running the MITgcm are located in here.
lsopt	Code for line search.
optim	Interface between the MITgcm and the line search code.

The most important directories are the `verification` directory to familiarize oneself with the MITgcm code, the `tools` directory for building the code and choosing the appropriate compiler for the system at hand, the `model` and `pkg` directories, which contain the main dynamics and optional numerics to run the users specific model experiment, and the `utils` directory for processing the model output.

The compilation of the code is performed by means of the `make` program, which uses a makefile that is created by the `genmake2` script provided by the MITgcm. This way, source files are pre-processed, compilers and optimization options are specified, and file dependencies are set. First, the user has to build the makefile using the command:

```
genmake2 -rootdir=/PATH/to/MITgcm/directory -mods=/PATH/to/code -
mpi -of /PATH/to/optfile
```

It is helpful to compile the code in a separate directory, e.g., `build`, especially when several simulations will be performed. This way, the simulation structure is easier to comprehend. The command line option `-rootdir` gives the path to the users' MITgcm source code, where all the directories outlined in Table S1.1 are located. Any alterations or modifications of the subroutines of the packages or main source code should be placed in the `code` directory, since the command line option `-mods` overrides the model source code with any identically-named files within this directory. The command line option `-mpi` enables Message Passing Interface (MPI) features to run the MITgcm using parallel computing. Determining the `optfile` used for a particular compilation is specified

by the command line option `-of`, which is the path to possible compilers located within the `tools` directory. After a successful execution the makefile is generated. Now, the dependencies have to be created, which is a list of files upon which other files depend on. This can be done with the command:

```
make depend
```

The last step is to compile the code with the command:

```
make
```

This way, the executable called `mitgcmuv` is created and the user is able to run its model simulation as outlined in section S1.4

S1.2 Packages overview

Apart from the newly developed packages `wiso` and `balance` a number of available packages were used for the current study. Below a brief description of each package is given.

DIAGNOSTICS package

The `diagnostics` package organizes the output of variables. There is a large selection of model diagnostics available, but none of them are enabled as default. Users must specify the diagnostics of interest and can even define new diagnostics in addition to the pre-defined ones. According to the periodic averaging interval set in `data.diagnostics`, the MITgcm will continually increment an array specifically allocated for the enabled diagnostics.

MNC package

The `mnc` package is a set of convenience routines that create, append, and read Network Common Data Form (NetCDF) files. NetCDF is a common file format for representing scientific data. This way, the output variables, as defined, e.g., in the `diagnostics` package, are conveniently arranged.

EXF package

The `exf` package prescribes the real-time external forcing fields of differing temporal forcing patterns. Climatological restoring and relaxation are comprised and bulk formulae to convert atmospheric fields to surface fluxes are implemented. Even on-the-fly interpolation of forcing fields on any grid onto the model grid are provided. Table S1.2

summarizes the atmospheric boundary conditions used in the current study to compute air-sea fluxes following the bulk forcing approach by *Large and Yeager* [2004].

Table S1.2: Atmospheric boundary condition files used in the current study.

Variable name	Description
uwind	Zonal surface wind velocity (m s^{-1})
vwind	Meridional surface wind velocity (m s^{-1})
wspeed	Surface wind speed (m s^{-1})
atemp	Surface air temperature ($^{\circ}\text{K}$)
aqh	Surface specific humidity (kg kg^{-1})
precip	Precipitation (m s^{-1})
snowprecip	Snow (m s^{-1})
runoff	River runoff (m s^{-1})
sdown	Downward shortwave radiation (W m^{-2})
ldown	Downward longwave radiation (W m^{-2})

SEAICE package

A dynamic and thermodynamic sea ice model with a viscous-plastic rheology can be coupled to the MITgcm via the `seaice` package. It uses a 2-category ice model to simulate ice thickness and concentration and includes “zero-layer” thermodynamics implying zero heat capacity for ice [*Losch et al.*, 2010].

GMREDI package

Coarse grid resolution models are not able to resolve eddies. The `gmredi` package parameterizes eddy-induced mixing. While the Gent-McWilliams (GM) scheme uses an advective flux to account for the transport effect of eddies [*Gent and McWilliams*, 1990], the Redi scheme uses a diffusion operator to mix properties along isopycnals [*Redi*, 1982].

PTRACERS package

The `ptracers` package initializes, advects, and diffuses passive tracers that do not affect the density of seawater.

GCHEM package

The `gchem` package provides a generic interface to the `ptracers` package. This way, any tracer experiment can be added to the code. Its purpose is to call the subroutines used by specific tracer experiments.

For overview purposes, Table S1.3 and Table S1.4 list all newly created subroutines and their purposes of the `wiso` and `balance` packages, which are also provided in the electronic appendix. Furthermore, each package contains header files. While `WISO.h` and `BALANCE.h` comprise all input fields and parameters stored as a COMMON Block of the respective package, `BALANCE_SIZE.h` determines the number of fields that will be cumulated and `BALANCE_OPTIONS.h` includes additional header files on which the `balance` package depends on.

Table S1.3: Name of the different subroutines of the `wiso` package and their purposes. The order of the subroutines corresponds to the calling tree within the MITgcm.

Subroutine	Purpose
<code>wiso_readparms</code>	Reads and initializes <code>wiso</code> package parameters from <code>data.wiso</code> .
<code>wiso_param</code>	Sets fixed <code>wiso</code> parameters needed for the tracer experiment.
<code>wiso_diagnostics_init</code>	Defines the diagnostics for the <code>wiso</code> package so that output files of the respective fields can be generated depending on the time averaging “frequency” in <code>data.diagnostics</code> .
<code>wiso_check</code>	Prints the <code>wiso</code> parameter summary and checks for consistency with the <code>exf</code> package.
<code>wiso_fields_load</code>	Reads in fields needed to calculate the tracer specific evaporation and surface fluxes.
<code>wiso_calc_evap</code>	Calculates the tracer specific evaporation.
<code>wiso_forcing</code>	Calculates the water isotope changes through air-sea fluxes. Further, diagnostics for output are filled within this subroutine.
<code>wiso_output</code>	Calls <code>wiso_monitor.F</code> .
<code>wiso_monitor</code>	When the <code>monitor</code> package is turned on, statistics like the minimum, maximum, mean, and standard deviation of the tracer fields are written as snapshots depending on the frequency “WISO_monfreq” set in <code>data.wiso</code> .

S1.3 Implementation of the `wiso` and `balance` packages into the source code

Both, the `wiso` and `balance` package have been embedded into the model source structure of the MITgcm as two separate packages. For the implementation, several files, which are provided in the electronic appendix, had to be modified. The `wiso` package is closely linked to the `gchem` package, which provides a structure where various tracer experiments can be added to the code by calling the different subroutines used for the

specific simulation. Thus, almost all modifications for the successful implementation of the `wiso` package affect the `gchem` package:

- GCHEM.h
- gchem_readparms.F
- gchem_init_fixed.F
- gchem_diagnostics_init.F
- gchem_check.F
- gchem_fields_load.F
- gchem_calc_tendency.F
- do_the_model_io.F

Changes within the `gchem_calc_tendency.F` subroutine are quite important, because it calls the `wiso` subroutines, which calculate the tracer specific evaporation and surface fluxes to determine the reactive tendencies. Without it, stable water isotopes would only be advected and diffused. Further, modifications within `GCHEM.h` allow that the `wiso` package is turned on/off.

Table S1.4: Name of the different subroutines of the `balance` package and their purposes. The order of the subroutine corresponds to the calling tree within the MITgcm.

Subroutine	Purpose
<code>balance_readparms</code>	Reads and initializes <code>balance</code> package parameters from <code>data.balance</code> .
<code>balance_init_varia</code>	Initializes all fields by setting them to zero.
<code>balance_fill_state</code>	Calls <code>balance_fill.F</code> and passes the field that has to be cumulated throughout a model year.
<code>balance_fill</code>	Calls <code>balance_fill_field.F</code> and passes the field that has to be cumulated throughout a model year. Additional constants are set within this subroutine that are needed in <code>balance_fill_field.F</code> .
<code>balance_fill_field</code>	Increments the counter, which determines the number of time steps a field has to be cumulated. Further, it sets the range of the field, calls <code>balance_field_cumulate.F</code> , and passes the field that has to be cumulated throughout a model year.
<code>balance_field_cumulate</code>	Cumulates the field.
<code>balance_write</code>	Checks whether it is time to calculate the time-average of the cumulated field. If so, it successively calls <code>balance_out.F</code> , <code>balance_clear.F</code> and <code>balance_calc_fac.F</code> .
<code>balance_out</code>	Calculates the time-average of the cumulated field.
<code>balance_clear</code>	Resets the fields and counters to zero.
<code>balance_calc_fac</code>	Calculates the correction factor for precipitation and tracer specific precipitation by means of the time-averaged fields.

The implementation of the `balance` package is slightly more extensive, since unlike the `wiso` package there is no main structure provided by a different package. Thus, it did not only affect different packages but also the model main source code as outlined above:

- `PARAMS.h`
- `packages_boot.F`
- `packages_readparms.F`
- `packages_init_variables.F`
- `forward_step.F`
- `do_the_model_io.F`
- `sea_ice_growth.F`
- `exf_getforcing.F`
- `exf_monitor.F`
- `wiso_fields_load.F`

While `PARAMS.h` and `packages_boot.F` are responsible for the `balance` package being a separate package that can be turned on/off individually, `packages_readparms.F`, `packages_init_variables.F`, `forward_step.F`, and `do_the_model_io.F` concern the calls of the different `balance` subroutines within the source code. Modifications within the packages (e.g., `exf` and `wiso`) refer to the application of the calculated correction factor to the respective precipitation field.

The `wiso` and `balance` packages both have to be located in the `pkg` directory of the MITgcm, while the modified files are copied into the `code` directory.

S1.4 Running the MITgcm with the `wiso` and `balance` packages

For the users' specific model simulation, a number of packages will be used. To select which packages will be compiled within the program a text file called `packages.conf` has to be created. It contains the list of package names for compilation and should be located in the `code` directory. Packages that are not listed in here are absent from the executable program and, cannot be activated afterwards. Thus, both “`wiso`” and “`balance`” have to be included for compilation. However, since the `wiso` package depends on the `gchem` and `ptracers` packages, both packages have to be included as well. Without them the compilation would fail. Some additional information for running passive tracers, like the stable water isotopes within the `wiso` package, are required. In `PTRACERS_SIZE.h` the number of tracers (here 3) that will be used is defined and in `GCHEM_OPTIONS.h` the compiler time option `GCHEM_SEPARATE_FORCING` has to be set to undefined,

```
#undef GCHEM_SEPARATE_FORCING
```

since changes due to the surface flux can easily be done within the regular tracer timestep.

To keep track of the different model simulations it is recommended to use different directories, e.g., `run` for the respective simulations. Both, the executable `mitcgmuv` and the input files have to be copied into the new directory. Further, even though the user already picked the different packages during compilation, they still have to be enabled at runtime by setting `usePACKAGENAME=.TRUE.` in `data.pkg`. This, on the other hand, does not refer to the `wiso` package. While both, the `gchem` and `ptracers` package are enabled in `data.pkg` the `wiso` package is turned on by setting `useWISO=.TRUE.` in `data.gchem`, which once more reveals the dependency on the `gchem` package. For each package a `data.packageName` file exists, where the runtime parameters are set. The `data.balance` file (shown below) contains the frequency in seconds, which determines the number of timesteps a field is cumulated.

`data.balance`

```
&BALANCE_LIST
  frequency = 31104000.,
&
```

Passive tracers are initialized by the `ptracers` package. Therefore a number of runtime parameters have to be set in `data.ptracers` (shown below). Whether the passive tracers are initialized from zero, from an initial file or read in from a pickup file is determined by `PTRACER_iter0`. If `PTRACERS_iter0 = nIter0` (`nIter0` is the start time of the model run) passive tracers are initialized from a file set in `PTRACERS_initialFile`. In case no file name exists, tracers are initially set to zero. If `PTRACERS_iter0 < nIter0`, then passive tracers are read from a pickup file. Further, the number of tracers used in the model simulation need to be set in `PTRACERS_numInUse`. Additionally, a number of parameters for each tracer can be set, including, e.g., the name (`PTRACERS_names`), whether to use the GM/Redi parameterization for isopycnal diffusion and eddy-induced mixing (`PTRACERS_useGMRedi`) and/or the K-Profile Parametrization (KPP) for vertical mixing (`PTRACERS_useKPP`) as well as the tracer concentration in freshwater (`PTRACERS_EvPrRn`). Since the isotopic surface fluxes are calculated within the `wiso` package, no additional concentration change through the freshwater flux is necessary and `PTRACERS_EvPrRn` is set to 0.

data.ptracers

```
&PTRACERS_PARM01
PTRACERS_numInUse=3,
PTRACERS_Iter0= 0,
# tracer 1 - h2o16
PTRACERS_names(1)='h2o16',
PTRACERS_long_names(1)='H2O',
PTRACERS_units(1)='mol/m^3',
PTRACERS_advScheme(1)=30,
PTRACERS_diffKh(1)=0.E3,
PTRACERS_diffKr(1)=3.E-5,
PTRACERS_useGMRedi(1)=.TRUE. ,
PTRACERS_useKPP(1)=.FALSE. ,
PTRACERS_initialFile(1)=' ',
PTRACERS_EvPrRn(1)= 0.,
# tracer 2 - h2o18
PTRACERS_names(2)='h2o18',
PTRACERS_units(2)='mol/m^3',
PTRACERS_advScheme(2)=30,
PTRACERS_diffKh(2)=0.E3,
PTRACERS_diffKr(2)=3.E-5,
PTRACERS_useGMRedi(2)=.TRUE. ,
PTRACERS_useKPP(2)=.FALSE. ,
PTRACERS_initialFile(2)=' ',
PTRACERS_EvPrRn(2)= 0.,
# tracer 3 - hdo
PTRACERS_names(3)='hdo',
PTRACERS_long_names(3)='HDO',
PTRACERS_units(3)='mol/m^3',
PTRACERS_advScheme(3)=30,
PTRACERS_diffKh(3)=0.E3,
PTRACERS_diffKr(3)=3.E-5,
PTRACERS_useGMRedi(3)=.TRUE. ,
PTRACERS_useKPP(3)=.FALSE. ,
PTRACERS_initialFile(3)=' ',
PTRACERS_EvPrRn(3)= 0.,
&
```

Fields that are required to calculate the tracer specific evaporation and surface fluxes within the `wiso` package are set in `data.wiso` (shown below). The unit of tracer specific precipitation and of river runoff is $\text{mol m}^{-2} \text{s}^{-1}$, while tracer specific humidity is read in kg kg^{-1} and wind speed in m s^{-1} . The wind speed file should be the same as for the `exf` package. Otherwise consistency is not given and the subroutine `wiso_check.F` will stop the simulation. Further, the frequency of snapshot output (`WISO_monfreq`) can be determined in here. If not, the default is set to the frequency of `monitorFreq`, which is set in the `data` file.

```
data.wiso
```

```
&WISO_FORCING
WISO_windFile      = 'wndSpd.bin',
WISO_preciph2o18File = 'precip_h2o18.bin',
WISO_preciphdoFile = 'precip_hdo.bin',
WISO_preciph2oFile  = 'precip_h2o16.bin',
WISO_aqhh2o18File  = 'hum_h2o18.bin',
WISO_aqhhdofile    = 'hum_hdo.bin',
WISO_aqhh2oFile    = 'hum_h2o16.bin',
WISO_runoffh2o18File = 'runoff_h2o18.bin',
WISO_runoffh2oFile  = 'runoff_h2o16.bin',
WISO_runoffhdoFile  = 'runoff_hdo.bin',
WISO_monFreq        = 3110400000.,
&
```

All files, depending on the users' specific simulation set up, have to be located in the `run` directory and the user can start the simulation with the following command:

```
mpirun -np 6 ./mitgcmuv > & output.txt
```

The number 6 determines the number of cores used during parallel computing. It is very helpful to redirect the output including error messages to the `output.txt` file in case the model encounters an error and stops.

During the simulation, the model produces a number of user defined output files depending on the variables set in the `diagnostics` package, either written according to a meta/data binary file format or as netCDF, which can be used for analysis.

S1.5 Electronic Appendix

In addition to the technical description of the MITgcm and the `wiso` and `balance` packages, an electronic appendix is handed in. It provides all subroutines, which have been adjusted and/or newly developed by the author, necessary for a successful simulation of the stable water isotopes within the MITgcm.

Supplement S2 Why do deep-sea $\delta^{18}\text{O}$ records resemble Antarctic temperature during Heinrich Events?

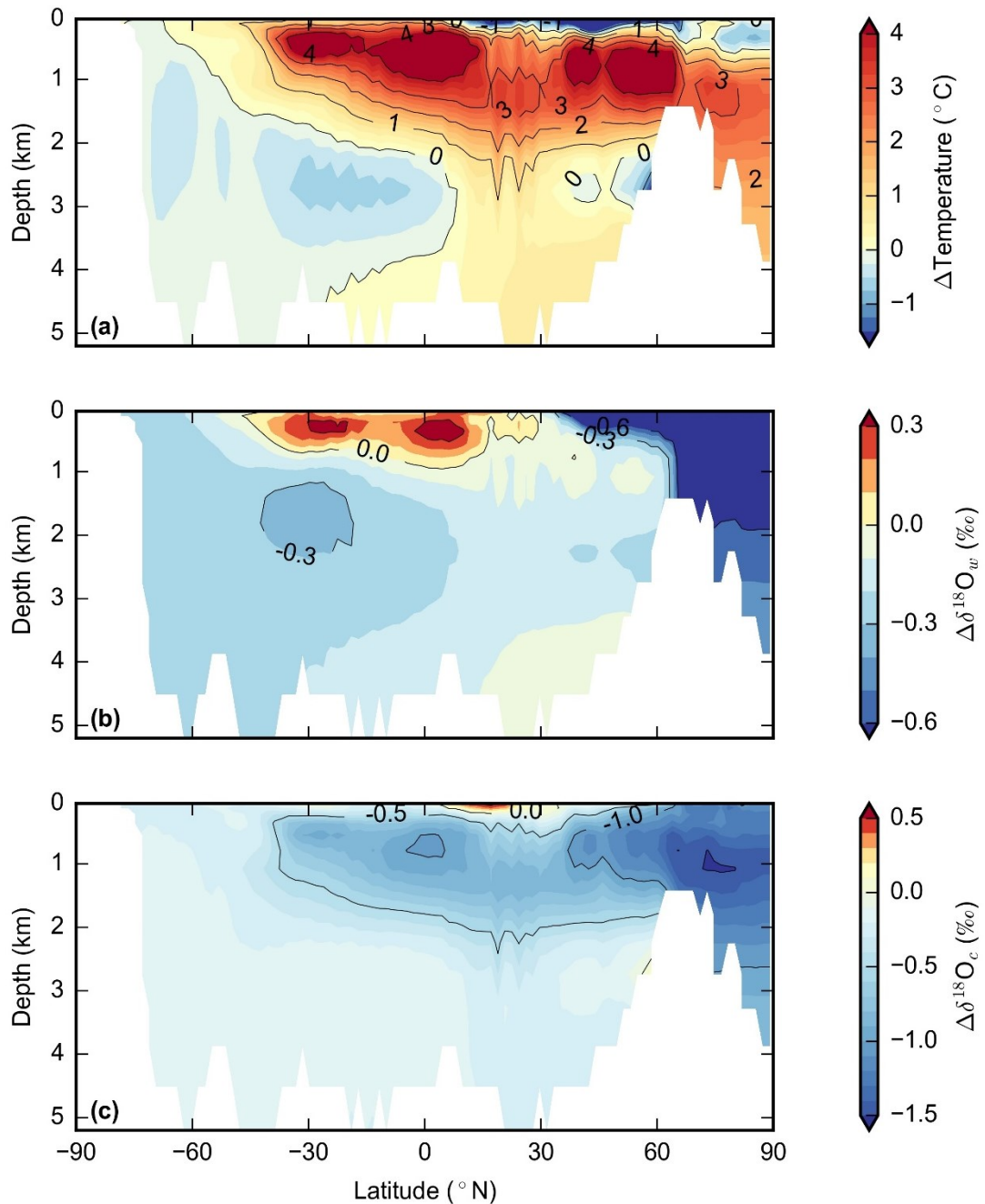


Figure S2.1: Atlantic zonally averaged (a) ΔT , (b) $\Delta\delta^{18}\text{O}_w$ and (c) $\Delta\delta^{18}\text{O}_c$. The anomalies (H1-LGM) were calculated by using the average of the last 100 years of each experiment.

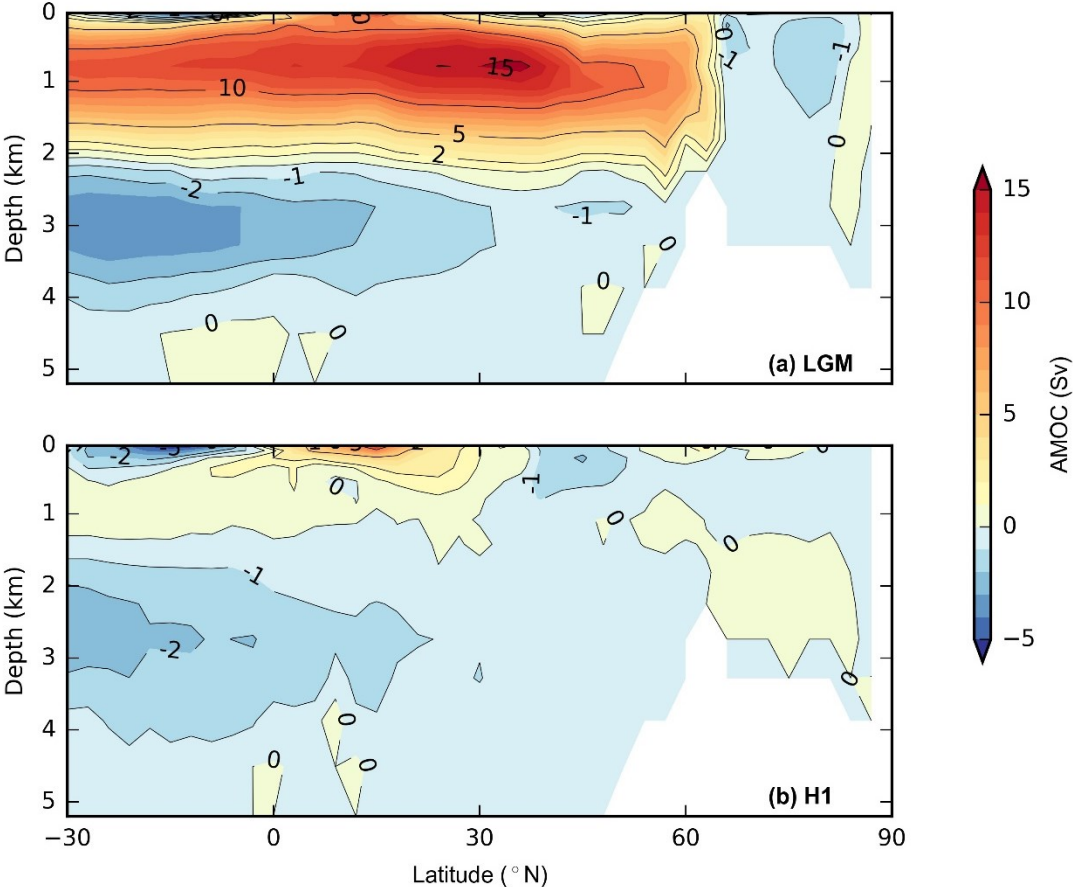


Figure S2.2: Stream function of the AMOC calculated for (a) the LGM and (b) the H1 averaged over the last 100 years of each simulation.

Acknowledgments

First, I would like to thank Prof. Dr. Michael Schulz for the opportunity to carry out this PhD project in his working group and within this exciting research field. The discussions and advice during our meetings were very helpful. I also would like to thank Prof. Dr. Michael Schulz and Prof. Dr. Heiko Pälike for reviewing my thesis.

Moreover, I would like to thank my supervisors André Paul and Stefan Mulitza for their constant support, guidance and trust throughout the years. Thank you for the many fruitful discussions and valuable ideas that helped me developing and advancing the thesis.

I would like to thank the DFG Research Center and MARUM for the financial support of the project and GLOMAR for funding my conference participation.

Furthermore, I am grateful to my colleagues. A special thanks goes to: Andreas Manschke for not only his technical support but also his open ears and spreading good mood and optimism around, Takasumi Kurahashi-Nakamura and Martin Losch for the many helpful discussions regarding the MITgcm, Ute Merkel for her moral support and encouraging words and Jeroen Groenefeld for sharing his expertise on foraminifera.

A big-thank you goes to my PhD fellows and friends from the geoscientific modeling group and FB1: Kerstin Kretschmer, Andrea Klus, Annegret Krandick and Tilia Breckenfelder. All the cheering up and happy moments we share are very special to me. These years would not have been as much fun without you guys. Thanks for your support!

Last but not least, I would like to thank those wonderful people who have accompanied me already before the PhD. Thanks for all the memorable activities we share including camping trips, cooking events and night outs with hilarious and profound conversations. In particular, I am thankful to my wonderful family including my parents, my sister and her family, as well as Stefan for all the positive distraction, long phone calls, never-ending support and encouragement. Thank you for always being there for me and believing in me, I could not have done it without you!